

Test of lepton flavour universality with rare beauty-quark decays at the LHCb experiment

Dissertation zur Erlangung des akademischen
Grades

Dr. rer. nat.

vorgelegt von

Alex Seuthe

geboren am 26.09.1993 in Hagen

Fakultät Physik
Technische Universität Dortmund

Dortmund, April 2022

Der Fakultät Physik der Technischen Universität Dortmund zur Erlangung des akademischen Grades eines Doktors der Naturwissenschaften vorgelegte Dissertation.

Gutachter:

Prof. Dr. Johannes Albrecht

Prof. Dr. Kevin Kröniger

Vorsitzende der Prüfungskommission:

Prof. Dr. Gudrun Hiller

Vertreter der wissenschaftlichen Mitarbeiter*innen:

Dr. Christian Sternemann

Datum der mündlichen Prüfung:

29. Juni 2022

Für Professor Dr. Bernhard Spaan, der am 9. Dezember 2021 viel zu früh von uns ging.

”Der Realitätsbegriff der Physik soll zuletzt so gefaßt werden, daß er die Totalität der Aspekte, wie sie sich für verschiedene Beobachter ergeben, vereint und daß er sie erklärt und verständlich macht; aber in ebendieser Totalität ist die Besonderheit der Gesichtspunkte nicht ausgelöscht, sondern aufbehalten und »aufgehoben«. In dieser ihrer Gesamtbewegung bestätigt und erfüllt die naturwissenschaftliche Erkenntnis innerhalb ihres eigenen Kreises ein allgemeines Aufbaugesetz des Geistes. Je mehr sie sich in sich selbst konzentriert und sich als das, was sie ist und will, begreift: um so klarer tritt das Moment heraus, in dem sie sich von allen andern Formen des Begreifens und Verstehens der Welt unterscheidet – und das Moment, das sie mit ihnen allen verbindet.”

Ernst Cassirer, Philosophie der symbolischen Formen: Dritter Teil: Phänomenologie der Erkenntnis, Felix Meiner Verlag, 2010, p.556.

Abstract

Recent measurements of the lepton flavour universality show evidence of a violation of the Standard Model of particle physics. However, further investigation with higher sensitivity is needed to either falsify or confirm the anomalies. This thesis describes the first simultaneous measurement of the lepton flavour universality ratios R_K with $B^+ \rightarrow K^+ \ell^+ \ell^-$ decays and $R_{K^{*0}}$ with $B^0 \rightarrow K^{*0} \ell^+ \ell^-$ decays using the entire current available data set of the LHCb experiment recorded during the years 2011 to 2018. Both ratios are evaluated in two regions of q^2 , which is the squared invariant mass of the dilepton system. Even though the central values of the results are kept blind and will only be published once the analysis has passed the collaboration-internal review process, the presented sensitivities on R_K and $R_{K^{*0}}$ already show that this will be the most precise test of lepton flavour universality with these decays to date. The analysis work described in this thesis comprises the first measurement of R_K at low q^2 at LHCb and an updated measurement of $R_{K^{*0}}$ with an enlarged data set. Statistical and systematic uncertainties as well as correlations between the four measurements are thus determined coherently for the first time and allow for improved interpretations. The calibration of the simulation used to determine the selection efficiency is a crucial component of the analysis to ensure that deviations of the measurements from the Standard Model expectation are not an effect due to remaining imperfections of the simulation. Therefore, a complex multi-stage calibration procedure has been developed together with an optimised selection strategy. Simulation of the signal decays is calibrated with the help of high-yield control samples chosen to minimise correlations between calibration and signal data sets. The experimental procedure of the analysis is validated by multiple stringent cross-checks.

Zusammenfassung

Jüngste Messungen der Lepton-Flavour-Universalität zeigen deutliche Hinweise auf eine Verletzung des Standardmodells der Teilchenphysik. Es sind jedoch weitere Untersuchungen erforderlich, um die Anomalien mit erhöhter Sensitivität zu bestätigen oder zu falsifizieren. Diese Dissertation beschreibt die erste simultane Messung der Lepton-Flavour-Universalitäts-Verhältnisse R_K mit $B^+ \rightarrow K^+ \ell^+ \ell^-$ -Zerfällen und $R_{K^{*0}}$ mit $B^0 \rightarrow K^{*0} \ell^+ \ell^-$ -Zerfällen unter Verwendung des gesamten derzeit verfügbaren Datensatzes des LHCb-Experiments, der in den Jahren 2011 bis 2018 aufgezeichnet wurde. Beide Verhältnisse werden in jeweils zwei Bereichen von q^2 , der quadrierten invarianten Masse des Dilepton-Systems, bestimmt. Auch wenn die Zentralwerte der Ergebnisse blind sind und erst veröffentlicht werden, wenn die Analyse den kollaborationsinternen Überprüfungsprozess durchlaufen hat, zeigen die vorgestellten Sensitivitäten für R_K und $R_{K^{*0}}$ bereits, dass dies der bisher genaueste Test der Lepton-Flavour-Universalität mit diesen Zerfällen sein wird. Die in dieser Dissertation beschriebene Analysearbeit umfasst die erste Messung von R_K im unteren q^2 -Bereich mit dem LHCb-Experiment und eine aktualisierte Messung von $R_{K^{*0}}$ mit einem vergrößerten Datensatz. Statistische und systematische Unsicherheiten sowie Korrelationen zwischen den vier Messungen werden dadurch erstmals kohärent bestimmt und ermöglichen verbesserte Interpretationen. Die Kalibrierung der Simulation, welche zur Bestimmung der Selektionseffizienz verwendet wird, ist ein entscheidender Bestandteil der Analyse, um sicherzustellen, dass eine mögliche Abweichung der Messung von der Erwartung des Standardmodells nicht ein Effekt durch verbliebene Imperfektionen der Simulation ist. Daher wurde ein komplexes mehrstufiges Kalibrierungsverfahren zusammen mit einer optimierten Selektionsstrategie entwickelt. Die Kalibrierung wird mit Hilfe von Kontrollkanälen durchgeführt, die so ausgewählt werden, dass die Korrelationen zwischen Kalibrierungs- und Signaldatensätzen minimiert werden. Das experimentelle Verfahren der Analyse wird durch mehrere stringente Cross-Checks validiert.

Contents

1	Introduction	1
2	Theoretical and experimental overview	5
2.1	The Standard Model of particle physics	5
2.1.1	Flavour physics	9
2.2	Rare $b \rightarrow s\ell^+\ell^-$ decays	11
2.2.1	Theoretical description	11
2.2.2	Phenomenology	13
2.3	Flavour anomalies in rare B -meson decays	14
2.3.1	Decay rate measurements	15
2.3.2	Angular analyses	17
2.3.3	Lepton flavour universality tests	17
2.3.4	Interpretation	21
3	The LHCb experiment at the LHC	25
3.1	The Large Hadron Collider at CERN	26
3.1.1	b -hadron production at the LHC	28
3.2	The LHCb detector	29
3.2.1	Track reconstruction system	31
3.2.2	Particle identification system	34
3.2.3	Trigger system	37
3.2.4	Electron reconstruction	40
3.2.5	Data processing and variable definitions	41
4	Author's contribution	45
5	Measurement strategy	45
5.1	Definition of signal regions and measured observables	47
5.2	Selection strategy	52
5.3	Efficiency measurement strategy	54
5.4	Yield measurement strategy	54
5.5	Data samples and simulation	55
6	Selection	57
6.1	Trigger selection	58
6.2	Reconstruction and stripping selection	59

6.3	Offline selection	61
6.3.1	Particle identification selection	62
6.3.2	Clone tracks	63
6.4	Exclusive background	64
6.5	Combinatorial and partially reconstructed background	66
6.5.1	Multivariate classification	67
6.5.2	Momentum imbalance technique	69
7	Calibration of simulation	71
7.1	Trigger configuration alignment	75
7.2	Particle identification	78
7.2.1	Calibration samples	79
7.2.2	PID calibration for hadrons and muons	79
7.2.3	PID calibration for electrons	80
7.2.4	Alternative calibration methods	83
7.3	Track reconstruction	83
7.4	Kinematics and event multiplicity	86
7.5	Trigger	87
7.5.1	L0 hardware trigger	88
7.5.2	HLT software trigger	94
7.6	Candidate reconstruction	99
7.7	Bin migration	102
8	Efficiencies	105
8.1	Geometric efficiency	105
8.2	Efficiency correlations	106
8.3	Measurement of the total calibrated efficiencies	107
9	Modelling of the invariant mass distributions	111
9.1	Fit ranges and fit setups	112
9.2	Signal descriptions in the rare and resonant modes	113
9.3	Background descriptions	113
9.4	Extended maximum likelihood fits to LHCb collision data	118
9.4.1	Fit sensitivities	122
10	Evaluation of systematic uncertainties	125
10.1	Uncertainties of the efficiencies	125
10.2	Uncertainties of the mass fits	128
10.3	Overall systematic uncertainties	130
11	Cross-checks	131
11.1	Integrated single ratio $r_{J/\psi}$	132
11.2	Integrated double ratio $R_{\psi(2S)}$	132
11.3	Differential single ratio $r_{J/\psi}$	133

11.4	Calibration dependency of the efficiency ratios	141
12	Conclusion and outlook	143
Appendices		
A	Appendix	149
A.1	Selection requirements	149
A.2	Track reconstruction calibration	153
A.3	Kinematic, multiplicity, and reconstruction calibration	159
A.4	HLT calibration weights	167
A.5	Geometric efficiencies	169
A.6	Total efficiencies by calibration step	171
A.7	Resonant mass fits	173
A.8	Cross-checks	175
	Bibliography	179
	Acknowledgement	199

1 Introduction

Since the dawn of physics, scientists have strived for a unified description of nature. Nicolaus Copernicus and Johannes Kepler tried to make sense of the course of the planets. Galileo Galilei attempted to unravel the natural laws of the sublunar cosmos. The outstanding achievement of Isaac Newton was to connect these two spheres in his famous axioms and the law of gravitation. Until the end of the 19th century, this tendency continued until classical physics seemed to have found its final theoretical description in the time of Hermann von Helmholtz and Gustav Kirchhoff. However, in the early 20th century, Max Planck, Albert Einstein, and others revolutionised the world of physics with their development of quantum physics and the theory of general relativity.

Since these paradigmatic changes, both the theories of the microcosm and gravity have been evolving. Gravitational waves, predicted 100 years ago by Einstein [1], were only found experimentally in 2016 [2]. In contrast to the gravitational theories, the Standard Model of particle physics describes the elementary particles and their interactions in the microcosm. It comprises three of the four known elementary forces of nature: the electromagnetic, weak, and strong force. The foundations of the theory were developed already in the 1960s [3–6]. It is the most accurate physical theory of the microcosm to date and provides precise descriptions of processes in high-energy particle physics. The theory predicted the existence of previously unknown particles, some of which were only experimentally detected decades later. For example, the Higgs boson was already postulated in 1964 [7–9], but experimentally observed by the ATLAS and CMS collaborations in 2012 [10, 11]. This discovery completes the observations of fundamental particles predicted by the Standard Model.

Consequently, one could speak of a conclusion of physics research in the field of elementary particle physics. But physics continues to face significant questions: for one thing, the unification of general relativity and the Standard Model in a higher-level theory is still pending. However, the Standard Model alone still offers intriguing mysteries like the particle mass hierarchy, dark matter and dark energy, or the amount of observed matter-antimatter asymmetries [12–19]. Together with other open questions, these findings suggest that the Standard Model can by no means be regarded as a complete theory. Therefore, the search for effects of potential new physics has continued, and these searches could hint at extensions or modifications to the Standard Model.

For many decades, research on these fundamental questions has been conducted with large-scale experiments, including those at the European Center for Nuclear Research (CERN). Since 2010, physicists have been using the Large Hadron Collider (LHC) to search for hints of new physics. This largest machine in the world is home to the four major experiments, ALICE, ATLAS, CMS, and LHCb, which are operated by

international collaborations of scientists. The effects of possible new physics are not yet observed but may occur on the one hand at very high energy scales that have not yet been investigated. On the other hand, potential new physics effects may occur with very weak couplings. For these two reasons, these experiments mainly investigate the decay products of high-energy proton-proton collisions, which the LHC provides. In so-called direct searches, unknown particles produced directly in the pp collisions could be detected via their decay products. However, their possible mass is kinematically constrained by the collision energy, allowing direct searches for particles with masses up to the order of $\mathcal{O}(1 \text{ TeV}/c^2)$.

Indirect searches look for evidence of new physics in quantum corrections, covering higher energy scales of up to $\mathcal{O}(100 \text{ TeV})$ [20, 21]. Here, small contributions from physics beyond the Standard Model can already lead to significant experimental deviations from the theoretical predictions. These indirect searches are usually performed as null tests of the Standard Model. Minor deviations between the predictions and precise experimental results can indicate new effects. In this case, possible new particles modify the rates of particular decays in loop processes, but are not detected directly. Rare decays are well suited for these measurements, since with more frequently occurring decays, small deviations would be hidden behind large signals from Standard Model processes.

The Large Hadron Collider beauty (LHCb) experiment is specialised for high-precision measurements in the field of flavour physics with hadrons containing b and c quarks. Two of the primary measurement types are studies of CP violation and the analysis of rare decays. Recent measurements with $b \rightarrow s\ell^+\ell^-$ transitions show anomalies in the sector of flavour physics, which deals with the transitions and decays of leptons and heavy quarks. The deviations can be interpreted within an effective field theory in a consistent picture (see. Section 2.3). Considering electroweak decays of b hadrons, according to the Standard Model the coupling strength of the leptons to the gauge bosons of the weak interaction is independent of their flavour. Thus, the interaction between the gauge bosons and all charged leptons is the same. This law is called lepton flavour universality (LFU) and is one of the fundamental features of the Standard Model. Some particularly meaningful observables used to test the LFU are ratios of branching fractions of two nearly-identical decays, but with electrons on one side and muons on the other in the final state. Thus, the observables $R_{K^{*0}}$ and R_K are defined as the ratios of the branching fractions of the decays $B^0 \rightarrow K^{*0}\mu^+\mu^-$ and $B^0 \rightarrow K^{*0}e^+e^-$, or $B^+ \rightarrow K^+\mu^+\mu^-$ and $B^+ \rightarrow K^+e^+e^-$, respectively.

Recent LHCb measurements of the ratio $R_{K^{*0}}$ show tensions with the SM predictions in the order of 2.1 to 2.5 standard deviations [22]. The most current LHCb measurement of R_K [23] shows an evidence of 3.1 standard deviations of a violation of LFU. Additionally, these results stand in the context of other experimental measurements by the LHCb collaboration and other experiments establishing a consistent picture of the “flavour anomalies”. Any further measurement of the ratios R_K and $R_{K^{*0}}$ is thus crucial to either falsify or strengthen the measured anomalies and advance the knowledge of the microcosm.

This thesis describes the experimental procedure of the first simultaneous measurement of the LFU ratios R_K and R_{K^*0} with the full LHCb data set recorded in the years 2011 to 2018. This data set corresponds to an integrated luminosity of 9.0 fb^{-1} with the collision energies of 7 TeV for 2011, 8 TeV for 2012, and 13 TeV for 2015 to 2018. The analysis is performed in two regions of the squared invariant mass q^2 of the dilepton system. They are defined as the low- q^2 region with $0.1 < q^2 < 1.1 \text{ GeV}^2/c^4$ and the central- q^2 region with $1.1 < q^2 < 6.0 \text{ GeV}^2/c^4$. This simultaneous analysis strategy allows correlations of the statistical and systematic uncertainties between the measurements of R_K and R_{K^*0} to be included for the first time. In addition, the simultaneous fits to all decay modes, trigger categories, and years of data taking allow for an accurate description of cross-feed background components.

The analysis includes the low- q^2 region for R_K , which is studied for the first time at the LHCb experiment. In addition, for the determination of R_{K^*0} , the complete LHCb data set including RUN 2 data, i.e., data recorded in 2015-2018, is exploited for the first time. In comparison to the previous measurements, an optimised choice of trigger categories is employed, leading to an improved precision by aligning the treatment of the electron and muon decay channels as much as possible. In addition, the whole analysis procedure is optimised and revisited.

Although the first measurement of R_K [24] relied on the cancellation of possible imperfections of the simulation in the ratio, this fact must be verified, and potential issues arising from simulation need to be excluded. Thus, a rigorous simulation calibration is needed to reduce possible imperfections of the final measurement. Therefore, this thesis presents a highly complex and sophisticated multi-step calibration chain, which is thoroughly validated.

Chapter 2 begins with an introduction to the Standard Model and the theory of flavour physics with an overview of the current flavour anomalies and an introduction to lepton flavour universality. Chapter 3 introduces the LHC and the LHCb experiment, which provided the data for this thesis. A general overview of the analysis strategy of the ratios R_K and R_{K^*0} can be found in Chapter 5. Chapter 6 describes the selection of the signal in these data. The calibration of the simulation, which is used to calculate the efficiencies, is covered in Chapter 7. Chapter 8 contains the calculation of the selection efficiencies, and Chapter 9 the extraction of the number of signal candidates with maximum likelihood fits to the distribution of their invariant masses. Chapter 10 and Chapter 11 present the determination of the systematic uncertainties, and the cross-checks for this analysis, which show the stability of the experimental procedure. Because the central values of the measurement are still blind at the time of the publication of this thesis, Chapter 12 provides an intermediate conclusion, including two aspects. First, the sensitivities for the measurements of R_K and R_{K^*0} are presented and compared to previous publications. Second, a summary of the impact and stability of the efficiency calibration summarises the effect of the overall efficiency calibration approach. It shows that, although the central values of the results are still blind, the suggested measurements will be the most precise as of today in all four q^2 regions for both decay modes.

2 Theoretical and experimental overview

This chapter comprises a short overview of the Standard Model as the current most precise theory of particle physics in Section 2.1. It includes a brief introduction to the field of flavour physics in Section 2.1.1. In this field, rare decays of the type $b \rightarrow s\ell^+\ell^-$ as a probe for new physics effects have increased attention recently. Section 2.2 depicts their theoretical description and their decay phenomenology. Section 2.3 summarises the recently observed flavour physics anomalies in rare B -meson decays. It includes a theoretical introduction and an experimental overview of the essential measurements of decays rates, angular observables, and tests of lepton flavour universality in Sections 2.3.1 to 2.3.3. Finally, Section 2.3.4 presents possible theoretical interpretations of the flavour anomalies.

2.1 The Standard Model of particle physics

The Standard Model of particle physics (SM) [3–6] is a relativistic quantum field theory that describes the fundamental particles and their interactions. In the following introduction, unless otherwise noted, reference is made to Ref.[25, 26].

Fundamental particles. The particle scheme in Fig. 2.1 shows an overview of the fundamental particles. The elementary constituents of matter are fermions with $\frac{1}{2}$ -integer spin and integer-spin bosons. The “flavour” distinguishes each unique particle type. The particles are six leptons and six quarks (q) and their antiparticles. Antiparticles of the six quarks and leptons have the same masses but inverted quantum numbers. The electron (e), muon (μ), and tau (τ) are the three families of leptons, comprising the group of charged leptons (ℓ). Each of these is associated with a neutral neutrino (ν_e, ν_μ, ν_τ). Similarly, there are three families in the quark sector. These three families consist of the up (u) and down (d) quarks, the charm (c) and strange (s) quarks, and the top (t) and beauty (b) quarks. The up-type quark group has an electromagnetic charge of $+\frac{2}{3}e$ and is made up of the u , c , and t quarks with the elementary charge e . The d , s , and b quarks form the group of down-type quarks having an electromagnetic charge of $-\frac{1}{3}e$. Colour charge is carried by quarks, with red, green, and blue as potential colours. Antiquarks carry anticolours, respectively. As a result, quarks can couple to the electroweak and strong interactions. In contrast, all leptons are colour neutral. Therefore, they can only couple electroweakly. In nature, quarks occur only in bound states as hadrons. The only exception from quarks that exist in bound states is the t

quark, which decays before building a bound state. Hadrons are particles composed of quarks, which are held together by the strong force. Here, mesons are quark systems made up of one quark and one antiquark ($q\bar{q}$), whereas baryons and antibaryons are made up of three quarks (qqq or $\bar{q}\bar{q}\bar{q}$). Particular important mesons for this thesis are the B^0 ($\bar{b}d$) meson with a mass of $(m = 5279.65 \pm 0.12) \text{ MeV}/c^2$ and the B^+ ($\bar{b}u$) meson with a mass of $m = (5279.34 \pm 0.12) \text{ MeV}/c^2$ [27]. Lighter mesons are the kaons K^+ ($u\bar{s}$) with a mass of $m = (493.677 \pm 0.016) \text{ MeV}/c^2$, K^0 ($u\bar{s}$, $m = (497.611 \pm 0.013) \text{ MeV}/c^2$), and the pions π^+ ($u\bar{d}$, $m = (139.57039 \pm 0.00018) \text{ MeV}/c^2$) and π^0 as a quantum mechanical superposition of the states $u\bar{u}$ and $d\bar{d}$ with a mass of $m = (134.9768 \pm 0.0005) \text{ MeV}/c^2$ [27]. There exist excited kaons with for example the K^{*0} , which decays into a charged kaon and a charged pion. This excited kaon is part of the decay which is investigated in this thesis as mentioned above. An example of a baryon is the proton, composed of two u quarks and one d quark. The Belle collaboration observed hadronic states compatible with quark systems composed of two quarks and two antiquarks, called tetra-quarks in 2003 [28]. These states were confirmed by the LHCb collaboration in 2017 [29]. Additionally, the LHCb collaboration published measurements of quantum states consistent with pentaquark systems composed of four quarks and one antiquark in 2015 [30], and more states in 2019 [31]. To date, a large number of other states, especially tetra-quark systems, have been discovered by the LHCb experiment [32, 33].

The mentioned fundamental particles of the SM have different masses on the order of $< 0.8 \text{ eV}/c$ of the electron neutrino and $172.76 \text{ GeV}/c^2$ of the top quark [27]. With the proton (uud) and the neutron (udd) all ordinary matter consists of those two light quarks, virtual quark-antiquark pairs, electrons in the electron shells of the atoms, and binding energy, so gluons and photons. In addition, there are the three almost massless neutrinos, which represent a permanent particle background. Because of their low interaction probability, neutrinos emitted by the Sun, for example, permanently penetrate the Earth without any noticeable effect. All other instable particles are created either in accelerator, in astronomical, or in atmospheric particle collisions or in nuclear decays. According to modern cosmological models they were also produced shortly after the Big Bang in the universe's early stages. Those particles are all unstable and decay rapidly into lighter particles.

Fundamental forces. The SM is a gauge theory with the group structure $SU(3)_C \times SU(2)_L \times U(1)_Y$. Here, the interactions of the elementary particles come about by gauge fields from invariances under local symmetry transformations. These fundamental forces are the electromagnetic, the strong, and the weak force. Particles with integer spin, called bosons, mediate the forces.

Within the theory of Quantum Chromodynamics (QCD) [6, 35], the $SU(3)_C$ group describes the strong force and creates the gluon fields, where C indicates the *colour charge*. This colour charge is conserved in the strong force interactions, which are mediated by gluons (g). Gluon-gluon coupling is possible as the gluons carry colour charge. Among the fundamental fermions, only quarks couple to the colour charge and thus the strong force because they can occur with three different colour charges.

Mass	2.16 MeV/c ²	1.27 GeV/c ²	172.76 GeV/c ²	0	125.25 GeV/c ²
Charge	+2/3	+2/3	+2/3	0	0
Spin	1/2	1/2	1/2	1	0
	u up	c charm	t top	g gluon	H Higgs boson
Quarks	4.67 MeV/c ²	93 MeV/c ²	4.18 GeV/c ²	0	
	-1/3	-1/3	-1/3	0	
	1/2	1/2	1/2	1	
	d down	s strange	b beauty	γ photon	
	0.511 MeV/c ²	105.7 MeV/c ²	1777 MeV/c ²	91.2 GeV/c ²	
	-1	-1	-1	0	
	1/2	1/2	1/2	1	
	e electron	μ muon	τ tau	Z Z boson	
Leptons	< 0.8 eV/c ²	< 0.19 MeV/c ²	< 18.2 MeV/c ²	80.4 GeV/c ²	
	0	0	0	±1	
	1/2	1/2	1/2	1	
	ν_e e neutrino	ν_μ μ neutrino	ν_τ τ neutrino	W W boson	
					Gauge Bosons

Figure 2.1 – Fundamental particles of the SM with values for the masses, electromagnetic charges and spins taken from Ref.[27]. The upper limit on the electron neutrino mass is taken from the recent publication of the KATRIN collaboration for the measurement of the electron antineutrino mass [34].

As the strong interaction strength α_s increases with distance, no colour-charged states can be observed freely in nature, but only colour-neutral bound states as hadrons, which is called *confinement*. Only the t quark decays so quickly that no hadronisation occurs. For high energies the coupling decreases, which is called *asymptotic freedom* [36, 37].

In the unified description of the electroweak force $SU(2)_L \times U(1)_Y$, three massless vector bosons W_1, W_2 , and W_3 are the generators of the $SU(2)_L$ symmetry and a massless vector boson B generates the $U(1)_Y$ symmetry. The W_i bosons only couple to left-handed (L) particles and right-handed antiparticles via the weak isospin T , where T_3 is its third component. In contrast, the B boson couples to the weak hypercharge Y independent of the weak isospin. The electroweak-interaction charges are connected to the electric charge Q through the equation $Y = Q - T_3$ [38, 39]. The SM does not include right-handed neutrinos as they do not couple to the weak interaction. The left-handed fermions exist as doublets of charged leptons and neutrinos or up- and down-type quarks pairs. In contrast to the left-handed fermions, right-handed fermions are defined as singlets in the SM and thus do not carry weak isospin.

In the Higgs mechanism [7–9], below the electroweak scale the $SU(2)_L \times U(1)_Y$ symmetry is spontaneously broken due to the non-vanishing vacuum expectation value of the Higgs field to $U(1)_Q$.

With that, the mediators of the forces are not the W_i or B bosons anymore but their linear combinations with

$$\begin{pmatrix} \gamma \\ Z \end{pmatrix} = \begin{pmatrix} \cos \theta_W & \sin \theta_W \\ -\sin \theta_W & \cos \theta_W \end{pmatrix} \begin{pmatrix} B \\ W_3 \end{pmatrix}, \quad (2.1)$$

with the weak mixing angle θ_W . Specifically, the massless photon (γ) is the exchange boson of the electromagnetic force coupling to Q . Neutrinos are thus the only fundamental fermions that are unaffected by the electromagnetic force. The mediators of the weak interaction are the neutral Z^0 boson and the W^\pm bosons, which are linear combinations of the $W_{1,2}$ bosons. Unlike the other gauge bosons, the Z^0 and W^\pm bosons gain mass due to the Higgs mechanism and are related by $\cos \theta_W = m_W/m_Z$ and couple to all twelve fermions.

As a consequence of introducing the scalar Higgs field ϕ , a massive particle with spin 0, the Higgs boson, is introduced. It was discovered by the ATLAS and CMS collaborations in 2012 [10, 11].

The Lagrangian of the Higgs field consists of a gauge interaction term, which couples to the electroweak bosons, a self-interaction term, and the *Yukawa interaction*. The Yukawa interaction term couples to the fermions. Thus the masses of the fermions are not generated by the Higgs mechanism but through the Yukawa interaction with the Higgs field.

Open questions of the SM. From cosmological measurements, the ordinary matter described by the SM accounts for only 5% of the energy distribution of our cosmos. Investigations of the rotational curves of galaxies and gravitational lensing show that there has to be additional mass, which experiments did not observe directly. Measurements of the propagation velocity of the universe show that also the energy density of the universe needs additional factors of size. Theories explain this by introducing hypothetical dark matter and dark energy [12–14], if there is no modification of the gravitational laws at long distances. However, the SM does not contain particles that are a suitable candidates to explain these two phenomena. Further investigations reveal that the SM’s anticipated imbalance of matter and antimatter is too tiny in comparison to astronomical data [18, 19]. Additionally, the SM has internal open questions: for example, it does not explain the hierarchy of the masses of the particles. The field of neutrino oscillations also still holds major open questions [15–17]. The SM also does not explain the structure of the gauge groups it consists of or the charges of the lepton families. In general, all hypothetical particles and effects that have not yet been discovered and are not described by the Lagrangian of the SM are called New Physics (NP). Many theoretical models that could extend the SM foresee new particles. Therefore, the search for new fundamental constituents is one of the main tasks of modern particle physics.

2.1.1 Flavour physics

Flavour physics deals with transitions and decays of leptons and quarks, such as the s , c , and b quark. Since the flavour quantum number refers to the particle type of the elementary particles, there are three different flavours in each of the quark and lepton sectors. In QCD the flavour quantum number is anchored as a global symmetry [25]. The electroweak theory violates this symmetry by decays via an exchange of a W boson in charged currents. The weak interaction couples to left-handed particles only, which leads to strong suppression of specific processes, such as the pion decay.

The Cabibbo-Kobayashi-Maskawa (CKM) matrix describes the transition amplitudes between different quarks as a quark-mixing matrix [40, 41]. Typically the up-type quarks are chosen in such a manner that the matrix \mathbf{V}_{CKM} transforms the eigenstates of the weak interaction d' , s' , and b' into the mass eigenstates d , s , and b , as shown in Eq. (2.2). The CKM matrix is a complex and unitary 3×3 matrix with the entries V_{ij} representing the probability of the quark q_j change into q_i , with

$$\begin{pmatrix} d \\ s \\ b \end{pmatrix} = \mathbf{V}_{\text{CKM}} \begin{pmatrix} d' \\ s' \\ b' \end{pmatrix} = \begin{pmatrix} V_{ud} & V_{us} & V_{ub} \\ V_{cd} & V_{cs} & V_{cb} \\ V_{td} & V_{ts} & V_{tb} \end{pmatrix} \begin{pmatrix} d' \\ s' \\ b' \end{pmatrix} = \begin{pmatrix} 0.97401 & 0.22650 & 0.00361 \\ 0.22636 & 0.97320 & 0.04053 \\ 0.00854 & 0.03978 & 0.999172 \end{pmatrix} \begin{pmatrix} d' \\ s' \\ b' \end{pmatrix}. \quad (2.2)$$

The values of the matrix shown without their uncertainties are taken from Ref.[27]. Because the diagonal entries have greater nominal values than the off-diagonal elements, the matrix structure implies that transitions within quark families are more likely than changes across families. Here, the changes occur under the exchange of a W^+ or W^- boson. Multiple experiments observe transitions of neutrinos in addition to quark transitions [15, 17, 42]. The PMNS matrix [43–45] is an equivalent of the theoretical description for the mixing of neutrinos. For charged leptons, on the other hand, no transition between generations can be detected. This fact leads to an equal coupling strength of the three lepton generations to the gauge fields within the SM, which is called lepton flavour universality (LFU). The Higgs symmetry breaking of the electroweak gauge group does not change this universality. The sole distinction between the interactions is due to the differing Yukawa interactions with the fermions.

Indirect measurements in flavour physics. So far, direct searches did not lead to evidences for heavy particles of NP in measurements by the ATLAS or CMS experiments at the LHC [46, 47].

But the history of flavour physics shows examples of so-called *indirect measurements*. For instance, after the experimental observation of the violation of the charge and parity symmetry, called CP violation, in K decays, the third quark family in the SM was predicted [41, 48]. However, their direct discovery happened much later as explained in Ref.[49]. As another example, the discovery of the $B^0 - \bar{B}^0$ mixing [50] could indirectly predict the large mass of the t quark, eight years before it was directly discovered [51, 52].

Thus, precision measurements in flavour physics can provide a complementary way to search. Indirect searches measure processes with only SM particles in the final state with high precision. Possible heavy particles in loop processes could influence decay rates or angular distributions of these decays. Their production could be possible because intermediate virtual particles can be significantly heavier than the initial and final state particles. Experimental deviations from the high precision theoretical predictions of the SM would indicate effects beyond the SM. Flavour-changing neutral currents (FCNCs) are processes in which the flavour of a fermion current changes while the electric charge remains constant. Although the SM forbids these processes at first order, they can occur at higher orders in loop diagrams. The decays are further suppressed by the GIM mechanism [53], creating a sensitive setting for NP searches. Quantum corrections involving heavy particles above the electroweak energy scale, for example, can be used to investigate energy scales in the order of $\mathcal{O}(50-100\text{TeV})$ [54-58] depending on the nature of possible NP effects. These effects at the loop level may influence decay rates and angular distributions of certain decays.

Rare decays. Today, in the search for NP effects, rare processes are examined. Their advantage is that small NP signals do not hide behind large SM signals, or effects of interference between the SM and NP processes can be seen if they are of similar magnitude. For this, particle physics of rare decays strives for ever higher precision in experiments and theoretical predictions. The LHCb experiment examines processes over many different scales of branching fractions. Fig. 2.2 shows these types of decays and their corresponding range of branching fractions. There are lepton-flavour-violating processes that are highly suppressed in the SM. Any increase in their branching fractions would be a clear hint for NP. Purely leptonic processes like the decay $B_{(s)} \rightarrow \mu^+ \mu^-$ are possible probes as well. Two types of decays showed intriguing hints for NP in recent years. On the one hand, there are semileptonic $b \rightarrow c\ell\nu$ decays, which occur via flavour changing charged currents (FCCC). On the other hand, the rare $b \rightarrow s\ell^+\ell^-$ FCNC processes occur via loop processes. In both decay types, the LHCb collaboration performs tests of LFU. A series of measurements from the LHCb experiment and other experiments investigating decays with the quark transition $b \rightarrow s\ell^+\ell^-$ show tensions with the SM (see Section 2.3). This thesis focuses on those rare $b \rightarrow s\ell^+\ell^-$ decays.

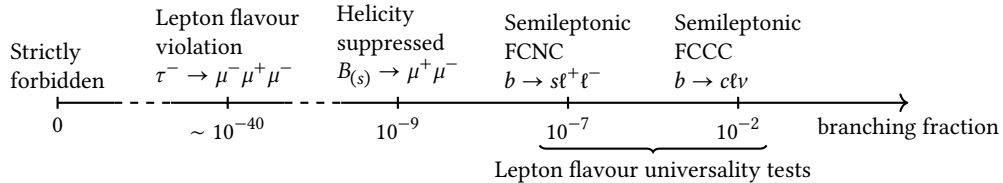


Figure 2.2 – Orders of magnitude of branching fractions for different processes that are studied at the LHCb experiment.

2.2 Rare $b \rightarrow s\ell^+\ell^-$ decays

The FCNC decay discussed in this thesis is the transition $b \rightarrow s\ell^+\ell^-$ with either muons or electrons in the final state. In this process, a b quark decays into an s quark with the emission of two charged leptons. Observables studied in $b \rightarrow s\ell^+\ell^-$ decays are branching fractions, angular distributions, and ratios of branching fractions that test lepton flavour universality (see Section 2.3.3). Since no tree-level neutral flavour-changing processes are allowed in the SM, this transition only occurs in loop processes which involve multiple charged transitions. Fig. 2.3 shows decay diagrams of the most common loop processes of this type. Here, a neutral current arises through the interaction of a charged current with the same fermion line entering twice. In an effective field theory the single diagrams are absorbed in the operators, which will be explained in detail in Section 2.2.1.

Because of their rarity, these decays provide an optimal resource for indirect NP searches as they are sensitive to small effects and possible tree diagram contributions from NP. Suppressed decays of B mesons, i.e., mesons containing a b quark, represent a particularly suitable system from both a theoretical and experimental point of view. These particles offer a very pure experimental signature, which will be explained in detail in Chapter 3. Refs.[59, 60] document early theoretical interest.

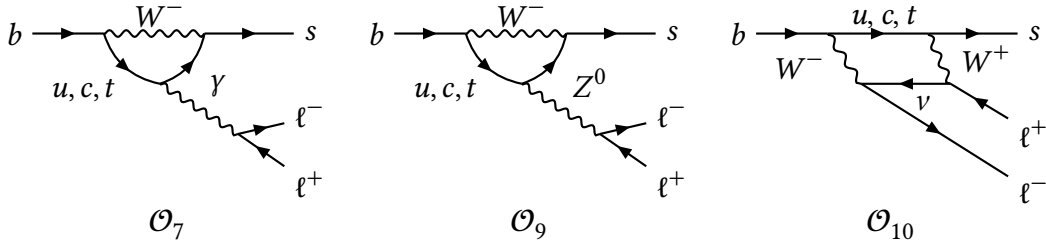


Figure 2.3 – Dominant decay diagrams for the decay $b \rightarrow s\ell^+\ell^-$ including the operators \mathcal{O}_7 , \mathcal{O}_9 , and \mathcal{O}_{10} .

2.2.1 Theoretical description

The $b \rightarrow s\ell^+\ell^-$ decays are a suitable NP probe from the theory point of view because precise predictions of observables sensitive to NP are possible. The energy scales of different factors included in this process are different, as can be seen in Fig. 2.4.

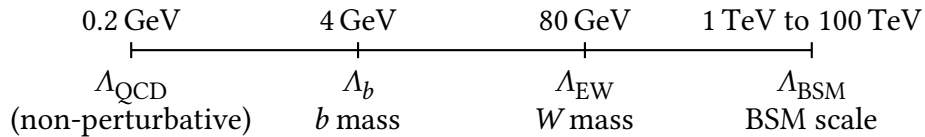


Figure 2.4 – Processes involved in $b \rightarrow s\ell^+\ell^-$ transitions at many different energy scales.

The mass of the b quark is significantly larger than the energy scale of QCD interactions Λ_{QCD} , where non-perturbative effects play a role. The b -quark mass, on the other hand, is substantially smaller than the electroweak energy scale, like the W and Z boson masses and the t -quark mass. This allows for a separation of the energy scales with the construction of an effective field theory (EFT) for the calculations of SM predictions.

With an operator product expansion (OPE), the EFT separates physical processes of different energy scales. It is designed analogously to the effective Fermi theory for the β -decay and is suitable for describing the dynamics of $b \rightarrow s\ell^+\ell^-$ decays mentioned before. The transition amplitude \mathcal{A} of a B meson decaying to the final state f is given by

$$\mathcal{A}(B \rightarrow f) = \langle f | \mathcal{H}_{\text{eff}} | B \rangle = \frac{G_F}{\sqrt{2}} V_{tb} V_{ts}^* \sum_{i=7,9,10} C_i(\mu) \langle f | \mathcal{O}_i(\mu) | B \rangle. \quad (2.3)$$

Here \mathcal{H}_{eff} is the effective Hamiltonian, G_F is the Fermi constant, and C_i as well as \mathcal{O}_i are the Wilson coefficients and operators depending on the energy μ . The b -quark mass is used as the threshold energy μ to separate the energy scales. The Wilson coefficients describe the high energy processes. Effects beyond the SM on high energy scales, such as heavy new particles, could modify these coefficients. According to the SM and in contrast to the Wilson operators, the Wilson coefficients can be calculated well in perturbation theory. They describe massive fields interacting at short distances and include the masses and couplings of heavy particles, such as the W and Z boson or t quark. Low-energy QCD effects that the current theory cannot describe in terms of perturbation theory are absorbed in the Wilson operators. These represent the effective vertices of the EFT with the Wilson coefficients as couplings. For $b \rightarrow s\ell^+\ell^-$ processes, the main contributing decay diagrams can be seen in Fig. 2.3. Shown are the photon emission operator \mathcal{O}_7 and the vector- and axial-vector transition operators \mathcal{O}_9 and \mathcal{O}_{10} . The operators have the form

$$\begin{aligned} \mathcal{O}_7 &= \frac{e}{16\pi^2} m_b (\bar{s} \sigma_{\mu\nu} P_R b) F^{\mu\nu} \\ \mathcal{O}_9 &= \frac{e^2}{16\pi^2} (\bar{s} \gamma_\mu P_L b) (\bar{\ell} \gamma^\mu \ell) \\ \mathcal{O}_{10} &= \frac{e^2}{16\pi^2} (\bar{s} \gamma_\mu P_L b) (\bar{\ell} \gamma^\mu \gamma_5 \ell), \end{aligned} \quad (2.4)$$

with the elementary charge e , tensors $\sigma_{\mu\nu} = i/2[\gamma_\mu, \gamma_\nu]$, and the electromagnetic field tensor $F^{\mu\nu}$. The left-handed chirality projectors are given as $P_L = (1 \mp \gamma_5)/2$ for the weak $V - A$ structure [61]. Fig. 2.5 shows the same processes but in the picture of the EFT, where the operators are shown as dashed blobs.

As explained in Section 2.1.1, the CKM matrix describes transitions of quark flavours. Thus, the quark transitions for the FCNC decay $b \rightarrow s\ell^+\ell^-$ depend on the quark flavours in the decay loop with the corresponding CKM matrix element. This flavour in the loop can be a t , c , or u quark. Due to the different sizes of the CKM matrix entries and its

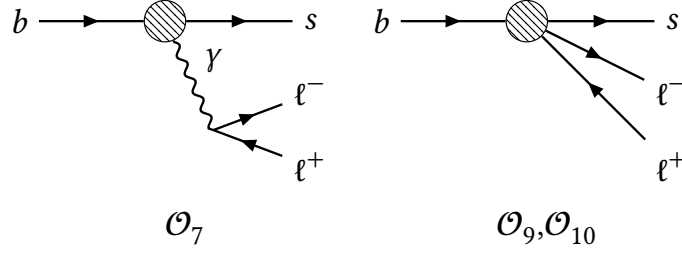


Figure 2.5 – $b \rightarrow s\ell^+\ell^-$ decays with the EFT approach. The dashed circles represent the local operators $\mathcal{O}_7, \mathcal{O}_9$, and \mathcal{O}_{10} corresponding to the radiative transition $b \rightarrow s\gamma \rightarrow s\ell^+\ell^-$ and the semileptonic FCNC $b \rightarrow s\ell^+\ell^-$ decays.

unitarity, the corresponding leading factor is the product of the matrix elements $V_{tb}V_{ts}^*$. The factor $V_{ub}V_{us}^*$ is Cabibbo suppressed. Purely leptonic or electroweak transitions such as the decay $b \rightarrow s\ell^+\ell^-$ have the advantage that no factors stemming from neutrinos in the decays have to be calculated. Similarly, in ratios of these decays with different lepton flavours, the CKM matrix-dependent fraction cancels out. In addition, theory predictions on non-local effects have significant uncertainties. They are limited to the hadronic fraction of these decays and cancel out in ratios of decay ratios as well. The cancellations of these two effects are another advantage of LFU ratios as will be described in Section 2.3.3.

2.2.2 Phenomenology

The processes studied in this thesis are the $B^0 \rightarrow K^{*0}\ell^+\ell^-$ and $B^+ \rightarrow K^+\ell^+\ell^-$ decays. The choice of charges written in the decays also implies the charge conjugated transitions. Both processes take place via $b \rightarrow s\ell^+\ell^-$ transitions with a q^2 -dependent decay rate $\frac{d\Gamma}{dq^2}$ as shown in Fig. 2.6. Here, q^2 is the momentum exchange in the $b \rightarrow s$ decays. Effectively this is the squared invariant mass $q^2 = m^2(\ell^+\ell^-)$ of the dilepton system. The dominant FCNC transitions, as shown in Fig. 2.3, lead to differential decay widths of the order of $\mathcal{O}(10^{-7})$ [62] in certain q^2 regions. An additional diagram appears near the photon pole with $q^2 = 0$, where the decay $b \rightarrow s\gamma \rightarrow s\ell^+\ell^-$ dominates. Thus, for the $B^0 \rightarrow K^{*0}e^+e^-$ decay near the photon pole, the electromagnetic photon Penguin operator C_7 dominates the spectrum. In Penguin decays, a quark changes its flavour in a loop with a Z or W boson interaction, while this quark further interacts in a tree-level transition (see the first diagram in Fig. 2.3). This effect is not apparent for the decay $B^+ \rightarrow K^+\ell^+\ell^-$ because the decay $B^+ \rightarrow K^+\gamma$ is not allowed due to spin conservation. It is not possible to combine the photon with a spin of 1 and the kaon with a spin of 0 to the B^+ meson with a spin of 0. Differences between the masses of electrons and muons in the lower q^2 region also lead to differences in the decay widths due to kinematic production differences of the leptons. In the region of light meson resonances such as η , $\rho(770)$, $\omega(782)$, $\eta'(958)$, and $\phi(1020)$, FCNC decays of the $b \rightarrow s$ and $b \rightarrow d$ transitions play a role. However, the branching fractions of the light meson resonances decaying into two leptons are of the order of $\mathcal{O}(10^{-4})$.

Consequently, the above decays are dominant. In q^2 regions around the charmonium resonances J/ψ and $\psi(2S)$, the spectrum is dominated by tree-level $b \rightarrow \bar{c}s$ decays. The charmonium resonances are composed of a c and a \bar{c} quark. In these decays, experiments confirmed LFU already to the percent level. Within the decay spectrum shown, charmonium resonances centre around a q^2 value of $9.6 \text{ GeV}^2/c^4$ for the J/ψ resonance and $13.6 \text{ GeV}^2/c^4$ for the $\psi(2S)$ resonance. Their decays are not proceeding through FCNC processes but are an inherent part of the collected data sets of the LHCb experiment. As a consequence, the two resonant regions are excluded in the analysis of the rare decays and are used as calibration and normalisation channels (see Chapter 5).

Form factor uncertainties and non-resonant $\bar{c}\bar{c}$ loop diagrams determine the SM theory uncertainties primarily. Consequently, as mentioned above, they only concern the hadronic decay part and cancel out outside the photon pole region in the observables' ratios. The region above the $\psi(2S)$ resonance is called the "high- q^2 region", where broad charmonium states occur that pollute the signal distributions.

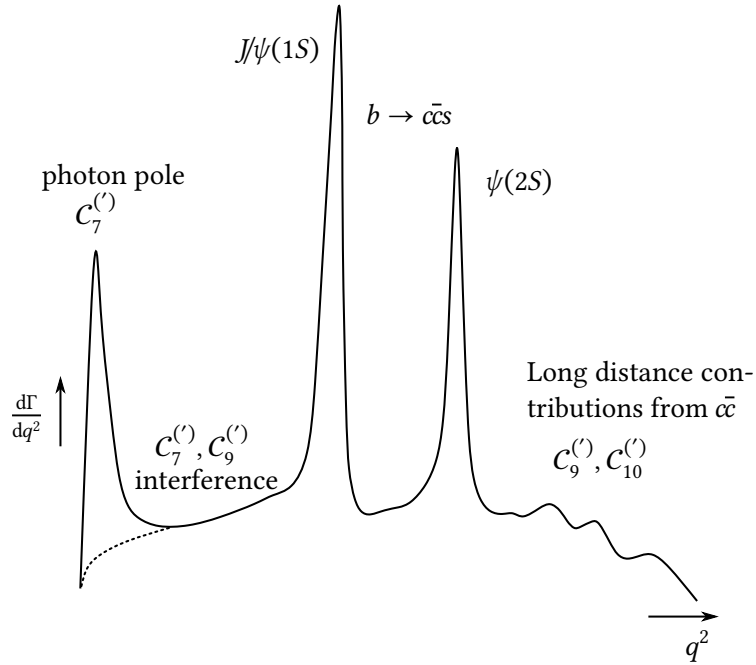


Figure 2.6 – Sketch of decay rates $\frac{d\Gamma}{dq^2}$ of the $b \rightarrow s\ell^+\ell^-$ transitions as a function of q^2 for the example of $B^0 \rightarrow K^{*0}\ell^+\ell^-$ and $B^+ \rightarrow K^+\ell^+\ell^-$ decays. The plot indicates the relevant Wilson coefficients and decay resonances. The dotted line shows that there is no photon pole for the decay rate of the decay $B^+ \rightarrow K^+\ell^+\ell^-$.

2.3 Flavour anomalies in rare B -meson decays

The Belle collaboration discovered the $B^+ \rightarrow K^+\ell^+\ell^-$ and $B^0 \rightarrow K^{*0}\ell^+\ell^-$ decays that are studied in this thesis in 2002 and 2003 [63, 64] having branching fractions in the order of $\mathcal{O}(10^{-7})$. Recent measurements found tensions in observables of those

decays. Together with a set of other observed discrepancies, those effects are called “flavour anomalies”. They are particularly intriguing because the anomalies can be interpreted in the same direction and form a consistent picture. There exist three authoritative classes of observables measured in B decays with $b \rightarrow s\ell^+\ell^-$ transitions where anomalies are present.

- There are measurements of the branching fractions of decays containing only muons. So far, measurements exist with the decays $B^0 \rightarrow K^{*0}\mu^+\mu^-$, $B^+ \rightarrow K^{*+}\mu^+\mu^-$, $B_s^0 \rightarrow \phi\mu^+\mu^-$, $B^0 \rightarrow K_S^0\mu^+\mu^-$, $\Lambda_b \rightarrow \Lambda\mu^+\mu^-$, and $B^+ \rightarrow K^+\mu^+\mu^-$. In measurements of this category, however, hadronic uncertainties are dominant in the theoretical predictions. These measurements are summarised in Section 2.3.1.
- In addition, observables are measured to parameterise the decay products’ angular distributions. There are optimised observables constructed so that their hadronic uncertainties cancel out at the leading order. Section 2.3.2 describes the measurements in detail.
- The cleanest class of observables are ratios of branching fractions of the same decay but different lepton flavours in the final state. Here, most of the hadronic uncertainties cancel out. Section 2.3.3 discusses their theoretical description and experimental results.

For a comprehensive overview of the tensions including theory predictions measured in the LFU area up to 2018, see Ref.[61]. Ref.[65] summarises theory work up to October 2021 for flavour anomalies with B -hadron decays. Finally, Ref.[66] gives a comprehensive theoretical and experimental review of the flavour anomalies in heavy-quark decays updated until summer 2021. Unless otherwise noted, these review publications serve as the source for the description of the flavour anomalies. The following section also includes recent experimental results by the LHCb collaboration that are not covered by listed review publications.

2.3.1 Decay rate measurements

The LHCb collaboration conducted measurements of differential branching fractions with the transition $b \rightarrow s\mu^+\mu^-$ for the decays $B^+ \rightarrow K^+\mu^+\mu^-$ [62], $B^0 \rightarrow K^{*0}\mu^+\mu^-$ [62, 67], $B_s^0 \rightarrow \phi\mu^+\mu^-$ [68, 69], $\Lambda_b^0 \rightarrow \Lambda\mu^+\mu^-$ [70], $B^+ \rightarrow K^{*+}\mu^+\mu^-$, and $B^0 \rightarrow K_S^0\mu^+\mu^-$ [62]. The CMS, Belle, and CDF collaborations conducted further measurements of similar decays [71–74] and several theory groups have computed SM predictions for those decays [75–77]. In addition, the measurement of the branching fraction of the baryonic decay $\Lambda_b^0 \rightarrow \Lambda\mu^+\mu^-$ by the LHCb experiment [70] shows systematically smaller values for low bins of q^2 compared to the theoretical predictions. Overall, it is observed that the decay rates of the decays with muons turn out to be lower than the predicted values. The deviations are among others in the q^2 -ranges, where the anomalies of the LFU are also measured. The largest deviation is measured by the

LHCb collaboration in the decay $B_s^0 \rightarrow \phi \mu^+ \mu^-$ in a q^2 range of $1.0 < q^2 < 6.0 \text{ GeV}^2/c^4$ [69]. The value lies 3.6 standard deviations (σ) below the SM prediction. The other tensions are each in the range of 1σ to 2σ from the theory prediction. Fig. 2.7 shows an overview of the measurements of the decay rates and their theory predictions of the four most important decays mentioned in this section. Although these measurements already see tensions to the SM, they are not fully conclusive on their own. Large theoretical uncertainties in the range of 20 – 30% limit the precision of the decay rate predictions due to hadronic effects and calculations of the form factors. In addition, non-factorising quark loop effects with c -quark loops of the form $b \rightarrow sq\bar{q}$ make the theoretical predictions even more challenging. But most models for NP in $b \rightarrow s\ell^+\ell^-$ decays expect differences in other observables such as the angular distributions in addition to deviations in individual decay rates.

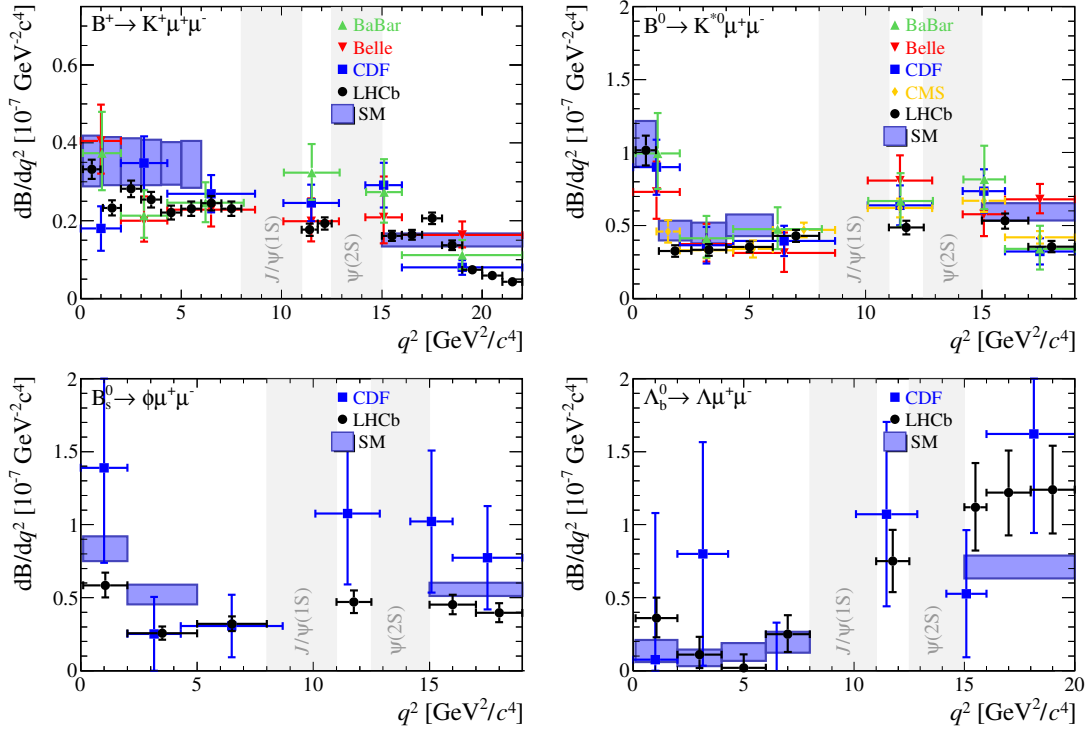


Figure 2.7 – Experimental results in comparison with theory predictions from $b \rightarrow s\mu^+\mu^-$ decay branching fraction measurements. Shown are the results for the decays $B^+ \rightarrow K^+\mu^+\mu^-$, $B^0 \rightarrow K^{*0}\mu^+\mu^-$, $B_s^0 \rightarrow \phi\mu^+\mu^-$, and $\Lambda_b^0 \rightarrow \Lambda\mu^+\mu^-$. The experimental data is from measurements of the BaBar [73], Belle [72], CDF [74], CMS [71], and LHCb collaborations [62, 67, 68, 70]. The SM theory predictions are from Ref.[75–77]. The plot is taken from Ref.[66] and does not include the recent update measurement of $B_s^0 \rightarrow \phi\mu^+\mu^-$ by the LHCb collaboration [69].

2.3.2 Angular analyses

Similar experimental tensions in tests of the SM are found in analyses of observables that parameterise the angular distributions of $B^0 \rightarrow K^{*0} \mu^+ \mu^-$ decays. The variables $P'_{i=4,5,6,8} = \frac{S_{j=4,5,7,8}}{\sqrt{F_L(1-F_L)}}$ represent constructed observables with reduced form factor dependency. Here S_j and F_L are bilinear combinations of the decay amplitude of the K^{*0} candidate that depend on q^2 [78]. S_j and F_L depend on both short-range effects sensitive to NP and form factors conditioned on long-range effects. The combinations $P'_{i=4,5,6,8}$, on the other hand, are largely free of form factor dependencies and thus particularly sensitive to potential NP.

Measurements of the Belle [72], CMS [71, 79, 80], CDF [81], and ATLAS [82] collaborations of these values show good agreement with the SM predictions. The same is true for a BaBar collaboration measurement from 2006 [83], whereas an updated measurement from 2016 reports tensions in F_L [84]. An LHCb measurement from 2013 [85] of the angular distributions of the decay $B^0 \rightarrow K^{*0} \mu^+ \mu^-$ with data recorded in 2011 shows a deviation from the theory prediction [75–77] of 3.7σ in the range of $4.30 < q^2 < 8.68 \text{ GeV}^2$. This measurement from 2013 established the first “flavour anomaly”. Together with the 2012 LHCb data with a total integrated luminosity of 3 fb^{-1} , a deviation from the SM of 3.4σ was measured in 2016 with a fit to multiple q^2 bins [86]. Adding the 2016 recorded data results in tensions of 2.5σ and 2.9σ in the q^2 ranges of $4.0 < q^2 < 6.0 \text{ GeV}^2/c^4$ and $6.0 < q^2 < 8.0 \text{ GeV}^2/c^4$ [87]. A further update with the full data set from the LHCb experiment of the years 2011 to 2018 yields a tension to the SM of 3.1σ [88].

An angular analysis published in 2017 by the Belle experiment with the decays $B^0 \rightarrow K^{*0} \ell^+ \ell^-$ and $B^+ \rightarrow K^{*+} \mu^+ \mu^-$ confirms this tension of the variable P'_5 with a deviation of 2.6σ from the theory prediction [89]. This measurement is supported by a result of the ATLAS collaboration [82]. However, investigation of the CMS collaboration finds good agreement with the SM [71], but with significant uncertainties. The LHCb collaboration measured tensions with the SM in the angular analysis of the decay $B_s^0 \rightarrow \phi \mu^+ \mu^-$ in 2015 [68], but a superseding update of the measurement shows good compatibility with the SM [90]. For a conclusive measurement or possible discovery of NP, further data need to be evaluated and methods improved. However, measurements of lepton flavour universality complete the classes of analyses where the flavour anomalies are reported.

2.3.3 Lepton flavour universality tests

According to the SM, the coupling strength of the leptons to the electroweak gauge bosons, W^\pm , Z , and γ , is independent of their flavour. Thus, the interaction between the gauge bosons and all leptons is the same. This principle is called lepton flavour universality (LFU) and is one of the fundamental postulates of the SM. The only differences between lepton flavours in the weak interaction of the SM come from kinematic effects induced by the lepton masses.

There exist two classes of LFU measurements. On the one hand, the decays investigated occur via tree-level processes and on the other, via loop-level decays.

LFU in tree-level decays. Particle physics experiments studied LFU extensively. They confirm LFU experimentally in the lowest order (tree-level) decays. This was done, for example, for the decays of mesons ($\pi \rightarrow \ell\nu$, $K \rightarrow \pi\ell\nu$) [91–93] and leptons [94]. In W -boson decays, LFU was validated at the percent level, and in Z -boson decays, at the permille level [95–105]. Recent measurements of the W -boson decays at the LHC supersede older LEP results resolving a tension of 2.5σ for the $W \rightarrow \tau\nu$ decay [106, 107]. Fig. 2.8 shows an overview of the main measurements of LFU measurements in tree-level decays.

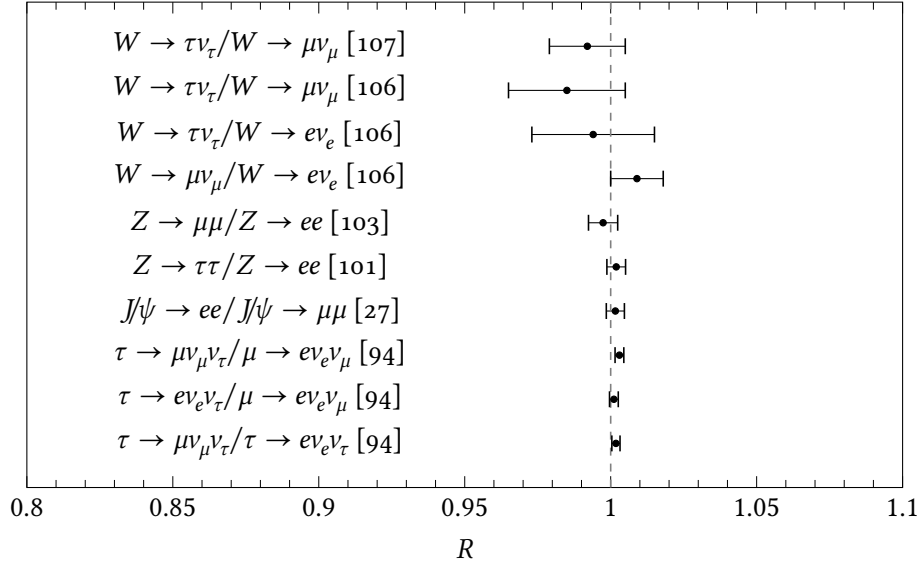


Figure 2.8 – Lepton flavour universality ratios R in purely leptonic, charmonium, and Z and W boson decays as charged currents. References for the single measurements are given in the plot.

Most important for this analysis, the measurement of LFU with the decays $J/\psi \rightarrow e^+e^-$ and $J/\psi \rightarrow \mu^+\mu^-$ results in [27]:

$$\frac{\Gamma(J/\psi \rightarrow e^+e^-)}{\Gamma(J/\psi \rightarrow \mu^+\mu^-)} = 1.0017 \pm 0.0031. \quad (2.5)$$

The lepton flavour universality of these decays is essential for this analysis, which uses the resonant J/ψ decays as normalisation channels (see Chapter 5).

LFU in loop-level decays. Higher-order rare decays, such as those studied in indirect searches of the LHCb experiment, are only considered in recent publications. Because of their particular experimental suitability (see Section 2.2), differences between decay rates of different lepton species in $b \rightarrow s\ell^+\ell^-$ decays have been studied for some

time. Although theoretical work initially considered $b \rightarrow s\tau^+\tau^-$ transitions [108–112], the experimental focus to date has largely been on electrons and muons in the final state as the decay $b \rightarrow s\tau^+\tau^-$ has not been observed yet. Measurements in decays of B mesons from the LHCb experiment show a consistent picture of deviations from the SM predictions. They expand the set of the anomalies observed in the measurements of the decay rates and angular variables. However, the statistical significance of these results is not yet high enough to draw any definitive conclusions on NP.

Current theoretical discussions problematise the influence of long-range hadronic effects, form factors and charm loops in the flavour anomalies in branching fraction and angular measurements [113–115]. As a consequence, observables with as few hadronic influences as possible are generated. So, to better control these effects, ratio tests of LFU are used where they cancel and where uncertainties are reduced. These particularly informative observables are ratios of branching fractions from two nearly identical decays, but with electrons on one side and muons on the other side in the final state [60]. They are defined as

$$R_H = \frac{\int_{q_{\min}^2}^{q_{\max}^2} \frac{dB(B \rightarrow H\mu^+\mu^-)}{dq^2} dq^2}{\int_{q_{\min}^2}^{q_{\max}^2} \frac{dB(B \rightarrow He^+e^-)}{dq^2} dq^2}, \quad (2.6)$$

where H stands for a hadron with an s quark, such as a K^+ or a K^* meson. For example, the observable $R_{K^{*0}}$ is formed as the ratio of the decays $B^0 \rightarrow K^{*0}\mu^+\mu^-$ and $B^0 \rightarrow K^{*0}e^+e^-$. The decay width is integrated over the squared dilepton mass q^2 . Equal hadronic content H in the fraction leads to the cancellation of uncertainties due to hadronic effects. It follows that very accurate theoretical predictions are possible. And for a wide range of q^2 sufficiently far from the kinematic threshold of dilepton production, the prediction of the SM for $R_K = R_{K^{*0}}$ is

$$R_H = 1.00 + \mathcal{O}\left(\frac{m_\mu^2}{m_b^2}\right), \quad (2.7)$$

with an uncertainty not larger than $\mathcal{O}(1\%)$ [60, 116, 117]. Further theoretical predictions can be found in Ref.[75, 113, 118–124] and show compatible results. Below a squared dilepton mass of $1 \text{ GeV}^2/c^4$, the kinematic effects of lepton production keep the LFU ratios well below unity. Because there are no hadronic uncertainties, the SM prediction is not systematically constrained. So any deviations from unity, as a result, can be interpreted as a strong result for new physics. Various models for NP expect deviations from the SM for these ratios (see Section 2.3.4).

As a consequence, the LHCb experiment and the Belle and BaBar collaborations have performed measurements of the ratios R_K , $R_{K^{*0}}$. Further measurements of LFU by the LHCb collaboration of $R_{K_S^0}$, $R_{K^{*+}}$, and R_{pK} complete the picture of the published measurements. These are explained in the following section.

Experimental results. So far, the LHCb collaboration has published various LFU measurements. In 2014, the measurement of the ratio R_K [24] was published for the first time with a result of

$$R_K(1.0 < q^2 < 6.0 \text{ GeV}^2/c^4) = 0.745_{-0.074}^{+0.090}(\text{stat.}) \pm 0.036 (\text{syst.}). \quad (2.8)$$

This result corresponds to a tension of 2.6σ from the SM predictions. The measurement uses data recorded by the LHCb experiment in 2011 and 2012.

The ratio R_{K^*0} is evaluated in two different regions of q^2 and was measured by the LHCb collaboration in 2017 [22] with

$$\begin{aligned} R_{K^*0}(0.045 < q^2 < 1.1 \text{ GeV}^2/c^4) &= 0.66_{-0.07}^{+0.11}(\text{stat.}) \pm 0.03 (\text{syst.}), \\ R_{K^*0}(1.1 < q^2 < 6.0 \text{ GeV}^2/c^4) &= 0.69_{-0.07}^{+0.11}(\text{stat.}) \pm 0.05 (\text{syst.}). \end{aligned} \quad (2.9)$$

The measurement includes data from the LHCb experiment up to the year 2012. This corresponds to a tension of 2.1σ to 2.3σ with the SM in the lower- q^2 region and 2.4σ to 2.5σ in the upper region. Note in this measurement that the lower- q^2 range contains large portions of the photon pole described above. An LHCb update of the R_K measurement [125] with data of the years 2011 to 2016 results in

$$R_K(1.0 < q^2 < 6.0 \text{ GeV}^2/c^4) = 0.846_{-0.054}^{+0.060}(\text{stat.})_{-0.014}^{+0.016}(\text{syst.}). \quad (2.10)$$

This measurement corresponds to a tension to the SM of 2.5σ . A recent measurement with the whole data set of the LHCb experiment [23] gives a value of

$$R_K(1.0 < q^2 < 6.0 \text{ GeV}^2/c^4) = 0.846_{-0.039}^{+0.042}(\text{stat.})_{-0.012}^{+0.013}(\text{syst.}). \quad (2.11)$$

This result corresponds to an SM tension of 3.1σ . The measurement inaccuracies are significantly statistically dominated. Underestimated uncertainties of the SM predictions could not explain an even more explicit confirmation. Measurements of the ratios R_K and R_{K^*0} of the Belle and BaBar collaborations from 2009 and 2012 report results compatible with the SM [72, 73]. They analyse B -meson decays from $Y(4S)$ decays produced in e^+e^- collisions. However, the determined ratios lie in different q^2 regions compared to the LHCb measurements, and the uncertainties are considerable here. An update of the result by the Belle collaboration, published in 2021, with the complete data set of the experiment, provides a similar result [73, 126]. Fig. 2.9 presents an overview of the most recent measurements of the ratios R_K and R_{K^*0} by the LHCb, BaBar, and Belle collaborations.

A measurement of LFU with baryonic $b \rightarrow s\ell^+\ell^-$ decays was performed by the LHCb experiment [128]. Here, the observable R_{pK} is measured as the ratio of the decays $\Lambda_b \rightarrow pK\mu^+\mu^-$ and $\Lambda_b \rightarrow pKe^+e^-$ in a q^2 range of $1.0 < q^2 < 6.0 \text{ GeV}^2/c^4$. The result is

$$R_{pK}(0.1 < q^2 < 6.0 \text{ GeV}^2/c^4) = 0.86_{-0.11}^{+0.14}(\text{stat.}) \pm 0.05 (\text{syst.}), \quad (2.12)$$

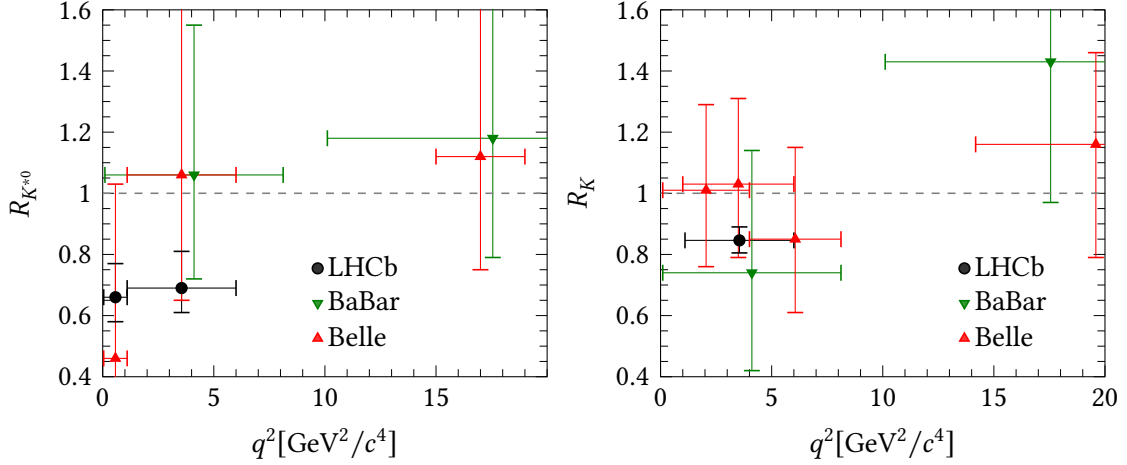


Figure 2.9 – Recent results of the lepton flavour universality tests (left) $R_{K^{*0}}$ and (right) R_K measured by the LHCb [22, 23], BaBar [73], and Belle [126, 127] collaborations. The dashed line indicates unity.

thus in agreement with unity within one standard deviation. One of the latest measurements of the LHCb collaboration presents the ratios $R_{K_S^0}$ and $R_{K^{*+}}$ [129], where the rare decays $B^0 \rightarrow K_S^0 \ell^+ \ell^-$ and $B^+ \rightarrow K^{*+} \ell^+ \ell^-$ are used. The results for these isospin partners of the decays investigated so far are

$$\begin{aligned} R_{K_S^0}(0.045 < q^2 < 6.0 \text{ GeV}^2/c^4) &= 0.66_{-0.14}^{+0.20} (\text{stat.})_{-0.03}^{+0.02} (\text{syst.}), \\ R_{K^{*+}}(1.1 < q^2 < 6.0 \text{ GeV}^2/c^4) &= 0.70_{-0.13}^{+0.18} (\text{stat.})_{-0.04}^{+0.03} (\text{syst.}). \end{aligned} \quad (2.13)$$

Individually they are compatible within 1.4σ and 1.5σ with the SM and combined within 2.0σ . The deviations show a similar pattern to previous measurements from the LHCb collaboration, where muon decays are observed less frequently than expected. Fig. 2.10 shows an overview including results for $R_{K_S^0}$ and $R_{K^{*+}}$ published by the Belle collaboration.

In tests of LFU with angular observables, the decay rate coefficients P'_i with reduced form factor uncertainties are combined [78, 119, 130, 131]. They measure P'_4 and P'_5 for electrons and muons in the final state individually and their difference $Q_i = P_i'^\mu - P_i'^e$. A publication by the Belle [89] shows tensions to the SM of these observables with a largest deviation of 2.6σ as well.

2.3.4 Interpretation

The single deviations mentioned above do not establish a significant departure from the SM expectations so far. But the overall picture shows a coherent tendency. In certain NP models, Wilson coefficients could carry different values for the same operators of different lepton flavours. This difference would for example occur, in models that

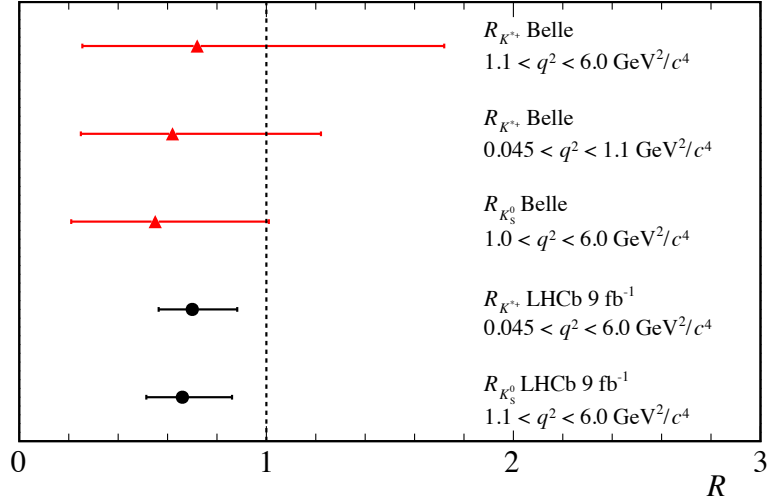


Figure 2.10 – Recent results of the lepton flavour universality tests $R_{K_S^0}$ and $R_{K^{*+}}$ measured by the LHCb experiment [129] and by the Belle collaboration [126, 127]. The figure is reproduced from the supplementary material of Ref.[129].

explain the masses of the leptons. Due to possible deviations in the LFU ratios, either the muon or the electron sector would strongly represent NP effects. Therefore, it makes sense to introduce a distinction between the operators $C_9^{\mu\mu}$ and C_9^{ee} . Global fits to the Wilson coefficients combining results from $b \rightarrow s\ell^+\ell^-$, $b \rightarrow s\gamma$, and $B_s^0 \rightarrow \ell^+\ell^-$ decays show lower values for $C_9^{\mu\mu}$ in comparison to the SM [132–134]. Fig. 2.11 shows two global fits with a shift in $C_9^{\mu\mu}$ and a smaller shift in $C_{10}^{\mu\mu}$. The results from different groups with different approaches form a coherent tendency. This altogether hints to a possible violation of LFU [132, 133, 135–138]. Including the look-elsewhere effect and fitting together all Wilson coefficients results in a global tension to the SM of 4.3σ [139]. However, the exact value of significance depends on the assumptions on the charm loops and other hadronic uncertainties and is still under investigation.

A common feature of the proposed NP models is that they all allow tree-level FCNC interactions. The most prominent explanations for the anomalies in R_K , $R_{K^{*0}}$, P_5' , and the divergent branching fractions involve new scalar and vector particles, specifically leptoquarks [141–144] or new heavy Z' gauge bosons [145, 146]. Fig. 2.12 shows two possible decay diagrams with leptoquarks or a heavy Z' boson. If any of these anomalies or models were experimentally confirmed by the LHCb collaboration and additional experiments, it would be a groundbreaking discovery in the field of particle physics. It could constitute the discovery of a new fundamental force. Ref.[147] gives an overview of possible NP models.

LFU tensions with the SM can be observed not only in the decay $b \rightarrow s\ell^+\ell^-$. Thus, for example, the tree-level decay type $b \rightarrow c\ell\nu$ can be used to form LFU ratios analogous to $R_{K^{*0}}$ or R_K . This decay is not a rare decay because its branching fraction lies in the order of $\mathcal{O}(10^{-2})$ as can be seen in Fig. 2.2.

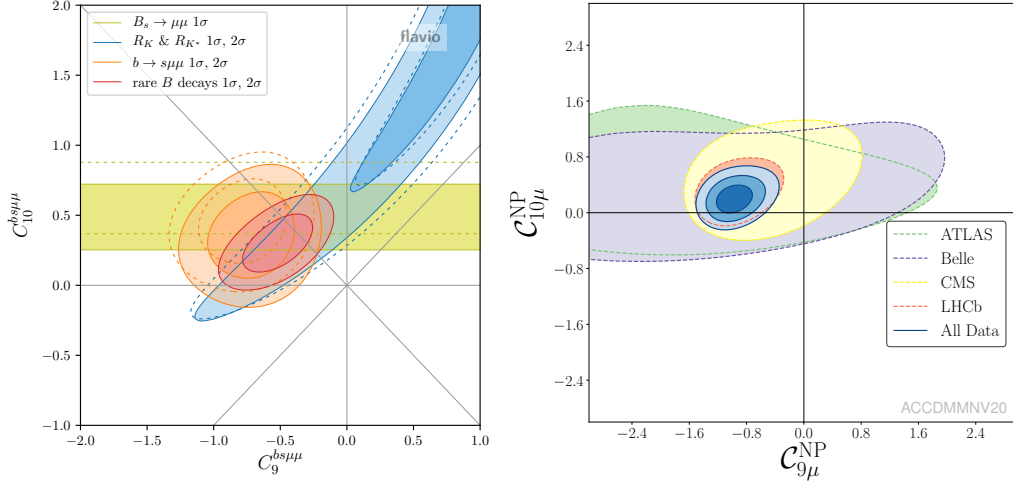


Figure 2.11 – Shifts of $C_9^{\mu\mu}$ and $C_{10}^{\mu\mu}$ from global fits to $b \rightarrow s\ell^+\ell^-$ processes with the SM prediction at the coordinate $(0, 0)$ in the plots using two different approaches [140] (left) and [133] (right). They show a consistent tension with the SM expectations. The left plot contains the 2021 results of the LHCb collaboration for the measurements of the decay $B_s^0 \rightarrow \mu^+\mu^-$ and the LFU ratio R_K with the full LHCb data set.

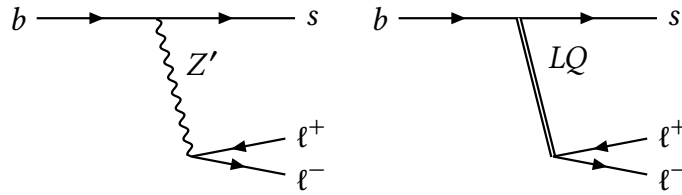


Figure 2.12 – Decay diagrams for possible NP contributions in $b \rightarrow s\ell^+\ell^-$ decays. Shown are diagrams with (left) heavy Z' bosons and (right) leptoquarks.

Decays of B mesons into D or D^* mesons comprise a charged lepton and the corresponding neutrino with

$$R(D^{(*)}) = \frac{\mathcal{B}(B \rightarrow D^{(*)}\tau\nu_\tau)}{\mathcal{B}(B \rightarrow D^{(*)}\ell\nu_\ell)} \quad \text{with } \ell = e, \mu. \quad (2.14)$$

A measurement of these ratios by the BaBar collaboration [148] shows evidence for deviations from the SM of 2.7σ and 2.0σ for R_{D^*} and R_D , respectively. A publication from 2015 of the ratio $\mathcal{B}(\bar{B}^0 \rightarrow D^{*+}\tau^-\bar{\nu}_\tau)/\mathcal{B}(\bar{B}^0 \rightarrow D^{*+}\mu^-\bar{\nu}_\mu)$ by the LHCb experiment [149] shows a deviation from the SM theory prediction of 2.1σ , whereas an updated 2017 measurement of the same ratio [150] is compatible with the SM prediction. Likewise, measurements from the Belle experiment of R_D and R_{D^*} [151, 152] show results consistent with the theory predictions. A global combination of the measurements of R_D and R_{D^*} determines a deviation of 2.3σ and 3.4σ for R_D and R_{D^*} , respectively [153], where systematic uncertainties dominate this class of results. The systematic uncer-

tainty is larger than the statistical error because of the challenging description of the background. The theory uncertainty is significant as well due to hadronic effects which do not cancel because of the large difference in the τ and μ masses.

Ref.[66] provides a full review of the current flavour anomalies in the heavy-quark decays and Ref.[65] presents a recent overview of possible theoretical explanations of the anomalies. It establishes connections to the open questions about dark matter, the $(g - 2)_\mu$ anomaly, current hadronic anomalies, and questions about the neutrino properties.

All in all, the flavour anomalies show an intriguing picture. However, more experimental measurements for higher precision is needed. The LHCb experiment is a perfect environment for those studies because its flavour physics programme mainly involves measurements of matter-antimatter asymmetries and rare decays of particles containing b or c quarks. In contrast to the ATLAS and CMS experiments, designed for direct searches for physics beyond the SM, the LHCb experiment is specialised for indirect measurements in the sector of flavour physics. The LHCb experiment provides high sensitivity for the possible observation of new heavy particles or modified couplings. The following chapter presents the LHCb detector at the LHC which is well suited for LFU tests because of its excellent particle identification, momentum resolution, and dedicated trigger system.

Potential new measurements with “parked data” by the CMS collaboration and complementary future measurements by the Belle II collaboration are discussed in Chapter 12.

3 The LHCb experiment at the LHC

With particle accelerators it is possible to accelerate particles to the highest energies using electromagnetic fields and thus explore their fundamental properties and interactions. In collisions, particles with masses many times higher than the rest mass of the colliding particles can be produced, as described by Einstein's energy-momentum relation. Usually, these produced particles decay quickly and leave signatures in the experiments' detectors, which allows their properties to be studied.

Development of particle accelerators. The history of particle accelerators goes back to the early cathode ray tubes developed by Ferdinand Braun [154]. Here, electrons are accelerated linearly in a high electric potential in vacuum. In contrast to this class of electrostatic particle accelerators, electrodynamic particle accelerators use alternating electromagnetic fields for acceleration and deflection. With the development of the cyclotron by Ernest O. Lawrence and M. Stanley Livingston from 1930 onwards, it became possible to accelerate particles on spiral trajectories to high energies by repeatedly passing through accelerating electric fields even without very high voltages [155]. The invention of synchrotrons from 1945 included relativistic effects of particles at high energies [156]. Intending to reach even higher energies, the technologies developed over the years, and the dimensions of the accelerators increased. Today, we speak of the two large classes of accelerators: first, in linear accelerators, there is no synchrotron radiation emitted, i.e., a loss of energy of the accelerated particles due to the deflection on circular paths. Second, it is however possible to bring particles to high energies in ring accelerators by repeated revolutions over a shorter distance.

Modern particle accelerators. In the 1950s, the technology of focusing particle beams with magnetic fields made it possible to build the first proton synchrotrons (PS) at CERN, allowing for energies in the range of $\mathcal{O}(30 \text{ GeV})$ to be achieved [157]. CERN is the European Organisation for Nuclear Research, founded in 1954 as a European project for peaceful fundamental research.

In storage rings, particles are collected and accelerated in circular trajectories. Examples of such storage rings are the Super Proton Synchrotron (SPS), which was put into operation at CERN in 1981. The Large Electron-Positron Collider (LEP) also operated there and was built at CERN in the same tunnel in which the Large Hadron Collider (LHC) was commissioned in 2008. The electron-positron storage ring PEP-II at the Stanford Linear Accelerator Center (SLAC) near Stanford University in California was conducting the BaBar experiment [158]. In Tsukuba, Japan, a similar complex

existed with the Belle experiment [159] at the electron-positron collider KEKB. The Belle II experiment replaced it in 2017 [160].

In general, high-energy particle physics knows two basic types of large-scale accelerator experiments today: on the one hand, there are electron-positron accelerators. At the, for example, SLAC and KEKB accelerators, electrons and positrons are accelerated at a centre-of-mass energy mainly corresponding to the $Y(4S)$ -resonance mass decaying into pairs of B mesons, allowing studies of rare $b \rightarrow s\ell^+\ell^-$ transitions. Large quantities of these b hadrons are produced in the collisions characterised by their purity with low background rates of other decays.

On the other hand, hadron accelerators such as the LHC collide protons, which are composite particles. Thus, one difference to the electron-positron colliders is that the decays of the colliding particles have significantly higher background rates. But in contrast to the production of B^0 and B^+ mesons via the $Y(4S)$ resonance as in electron-positron colliders, it is possible to produce all b -hadron species. This allows for a variety of tests of lepton flavour universality to be performed. Since the present thesis deals with data from the LHCb experiment at the LHC, this chapter will now introduce the LHC and the production of b hadrons in Section 3.1 as well as the LHCb detector and its components in Section 3.2.

3.1 The Large Hadron Collider at CERN

The Large Hadron Collider (LHC) [161, 162] is a ring-shaped particle accelerator at the European nuclear research centre CERN near Geneva. It is the largest and most powerful particle accelerator in the world.

The LHC is located in an approximately 26.7 km long underground tunnel that initially housed the LEP collider. It brings protons into collision at a centre-of-mass energy of up to $\sqrt{s} = 13$ TeV after acceleration in two opposing beam pipes. A chain of pre-accelerators precedes the LHC. Fig. 3.1 shows the accelerator complex at CERN. Here, Hydrogen atoms are fed into the Linear Accelerator 2 (LINAC2), which ionises them to hydrogen nuclei, i.e., protons, and provides acceleration to an energy of 50 MeV. The protons are then brought to an energy of 1.4 GeV in the circular Proton Synchrotron Booster (PS BOOSTER). After their further acceleration in the Proton Synchrotron (PS) and Super Proton Synchrotron (SPS), they reach an energy of 450 GeV before they reach the LHC. Remarkably, individual accelerators of this chain had been in operation for decades before the construction of the LHC already.

Superconducting dipole magnets with a magnetic field strength of up to 8.3 T keep the particles on their trajectories while being accelerated through radio frequency cavities. Additionally, the beam is focused using quadrupole magnets.

The LHC achieved different collision energies in its operation periods. Between 2010 and 2012 (RUN 1), it was 7 TeV and 8 TeV. In the subsequent years from 2015 to 2018 (RUN 2), the energy was increased to 13 TeV. The data collection of RUN 2 ended in December 2018, and this dissertation uses the entire data set of the years 2011 to 2018. The beams are not a continuous stream of particles, but are divided in packets

of protons, called “bunches”. The temporal spacing between the bunches was 50 ns instead of the originally targeted 25 ns for improved beam stability [163]. However, the spacing was then reduced to 25 ns as of the year 2015. The proton beam consists of up to 2808 proton bunches with about 1.15×10^{11} protons per bunch. The protons collide at four interaction points in the accelerator tunnel, where the detectors of the LHCb [164], CMS [165], ATLAS [166], and ALICE [167] experiments are located. The ATLAS and CMS experiments are multi-purpose detectors designed to cover the entire solid angle around the interaction points. They cover a broad programme of physics analyses that, for example, led to the discovery of the Higgs particle in 2012 [10, 11]. The ALICE experiment is mainly dedicated to matter in heavy-ion collisions and studies of quark gluon plasma.

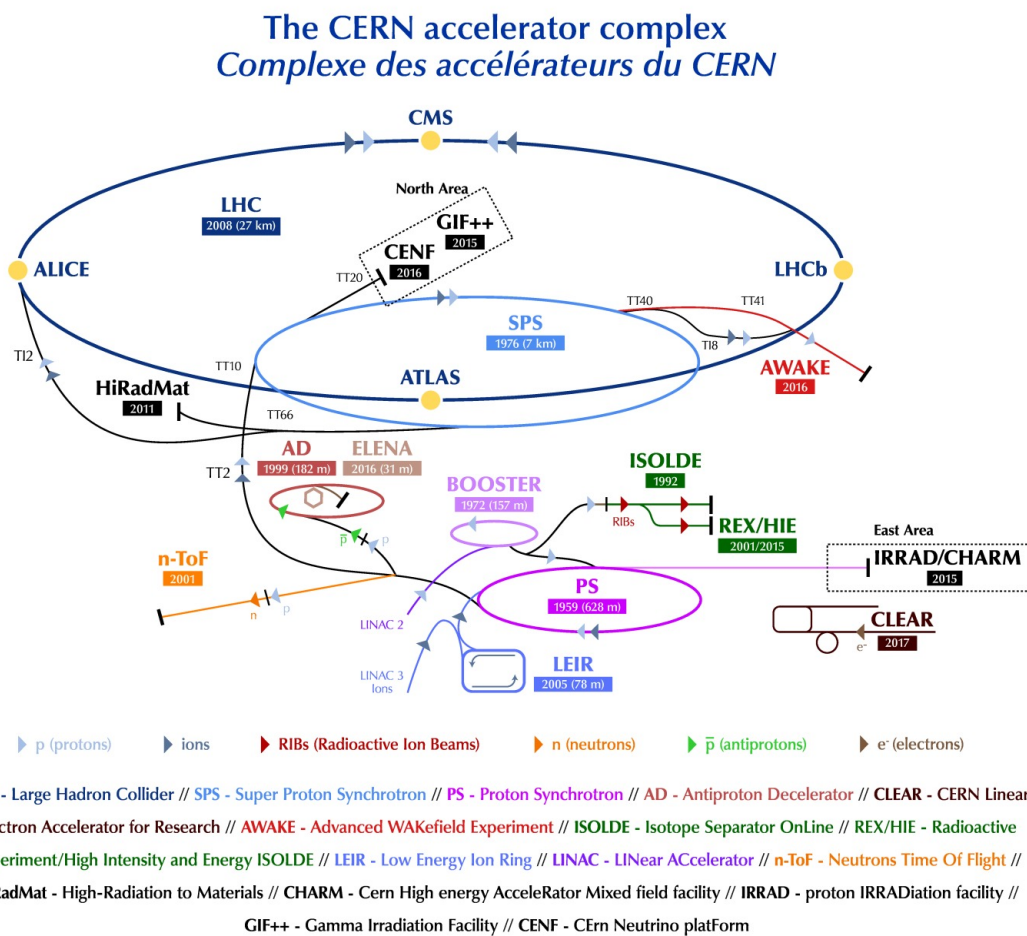


Figure 3.1 – CERN accelerator complex as existing in the year 2019 [168] with the LHC provided with pre-accelerated protons by other accelerators. The LHCb experiment can be seen as one of the four large experiments at the LHC.

3.1.1 b -hadron production at the LHC

The B mesons investigated in this thesis contain b quarks produced in the pp collisions at the LHC. The protons are composite systems of quarks and gluons. Consequently, collisions of these partons produce b quarks in quark-antiquark annihilations or predominantly gluon-gluon fusions at the centre-of-mass energy of the LHC. Since the dominant strong interaction is flavour-preserving, the produced quarks occur as $b\bar{b}$ -quark pairs. The interacting gluons have a high possibility of large momentum variances given the high energy of the collisions. Also, the centre-of-mass energy of the collisions is much higher than the b mass. It follows that the $b\bar{b}$ -quark pairs have considerable momentum and relativistic boost along the beam axis, which can be described with the polar angle θ with respect to this axis. With it, the Lorentz invariant quantity of the pseudorapidity

$$\eta = -\ln \tan \frac{\theta}{2} \quad (3.1)$$

can be constructed. Hadronisation of the b quarks with lighter quark types can produce B^0, B^+, B_s^0 , or Λ_b particles and the large mass of the b quarks allows the b hadrons to decay into various lighter electroweak decay modes. Thus, it is possible to perform a variety of tests of LFU at the LHC. Due to the high momentum of the b quarks and the highly boosted decay topology, it is possible to reconstruct the decay vertex with good quality and distinguish it from the background. The lifetime of the b quark is high enough to observe a visible displacement of its decay vertex, with a typical decay length of about 2 cm. However, the contribution of prompt background is high in the environment of a hadronic accelerator like the LHC. One reason for the high background contamination is the nature of the proton-proton collisions as composited particles. Another reason is the production rates of particular particle species. Within its detector acceptance the LHCb experiment measured the cross section of inelastic production of $b\bar{b}$ -quark pairs with the process $pp \rightarrow b\bar{b}X$ to be $72.0 \pm 0.3 \pm 6.8\mu\text{b}$ at 7 TeV centre-of-mass energy and $144 \pm 1 \pm 21\mu\text{b}$ at 13 TeV [169]. Whereas the total inelastic cross section is $55.0 \pm 2.4\text{mb}$ at a centre-of-mass energy of 7 TeV [170] and $62.2 \pm 2.5\text{mb}$ at 13 TeV [171]. As a consequence, the background rate is much higher than the rate of quark pairs produced. But due to the high mass of B mesons produced, the child particles receive a high transverse momentum, allowing efficient work of the triggers at the LHCb experiment.

In its construction, the LHCb detector covers a limited solid angle, expressed as pseudorapidity, of $2 < \eta < 5$. This angle corresponds to the preferred production direction of the $b\bar{b}$ -quark pairs, as will be explained in Section 3.2. Fig. 3.2 shows their angular distribution and the range covered by the LHCb experiment. The following section discusses the design of the detector in detail.

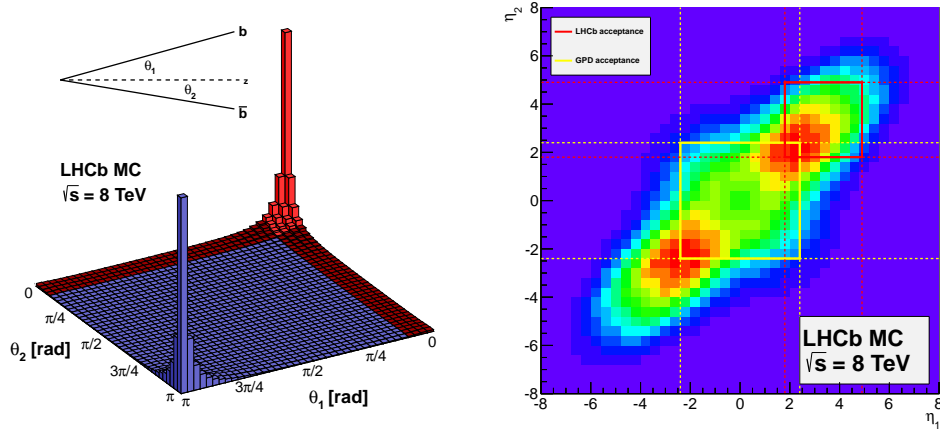


Figure 3.2 – Angular (left) and pseudorapidity (right) distributions of $b\bar{b}$ -quark pair production rates at the LHC with a centre-of-mass energy of $\sqrt{s} = 8$ TeV. The acceptance of the LHCb experiment is indicated by the red area. [172]

3.2 The LHCb detector

The Large Hadron Collider Beauty (LHCb) experiment specialises in high-precision measurements in the field of flavour physics with hadrons containing b and c quarks. Two of the main areas of measurements are studies of CP -violating decays and the analysis of rare decays, where small contributions from physics beyond the SM can already lead to significant experimental deviations from theory predictions. In both cases, indirect measurements are the key to NP searches. The LHCb collaboration comprises about 1400 members from 86 institutes in 18 countries (as of January 2021).

The LHCb detector is a single-arm forward spectrometer with an angular acceptance from 10 mrad to 300 mrad in the horizontal plane and from 10 mrad to 250 mrad in the vertical plane [164]. Only around 4% of the solid angle is covered by this range. But as described in Section 3.1.1 this region includes the dominant production direction and thus approximately 25% of the $b\bar{b}$ pairs produced. Fig. 3.3 shows the schematic structure of the detector.

Compared to the ATLAS and CMS experiments, the LHCb experiment does not operate at the maximum possible instantaneous luminosity. Instead of an instantaneous luminosity of $\mathcal{L} = 1 \cdot 10^{34} \text{ cm}^{-2}\text{s}^{-1}$ as provided by LHC, the LHCb detector operates at $\mathcal{L} = 2 \cdot 10^{32} \text{ cm}^{-2}\text{s}^{-1}$ [164]. However, due to the well functioning software and hardware, a higher data rate could be recorded by the experiment in practice. At the LHCb experiment, the proton beams are less focused, with the overlap adjusted in real-time to allow uniform data taking. In this environment, an operation of the trigger system with nearly constant settings and a reduction in systematic uncertainties is possible. This reduction of the effective number of pp collisions also has the advantage of reducing the detector occupancy and radiation damage to the instruments. This configuration has made it possible to record the world's largest data set of $b\bar{b}$ -quark

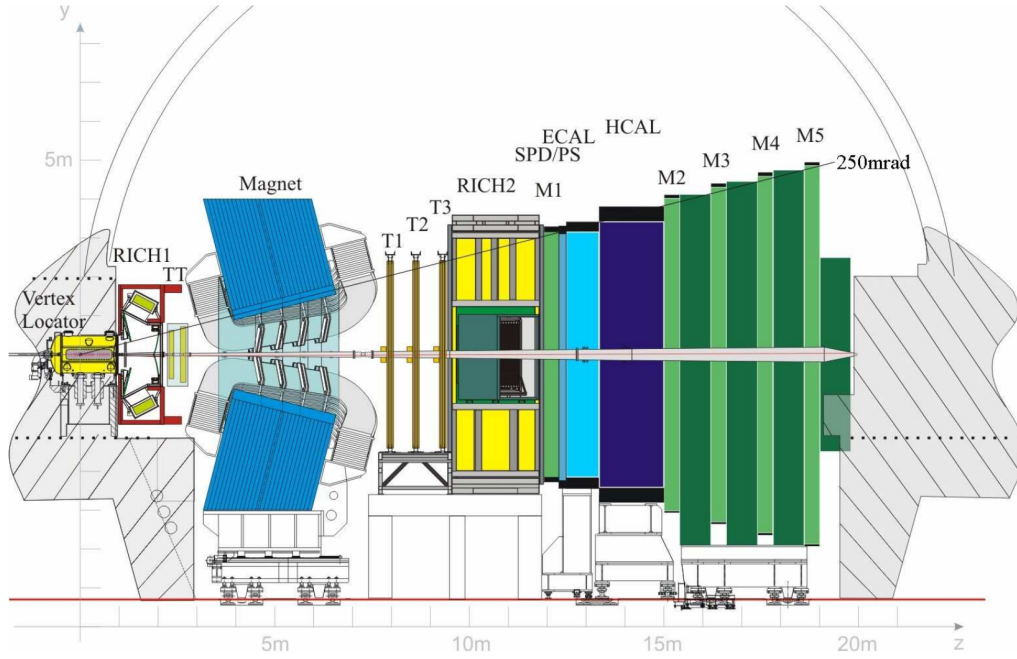


Figure 3.3 – Schematic view of the LHCb detector. From left to right, the following detector components are shown: the VELO, which encloses the interaction point of the protons, the two RICH detectors, the tracking system including the magnet, the calorimeter system, and the muon chambers. [164]

pairs. Here, the number of recorded events N results from the instantaneous luminosity \mathcal{L} and the effective cross-section σ with $N = \sigma \cdot \int \mathcal{L}(t)dt$. Fig. 3.4 shows the integrated luminosity recorded over the different periods of data taking and Table 3.1 shows the phases with corresponding collision energies and integrated luminosities. The data taking period between of 2011 and 2012 is called RUN 1, RUN 2P1 for 2015 to 2016, and RUN 2P2 for 2017 to 2018, giving a total approximate integrated luminosity of 9 fb^{-1} .

The LHCb experiment has excellent vertex and track reconstruction capabilities and the possibility of precision momentum measurements. The Vertex Locator (VELO) is a silicon strip detector that encloses the collision point of the protons. Its components can be moved to a few millimetres near the interaction point, allowing excellent resolution and reconstruction of the production and decay vertices of the b hadrons. Similar to the VELO, the Tracker Turicensis (TT) is also a silicon strip detector, followed by the experiment's magnet with a magnetic field of 4 Tm and three other tracking stations (T1, T2, and T3), which together form the detector's tracking system. Because of its multi-stage particle identification (PID) system, the LHCb detector can precisely discriminate different final states of the decays. This represents a unique feature of the LHCb design due to their high precision. Such delicate instrumentation would hardly be possible in an experiment covering the entire solid angle because of its size and shape. The PID system is comprised of two ring-imaging Cherenkov detectors

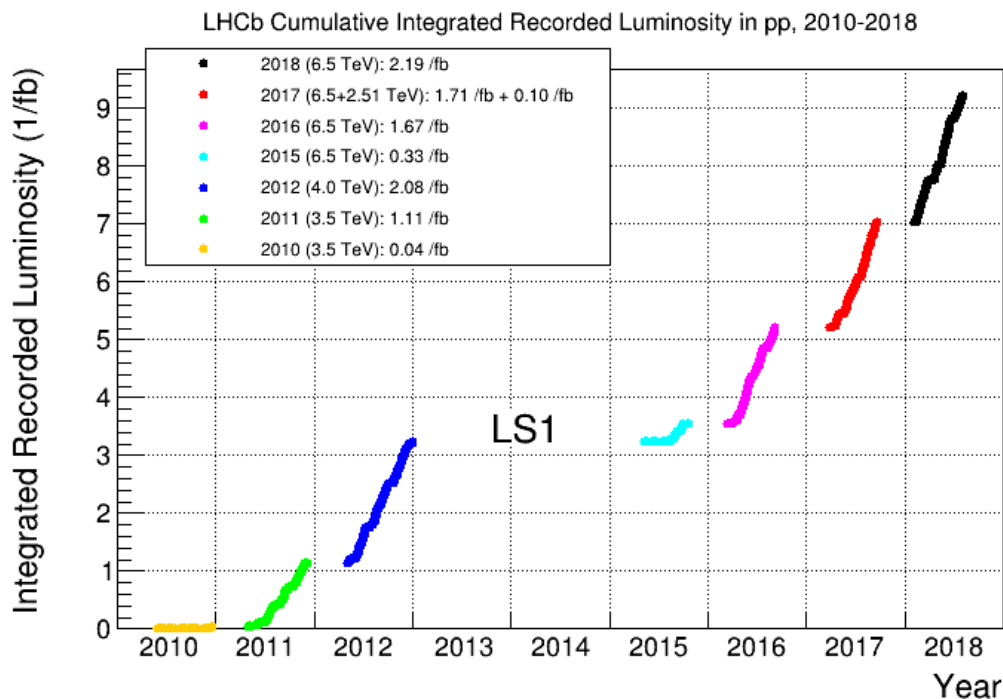


Figure 3.4 – Cumulative integrated luminosity collected by the LHCb experiment over time. The years of RUN 1 (2011 – 2012) are indicated in green and dark blue. The years of RUN 2 (2015, 2016, 2017, 2018) are coloured in light blue, magenta, red, and black. [173]

(RICH) that discriminate between kaons, pions, and protons, as well as a calorimeter system (SPD, PS, ECAL, and HCAL) that distinguishes between photons, electrons, and hadrons. In addition, muons are detected explicitly in the muon chambers (M1-M5) at the end of the detector. Charged pions, kaons, protons, electrons, muons, and photons are considered approximately stable within the detector because of their long lifetime. However, unstable particles, such as the B mesons, are reconstructed from combinations of traces of these stable particles. The following sections give details on the track reconstruction and particle identification system, followed by an explanation of the trigger system, electron reconstruction, and LHCb’s data processing chain.

3.2.1 Track reconstruction system

To reliably perform track and vertex reconstructions as well as momentum measurements in a hadronic environment with high track multiplicities, the LHCb experiment is equipped with a particular tracking system. With the inputs from the individual sub-detectors, the system reconstructs charged particle trajectories. The Vertex Locator (VELO) is a silicon strip detector and surrounds the interaction point of the pp collisions and allows high spatial resolution. Likewise, the Tracker Turicensis (TT) is a large silicon strip detector placed upstream of the detector’s magnet. Behind this detector component, the magnet bends the tracks of charged particles for momentum measurements. Two regularly changing magnet polarities called *MagUp* and *MagDown* mitigate

Table 3.1 – Overview of data taking periods of the LHCb experiment by years and run periods with the corresponding centre-of-mass energies of the pp collisions and the recorded integrated luminosity.

Period of data taking		Centre-of-mass energy	Integrated luminosity
RUN 1	2011	7 TeV	$\sim 1.11 \text{ fb}^{-1}$
	2012	8 TeV	$\sim 2.08 \text{ fb}^{-1}$
RUN 2P1	2015	13 TeV	$\sim 0.33 \text{ fb}^{-1}$
	2016	13 TeV	$\sim 1.67 \text{ fb}^{-1}$
RUN 2P1	2017	13 TeV	$\sim 1.71 \text{ fb}^{-1}$
	2018	13 TeV	$\sim 2.19 \text{ fb}^{-1}$

possible detection asymmetries. Next are the three tracking stations T1-T3, consisting of the inner tracker (IT) made of silicon strips and the outer tracker (OT) instrumented with straw tubes. Finally, Fig. 3.5 shows a schematic sketch of the tracking system with different track types as reconstructed by the LHCb experiment. Long tracks have hits in the VELO, TT, and tracking stations and are reconstructed efficiently. On the other hand, Downstream tracks leave no traces in the VELO but the TT and the tracking stations. VELO tracks, upstream tracks, and T tracks play a role in various algorithms of the track reconstruction. For example, VELO tracks are used to reconstruct the primary vertex of decays.

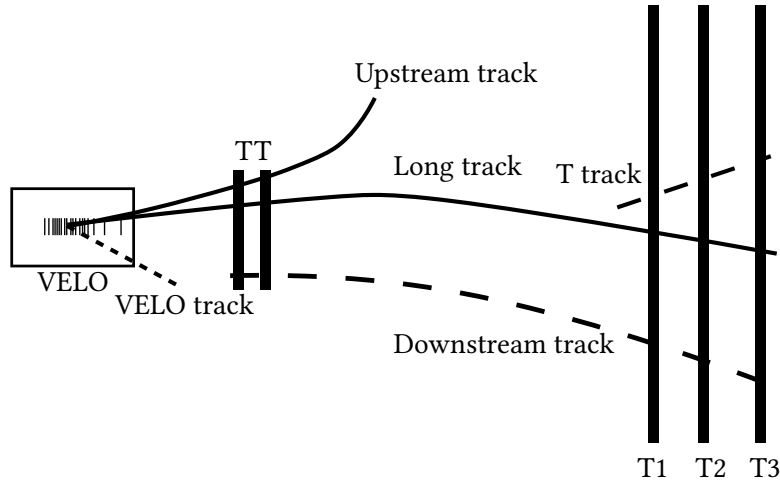


Figure 3.5 – Track types reconstructed in the LHCb detector.

Vertex Locator. The interaction point is surrounded by the Vertex Locator (VELO) [174, 175], which determines the position of the primary vertices (PV) and secondary decay vertices (SV) of the b hadrons. It is also the first part of the tracking system.

These particles typically have a flight distance of a few millimetres until they decay. With the VELO, it is possible to achieve outstanding performance with a spatial hit resolution of up to $4\ \mu\text{m}$. Fig. 3.6 shows its structure of disk-shaped $R - \phi$ silicon detectors, which are arranged with offsets to each other around the beam axis. The R and ϕ sensors are fitted with silicon strips in such a way that they can determine the radial and azimuthal coordinates of traversing particles, respectively. These 21 modules per half of the detector have a radius of 42 mm. When the detector is in operation, their distance to the proton beam is reduced to about 8 mm. Each half of the VELO is separated from the beam vacuum by a corrugated aluminium foil (RF-foil).

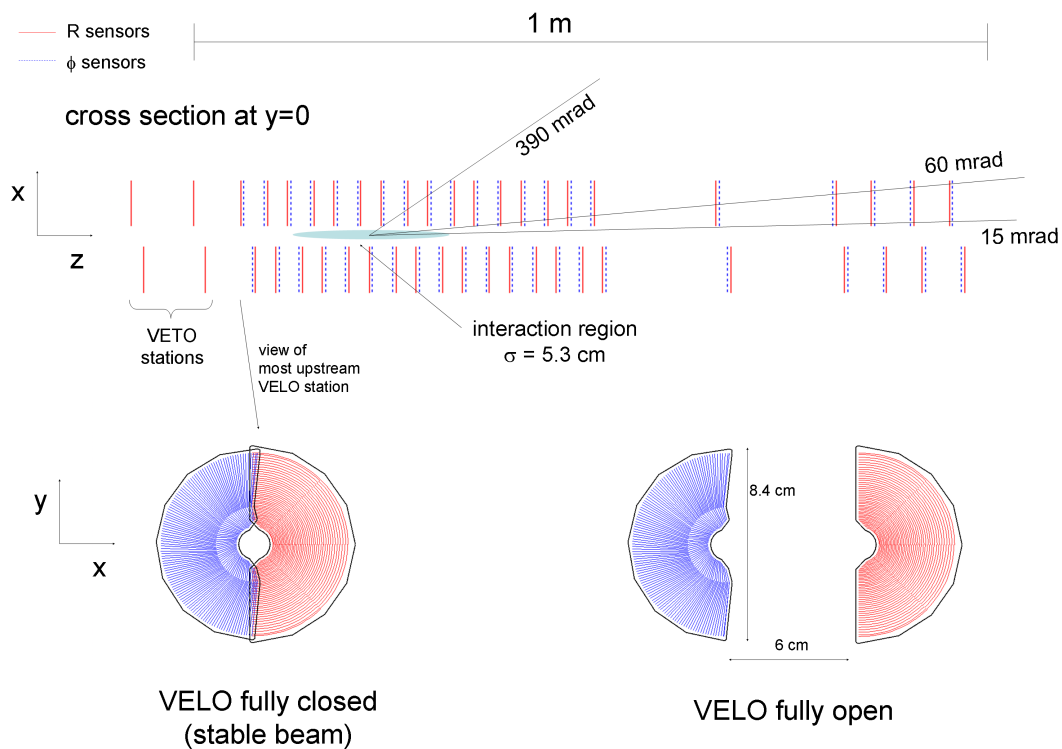


Figure 3.6 – Sketch of the VELO’s cross section and sketches of R and Phi sensors of the closed and fully opened VELO [164].

Tracker Turicensis. The Tracker Turicensis (TT) is located behind the RICH1 detector and is a silicon strip detector. It consists of two stations, each comprising two detector layers. The TT achieves single hit resolutions up to $50\ \mu\text{m}$ and contributes to the momentum measurement of the tracks and is the starting point of downstream track reconstruction. In addition, the TT can detect low-energy particle tracks, leaving the detector acceptance after the magnet.

Tracking stations. The three tracking stations (T1-T3) consist each of the Inner Tracker (IT) [176] and the surrounding Outer Tracker (OT) [177, 178]. Each tracking station also comprises four offset detector layers. The IT is a silicon strip detector, whereas the OT is a drift time detector and consists of straw tubes, which contain an argon gas mixture. The ionisation clusters in the OT determine the reconstructed hits.

3.2.2 Particle identification system

In this thesis, decays with electrons, muons, kaons, and pions in the final state are investigated. The tracking system reconstructs their trajectories, but the PID system determines their particle type. Data analyses both employ individual and combined information from the PID detector components.

In detail, the PID system consists of two ring-imaging Cherenkov detectors (RICH1 and RICH2), the calorimeter system, and the muon chambers. The Cherenkov detectors allow for the accurate separation of charged hadrons, such as kaons, pions, and protons. They are also used to identify electrons and muons. The calorimeter system can detect electrons, photons, and hadrons by measuring their energy. The muon system (M1-M5) reconstructs muon tracks based on the hits they leave behind.

RICH detectors. The LHCb detector is instrumented with two RICH detectors [179, 180]. Fig. 3.3 shows that RICH1 is positioned right after the VELO and RICH2 after the tracking stations T1-T3. Both detectors exploit the Cherenkov effect, which occurs when a particle moves faster than the phase velocity of light in a medium. In this case, Cherenkov photons are emitted in a cone with the Cherenkov angle θ_C with

$$\cos \theta_C = \frac{c}{nv} = \frac{1}{n} \sqrt{1 + \left(\frac{mc}{p}\right)^2}. \quad (3.2)$$

Here c is the speed of light in vacuum, v is the velocity of the propagating particle, and n is the refractive index of the medium. With its resulting velocity v and the reconstructed momentum p , the mass m of the particle is determined, with the reconstructed momentum provided by the tracking system. Following this principle, the RICH1 and RICH2 detectors differ significantly because of the gas they are filled with. While the RICH1 detector contains C_4F_{10} with a refractive index of $n = 1.0014$, in RICH2 CF_4 gas with a refractive index of $n = 1.0005$ is employed. As a result, RICH1 can identify particles with a lower momentum between 1 and 60 GeV/ c and RICH2 with a higher momentum between 15 and 100 GeV/ c . Fig. 3.7a shows that a system of mirrors guides the Cherenkov light onto hybrid photons detectors, on which it leaves circular patterns. From these patterns, algorithms determine the Cherenkov angle θ_C . The aerogel shown was removed after RUN 1 because it could not precisely identify kaons below the C_4F_{10} Cherenkov threshold due to the large number of photons in the RICH1 detector. Its removal consequently allowed to use the full radiator volume [181]. Fig. 3.7b shows the momentum dependence of the Cherenkov angle for different particle species crossing RICH1.

A different algorithm assigns the Cherenkov rings to individual tracks and combines it with information from the calorimeter system and the muon system as likelihoods $\mathcal{L} = \mathcal{L}_{\text{RICH}} \cdot \mathcal{L}_{\text{Calo}} \cdot \mathcal{L}_{\text{Muon}}$. The discriminating variable $\text{DLL}_{X\pi}$ is the difference of the logarithmic likelihoods (DLL) of the particle hypotheses of a particle X and a pion. The pion is used here because it is the most abundant particle in the LHCb detector. The variable is calculated as

$$\text{DLL}_{X\pi} = \Delta \ln \mathcal{L}_{X\pi} = \ln \mathcal{L}_X - \ln \mathcal{L}_\pi. \quad (3.3)$$

Another class of discriminating PID variables combines inputs of all detector components of the PID system in a neural network [182]. The resulting variables are called ProbNN and give the probability of a track being a specific particle type.

Fig. 3.7b shows that for individual particle species there are momentum ranges in which separation is not reliably possible. For example, the Cherenkov angles behave similarly for all particle species for large momentum. Fig. 3.7c shows the resulting particle identification performance. The identification efficiency for kaons with two different cuts to the $\text{DLL}_{K\pi}$ quantity is shown, which consequently decreases significantly with high momentum but shows high quality for the medium momentum range. The mis-identification rate of pions, on the other hand, is low and increases with higher particle momentum.

Calorimeter system. In addition to the discrimination provided by the RICH detectors, the calorimeter system [180] allows to distinguish between electrons, photons, and hadrons. This detector system, which is placed between muon stations M1 and M2, is also employed in the trigger. Fig. 3.8 shows the structure of the calorimeter system. It consists of four subdetectors, the Scintillating Pad Detector (SPD), the Preshower (PS), the Electromagnetic Calorimeter (ECAL), and the Hadronic Calorimeter (HCAL). The SPD and PS are two scintillator pad detectors separated by a lead absorber. The lead separation with 2.5 radiation lengths X_0 causes photons and electrons to start already generating particle showers. Consequently, the PS detects this shower. Electrons also produce showers in the SPD, making it possible to distinguish them from photons that do not leave any hits there. The ECAL follows the ‘‘Shashlik’’ construction principle of alternating beams of scintillator material and of lead absorbers. The electromagnetic showers leave all their energy in the ECAL, corresponding to 25 radiation lengths. This length is much smaller than the hadronic interaction length. Thus hadrons are not entirely shielded in the ECAL.

In contrast, the HCAL is composed of iron absorbers and scintillator material and measures the energy of hadrons. Its detector size corresponds to 5.6 hadronic interaction lengths, so hadrons deposit nearly all their energy in this detector component. The HCAL information is mainly used to identify hadronic clusters utilised by the trigger system. Wavelength-shifting fibres guide the scintillator light into photomultipliers that measure it. Depending on the proximity to the beam axis, the calorimeters are divided into regions with different segmentation to accommodate a higher track density near the beam axis.

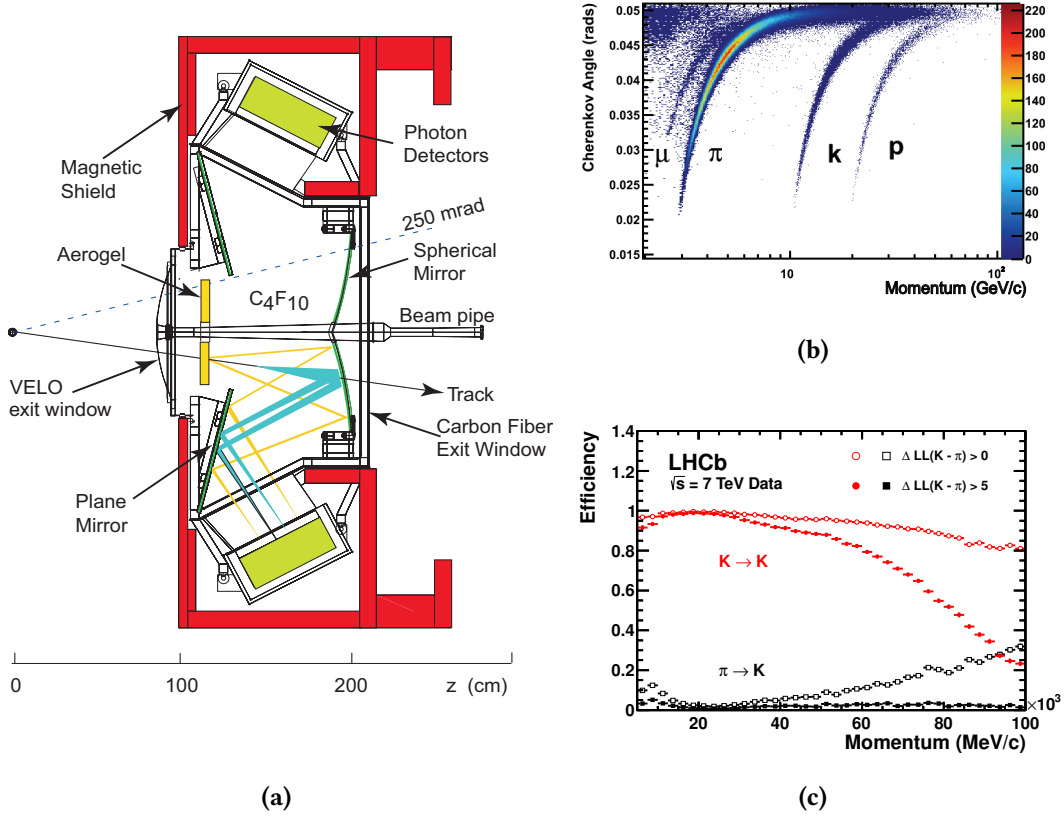


Figure 3.7 – (a) Sketch of the RICH1 detector with Aerogel modules, which were removed after RUN 1 [164]. (b) Reconstructed Cherenkov angle θ as a function of different particle types’ track momenta in the C_4F_{10} radiator [179]. (c) Kaon PID identification efficiency and pion mis-identification rate as a function of their track momenta. The plot shows efficiencies for two different $DLL_{K\pi}$ requirements [179].

Muon stations. Part of the decays discussed in this thesis contain muons in their final state. They are detected by LHCb’s muon system [184, 185] which is composed of five stations, M1-M5. M1 is the first station, placed in front of the calorimeter system. Behind this system and behind further 80 cm thick iron shielding separating the individual stations the other stations M2-M4 are located. Only muons with an energy of the order of several GeV can penetrate to the muon system. Thus other particle species are effectively shielded, enabling a very pure particle identification. Four regions, R1-R4, segment the single muon stations. All sub-detector layers consist of multi-wire proportional chambers (sMWPCs). Only the innermost layer of M1 around the beam axis consists of triple gas electron multipliers (sGEMs), which are more resistant to radiation damage. Fig. 3.9 shows the cross-section of the Muon system and the regions of the individual stations, which offer finer granularity with increasing proximity to the beamline.

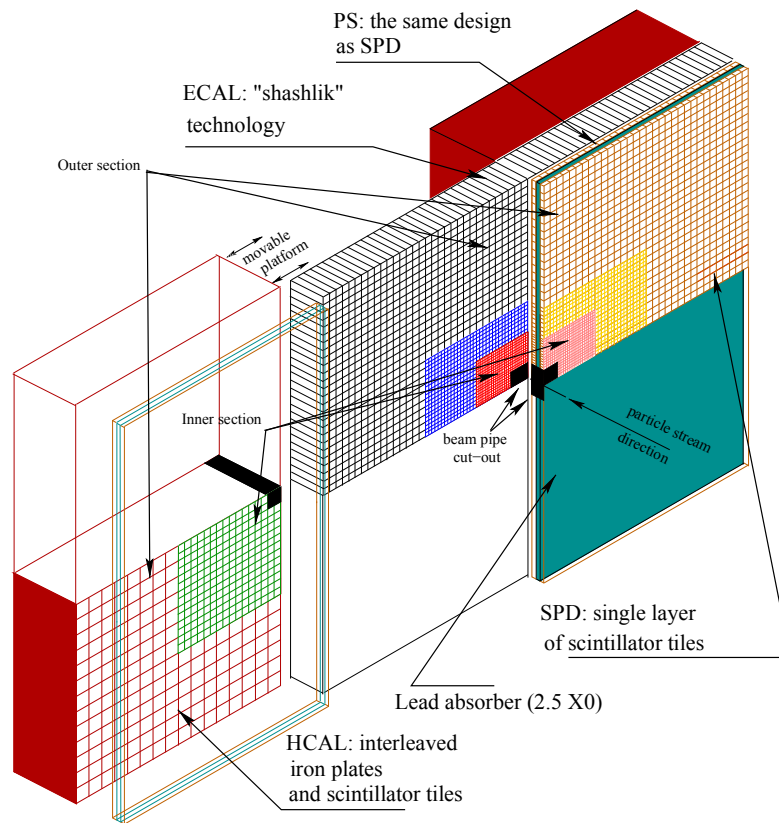


Figure 3.8 – Layout of the calorimeter system consisting of the SPD, PS, ECAL, and HCAL [183].

3.2.3 Trigger system

The collision rate is about 15 MHz in RUN 1 and about 30 MHz in RUN 2 [186]. With an average event size of 60 – 70 kB [187, 188], this would result in a data rate of about 2 TB s^{-1} . As the resulting amount of data cannot be fully stored, a trigger system reduces the event rate by filtering out interesting events [189, 190]. This system comprises the hardware trigger (L0) and the software-based High Level Trigger (HLT). Synchronously to the bunch crossing rate, the L0 trigger decides whether an event is processed based on inputs from the calorimeters and the muon stations. As a result, the event rate is lowered to 1 MHz. This reduction enables the subsequent complete reconstruction of the event, including information from all detector outputs with the HLT. In this complex procedure, the HLT operated in RUN 1 with an event rate of 2 kHz to 5 kHz.

L0 trigger. For this thesis, decays with muons and electrons in the final state are particularly relevant. Different sets of trigger requirements are called “trigger lines”.

3 The LHCb experiment at the LHC

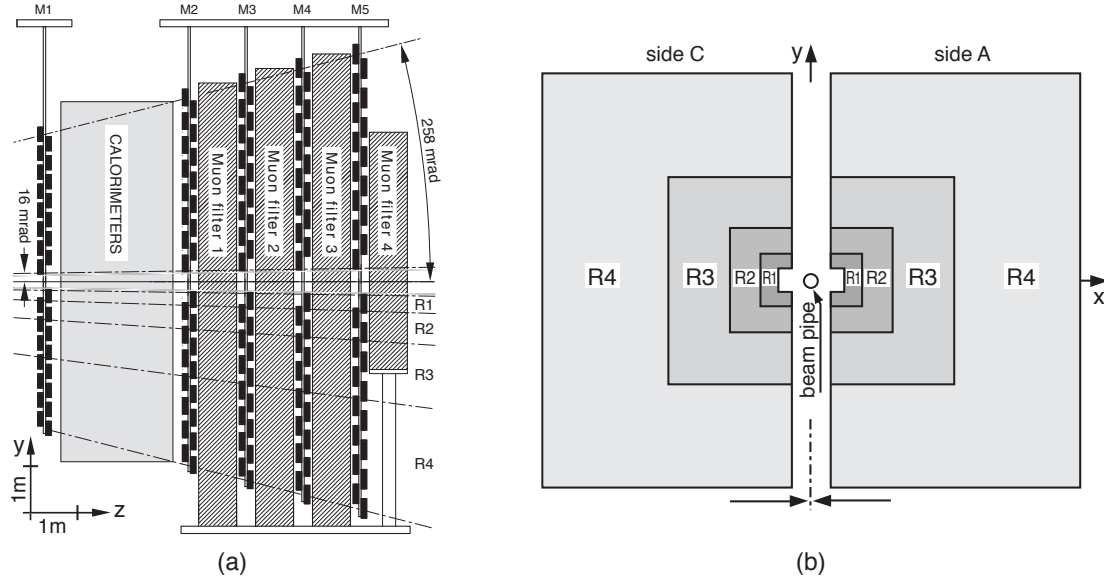


Figure 3.9 – a) Sketch of the muon stations and b) detector regions R1-R4 of each station [184].

The $L0$ muon trigger requirements employ simple detector information from the muon stations and the calorimeter system. Transverse momenta of the muons are determined here as a selection criterion from measurements of the muon stations. The muon momentum reconstruction straightforwardly uses the comparatively small number of hits in the muon chambers. Table 3.2 shows the trigger thresholds for single muon candidates ($L0\text{Muon}$).

The trigger lines $L0\text{Hadron}$, $L0\text{Electron}$, and $L0\text{Photon}$ use information of the SPD and PS. Additionally, the $L0\text{Electron}$ trigger line requires a minimum transverse energy measured in the calorimeter system. Here, the definition of the transverse energy is

$$E_T = \sum_{i=1}^4 E_i \sin \theta_i, \quad (3.4)$$

with the energy E_i of the ECAL cluster cell i . This cell's vector to the collision point has an angle θ_i in the z axis [191]. In addition, at least one to two PS hits and at least one SPD hit are required. The trigger line $L0\text{Hadron}$ uses a similar procedure but with information from the HCAL and the SPD only.

To keep the event rate low enough, the number of hits per event in the SPD during RUN 1 (RUN 2) must be less than 600(450) for both the $L0\text{Muon}$ and $L0\text{Electron}$ trigger requirements.

The $L0\text{Hadron}$ trigger has much stricter filtering conditions and is thus much more inefficient than the $L0\text{Muon}$ or $L0\text{Electron}$ lines. This choice reduces the data rate sufficiently for further processing steps. Table 3.2 shows the individual requirements of the three trigger lines.

Table 3.2 – Typical L0 trigger thresholds for the different years of data taking [189–191].

L0 Trigger	Requirement	2011	2012	2015	2016	2017	2018
L0Muon	$p_T(\mu)[\text{GeV}/c]$	> 1.48	> 1.76	> 2.8	> 1.8	> 1.35	> 1.35
L0Electron	$E_T[\text{GeV}]$	> 2.5	> 3.0	> 2.7	> 2.4	> 2.11	> 2.11
L0Hadron	$E_T[\text{GeV}]$	> 3.5	> 3.7	> 3.6	> 3.7	> 3.46	> 3.46

High Level Trigger. Only events that pass through the L0 are processed by the HLT, which is made up of two stages: HLT1 and HLT2. Here, a partial reconstruction of the events using signatures of displaced vertices and tracks of dimuon pairs occurs. Photons are not detected directly as calorimeter objects in the HLT but are triggered indirectly via other particle tracks. There also exists no direct trigger for dielectron pairs.

In the HLT1, a partial event reconstruction takes place, using the track quality, track momenta, PV displacement, track combinations, and further requirements on the tracks. For the Muon trigger HLT1TrackMuon, only events passing the L0Muon trigger are processed. In the trigger line HLT1TrackAllL0, on the other hand, all events passing the L0 are processed.

In the HLT2, a complete event reconstruction occurs, with inputs from all detector components calibrated in an ideal case. However, the detector responses significantly depend on environmental and other experimental influences. Therefore, the requirements of the trigger lines must be adjusted at regular intervals. Trigger configuration keys (TCKs) document the respective settings for these adjustments. The trigger line HLT2DiMuonDetached comprises requirements according to properties typical for dimuon vertices, which include the distance of the decay vertices from the PV. The HLT1TrackMVA trigger uses a machine-learning based trigger implementation that triggers on a minimum transverse momentum and impact parameter significance regarding primary vertices of a given track. Topological inclusive B trigger lines are the Topo[2, 3, 4]BodyBBDT and Topo[2, 3, 4](Mu, E)BodyBBDT lines [192]. They employ combinations of tracks and, in the latter case, specific identification of electrons and muons using boosted decision trees (BDTs).

The outputs of the two HLT triggers are stored in so-called streams. In the Full stream, the entire information of the individual detector components for the events is preserved as raw data. This format enables subsequent optimisations or detailed reconstructions. A further central pre-selection, the so-called stripping, reduces the data size of the events. Additionally, in the Turbo stream, introduced in RUN 2 of the experiment [193], real-time analyses can be carried out for various purposes. In this case, however, the amount of data is smaller because only parts of the detector information of the events is stored. Besides the use for various measurements, one example of its use is to obtain the PID calibration data.

L0 trigger strategy. After the events have passed the L0 trigger, they are categorised. If the trigger decision was made exclusively by traces of the reconstructed signal decay, the category Triggered on Signal (TOS) is assigned. Triggered independent of Signal (TIS) is assigned if the trigger fires due to tracks not associated with the signal. When both types of tracks explicitly contribute, the rarer category Triggered on Both (TOB) is used. Fig. 3.10 shows this schematically for the decays $B^+ \rightarrow K^+ \mu^+ \mu^-$ and $B^+ \rightarrow K^+ e^+ e^-$. Here, the reconstructed signal consists of the leptons, the kaon tracks, and, in the case of the electrons, a reconstructed photon. Tracks emanating from the primary vertex that do not belong to the reconstructed signal are indicated in green with an orange cluster. Since the reconstruction of muons and electrons occurs in different detector components, their efficiencies in the electron and muon triggers are also clearly distinct. In this thesis, the TIS category is chosen as the primary trigger category, independent of the lepton flavour of the final signal state. This choice mitigates the trigger differences of muon and electrons. Chapter 5 contains more details on the trigger strategy.

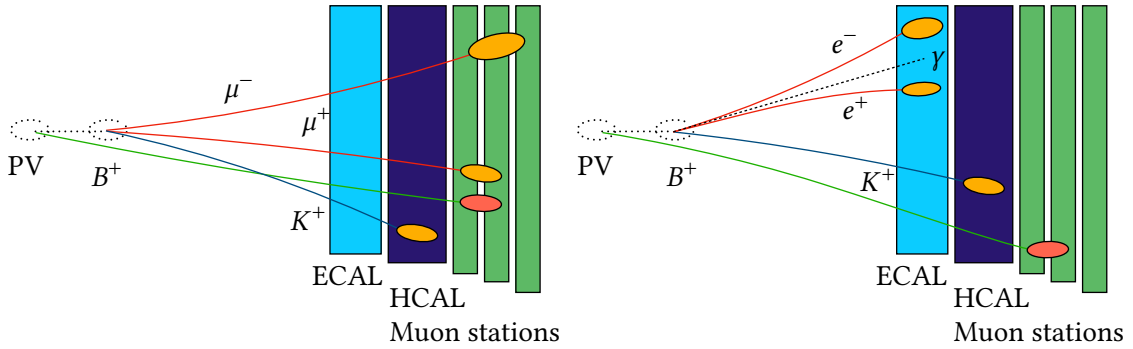


Figure 3.10 – Schematic view of the decays (left) $B^+ \rightarrow K^+ \mu^+ \mu^-$ and (right) $B^+ \rightarrow K^+ e^+ e^-$ in the LHCb detector with the SPD, HCAL, and muon stations. The green line indicates the part of the decay that is not associated to the reconstructed signal candidates.

3.2.4 Electron reconstruction

Due to their low mass, electrons can only be reliably detected by the RICH in the very low momentum range. Therefore, electron identification uses a specific signature consisting of hits in the SPD and showers in the ECAL, where they distinctively lose their total energy. Furthermore, the distinction from hadron showers in the ECAL is possible because the showers emit most of their energy in the HCAL. Through the signature in the SPD, electrons can thus also be distinguished from photons.

Bremsstrahlung emission occurs when the velocity vector of charged particles is changed. The two primary sources for bremsstrahlung are material interactions and deflection in the magnetic field. The radiation emitted in the direction of flight leads to a loss of energy of the particles. The effect is inversely proportional to the fourth power of the particle mass. Thus, it is much stronger for electrons than for the

heavier muons. For this reason, precise electron reconstruction is one of the leading experimental challenges of the LFU measurements at the LHCb detector. On the one hand, bremsstrahlung emission complicates the reconstruction, and on the other hand, the momentum resolution is diluted. Thus, the LHCb experiment has a dedicated electron reconstruction system that recovers bremsstrahlung photons.

Different cases for the bremsstrahlung reconstruction exist depending on the radiation emission region. First, after crossing the magnetic field, the same calorimeter cell usually measures photons and the corresponding electron. A distinction is therefore not possible. However, the momentum is already determined from the bending in the magnetic field before the emission. Second, the fact that charged particles generate photons within the magnetic field is experimentally improbable due to the magnet region's low material budget.

Finally, the most challenging reconstruction case is when the emission occurs before the particle passes the magnetic field influencing the momentum determination. In this case, a dedicated reconstruction method is used, which includes the lost energy by assigning the emitted photons to the corresponding electron. The ECAL measures the energy of the emitted photons. However, these are located in other calorimeter cells than the deflected electron. Therefore, an algorithm assigns photon clusters in the ECAL, which is associated with the electron tracks in a specific range. Then, an extrapolation of the electron track based on hits in the VELO and the TT determines this region. The additional photon energy thus is assigned to the momentum of the electron. Anyways, a fraction of the photons is not correctly assigned or lost due to the minimum momentum required for the reconstruction. As a result, the precision of the electron momentum is significantly reduced and additionally increased by the limited resolution of the ECAL.

3.2.5 Data processing and variable definitions

A dedicated LHCb software chain reconstructs events that pass the L0 trigger. The GAUDI framework [194] provides the overarching framework to produce two classes of data sets which this analysis uses. First, data has been recorded with the LHCb detector (data). Additionally, most measurements employ events generated in Monte Carlo simulation. Simulation samples are used in this thesis to describe signal shapes, background modelling, and detector efficiencies.

Fig. 3.11 shows the processing flow for these two classes of data. In the case of simulation, the pp collisions and subsequent interactions and decays are generated under the GAUSS framework [195]. The initial collisions are simulated with the PYTHIA software [196] in the LHCb configuration [197]. Subsequent decays are simulated by the EVTGEN software [198], with the package PHOTOS [199] adding Bremsstrahlung effects. GEANT4 [200] simulates the particle propagations and material interactions within the LHCb detector. The simulation of the digitisation of the detector output, which otherwise takes place in the detector hardware, is performed with the BOOLE package [201]. Simulated events and the events recorded in the detector are then processed in the same analysis chain to reconstruct the simulation identically to the

recorded detector data. With the package MOORE [202], the events in the HLT trigger are processed as described in Section 3.2.3. Afterwards, the BRUNEL software [203] combines reconstructed track and particle identification information to proto-particles. The resulting data format is called Data Summary Tape File (DST), which also contains the truth information of the simulated events before reconstruction. Storing the truth information means that both the reconstructed and original properties of the simulation are known, which can later be used, for example, to check the quality of the individual reconstruction steps. Within the DAVINCI package [204], a centralised selection filters the events and creates the final particle candidates. The corresponding requirements for this analysis can be found in Section 6.2 and Section 6.1. Finally, the nTuple format of the analysis software ROOT [205] stores the results.

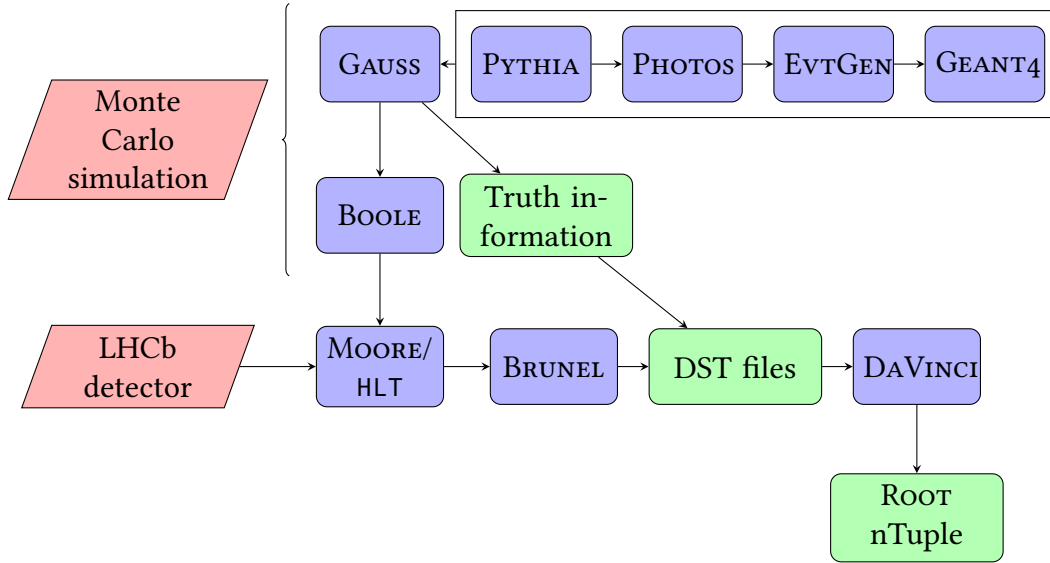


Figure 3.11 – LHCb software chain for the (top) production of simulation and the (bottom) processing of raw LHCb detector data. The software packages are shown in blue and the different data formats in green.

The resulting ROOT nTuples typically contain a set of variables of the reconstructed events and particle candidates. In the decay $A \rightarrow a + b$, A is the initial particle. a and b are the associated tracks from which the reconstruction of A occurs. The particle candidate A is produced in the pp collisions in the primary vertex (PV), traverses the detector with a flight distance (FD) and decays after a short time at the secondary vertex (SV). Fig. 3.12 shows related common kinematic decay properties and Table 3.3 lists their definitions, and other typical variables used in this thesis.

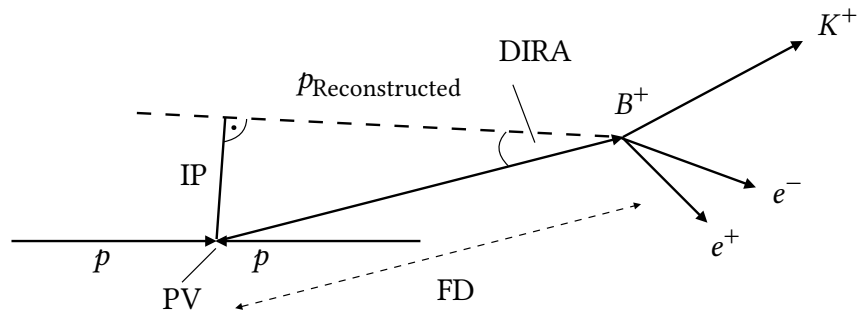


Figure 3.12 – Common kinematic variables of signal decay $B^+ \rightarrow K^+ e^+ e^-$ with the protons p , the kinematic variables PV, FD, IP, DIRA, and the reconstructed B -meson momentum, $p_{\text{Reconstructed}}$.

Table 3.3 – Definitions of common variables in this thesis.

Variable	Definition
$m(ab)$	Invariant mass of the two-body system of the tracks a and b .
$ m(ab) - m(c)_{\text{PDG}} $	Deviation of the invariant mass of the system of the particles a and b from the averaged value of the mass of particle c as given by the Particle Data Group (PDG) [27].
p	Particle momentum.
p_{T}	Transverse particle momentum: Momentum component transversal to the beam pipe.
$\text{isMuon}(a)$	Requirement that track a is consistent with a muon hypothesis. Based on muon system information.
$\text{InAccMuon}(a), \text{hasMuon}(a)$	Requirement of track a to be in the acceptance of the muon stations or having hits in the muon system.
$\text{hasRich}(a), \text{hasCalo}(a)$	Requirement of track a reconstructed with information of the RICH detectors or calorimeter system.
χ_{IP}^2	Difference in the χ^2 of the PV reconstruction fit when including the particle candidate A or not.
χ_{FD}^2	Flight distance FD of particle A divided by its experimental uncertainty.
ndf	Number of degrees of freedom.
$\chi_{\text{vtx}}^2(A)$	χ^2 of the fit of the decay vertex for particle A .
$\chi_{\text{vtx}}^2(A)/\text{ndf}$	χ^2 of the fit of the decay vertex for particle A divided by the number of degrees of freedom.
$\chi_{\text{track}}^2(a)$	χ^2 of the fit of track a .
$\text{DIRA}(A)$	As shown in Fig. 3.12, it is the angle between the momentum vector of particle A and the vector between the PV and the decay vertex of particle A .
$\text{PIDx}(a)$	Difference of log-likelihoods of track a being particle type x and being a pion with information from the calorimeter and RICH systems.
$\text{ProbNNx}(a)$	Probability that the track a is of particle type x . The variable is computed with a neural network combining inputs from the detector components.
$\text{GhostProb}(a)$	Probability of track a reconstructed as fake track from a random combination of tracks.
nTracks	Number of tracks in the event.
nPVs	Number of primary vertices of the event.
nVeloTracks	Number of VELO tracks of the event.
nSPDHits	Number of hits in the SPD.
$\theta(a, b)$	Angle between the tracks a and b .

4 Author's contribution

The author carried out the measurement presented in this thesis within the LHCb collaboration, which implies the usage of common software to analyse the collected data. The specific analysis work from which this thesis originates has been accomplished within an analysis team, where the author is a main proponent and is listed collaboration internally as one of the three contact authors. Substantial contributions have been made by Dr Renato Quagliani, Dr Simone Bifani, Stephan Escher, Sebastian Schmitt, and (with their doctoral thesis) Dr Fabrice Desse [206], Dr Ryan Calladine [207], and Dr Da Yu Tou [208]. The author's contributions to the measurement are included in the analysis steps, which are listed in the Chapters 5 to 8 and 10 to 12. In the development of the fits to the invariant mass of the B mesons, which are presented in Chapter 9, the author was only marginally involved.

The measurement has reached the collaboration-wide review process, and the publication is in preparation. Figures that are taken from the paper draft [209] are referenced separately.

The complete analysis code is available at the CERN analysis-code repository, including comprehensive documentation. In addition, all data sets used are preserved in the CERN storage system.

5 Measurement strategy

This chapter describes the strategy of measuring the observables R_K and R_{K^*0} , explains the architecture of the data analysis, and motivates general choices of experimental methods. Consequently, the subsequent chapters of this thesis will present the individual experimental steps in detail. The thesis's overarching goal is to simultaneously measure the R_K and R_{K^*0} observables as a null test of the SM predictions using the entire data set of the LHCb experiment collected from 2011 to 2018. Novel experimental approaches optimise the statistical significance of the signal contribution, and thus the signal purity, compared to previous measurements of these quantities. As one part of this optimisation, this measurement aligns the treatment of the different final states of the decay channels as much as possible to mitigate experimental differences between the electron and muon modes.

Because of their similar decay topologies, the analysis strategy is similar for all decay channels. Thus, a coherent software framework has been developed to measure LFU

ratios in various decay modes. This development allows a consistent evaluation of the different data sets and complete and convenient reproducibility of the results, because of automatised and extensively documented workflows and processing chains.

The variables R_K and R_{K^*0} , theoretically introduced in Eq. (2.6), are experimentally measured as double ratios. So, the ratio of the rare muon and electron branching fractions are divided by the same ratio but with the resonant decays modes. The resonant signal decays via the J/ψ resonance are chosen, so in this case, the control channels $B^0 \rightarrow K^{*0} J/\psi (\rightarrow \ell^+ \ell^-)$ and $B^+ \rightarrow K^+ J/\psi (\rightarrow \ell^+ \ell^-)$. This choice is motivated by the similarity between the signal and control channels in combination with the abundant number of pure and easy to select signal candidates in these modes. Furthermore, these resonant decay channels are also utilised to calibrate and validate the simulation. A peculiarity of the here presented analysis is that the resonant B^+ and B^0 calibration modes are crossed with the rare signal modes. In that way, the calibration samples are distinct from the decays that are used in the normalisation mode of the final measurement. Thus, unwanted correlations are avoided.

The main advantage of the double ratio approach is that systematic uncertainties largely cancel out thanks to the topologies of the resonant and rare modes. This is why their systematic experimental uncertainties are so similar. Additionally, the double ratio can compensate for reconstruction differences between the muon and electron channels, primarily caused by bremsstrahlung effects and different trigger performances.

These different decay channels are investigated in specific regions of the squared dilepton mass q^2 . So, the rare decay modes are measured in two q^2 regions in this analysis, as the previous LHCb measurement of R_{K^*0} did (see Section 2.3.3). However, in contrast to the prior measurement of R_K , this thesis describes the first measurement in two different q^2 regions performed by the LHCb experiment. Section 5.1 describes the definition of the signal regions and the definitions of the ratios R_K and R_{K^*0} in detail.

In addition to splitting the data into q^2 regions, the different periods of data taking (2011+2012, 2015+2016, and 2017+2018) are considered in the data analysis to take into account their distinctive properties properly. These specifications are different because, for example, changes in the detector setting, the specific LHC run conditions per year, or due to changes in the reconstruction setup. Finally, Section 5.5 describes the general approach concerning the data samples and simulation in detail.

Coming to the experimental methods, the relevant quantities that need to be determined are each decay mode's number of signal candidates and the reconstruction and selection efficiencies included in the double ratio. Section 5.2 describes the strategy of selecting the signal, Section 5.3 presents the approach of determining the efficiencies, and Section 5.4 discusses the general procedure of extracting the number of signal candidates. Here, the precise treatment of the experimental differences between the reconstruction of electrons and muons is the main challenge of this measurement. In particular, the electron reconstruction needs special care. One reason for this is, that it is more challenging to trigger dielectron pairs due to significantly lower trigger efficiencies (see Section 3.2.3). Therefore, the measurement of the electron channels

limits the precision of the measurement, which is thus statistically limited. The second reason is, that the electrons' considerably higher emission of bremsstrahlung needs a dedicated treatment. Although there is a dedicated bremsstrahlung recovery procedure in the LHCb experiment, the resolution of the reconstructed mass of the B mesons is significantly limited compared to that of muons. Thus, the described strategy distinguishes between three bremsstrahlung categories, determined by whether zero, one, or two and more bremsstrahlung photons are recovered for the dilepton system.

To protect the presented analysis from a possible experimenter's bias, a blinding of the final results is used. This means that the efficiencies of the rare signal modes are not determined until the very end of the procedure. But in contrast, the number of rare signal candidates is not blind because it allows for an early detection of potential mis-modelling of the mass distributions. Additionally, extensive cross-checks validate the experimental scheme. Here, one of the most stringent cross-checks is the single ratio of the resonant modes. In contrast to the double ratios, any significant deviation from unity would indicate systematic issues of the measurement because, in this case, no systematic uncertainties cancel out.

Invariant mass distributions. Fig. 5.1 shows the distributions of the reconstructed masses of the $K^+\pi^-\ell^+\ell^-$ and $K^+\ell^+\ell^-$ systems as a function of the squared invariant mass of the dilepton system q^2 . The vertical bands over the entire q^2 range show the signal decay. The distinct peaks within this structure stem from the resonant decays through the J/ψ and $\psi(2S)$ resonances in two leptons. The horizontal bands with the same q^2 value as the two resonances but different invariant masses consist of combinations of randomly reconstructed J/ψ or $\psi(2S)$ candidates not belonging to the signal decay with additionally reconstructed kaons and pions. The same effect is possible without the resonances reconstructed, but only kaons or pions. This class of reconstructed decays is called "combinatorial background". The diagonal structures indicate decays for which the bremsstrahlung or final-state radiation recovery procedure added less or more photons than had been initially emitted by the leptons. Final state radiation means the QED effect of a photon emitted with low momentum, rather than as a material interaction effect. By this, the system's invariant mass and q^2 are modified, and the structure of the system is washed out. For the electron mode, it is apparent that the spectrum is much more diluted. This occurs because of the significantly larger amount of emitted bremsstrahlung photons and lower detector precisions for the electron reconstruction.

5.1 Definition of signal regions and measured observables

Signal regions. The decay rates and Wilson coefficients of the decays under investigation are q^2 -dependent. Thus, to distinguish their possible contributions and properly treat specific decay and background properties, the analysis is performed in

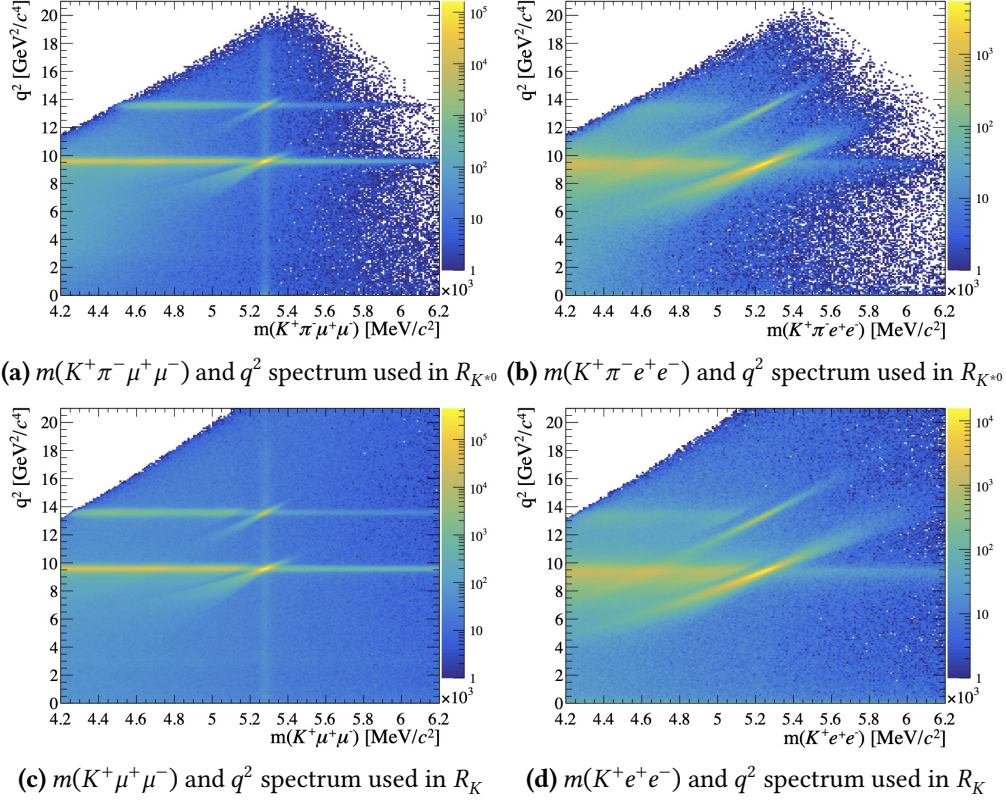


Figure 5.1 – Invariant mass spectrum $m(K^+\pi^-\ell^+\ell^-)$ (for $R_{K^{*0}}$) and $m(K^+\ell^+\ell^-)$ (for R_K) versus the squared invariant mass of the dilepton system q^2 . The plots show the distributions for the muon (left) and electron (right) modes using the full LHCb data set. The data is filtered by the full measurement selection except the q^2 range requirements.

different q^2 regions. Section 2.2.2 describes the phenomenology of the $B^0 \rightarrow K^{*0}\ell^+\ell^-$, and $B^+ \rightarrow K^+\ell^+\ell^-$ decays with the q^2 -dependent spectrum of their decay rates.

For the simultaneous analysis of R_K and $R_{K^{*0}}$, the q^2 ranges are identical for both ratios. They are chosen in such a way that, on the one hand, to be comparable with already published measurements (see Section 2.3.3). On the other hand, they are chosen to be as sensitive as possible to possible effects of NP and to contain as little interfering background as possible. This approach implies two general requirements: First, the analysis excludes q^2 regions in which $\bar{c}\bar{c}$ resonances predominate. These resonances have such high SM decay rates that they mask possible NP effects. As a second requirement, the choice of q^2 ranges must separate regions in which different Wilson coefficients contribute. Only in this way can the possible effects of NP be attributed to specific coefficients. Here, the ratio R_K is comparatively independent of q^2 , whereas the ratio $R_{K^{*0}}$ shows explicit dependencies on possible contributions of NP in the form of modified Wilson coefficients. This dependency is especially visible for the measurement of $R_{K^{*0}}$ in the region of the photon pole at $q^2 = 0$ (see Fig. 5.2). Consequently, the measurement investigates the rare and resonant decays in two q^2 regions each. Fig. 5.3 shows an overview of the ranges. The region with a high

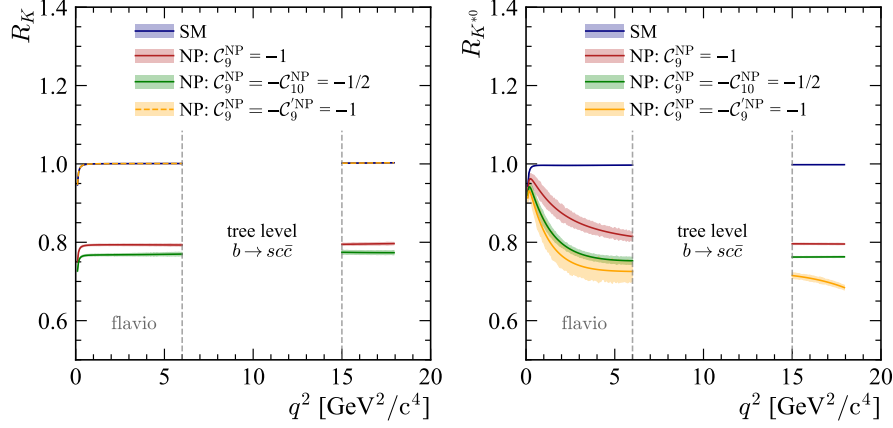


Figure 5.2 – R_K (left) and $R_{K^{*0}}$ (right) spectrum over q^2 range with modified Wilson coefficients that could resemble NP contributions [209].

value of $q^2 > 15 \text{ GeV}^2/c^4$ is excluded from the analysis because the description of the background is much more complicated here. However, a parallel study of the LHCb collaboration deals separately with this range. In all cases, to reconstruct the K^{*} particle in the case of the $R_{K^{*0}}$ measurement, the mass region dominated by the $K^{*0}(892)$ state is selected. The individual q^2 ranges, which for the rare decays are called "low q^2 " and "central q^2 ", are described in the following:

- **Low q^2 :** The rare decays $B^+ \rightarrow K^+ \ell^+ \ell^-$ and $B^0 \rightarrow K^{*0} \ell^+ \ell^-$ are studied in the low- q^2 range of $0.1 - 1.1 \text{ GeV}^2/c^4$. Choosing the upper boundary includes the region around the $\phi(1020)$ resonance. Chapter 9 describes the specific modelling of this background component. The lower boundary of the region is selected so that the predicted ratio $R_{K^{*0}}$ is as close as possible to unity. This choice excludes the photon pole region [116]. In the case of the $R_{K^{*0}}$ measurement, the lower limit was raised from $0.045 \text{ GeV}^2/c^4$ to $0.1 \text{ GeV}^2/c^4$ compared to the previous LHCb measurement [22]. The value of $0.045 \text{ GeV}^2/c^4$ corresponds to the minimum kinetic energy needed to generate the muon pairs of the signal decay. Thus, the previous study, which only examined a smaller data subset, increased the number of signal candidates that way. This choice came at the price of high contamination of the electron channel with parts of the photon poles, leading to significant deviations from LFU with an expected value of about $R_{K^{*0}} \sim 0.9$ in the SM. In contrast in this thesis, the exclusion of the photon pole leads to a predicted value of $R_{K^{*0}} \sim 0.98$ according to SM calculations, which is significantly closer to the expectation for the central- q^2 region with $R_{K^{*0}} = 1.00$. Compared to the previous measurements of the LHCb collaboration of R_K [23], this q^2 definition does not change.
- **Central q^2 :** The rare decays in the central- q^2 region are selected within a q^2 range of $1.1 - 6.0 \text{ GeV}^2/c^4$. This range is identical to previously published measurements of R_K and $R_{K^{*0}}$ by the LHCb collaboration. The lower limit largely excludes the

$\phi(1020)$ resonance, treated separately in the low- q^2 range. As an upper limit, the value at the same time leaves the number of signal candidates as high as possible, but also, does exclude dominant parts of diluted $J/\psi \rightarrow e^+e^-$ decays, where bremsstrahlung and final state radiation effects smear their resolution (see Section 3.2.4). Chapter 9 describes the modelling of remaining background contamination of the J/ψ resonance.

- Resonant q^2 : The q^2 regions including the resonant charmonium decays $B^+ \rightarrow K^+ J/\psi(\rightarrow \ell^+\ell^-)$ and $B^0 \rightarrow K^{*0} J/\psi(\rightarrow \ell^+\ell^-)$ lie above the rare q^2 regions. For the J/ψ resonance, a range of $6.0 - 11.0 \text{ GeV}^2/c^4$ and $11.0 - 15.0 \text{ GeV}^2/c^4$ for the $\psi(2S)$ resonance is used in the electron channel. For the muon channel, the resonances occur in much narrower regions compared to the electron channels due to negligible bremsstrahlung effects. These regions are selected as a band of $100 \text{ MeV}/c^2$ around the known particle masses of the J/ψ and $\psi(2S)$ resonances with $|m(\ell^+\ell^-) - m_{J/\psi}^{\text{PDG}}| < 100 \text{ MeV}/c^2$ and $|m(\ell^+\ell^-) - m_{\psi(2S)}^{\text{PDG}}| < 100 \text{ MeV}/c^2$, respectively.

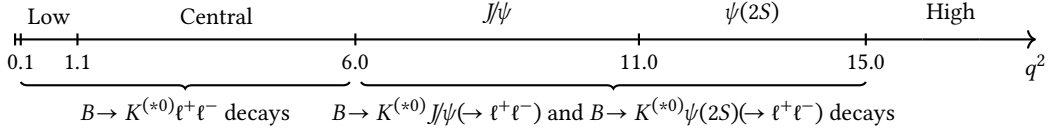


Figure 5.3 – Analysis regions of the squared invariant mass of the dilepton system q^2 . This analysis measures the rare decays $B^+ \rightarrow K^+ \ell^+ \ell^-$ and $B^0 \rightarrow K^{*0} \ell^+ \ell^-$ in the low and central regions together with the resonant decays $B^+ \rightarrow K^+ J/\psi(\rightarrow \ell^+ \ell^-)$, $B^0 \rightarrow K^{*0} J/\psi(\rightarrow \ell^+ \ell^-)$, $B^+ \rightarrow K^+ \psi(2S)(\rightarrow \ell^+ \ell^-)$, and $B^0 \rightarrow K^{*0} \psi(2S)(\rightarrow \ell^+ \ell^-)$. The resonant modes for the muon case are selected with $|m(\ell^+\ell^-) - m_{J/\psi}^{\text{PDG}}| < 100 \text{ MeV}/c^2$ and $|m(\ell^+\ell^-) - m_{\psi(2S)}^{\text{PDG}}| < 100 \text{ MeV}/c^2$.

Observables. In their given q^2 region, the observables R_K and $R_{K^{*0}}$ are defined according to Eq. (2.6) as

$$R_K^{SR} = \frac{\mathcal{B}(B^+ \rightarrow K \mu^+ \mu^-)}{\mathcal{B}(B^+ \rightarrow K e^+ e^-)} = \frac{N_{B^+ \rightarrow K^+ \mu^+ \mu^-}}{N_{B^+ \rightarrow K^+ e^+ e^-}} \cdot \frac{\varepsilon_{B^+ \rightarrow K^+ e^+ e^-}}{\varepsilon_{B^+ \rightarrow K^+ \mu^+ \mu^-}} \quad (5.1)$$

and

$$R_{K^{*0}}^{SR} = \frac{\mathcal{B}(B^0 \rightarrow K^{*0} \mu^+ \mu^-)}{\mathcal{B}(B^0 \rightarrow K^{*0} e^+ e^-)} = \frac{N_{B^0 \rightarrow K^{*0} \mu^+ \mu^-}}{N_{B^0 \rightarrow K^{*0} e^+ e^-}} \cdot \frac{\varepsilon_{B^0 \rightarrow K^{*0} e^+ e^-}}{\varepsilon_{B^0 \rightarrow K^{*0} \mu^+ \mu^-}}. \quad (5.2)$$

The label *SR* indicates that the variables are single ratios of the branching fractions of the rare muon and electron decay modes. Experimentally they are measured as the ratios of the number of signal candidates N corrected with the efficiencies ε .

However, the final ratios are computed as double ratios to reduce systematic experimental uncertainties due to different detector interactions for muons and electrons.

Here, the single ratios are multiplied by the lepton-flavour universal ratios of the resonant decays $B^+ \rightarrow K^+ J/\psi(\rightarrow \ell^+ \ell^-)$ or $B^0 \rightarrow K^{*0} J/\psi(\rightarrow \ell^+ \ell^-)$. Their ratio was measured to be unity [61]. So, the previously described uncertainties cancel out down to kinematic differences between the rare and resonant decays in the double ratio following the definitions

$$R_K = \frac{N_{B^+ \rightarrow K^+ \mu^+ \mu^-}}{N_{B^+ \rightarrow K^+ J/\psi(\rightarrow \mu^+ \mu^-)}} \cdot \frac{N_{B^+ \rightarrow K^+ J/\psi(\rightarrow e^+ e^-)}}{N_{B^+ \rightarrow K^+ e^+ e^-}} \cdot \frac{\varepsilon_{B^+ \rightarrow K^+ J/\psi(\rightarrow \mu^+ \mu^-)}}{\varepsilon_{B^+ \rightarrow K^+ \mu^+ \mu^-}} \cdot \frac{\varepsilon_{B^+ \rightarrow K^+ e^+ e^-}}{\varepsilon_{B^+ \rightarrow K^+ J/\psi(\rightarrow e^+ e^-)}} \quad (5.3)$$

and

$$R_{K^{*0}} = \frac{N_{B^0 \rightarrow K^{*0} \mu^+ \mu^-}}{N_{B^0 \rightarrow K^{*0} J/\psi(\rightarrow \mu^+ \mu^-)}} \cdot \frac{N_{B^0 \rightarrow K^{*0} J/\psi(\rightarrow e^+ e^-)}}{N_{B^0 \rightarrow K^{*0} e^+ e^-}} \cdot \frac{\varepsilon_{B^0 \rightarrow K^{*0} J/\psi(\rightarrow \mu^+ \mu^-)}}{\varepsilon_{B^0 \rightarrow K^{*0} \mu^+ \mu^-}} \cdot \frac{\varepsilon_{B^0 \rightarrow K^{*0} e^+ e^-}}{\varepsilon_{B^0 \rightarrow K^{*0} J/\psi(\rightarrow e^+ e^-)}}. \quad (5.4)$$

The single ratios of the resonant J/ψ decays are also used stand-alone for cross-checks of the analysis steps because here systematic uncertainties do not cancel out in this case (see Chapter 11). They are defined as

$$r_{J/\psi}^K = \frac{N_{B^+ \rightarrow K^+ J/\psi(\rightarrow \mu^+ \mu^-)}}{N_{B^+ \rightarrow K^+ J/\psi(\rightarrow e^+ e^-)}} \cdot \frac{\varepsilon_{B^+ \rightarrow K^+ J/\psi(\rightarrow e^+ e^-)}}{\varepsilon_{B^+ \rightarrow K^+ J/\psi(\rightarrow \mu^+ \mu^-)}} \quad (5.5)$$

and

$$r_{J/\psi}^{K^{*0}} = \frac{N_{B^0 \rightarrow K^{*0} J/\psi(\rightarrow \mu^+ \mu^-)}}{N_{B^0 \rightarrow K^{*0} J/\psi(\rightarrow e^+ e^-)}} \cdot \frac{\varepsilon_{B^0 \rightarrow K^{*0} J/\psi(\rightarrow e^+ e^-)}}{\varepsilon_{B^0 \rightarrow K^{*0} J/\psi(\rightarrow \mu^+ \mu^-)}}. \quad (5.6)$$

With these $r_{J/\psi}$ ratios, and as a further cross-check, the double ratios $R_{\psi(2S)}^K$ and $R_{\psi(2S)}^{K^{*0}}$ include the resonant $\psi(2S)$ decay modes with

$$R_{\psi(2S)}^K = \frac{\mathcal{B}(B^+ \rightarrow K^+ \psi(2S)(\rightarrow \mu^+ \mu^-))}{\mathcal{B}(B^+ \rightarrow K^+ \psi(2S)(\rightarrow e^+ e^-))} \cdot \frac{\mathcal{B}(B^+ \rightarrow K^+ J/\psi(\rightarrow e^+ e^-))}{\mathcal{B}(B^+ \rightarrow K^+ J/\psi(\rightarrow \mu^+ \mu^-))} \quad (5.7)$$

and

$$R_{\psi(2S)}^{K^{*0}} = \frac{\mathcal{B}(B^0 \rightarrow K^{*0} \psi(2S)(\rightarrow \mu^+ \mu^-))}{\mathcal{B}(B^0 \rightarrow K^{*0} \psi(2S)(\rightarrow e^+ e^-))} \cdot \frac{\mathcal{B}(B^0 \rightarrow K^{*0} J/\psi(\rightarrow e^+ e^-))}{\mathcal{B}(B^0 \rightarrow K^{*0} J/\psi(\rightarrow \mu^+ \mu^-))}. \quad (5.8)$$

To achieve the primary goal of measuring R_K and $R_{K^{*0}}$, it is crucial to ensure that the ratios $r_{J/\psi}^K$ and $r_{J/\psi}^{K^{*0}}$ remain stable with respect to unity. The stability validates the experimental integrity of the approach and methods used. The following sections describe the strategy of the signal selection and the determination of the efficiencies and signal yields.

5.2 Selection strategy

This section motivates the three stages of signal selection and provides a general overview. Chapter 6 will present all three in detail. The three stages concerned are the trigger selection, the centralised selection, and the analysis specific final offline selection.

Trigger selection. Because of its simpler calibration, the description of the trigger selection starts with the HLT. The HLT decisions employ properties of reconstructed particles, as Section 3.2.3 describes. This analysis selects only events that have passed the HLT trigger due to the presence of a reconstructed signal candidate (TOS). A much smaller fraction of events that passed the trigger due to other particles created in the pp collisions (TIS) is used for the efficiency calibrations (see Section 7.5). This means that exclusively selecting the TOS category does not lead to a significant loss of signal candidates. Since the later offline selection and the HLT trigger selection are both based on reconstructed track information and particle identification information, the efficiency determination is similar. In contrast, transverse energies, particle momenta, and detector occupancies are the inputs of the L0 trigger lines (see Section 3.2.3). This difference in trigger inputs results in four significant deviations from the HLT trigger strategy. First, the resolution of the L0 input quantities is significantly lower than the resolution of the fully reconstructed events. Second, the simulation does not describe these quantities precisely. Third, there are significant differences between the trigger conditions for electrons and muons. Fourth, discarding the TIS events is impossible because their fraction is significantly larger than in the HLT case. As a consequence of these challenges this thesis optimises several aspects of the analysis strategy: Previous measurements of R_K and R_{K^*0} by the LHCb experiment used two exclusive trigger categories with the L0 TOS as the primary category. While in the case of muons the majority of the reconstructed candidates obeys the TOS conditions of the trigger, in the electron channel this is typically only slightly more than half. This mismatch can be explained for the electron channel by the comparatively stricter selection criteria and the associated lower signal efficiencies. Thus, the proportion of electron TIS events accounts for about half of all triggered events in this mode. To mitigate this imbalance of the number of signal candidates per trigger category and the four specific points mentioned above, this analysis adjusts the usual choice of trigger categories. However, the analysis still employs two different L0 trigger categories, in which the individual analysis steps are performed separately to take into account their respective characteristics.

The TIS category for both electrons and muons is the new primary L0 trigger category. Here L0I stands for L0 triggered *independent* from signal. Because the trigger and reconstruction efficiency is generally much higher for muons than for electrons, the absolute number of muon signal candidates in the TIS category is still larger than for electrons. In the secondary L0 category, events are either chosen by the L0Muon TOS or the L0E TOS trigger (L0L for L0 *lepton*) and are not included in the primary L0I category. Another difference from the previous analyses concerns the usage of hadron

trigger lines. The $L0Hadron$ trigger line has a different performance for K^+ and K^{*0} in the hadronic calorimeter. Subsequently, this category is excluded from in the updated strategy. In this case, the price of a negligible loss of signal candidates facilitates the description of efficiencies and background contributions. Fig. 5.4 shows a schematic overview of the trigger selection strategy used in this thesis in comparison with the strategy used in the previous studies.

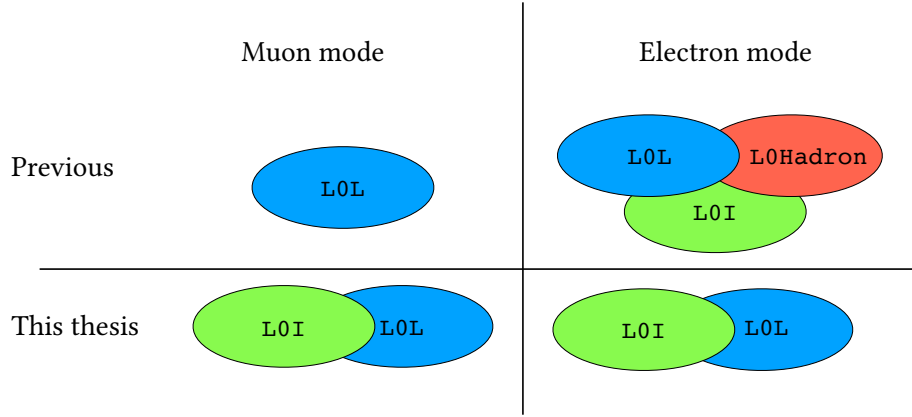


Figure 5.4 – Schematic view of the trigger categories used in this analysis compared to the previous choice, which was, for example, employed in the 2017 measurement of $R_{K^{*0}}$ by the LHCb collaboration [22].

This novel trigger strategy brings several advantages that mitigate the discrepancies between the electron and muon modes: As a first benefit of this strategy choice, two almost equal trigger categories for the electrons exist, with a simultaneously increased number of number of muon signal candidates. Second, differences in trigger efficiencies between electrons and muons in the TIS category are reduced because the TIS category does not employ the final state topology of the signal, but the remaining particles produced in the pp collisions, which are mostly independent of the final state leptons of the signal decays. As a result, only correlations between the signal decays and the rest of the particles produced could induce a remaining discrepancy. Thus, the trigger efficiencies of muons and electrons in the TIS category are maximally aligned (cf. Section 3.2.3). This alignment approach also mitigates differences in the kinematic quantities in data and simulation. Additionally, an exclusion of the $L0Photon$ trigger prevents kinematic differences, which are caused by bremsstrahlung photons of the electrons. In the case of using the $L0Photon$ trigger, bremsstrahlung photons not assigned to the signal would have been a diluting input to the TIS category. Section 6.1 presents the complete list of specific trigger conditions.

Stripping and offline selection. The “stripping” as the centralised preselection reduces the size of the data samples and imposes initial conditions on the reconstructed particle candidates. After this centralised processing step, the analysis-specific offline selection filters the signal. Here, the offline selection comprises filter conditions on the particle candidates, which include PID requirements, multivariate classifiers (MVA),

and the requirements to exclude specific background components. The PID criteria suppress signal-like backgrounds originating from decays of B hadrons, and the first MVA reduces combinatorial background. In the case of the electron channel, a second MVA reduces partially reconstructed decays. Chapter 6 describes these and all other selection steps in detail.

5.3 Efficiency measurement strategy

The extraction of the efficiencies consists of several partial efficiencies of the detector component responses and selection steps. The efficiencies are determined with data-driven approaches or with simulation. In some instances, however, the simulation cannot reproduce the detector responses reliably, so it needs a calibration. For this purpose, ratios of control channel efficiencies from data and simulation are determined to calibrate the simulation. This approach aligns the efficiencies between data and simulation, where kinematic quantities, which define the properties of the particles and tracks to calibrate, parameterise the calibrations. These data-simulation based corrections are mainly applied in the cases of particle identification, trigger, and tracking efficiencies.

A unique feature of this analysis is the simultaneous determination of R_K and R_{K^*0} . This novel strategy allows swapping the control channels between the two measurements. It is thus possible to achieve the efficiency calibrations for the measurement of R_K with the control channels $B^0 \rightarrow K^{*0} J/\psi (\rightarrow \ell^+ \ell^-)$ and vice versa for R_{K^*0} . This feature significantly reduces undesired correlations. Chapter 7 describes the calibration of the simulation, which is used to compute the efficiencies as described in Chapter 8.

5.4 Yield measurement strategy

The number of signal candidates for the rare and resonant decay modes is measured with one-dimensional maximum likelihood fits to the reconstructed mass of the B mesons. All signal channels, trigger categories, data-taking periods, and q^2 ranges are fitted at the same time. A primary advantage of this simultaneous approach is a substantial improvement of the handling of background components in the fits. This possibility of constraining background is especially important in the case of partially reconstructed decays of $B^0 \rightarrow K^{*0} e^+ e^-$, which is an essential background component modelling the $B^+ \rightarrow K^+ e^+ e^-$ decay candidates. For the partially reconstructed background of $B^+ \rightarrow K^+ e^+ e^-$, a pion in the decay $B^+ \rightarrow K^{*+} (\rightarrow K^+ \pi^0) e^+ e^-$ is not reconstructed. As the consequence, the reconstructed decay mimics the R_K signal. Now, the yield of the fully reconstructed decay $B^0 \rightarrow K^{*0} e^+ e^-$ constrains the background component in the $B^+ \rightarrow K^+ \ell^+ \ell^-$ fit.

For the first time, it is possible to determine the direct correlation of R_K and R_{K^*0} , because they are measured simultaneously. Consequently, it is possible to obtain the covariance matrix of the statistical and systematic uncertainties of R_K and R_{K^*0} .

Chapter 9 describes the modelling of the reconstructed invariant mass of the B mesons and the determination of the number of signal candidates. Finally, Chapter 12 presents the sensitivities of the results while the final values of R_K and R_{K^*0} are still kept blind.

5.5 Data samples and simulation

The described analysis uses the entire LHCb data set from pp collisions collected up to 2018. Individual phases of data collection are referred to as RUN 1 (2011 and 2012), RUN 2P1 (2015 and 2016), and RUN 2P2 (2017 and 2018). These individual data samples can be further divided depending on the configuration of the data taking. "Trigger Configuration Keys" (TCK) encode the trigger settings in the form of unique alphanumerical strings. In the case of data taking with the detector, these trigger settings repeatedly need adjustment to allow for consistent data quality as the detector conditions and most importantly how and how long the proton beam is provided by the LHC changes over time. For example, one hour of beam time from the LHC compared to 20 hours of beam time must both be recorded with consistent quality by the LHCb experiment and processed in the server farm. As a result, there is a composition of different TCKs in the data samples. For simulation, there is usually only one TCK because the simulation production does not include these changes. Therefore, the differences between the trigger settings of the data samples and simulation must be adjusted so that the simulation adequately describes the data. Chapter 6 and Chapter 7 also describe these alignment cuts of the trigger settings, which also have a direct influence on the simulation calibrations.

6 Selection

It is essential to control possible background contaminations of the signal while achieving the best possible sensitivity. Different selection steps are developed to filter the signal samples previous to computing the efficiency and fits to the invariant B masses to extract the number of signal candidates. The selection of the data samples consists of the following steps:

- **Trigger selection:** Data of the LHCb detector and simulation are filtered by the $L0$ trigger as well as by the HLT1 and HLT2 triggers. Section 6.1 describes the set of trigger requirements employed with their corresponding selection conditions.
- **Candidate reconstruction and centralised selection:** After the trigger selection, the next processing step includes a full reconstruction of all products of the proton-proton collision. The step also contains the centralised experiment-wide “stripping” selection, which aims at reducing the size of the data stored. Section 6.2 describes the selection requirements applied in this step. The “truth matching” consists of further conditions imposed on simulated samples and is also presented in this section.
- **General offline selection:** The centralised selection is followed by the analysis-specific offline selection, which is called “preselection” in the following. Here, after splitting the data samples into q^2 regions and trigger categories, general criteria are applied to the decay candidates to optimise the signal quality. Section 6.3 presents the requirements of this offline selection. Specifically, PID requirements filter out backgrounds that have been incorrectly identified (see Section 6.3.1). In another substep, so-called “clone tracks” are filtered out (details in Section 6.3.2).
- **Exclusive background selection:** Although the signal purity is already high after the preselection, additional background contributions must be handled. These sources of background are either modelled separately in the fits to the invariant mass (see Chapter 9) or removed with exclusive filter conditions. As the background components differ significantly for the decay modes, they are treated separately for the R_K and R_{K^*0} final states. Section 6.4 describes the corresponding selection.
- **Combinatorial and partially reconstructed background selection:** After this dedicated background component filtering, two other types of background contributions need further handling: multivariate classifiers are used to suppress

combinatorial and partially reconstructed background, which are described in Section 6.5. In addition, the HOP mass variable is used to filter further partially reconstructed low-mass background in the electron channel.

In general, to ensure the highest possible comparability and coherence of the R_K and R_{K^*0} measurements, the corresponding selections are designed to be as similar as possible.

6.1 Trigger selection

Section 3.2.3 describes the general trigger system of the LHCb experiment. After this introduction, Section 5.2 describes the triggering approach used for the measurement of R_K and R_{K^*0} presented in this thesis. As a reminder, the trigger system of the experiment consists of the L0 hardware trigger and the HLT trigger with two stages HLT1 and HLT2. For the hardware trigger, the analysis is performed in two L0 trigger categories chosen to reduce differences between electrons and muons as much as possible. The differences stem from distinct detector interactions of electrons and muons.

Hardware trigger L0 selection The L0I trigger category is the primary trigger category of this measurement. It contains events, where the part of the events that induced the trigger to fire are not part of the reconstructed signal decay. The category is formed as the logical OR of the L0Hadron_TIS, L0Muon_TIS, and L0Electron_TIS trigger lines for the B -meson candidates. In this case, for example, the L0Electron_TIS trigger line is fired when a track that is not part of the reconstructed B meson ($B^0 \rightarrow K^{*0}(\rightarrow K^+\pi^-)\ell^+\ell^-$ or $B^+ \rightarrow K^+\ell^+\ell^-$) satisfies the L0Electron_TOS trigger conditions. The primary trigger category L0I, which stands for “L0 triggered *independent* of signal”, is a concatenation of these three trigger requirements. The L0Lepton category, called L0L, is defined for electrons and muons by concatenating the L0Electron_TOS or L0Muon_TOS trigger lines respectively for the two lepton tracks of the signal decay. These trigger categories exclude the L0I category to form an independent selection. Consequently the definition of the three L0 trigger categories is

$$\mathbf{L0I}: \text{L0Hadron_TIS}(B) \parallel \text{L0Muon_TIS}(B) \parallel \text{L0Electron_TIS}(B),$$

$$\mathbf{L0M!}: (\text{L0Muon_TOS}(\mu_1) \parallel \text{L0Muon_TOS}(\mu_2)) \&\& ! \text{L0I},$$

$$\mathbf{L0E!}: (\text{L0Electron_TOS}(e_1) \parallel \text{L0Electron_TOS}(e_2)) \&\& ! \text{L0I}.$$

The following convention is used in this thesis: If the trigger categories are defined such that no other category is excluded, then they are called “inclusive” trigger categories and are indicated with the simple notation L0I, L0Muon, or L0Electron. However, if a trigger category is excluded, it is indicated with the notation L0I!, L0M!, or L0E!.

Software trigger HLT selection The strategy for the HLT, which is composed of the two stages HLT1 and HLT2, is described above in Section 5.2. This analysis employs the same trigger lines as used in the 2017 $R_{K^{*0}}$ [22] measurement conducted by the LHCb collaboration. For HLT2 it does not use HLT2 _4-track topological triggers, since there is no fourth particle in the final state for the R_K measurement. This choice maximally aligns the trigger lines used, thus increasing comparability and improving the portability of the efficiency calibrations later. Table 6.1 presents an overview of the HLT selection, where all trigger requirements are TOS. While the HLT1 level trigger lines use general kinematic track information, the HLT2 requirements use topological trigger lines, which make use of the displaced topology of decay of a B meson to a final state containing two or three charged tracks (cf. Ref.[191]). A more detailed description of the single trigger lines is given in Section 3.2.3.

Table 6.1 – Overview of the HLT requirements for electron and muon modes for the measurements of R_K and $R_{K^{*0}}$ per years of data taking.

	Muon modes	Electron modes
2011, 2012		
	Hlt1TrackAllL0	
HLT2	Hlt2Topo[2,3]BodyBBDT	
	Hlt2TopoMu[2,3]BodyBBDT	Hlt2TopoE[2,3]BodyBBDT
2015		
	Hlt1TrackMVA	
HLT2	Hlt2Topo[2,3]Body	
	Hlt2TopoMu[2,3]Body	
2016, 2017, 2018		
	Hlt1TrackMVA	
	Hlt2Topo[2,3]Body	
HLT2	Hlt2TopoMu[2,3]Body	Hlt2TopoE[2,3]Body
	Hlt2TopoMuMu[2,3]Body	Hlt2TopoEE[2,3]Body

As the rapidly changing data-taking conditions are not always well represented in the simulated samples, an alignment of the TCKs between simulation and data is applied as a further selection step. This alignment is a key part of the simulation calibration described in Chapter 7.

6.2 Reconstruction and stripping selection

In the centralised reconstruction and “stripping” processing step, requirements filter and form the particle candidates for the decays. Specific selections and reconstruction procedures are bundled in sets called “stripping lines”. In this thesis, the stripping

lines Bu2LLKmmLine and Bu2LLKeeLine2 select the signal decays for the muon and electron decay modes, respectively. Table A.1 in the Appendix lists the stripping requirements of the two lines. They are identical for the electron and muon channel and the measurements of R_K and R_{K^*0} except where indicated.

The tracking system of the LHCb detector is presented in Section 3.2.1. On the software side, the reconstruction starts with the reconstruction of the most commonly used long tracks. The first step of the reconstruction of the long tracks is identifying and forming straight VELO tracks. Because the magnetic field of the detector is negligible in the VELO, no bending occurs. The VELO tracks are then combined with information from the TT or already reconstructed TT tracks. The tracking is performed and further optimised using the Kalman filter fit [210]. Consequently, the reconstruction of a B -meson candidate starts with the composition of the dilepton system from two lepton tracks with opposite electric charge, each with a transverse momentum of $p_T > 300 \text{ MeV}/c$, $\chi_{\text{IP}}^2 > 9$, and relatively loose PID requirements. Additionally, the resulting dilepton system must have a displacement from the primary vertex and a minimum quality of its vertex fit. Bremsstrahlung photons are reconstructed and assigned to the lepton tracks with a dedicated bremsstrahlung recovery algorithm (see. Section 3.2.4). Analogously, in the case of the measurement of R_{K^*0} , the reconstruction of the K^{*0} particle is done from a charged pion and a charged kaon track. The reconstructed mass of the K^{*0} must lie within a mass window of $300 \text{ MeV}/c^2$ around the known mass of the K^{*0} meson. The B^0 - or B^+ -meson candidate is reconstructed from the K^{*0} candidate or a K^+ candidate, respectively, and the dilepton system. For the B meson, a minimum displacement from the primary vertex and a minimum quality of the vertex fit is required. The selection also includes a condition on the DIRA variable. Events with very high track multiplicity are removed by applying a requirement on the corresponding proxy variable of $\text{nSPDHits} < 600$ in RUN 1 and $\text{nSPDHits} < 450$ in RUN 2, respectively. Table 3.3 shows an overview of the meanings of the individual variables.

In this thesis, the PID conditions are not imposed as direct cuts on simulation, but as weighting efficiency factors, the PID requirements listed in the stripping overview are only applied to data. In the case of simulation, these are removed from the stripping line definitions. Section 6.3.1 provides a detailed description of the PID selection and Section 7.2 presents the determination of the PID efficiency calibration.

Truth matching. To model the signal distribution in data, as well as to estimate the signal selection efficiencies, a clean sample of simulated signal candidates is required. However, signal simulation, being processed through the same reconstruction algorithm as the data, is polluted by candidates which are not properly reconstructed. Those candidates originate, for example, from combinations of the other tracks in the event. To select only the true signal candidates, the reconstructed candidates of the simulation samples are classified as signal or specific background categories via the “truth matching” procedure. For this classification, various background hypotheses are tested with an algorithm designed for this purpose [211]. If none of these hypotheses

fit, the simulation candidate is classified as fully signal. Thus, for example, for the signal category that corresponds to perfectly reconstructed candidates, all reconstructed track types must match the initially generated truth information. Depending on the intended use within the analysis described here, different truth matching criteria are applied.

- **For the calibration of the simulation**, which is described in Chapter 7, fully correctly reconstructed *Signal*, *Quasi-signal*, and *Low-mass background* are used. *Quasi-signal* means that the decay was correctly and completely reconstructed, but an intermediate resonance or particle of the decay cascade was incorrectly identified. In the case of *Low-Mass background*, there is no mis-identification. Still, the decay was not completely reconstructed because, for example, a daughter particle of the decay to be reconstructed left the detector acceptance. In addition, for the low-mass background, the parent particle of the decay must have a mass of at most 100 MeV/ c above the reconstructed parent particle.
- **For the training and test data sets of the multivariate classifiers** described in Section 6.5 and in the fits to the invariant mass of the B mesons described in Chapter 9, the categories *Signal*, *Quasi-signal*, *Low-mass background* or *Ghost* are employed. In the case of the *Ghost* category, a final state track was not assigned to any of the original generated simulation particles.
- **For the calculation of efficiencies** with simulation, which is described in Chapter 7, the categories *Signal*, *Quasi-signal*, *Low-mass background* or *Ghost* are used. An additional condition is that at most one track was reconstructed incorrectly.

In the case of multiple signal candidates per event, the most signal-like category is selected. Most-signal like means here the candidate with the smallest truth matching ID. If there are multiple candidates of the *Signal* category in an event, one of them is chosen at random.

6.3 Offline selection

After the centralised reconstruction and stripping selection, the offline processing further selects the data. It consists of detector acceptance, track momenta, fit quality, and PID requirements. To complete the list of offline selection requirements Table 6.2 presents a summary of the q^2 region definitions introduced in Section 5.1. Finally, Table A.2 shows an overview of the additional offline selection requirements in five groups. The detector acceptance selection removes tracks that interact with the innermost region of the ECAL. This removal optimises the agreement between simulation and data, because the central ECAL region is part of the simulation but is not read out during the LHCb data taking. The inner region is excluded with a corresponding geometrical requirement. Additionally, tracks must lie in the remaining ECAL acceptance. The requirement that electron tracks within the ECAL have a minimum

distance greater than 100 mm from each other ensures that sufficient reconstruction of their properties is possible without overlapping interaction clusters. Constraints on the transverse momentum of the kaons and the invariant mass of the K^{*0} candidate are already required in the stripping selection (see Table A.1) but are tightened in the offline selection to achieve a higher signal purity. Requirements on the PID are explained below in Section 6.3.1 in detail. Since separate calibration data samples are used to determine the PID efficiencies the offline selection must be adapted as closely as possible to the selection of the calibration samples. Together with additional conditions on tracks regarding further sub-detector acceptances and the track multiplicity of the event, selection criteria on the particle momenta and fit qualities define the class of quality and calibration criteria.

In addition, all tracks of the final states must have a minimum angle to each other to avoid reconstruction from duplicated tracks, so-called “clones”, which Section 6.3.2 explains in detail.

The criteria are optimised to be as identical as possible for the R_K and $R_{K^{*0}}$ measurements and within the rare and resonant decay channels. For example, differences in the stripping lines for R_K and $R_{K^{*0}}$ are compensated for as much as possible by the offline selection.

Table 6.2 – Requirements to select the various q^2 regions of this analysis in resonant and rare decay modes.

Decay mode	q^2 selection
Electron mode J/ψ region	$6 < q^2 < 11 \text{ GeV}^2/c^4$
Muon mode J/ψ region	$ m(\mu\mu) - m(J/\psi)_{\text{PDG}} < 100 \text{ MeV}/c^2$
Electron mode $\psi(2S)$ region	$11 < q^2 < 15 \text{ GeV}^2/c^4$
Muon mode $\psi(2S)$ region	$ m(\mu\mu) - m(\psi(2S))_{\text{PDG}} < 100 \text{ MeV}/c^2$
Low- q^2 region	$0.1 < q^2 < 1.1 \text{ GeV}^2/c^4$
Central- q^2 region	$1.1 < q^2 < 6.0 \text{ GeV}^2/c^4$

6.3.1 Particle identification selection

The relatively loose PID requirements of the stripping listed in Table A.1 are tightened in the offline selection. With that, the analysis aims to suppress background contributions where tracks are mis-identified or mutually interchanged during the reconstruction, e.g., a kaon with a pion in the final states of signal decays. Because the pions represent the most abundant particle type in the LHCb detector mis-identifications with pions are the most common case. But there are also non-negligible contributions from final state particles mis-identified from original kaons or protons. Direct requirements on PID-related variables reduce these background contributions in data. However, for simulation, for example, to determine efficiencies, this is handled differently. Here, event-wise calibration factors are applied, previously determined with a

data-simulation-based procedure. This procedure is explained in detail in Section 7.2. The computation of the calibration factors uses the same PID conditions as on data, which are described below and listed in Table A.2 under “PID” for the individual tracks. To determine the efficiencies correctly, calibration and signal data must be as consistent as possible. For this reason, the selection requirements are applied to the different data sets. Table A.2 lists these requirements under “Calibration”. These conditions consist of further kinematic requirements and conditions on geometric variables concerning the detector acceptance and track quality requirements. The kinematic boundaries on the momenta of the tracks ensure that the same kinematic range is covered between the two sample types. Equal coverage is essential here because the correction factors calculated later are parameterised via the kinematic properties of the particles. Concerning the detector acceptance conditions, all tracks must have hits in the RICH detectors, which is ensured by the variable `hasRICH`. In addition, the electron tracks must have left energy clusters in the calorimeter (`hasCalo`), and muon tracks must be in the acceptance of muon system (`inMuonAcc`).

The actual PID requirements combine, on the one hand, selection criteria that identify particle types and, on the other hand, conditions that filter out mis-identified backgrounds. In the case of hadron selection for kaons and pions, the criteria $\text{ProbNNk} \cdot (1 - \text{ProbNNp}) > 0.05$ or $\text{ProbNNpi} \cdot (1 - \text{ProbNNk}) \cdot (1 - \text{ProbNNp}) > 0.1$ require the tracks to have a minimal agreement with their assigned particle hypothesis as a kaon or a pion, and simultaneously reduce mis-identifications as protons or kaons, respectively. The `ProbNN` variables used with this requirement are explained in Section 3.2.2. In addition, for the kaon candidates the use of the delta log-likelihoods PID variables suppresses further pion mis-identifications. Also for the leptons, conditions are imposed on the `ProbNN` variables to require minimum compatibility with their particle hypotheses. Similarly, the requirement on the `PIDe` variable for electrons filters out mis-identified pions. This additional requirement is unnecessary for muons due to the nature of their detection in the muon system, where pions are no longer abundant because of the iron shielding of the system.

6.3.2 Clone tracks

Different track reconstruction algorithms and sub-detectors in the tracking system of the LHCb experiment can lead to copies of the same track or sub-tracks as parts of the full track in single detector components from other tracks in the reconstruction. If two tracks share at least 70 % of their total hits in the detector, they are explicitly labelled as “clone tracks”. Usually, these are removed within the tracking reconstruction by an algorithm [212, 213]. However, it may be the case that a non-negligible fraction of clone candidates survive this filtering, because they have less than 70 % shared hits. So, for example, for electrons, bremsstrahlung can change the direction of a track. Thus, a set of hits in the VELO can be assigned to several tracks in the tracking stations. Therefore, the clone tracks share their VELO hits but have different momentum and particle hypotheses and thus represent a non-negligible background contribution. They are not identified and labelled as clone tracks because of the limited detector

resolution. To remove those events, a small angle between the tracks of all pairs of final state particles indicates the existence of clone tracks. They are suppressed with a requirement on the angles between all track pairs to be greater than 0.5 mrad, which keeps the signal efficiency close to 100 %.

6.4 Exclusive background

After the general selection, further background contributions occur in the range of the invariant mass of the B mesons, where the signal candidates are extracted with maximum likelihood fits. These remaining background contributions are handled in two different ways: either they have to be modelled separately in the maximum likelihood fits or they are suppressed by dedicated selection requirements if possible. The background components consist of three classes.

- First, there are decays with mis-identified final state particles, with a wrong particle hypothesis assigned. Thus, this mis-identification leads to a wrong mass hypothesis within the reconstruction. In many cases, these backgrounds can be filtered out by changing back the mass hypothesis of the mis-identified particle to its true value. With that, the reconstruction of an intermediate resonance is possible. Dedicated cuts remove this resonance from the data sample. To achieve higher signal efficiencies, in some cases, additional strict PID constraints on the mis-identified particle allow for looser veto cuts on the resonances.
- Second, partially reconstructed background decays consist of at least four or five final state particles in the case of the measurement of R_K or R_{K^*0} , respectively. Here, only a fraction of the final state particles is reconstructed and consequently can mimic the signal decay. The remaining particles, which are not included, carry away momentum, which is why this type of background is found mainly in the lower region of the reconstructed B mass (“lower sideband”). The partially reconstructed backgrounds are filtered out either by vetoes on reconstructed particle masses, handled with a multivariate classifier as explained in Section 6.5, or treated as components in the modelling of the mass fits.
- Third, combinatorial background is reduced by another multivariate classifier. Residual contributions are described in the mass fit.

The different decay-specific selection criteria are designed separately for the measurement of R_K and R_{K^*0} . In the case of mis-identification backgrounds, the number of background decays for the measurement of R_K is smaller since there is only one hadron in the final state to be mis-reconstructed. The same reasoning applies to the partially reconstructed background. A summary of the background selection requirements can be found in Table 6.3.

B^+ mode. For the B^+ -decay mode, the following mis-reconstructed and partially reconstructed decays are vetoed:

The decay $B^+ \rightarrow \bar{D}^0(\rightarrow K^+\pi^-)\ell^+\nu_\ell$ is reconstructed as signal when the pion is mis-identified as a charged lepton. The background of this type is filtered out by calculating the invariant mass of the kaon and the lepton with opposite charges under the pion-mass hypothesis on the lepton in data. If this agrees with the known D^0 mass with less than $40 \text{ MeV}/c^2$ difference, the lepton must pass tight PID criteria in order to not filter out the specific signal candidate.

For the decay $B^+ \rightarrow \bar{D}^0(\rightarrow K^+\ell^-\bar{\nu}_\ell)\ell^+\nu_\ell$, two additional neutrinos not detected in the LHCb experiment lead to a possible false reconstruction as a signal. To suppress this background contribution the invariant mass of the system consisting of the kaon and oppositely charged lepton is calculated. If this mass is lower than the D^0 -mass region with a threshold of $1780 \text{ MeV}/c^2$ the corresponding candidates are removed.

For the so-called ‘‘hadron-lepton swap’’, a twofold mis-identification occurs between the kaon and a charged lepton. Under this swap, the resonant signal decays may be reconstructed as signal because the invariant mass of the $K^+\ell^+\ell^-$ system is consequently reconstructed closely to the B^+ -meson mass. If the invariant masses of the muon and kaon candidates deviate by less than $60 \text{ MeV}/c^2$ from the known mass of the J/ψ or $\psi(2S)$ resonances under the muon-mass hypothesis, the muon candidate must fulfil rigorous particle identification requirements. If this is the case the leptons are also subject to strict PID conditions. For electrons, this requirement is applied if the invariant mass of the $K^+\ell^+\ell^-$ system deviates less than $60 \text{ MeV}/c^2$ from the known B^+ -meson mass. The invariant mass of the system is computed under switched mass hypotheses with a constraint of the mass of the dilepton system on the known J/ψ - or $\psi(2S)$ -meson mass.

B^0 mode. For the B^0 signal decays, the following background contributions need to be suppressed with dedicated selection requirements: If one of the kaons in the decay $B_s^0 \rightarrow \phi(1020)(\rightarrow K^+K^-)\ell^+\ell^-$ is identified as a pion, the decay can be mis-reconstructed as signal. Background suppression is achieved by calculating the invariant mass of the $K^+\pi^-$ system under the kaon-mass hypothesis for the pion. If the this mass lies below the ϕ -mass region, the pion of the signal candidate must fulfill strict PID criteria to not being filtered out. The two decays $B^0 \rightarrow \bar{D}^0(\rightarrow K^+\pi^-)\pi^-\ell^+\nu_\ell$ and $B^0 \rightarrow D^-(\rightarrow K^{*0}(\rightarrow K^+\pi^-)\pi^-)\ell^+\nu_\ell$ can be reconstructed as a signal if the neutrino is not detected and a pion is mis-identified as a lepton. In both cases, either the invariant mass of the $K^+\ell^-$ or $K^+\pi^-\ell^-$ system, computed with the pion-mass hypothesis assigned to the lepton, must be incompatible with the known \bar{D}^0 or D^- mass, respectively, or obey stringent PID conditions.

If two neutrinos are not reconstructed, the $B^0 \rightarrow D^-(\rightarrow K^{*0}(\rightarrow K^+\pi^-)\ell^-\bar{\nu}_\ell)\ell^+\nu_\ell$ decay can be reconstructed as a signal. To filter it out, the invariant mass of the $K\pi$ system and the lepton oppositely charged to the kaon must be greater than $1780 \text{ MeV}/c^2$. The background decay $B^+ \rightarrow K^+\ell^+\ell^-$ can be falsely reconstructed as a signal under the capture of a random pion. It is suppressed by calculating two invariant

Table 6.3 – Exclusive background selection.

Background decay	Selection requirement
B^+ mode	
$B^+ \rightarrow (\bar{D}^0 \rightarrow K^+ \pi^-) \ell^+ \nu_\ell$	$! (m(K^+(\ell^- \rightarrow \pi^-)) - m(D^0)_{\text{PDG}} < 40 \text{ MeV}/c^2$ && $L_ProbNNL < 0.8)$
$B^+ \rightarrow (\bar{D}^0 \rightarrow K^+ \ell^- \bar{\nu}_\ell) \ell^+ \nu_\ell$	$m(K^+ \ell^-) > 1885 \text{ MeV}/c^2$
$K \leftrightarrow \mu$	$! (m((\mu \rightarrow K)\mu) - m(J/\psi/\psi(2S))_{\text{PDG}} < 60 \text{ MeV}/c^2$ && $M_ProbNNmu < 0.8)$
$K \leftrightarrow e$	$! (m((e \rightarrow K)e)_{J/\psi/\psi(2S) \text{ constrained}} - m(B^+)_{\text{PDG}} < 60 \text{ MeV}/c^2$ && $K_ProbNNe < 0.8)$
B^0 mode	
$B_s^0 \rightarrow \phi(1020)(\rightarrow K^+ K^-) \ell^+ \ell^-$	$! (m(K(\pi \rightarrow K)) < 1040 \text{ MeV}/c^2 \text{ \&\& } \text{Pi_ProbNNpi} < 0.8)$
$B^0 \rightarrow \bar{D}^0(\rightarrow K^+ \pi^-) \pi^- \ell^+ \nu_\ell$	$! (m(K^+(\ell^- \rightarrow \pi^-)) - m(D^0)_{\text{PDG}} < 30 \text{ MeV}/c^2$ && $L_ProbNNL < 0.8)$
$B^0 \rightarrow D^-(\rightarrow K^{*0}(\rightarrow K^+ \pi^-) \pi^-) \ell^+ \nu_\ell$	$! (m(K^+ \pi^+(\ell^- \rightarrow \pi^-)) - m(D^-)_{\text{PDG}} < 30 \text{ MeV}/c^2$ && $L_ProbNNL < 0.8)$
$B^0 \rightarrow D^-(\rightarrow K^{*0}(\rightarrow K^+ \pi^-) \ell^- \bar{\nu}_\ell) \ell^+ \nu_\ell$	$m(K^+ \pi^-) > 1780 \text{ MeV}/c^2$
$B^+ \rightarrow K^+ \ell^+ \ell^-$	$\max(m(K^+ \ell^+ \ell^-), m(\pi^+ \rightarrow K^+) \ell^+ \ell^-) < 5100 \text{ MeV}/c^2$
$h \leftrightarrow \ell$	$! (m((\mu \rightarrow h)\mu) - m(J/\psi/\psi(2S))_{\text{PDG}} < 60 \text{ MeV}/c^2$ && $M_ProbNNmu < 0.8)$ $! (m((h \rightarrow e)h(e \rightarrow h)e)_{J/\psi/\psi(2S) \text{ constrained}} - m(B^0)_{\text{PDG}} < 60 \text{ MeV}/c^2$ && $E_ProbNNe < 0.8)$
All modes	
$B \rightarrow \psi(2S)(\rightarrow J/\psi X)Y$	$ m(B)_{\psi(2S) \text{ constrained}} - m(B)_{\text{PDG}} < 200 \text{ MeV}/c^2$

masses. Once it is the invariant mass of the $K^+ \ell^+ \ell^-$ system and once of the $\pi \ell^+ \ell^-$ system with the kaon-mass hypothesis assigned to the pion. The maximum of these two invariant masses must be smaller than $5100 \text{ MeV}/c^2$. Significant contributions of this background decay are also reduced by the multivariate classifier against combinatorial background (see Section 6.5.1). For the hadron-lepton swap, the same approach as described above for the B^+ decay channel is valid.

The cascade decay $B \rightarrow \psi(2S)(\rightarrow J/\psi X)Y$ is suppressed by requiring the invariant B -meson mass constrained with the known $\psi(2S)$ -meson mass to differ less than $200 \text{ MeV}/c^2$ from the known B -meson mass.

6.5 Combinatorial and partially reconstructed background

Beyond the previously described selection steps, multivariate classifiers trained on simulation and collision data suppress combinatorial and partially reconstructed back-

ground (see Section 6.5.1). In addition, Section 6.5.2 describes an additional technique, which employs momentum imbalances to further reduce partially reconstructed background.

6.5.1 Multivariate classification

Multivariate data analysis (MVA) examines multiple decay features simultaneously. In this thesis, multivariate classification represents a powerful tool for signal-background discrimination. In this case, supervised machine learning with labelled data samples is employed. With labelled training samples, the machine-learning classifier is trained to differentiate between signal and background. During the training of the classifier, the algorithm minimises a loss function, which indicates the difference between the true information indicated by the labelling and the classifier’s prediction. Employing the concept of decision trees, a Boosted Decision Tree (BDT) [214] is used. During the training of the BDT single decision trees as weak learners are combined via gradient boosting [215] to optimise the decision power. This means that the BDT combines an ensemble of decision trees trained iteratively accounting for previous mis-classifications.

As a specific implementation the CATBOOST BDT [216] in combination with the “Reproducible Experiment Platform” [217] framework is chosen.

Set of classifiers. Separate classifiers are trained to suppress the combinatorial background for the muon and electron channels, as well as for the partially reconstructed background for the electron channel. Partially reconstructed backgrounds are significant for the electron decay modes. Their mass resolution is lower compared to the muon decay modes leading to a considerable overlap of signal and possible background components.

A separate classifier training for R_K and R_{K^*0} and all three data taking periods results in training of 12 different classifiers for the combinatorial background BDTs and training of 6 different classifiers for the partially reconstructed background BDTs.

Training data sets and cross-validation. Simulation of the rare decays $B^0 \rightarrow K^{*0} \ell^+ \ell^-$ and $B^+ \rightarrow K^+ \ell^+ \ell^-$ is employed as the signal proxy. A test showed that the usage of calibrated simulation does not cause a difference in performance. Thus, uncalibrated simulation is used in the training of the multivariate classifiers. Signal candidates from collision data that have an invariant B mass above $5400 \text{ MeV}/c^2$ or $5600 \text{ MeV}/c^2$ for muons and electrons, respectively, and below $6779 \text{ MeV}/c^2$ for both form the combinatorial background proxy. Finally, specific simulation samples resemble the partially reconstructed background. Before the training, the analysis selection as described above filters the input samples. To have enough training data left after this selection and to allow statistically meaningful training, the background samples for the two q^2 ranges of the rare decay channels are used together in each case. These merged

data sets allow obtaining balanced, i.e. equally sized, training data sets for signal and background, thus avoiding statistical bias.

Another method to prevent biases is cross-validation based on the k -folding method [218]. Here, for each of the classifiers described above, $k = 10$ different instances are trained, each omitting other 10% of the training data. After the training, the classifiers perform the predictions on this remaining 10% for performance validation. This method avoids the case that simulation or data events are classified with the same BDT where they were used as a training sample. If this method would not be applied it could lead to fake structures in the data in case of severe overtraining.

For the partially reconstructed background BDTs, the decay $B^0 \rightarrow K^{*0} e^+ e^-$ reconstructed as $B^+ \rightarrow K^+ e^+ e^-$ is used as a background proxy. This decay is identified as the signal when the reconstruction does not include the charged pion. For the B^0 decay mode, the simulated background decay $B^+ \rightarrow K^+ \pi^+ \pi^- e^+ e^-$ is used, which mimics the signal if one of the charged pions is not reconstructed. Cross-validation is not required because the background proxy sample is not used in the further analysis. Consequently, the danger that the sample is categorised with the classifier it was also used for in the training is not existing.

Classifier input variables. As input features for the classifiers, 23 variables are selected for the B^0 decays, and 16 variables for the B^+ decays. Table A.3 presents these input variables for the combinatorial background classifier. These are mainly kinematic, topological, and decay vertex properties of the different particles involved in the decay. They were selected from a broader range of variables for which the individual distributions between signal and background differ significantly. The final feature selection employs backward elimination, in which the least important variables according to the feature importance of the CATBOOST BDT algorithm are removed in iterated trainings. Only those variables are discarded, which improve the classifier performance as measured in terms of the area under the Receiver Operating Characteristics (ROC) curve of less than 1%. Here, the false positive rate versus the true positive rate corresponding to various classifier output threshold defines the ROC curve. The same procedure applies for the BDTs against the partially reconstructed underground. In addition to the kinematic and geometric variables already mentioned, so-called isolation variables are added as input here. These isolation variables are, for example, calculated in cones of 0.5 mrad around the lepton candidates including possible other charged particles within this cone to distinguish the signal decay from potential background contributions.

In addition to the iterative selection of input variables, a systematic variation of the BDT hyperparameters optimises the classifier performance.

Classifiers output optimisation. After the two classifiers have been applied to the analysis data sets, thresholds on their continuous output must be optimised. This optimisation is performed simultaneously to suppress both combinatorial and partially reconstructed backgrounds for the electron mode. For the muon mode the same

procedure is followed but as a one-dimensional optimisation for suppression of the combinatorial background. Here, the significance is optimised using a figure of merit defined as $N_S/\sqrt{(N_S + N_B)}$ as the expectation of signal and background candidates. The expected number of rare signal candidates N_S is estimated with the number of simulated J/ψ decay candidates, which is then scaled by the ratio of the rare and resonant decays widths in the SM. The expected number of background candidates N_B , on the other hand, is computed using fits to data.

6.5.2 Momentum imbalance technique

Further suppression of partially reconstructed background is achieved, in addition to the BDT classifier by using the so-called HOP mass [219] for the electron channel. This suppression is particularly effective for low-mass background. To suppress this background contribution, the ratio of the momentum components of the signal hadrons and the dielectron system orthogonal to the flight direction of the reconstructed B meson is calculated as a factor

$$\alpha_{\text{HOP}} = \frac{p_{\perp}(\text{Hadrons})}{p_{\perp}(e^+e^-)}. \quad (6.1)$$

The momentum of the dielectron system is corrected here with

$$p_{\text{Corrected}}(e^+e^-) = \alpha_{\text{HOP}} \cdot p(e^+e^-). \quad (6.2)$$

With the help of this corrected momentum, a corrected mass m_{HOP} of the reconstructed signal decays $B^+ \rightarrow K^+e^+e^-$ and $B^0 \rightarrow K^{*0}e^+e^-$ is calculated. For bremsstrahlung emission, the ratios do not significantly deviate from unity, given the detector resolution, because the photons are emitted colinearly to the electron direction of flight. For partially reconstructed background, the assumption that the momentum correction also applies to the longitudinal component does not hold. The reason for this is that the momentum imbalance is not caused by bremsstrahlung emission but by missing tracks in the reconstruction. As a consequence, the HOP-corrected mass m_{HOP} for signal and partially reconstructed background show differences that can be used to discriminate the two components. Fig. 6.1 shows this exemplarily for the corrected mass m_{HOP} of the signal decays and partially reconstructed background components. As already used for the training of the multivariate classifiers, simulated $B^0 \rightarrow K^{*0} (\rightarrow K^+\pi^-)e^+e^-$ and $B^+ \rightarrow K^+\pi^-\pi^+e^+e^-$ decay samples resemble the background for R_K and $R_{K^{*0}}$, respectively.

Optimal selection cuts on the corrected mass m_{HOP} are determined analogously to the optimisation of the MVA classifier outputs. However, the HOP optimisation already applies the BDT selection. The cut values are $m_{\text{HOP}} < 4800 \text{ MeV}/c^2$ for the low- q^2 region and $m_{\text{HOP}} < 4700 \text{ MeV}/c^2$ in the central- q^2 region.

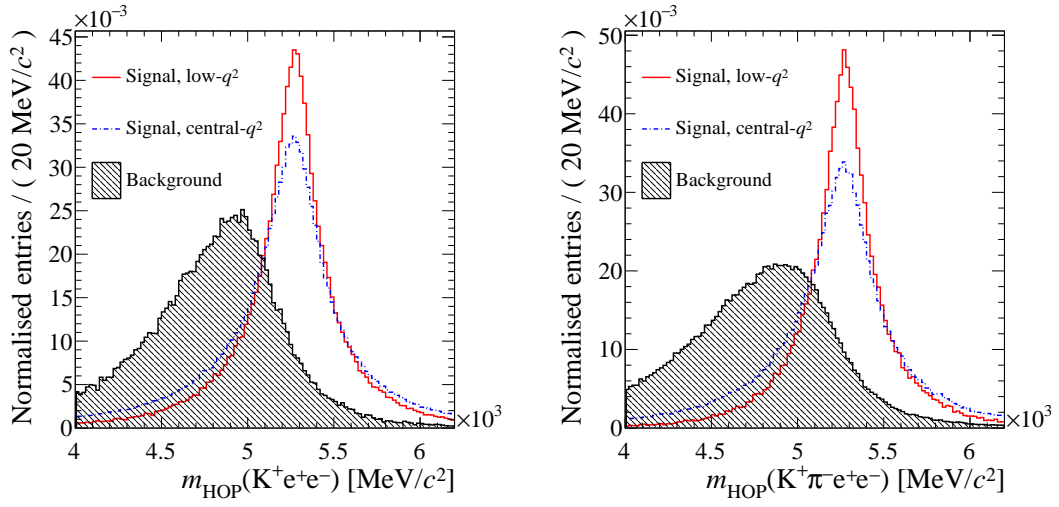


Figure 6.1 – Corrected mass m_{HOP} for simulated decays (left) $B^+ \rightarrow K^+ e^+ e^-$ and (right) $B^0 \rightarrow K^{*0} e^+ e^-$ compared with simulated partially reconstructed background ($B^0 \rightarrow K^{*0} (\rightarrow K^+ \pi^-) e^+ e^-$ and $B^+ \rightarrow K^+ \pi^- \pi^+ e^+ e^-$) in grey. Shown in red solid line are the distributions for the low- q^2 region and in dashed blue for the central- q^2 region.

7 Calibration of simulation

The signal efficiencies along with the number of signal candidates are the main components of the measurement of the quantities R_K and R_{K^*0} . For preparing both ingredients simulation is employed: first, most steps of the calculation of the efficiencies employ simulated signal decays. Second, in the fits to the invariant mass of the $K^+\ell^+\ell^-$ and $K^+\pi\ell^+\ell^-$ data, simulation is used to model signal and background components. Since this simulation does not perfectly describe all conditions of the LHC collisions, b -quark hadronisation, the LHCb detector, and the particle decay dynamics, it has to be *calibrated* to guarantee accurate modelling of the detector response and underlying physics processes. Here, the most important calibration steps are validating the agreement between the simulated particle kinematics and the event multiplicity with the data distributions, the performance of the L0 and HLT triggers, an accurate description of the event reconstruction, and the performance of the PID system. The requirement of a precise description of the efficiencies, and a maximum possible understanding of the remaining differences between the detection of decays with muons or electrons in the final state, makes the simulation calibration an essential part of the measurement.

The calibration of the simulation is performed with specific data control channels. These calibration samples are available in high purity and a large number of signal candidates, thus enabling precise calibration. Since R_K and R_{K^*0} are determined simultaneously, one of the method's main advantages presented in this chapter is the interchangeability of the calculated calibrations. It will be shown in the following that the calibrations determined with the control channels $B^+ \rightarrow K^+ J/\psi(\rightarrow \ell^+\ell^-)$ and $B^0 \rightarrow K^{*0} J/\psi(\rightarrow \ell^+\ell^-)$ can be applied for the measurement of R_{K^*0} and R_K respectively. That means that the calibrations for the measurement of R_K are computed with the B^0 control channel and vice versa for the measurement of R_{K^*0} . This strategy has the advantage that the calibration data is not at the same time used for the normalisation in the same measurement (see Eqs. (5.3) and (5.4)). So this method decouples the uncertainties of the normalisation channel and the calibration of the simulation. Chapter 11 shows the portability of the calibration procedure of the two decay channels in different cross-checks. To account for possible differences of the data taking, all calibrations are determined separately in the individual years of data collection of the LHCb detector.

Since different types of data and calibration methods are needed to calibrate the variety of efficiencies, a sequence of correction steps is developed. Except for the last calibration step, all other methods compute weights w that encode either calibration factors to correct specific efficiencies or they encode calibrated efficiencies directly. For the final efficiency computation these weights are multiplied and statistically taken into account. Fig. 7.1 shows an overview of the calibration strategy:

- PID response, w_{PID} : The PID response is calibrated using a data-driven method. The decays that make up the calibration data are $B \rightarrow K^{(*)0} J/\psi (\rightarrow \ell^+ \ell^-)$, $J/\psi \rightarrow \mu^+ \mu^-$, and abundant decays of c hadrons. For the simulation calibration the weight factors w_{PID} are calculated. These weights are the efficiencies of the PID selection. Section 7.2 describes the PID calibration in detail.
- Track reconstruction, w_{TRK} : In the case of track reconstruction, there is good agreement between simulation and data for hadron and muon tracks. In the case of electrons, the efficiencies of the track reconstruction are calibrated with the weights w_{TRK} . The samples used for this purpose in a data-driven method include the control channels $B \rightarrow K^{(*)0} J/\psi (\rightarrow \ell^+ \ell^-)$ as well as inclusive samples of $J/\psi \rightarrow \ell^+ \ell^-$ decays. Section 7.3 presents the calibration of the track reconstruction efficiencies.
- B -meson kinematics and event multiplicity, $w_{\text{Mult\&Kin}}$: Using the control channels $B \rightarrow K^{(*)0} J/\psi (\rightarrow \ell^+ \ell^-)$, the event multiplicity (number of particles produced in the proton-proton collisions and corresponding tracks in the event) and kinematic quantities of the B mesons are calibrated. The calibration data used for this purpose are pre-calibrated beforehand in a *prior calibration chain*. This pre-treatment reduces possible imperfections concerning PID and trigger response of the calibration samples, thus showing minimal bias of their kinematic selections when extracting the kinematic reweighting factors. Fig. 7.1 shows the scheme of this separate calibration procedure, which is described in more detail with the associated calibration step of the kinematic properties and the track multiplicity in Section 7.4.
- L0 trigger, w_{L0} : The efficiency of the L0 trigger is calibrated using a data-driven method with the control channels $B \rightarrow K^{(*)0} J/\psi (\rightarrow \ell^+ \ell^-)$. For this purpose, ratios of the efficiencies on detector data and simulation are calculated in the individual trigger categories of the analysis (see Section 6.1) as a function of the decay kinematics. Section 7.5.1 contains a detailed description about this calibration step.
- HLT trigger, w_{HLT} : For the calibration of the HLT efficiencies, the weights w_{HLT} are determined similarly to the w_{L0} weights. Section 7.5.2 describes the calibration of the HLT efficiencies.
- Candidate reconstruction, w_{Reco} : In this calibration step, the qualities of the reconstructed properties of the B mesons are calibrated with the use of the control samples $B \rightarrow K^{(*)0} J/\psi (\rightarrow \ell^+ \ell^-)$. The calibration weights w_{Reco} determined therein compensate for differences in the distributions of χ_{IP}^2 and χ_{vtx}^2 . Section 7.6 presents this step in detail.
- q^2 bin migration: The last calibration step is to correct the efficiency of the q^2 selection described in Table 6.2. In doing so, possible migrations of events

between the individual q^2 regions, due to bremsstrahlung radiation and resolution differences between data and simulation are compensated for. This last step of the calibration procedure is described in Section 7.7.

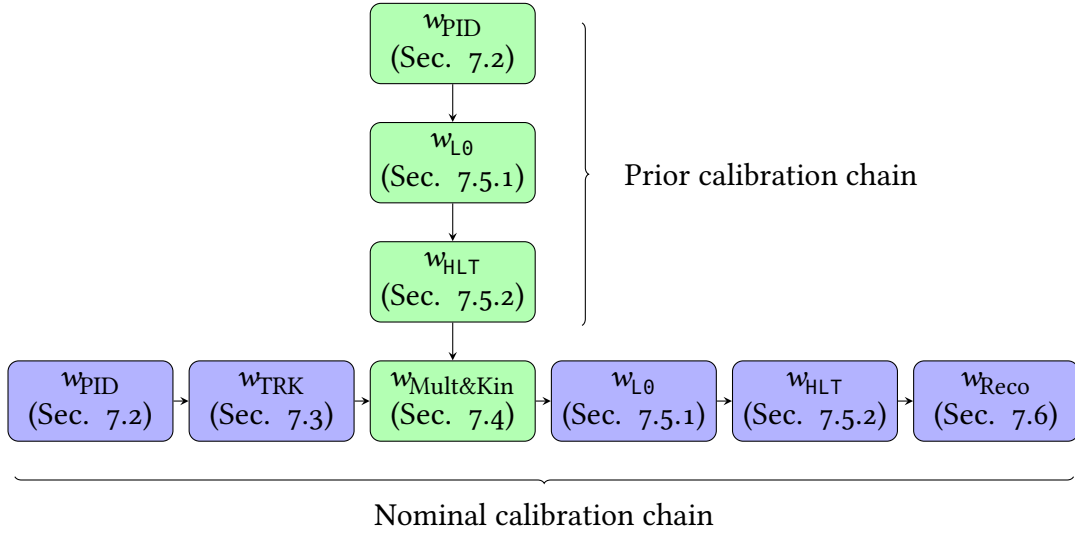


Figure 7.1 – The nominal (blue) and prior (green) calibration chains. The prior chain applies the w_{PID} , w_{L0} , and w_{HLT} calibrations before accessing the B kinematics and underlying event multiplicity distributions. Thus, it pre-calibrates the calibration sample, which is used to compute the $w_{\text{Mult\&Kin}}$ calibration. This pre-calibration is performed on a very strictly selected calibration sample but using similar methods as employed in the main calibration chain.

As Fig. 7.1 shows, all calibration steps are performed sequentially except for those of the B -meson kinematics and event multiplicity. Thus, to compute the $(n + 1)^{\text{th}}$ calibration step, the previous n steps are executed, and their respective calibration weights are applied. The entire product of the calibration weights are designated as $w(B^0)$ for the decay channel $B^0 \rightarrow K^{*0} J/\psi(\rightarrow \ell^+ \ell^-)$ and $w(B^+)$ for the channels $B^+ \rightarrow K^+ J/\psi(\rightarrow \ell^+ \ell^-)$.

All steps presented here use data-driven methods that were either significantly further developed or completely newly developed within this thesis. In most cases, differences between the efficiencies calculated on detector data and the simulation of the control channels are measured. Then, the ratios of these parameters, which compensate for possible differences between data and simulation, are applied to both the normalisation channels and the rare signal decay channels. An alternative procedure is used for the hadrons and muons to calibrate their PID efficiencies. Here, the PID efficiency for the individual tracks is determined directly on PID calibration data and applied as a per-track weight. For the PID efficiencies of the electrons, this procedure has proven to be insufficiently precise, which is why a method was developed that uses ratios of data and simulation efficiencies for the calibration.

To calculate the calibration weights $w_{\text{Mult\&Kin}}$ and w_{Reco} , a BDT is applied in a dedicated approach to compensate for differences in the distributions on data and

simulation. In this approach, the calibration weights are systematically adjusted until the multivariate classifier can no longer distinguish between data and simulation.

Prior calibration chain. One of the features developed in this analysis, as described above, concerns the extraction of calibration factors for the kinematic properties of the B mesons and the event multiplicity. Since these distributions affect the properties of the initial B mesons only, they must be independent of the final states of the decays, i.e., portable between decays with electrons or muons in the final state. Fig. 7.2 demonstrates this fact by comparing simulation distributions for the transverse momentum p_T and the pseudorapidity η of the B mesons, and the track multiplicity n_{Tracks} . Therefore, the calibrations must be calculated on a sample with the smallest possible differences between electrons and muons after reconstructing the signal candidates.

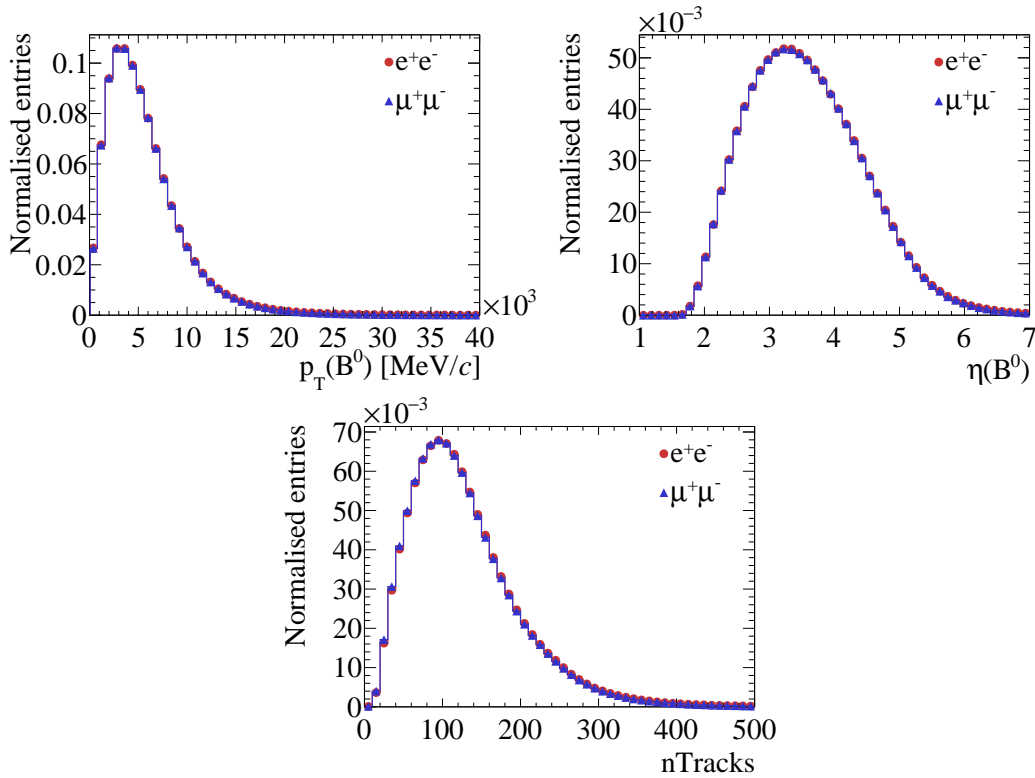


Figure 7.2 – Comparison of variables used in the $w_{\text{Mult\&Kin}}$ calibration between (blue) $B^0 \rightarrow K^{*0} J/\psi(\rightarrow e^+e^-)$ and (red) $B^0 \rightarrow K^{*0} J/\psi(\rightarrow \mu^+\mu^-)$ on generator level simulation.

The control channel $B \rightarrow K^{(*0)} J/\psi(\rightarrow \mu^+\mu^-)$ in the inclusive trigger category L0M is used to determine the calibration weights since the largest number of signal candidates is present here. The high number of candidates enables the lowest possible uncertainty on the calibration weights. These weights are then applied to all other trigger categories on both the electron and the muon channel. Because of potential differences between electron and muon channels, effects arising from the trigger selection of the inclusive L0M category must be compensated. For this reason, a calibration of the L0 and HLT

efficiencies is performed on the control sample beforehand together with a very tight trigger requirement alignment. Such a strict alignment cannot be aligned in the nominal calibration procedure, because the associated loss of a significant proportion of the signal candidates would not be tolerable. Therefore, in the nominal chain, an alternative alignment of the data-simulation differences of the TCKs is performed. Section 7.1 describes the details of the alignment of the trigger conditions for the prior and main calibration chain.

7.1 Trigger configuration alignment

The two triggers L0 and HLT operate with settings that change over time with varying data taking conditions. One of the main reasons for these changes is the conception of the LHCb trigger system and the optimisation of its capacity. For example, a limited disk memory buffer temporarily stores the data before it is processed by the HLT2. So in case the buffer is filled up because of, for example, changing LHC conditions, the trigger settings are modified so that fewer data passes the L0 and HLT1 trigger and is stored in the buffer. Another possible reason for changing the trigger conditions is to allow for an updated selection strategy or correct imperfect selection criteria of the HLT setup.

These trigger settings, which are reflected in different requirements of the trigger reconstruction and selection, are indicated by *Trigger Configuration Keys* (TCKs) as alphanumeric abbreviations. However, in simulation this is done with only one trigger setting that does not resemble these data variations. Table 7.1 shows a summary of the alignment methods as well as the samples and calibration chains on which these methods are applied.

Table 7.1 – Summary of trigger alignments and where they are applied.

Trigger Alignment	Sample		Calibration chain	
	Data	Simulation	Main	Prior
L0 TCK alignment	✓	✗	✗	✓
HLT1 threshold emulation - 2012	✗	✓	✓	✓
HLT1 threshold emulation - 2016	✗	✓	✓	✗
Electron L0 threshold emulation	✓	✓	✓	✗

L0 TCK alignment. In the case of the prior correction chain, to pre-calibrate the $w_{\text{Mult\&Kin}}$ and w_{Reco} calibration sample, only those TCKs in data that match those in simulation samples are selected. This strict filtering is necessary, as described above, to compensate for possible differences between the muon and electron channels for the sample used to calculate $w_{\text{Mult\&Kin}}$. However, this is accompanied by a large loss of

signal candidates in data and is thus not suitable for the main calibration chain. TCKs of the L0Muon trigger are selected in which the threshold on the transverse momentum of the firing muon is identical to the threshold after the simulation TCK.

HLT1 threshold emulation. If the trigger thresholds referring to the simulation TCKs are all less or equally tight as those ones referring to data, it is possible to adjust the simulation trigger selection. This adjustment involves emulating the proportions of the respective TCKs in data for simulation and can be performed for the HLT1 requirements in 2012 and 2016. In these two years significant changes were made to the trigger settings during data collection.

During the data taking in 2012, at least one track must meet the conditions of the HLT1AllTrackL0 trigger. Since all trigger of its requirements in simulation are less strict or the same as in the detector data, the simulation can be adjusted according to portions occurring in the data. For this purpose, the trigger thresholds are emulated proportionally.

Since the 2016 data taking, the additional HLT1TrackMVA trigger condition was used (see Table 6.1). This contains an adjustable condition, which can be set via the parameter b with

$$(p_T(\text{GeV}) > 25 \ \&\& \ \log \chi_{IP}^2 > 7.4) \parallel (\log \chi_{IP}^2 > \frac{1}{(p_T(\text{GeV})-1)^2} + \frac{b}{25} \cdot (25 - p_T(\text{GeV})) + \log(7.4)). \quad (7.1)$$

Table 7.2 lists the mixture of the three different values for the parameter b , which exist in the different TCKs of the 2016 data. For 2017 and 2018 data only one setting was used. In the simulation, the parameter is fixed at $b = 1.1$. Thus, for simulation it is possible to emulate these fractions with corresponding b values by applying the requirement shown in Eq. (7.1).

Table 7.2 – Fractions of candidates with a TCK corresponding to a parameter b for the HLT threshold in data recorded in 2016.

Polarity	$b = 1.1$ [%]	$b = 1.6$ [%]	$b = 2.3$ [%]
<i>MagDown</i>	89.8	0.0	10.2
<i>MagUp</i>	30.0	15.5	54.5

Fig. 7.3 shows the corresponding distributions in a simulation sample of the decay for the three different values of the parameter b .

The HLT the adjustment described here is carried out exclusively on simulation and not on data. Furthermore, the method used for the 2012 simulation is applied to both the prior and the main correction chain. In contrast, the procedure for the 2016 simulation is not applied to the prior correction chain because an adjustment of the L0 TCKs as described above is already mitigating the observed discrepancies to a sufficient extent.

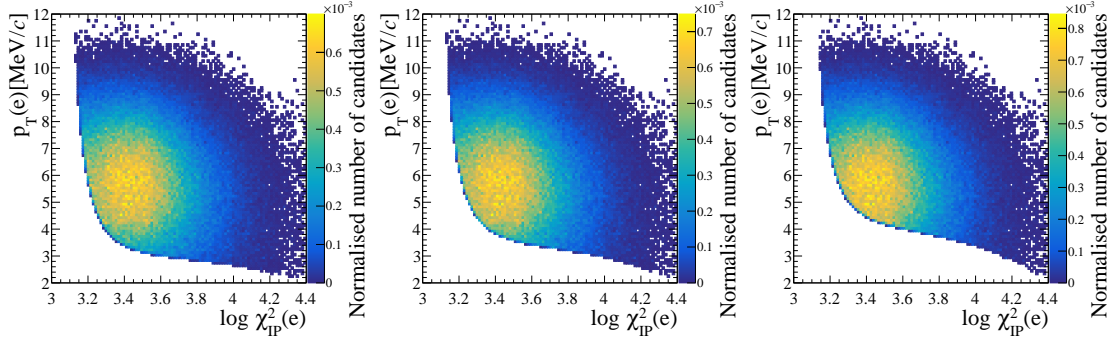


Figure 7.3 – Distributions of transverse momentum p_T and $\log \chi_{IP}^2$ of one of the electrons of the decay $B^0 \rightarrow K^{*0} J/\psi (\rightarrow e^+ e^-)$ with three different values of the parameter b with (left to right) $b = 1.1, 1.6, 2.3$. The parameter b is an input to Eq. (7.1) as a requirement of the HLT1TrackMVA trigger.

Electron L0 threshold emulation. For the L0 electron trigger in the nominal calibration chain, no events can be discarded in which the TCKs do not match, since the sensitivity of the measurement is primarily determined by the number of electron signal candidates. To compensate for possible differences between the trigger settings, the transverse energy threshold is emulated here on both data and simulation to align the associated L0Electron trigger decisions. Due to ageing effects of the calorimeter cells, the significance of the transverse energy E_T^{L0} is measured with their changes, which is not the case in the simulation. The corresponding thresholds must thus be adjusted and emulated on either data or simulation, depending on which sample the conditions are stricter. In addition to L0Electron requirement, the following condition is thus imposed on the transverse energy of the final state electrons with

$$\text{L0Electron}(e_{1,2}) \ \&\& \ E_T^{L0}(e_{1,2}) > E_T^{L0}(e_{1,2})(\text{TCK}). \quad (7.2)$$

The corresponding values for E_T^{L0} are given in Table 7.3. This additional requirement approximates this kinematic quantity of electrons passing the L0Electron trigger.

Table 7.3 – Alignment values for the E_T^{L0} requirement of the L0Electron trigger.

Year	E_T^{L0} [MeV]
2011	2500
2012	3000
2015	3000
2016	2700
2017	2700
2018	2400

7.2 Particle identification

The simulation does not describe the PID response reliably because of, for example, imperfect descriptions of detector responses like of secondary particles produced in material interactions, which affect the event multiplicity and calorimeter performance, or the propagation of optical photons in the RICH detector. For this reason, data-driven calibration procedures based on calibration samples are used to determine the calibration weights w_{PID} to precisely extract the efficiencies. The PIDCalib framework [220] provides the samples with their selection as described in Section 7.2.1. For the calibration, three-dimensional calibration maps are calculated as a function of the decay kinematics and multiplicity. The calibration maps either directly encode PID selection efficiencies or are correction factors as ratios between data and simulation efficiencies. Here, the approach for muon or hadron maps differs from the electron approach. Section 7.2.2 describes the calibration for muons and hadrons and Section 7.2.3 describes the calibration for electrons. For the extraction of efficiencies on data, a *tag-and-probe* method uses one *tag* particle selected with relatively tight requirements, filtering the relevant signal decay. On that filtered sample, the PID efficiency is measured with the corresponding *probe* particle. For those particles no PID selection is applied and the efficiency is calculated with the number of candidates before and after the concerned PID requirement. For the calculation of the electron calibration maps, a new *fit-and-count* approach uses both calibration data and simulation. The two approaches mentioned before can be described as follows.

- **PID efficiency:** For muons and hadrons, the calibration maps contain efficiencies as weights, which are calculated with the calibration data. These directly are the efficiencies of passing the PID selection criteria (see Section 6.3) and replace the direct selection.
- **PID reweighting:** Instead of encoding the efficiencies directly in the calibration weights, the efficiency of the PID selection is determined on simulation, and the selection criteria are applied directly compared to the first method. However, the simulation must be calibrated in this case, which is done with efficiency ratios between data and simulation. The advantage of this approach is that with the use of simulation the efficiency correlations of particles can be taken into account. Because, in comparison to muons and hadrons, PID correlation effects between the two electrons of the dilepton system are found to be not negligible (see Section 7.2.3), this approach is used for electrons.

Additionally, a cross-check described in Section 7.2.4 computes the efficiencies with two orthogonal approaches with consistent results.

Kinematic variables of the particles and the track multiplicity parameterise the calibration maps. A distinction is made between *ID* maps and *mis-ID* maps.

- The *ID* maps contain calibration weights for specific particle types that pass the PID selection, i.e., correctly identified particles. For example, the kaon ID calibration maps use the kaon calibration sample under the kaon PID criteria.

- The *mis-ID* maps include calibration weights for particles of type A that have passed the PID selection criteria for particle type C . In the case of the efficiency maps, this corresponds to the mis-identification rate of $A \rightarrow C$ under the particle C PID criteria. For example, one *mis-ID* map resembles $\mu \rightarrow K$ mis-identification with the muon calibration sample and the kaon PID requirements.

7.2.1 Calibration samples

All methods for the PID calibration applied in this thesis use calibration samples centrally recorded during the LHCb data taking [221, 222]. Table 7.4 lists the decays composing these samples according to the calibration particle types. Very clean data quality and a high abundance of signal candidates characterise those samples. The calibration samples for RUN 1 are selected within the stripping, and for RUN 2 with a dedicated online stream of data taking, called TurCa1 Turbo Stream [223]. There was an error in the selection criteria in the case of the electron samples for 2016, which is why offline-selected samples are used here as well. Of the two available samples for the muon calibration, the inclusive sample with prompt $J/\psi \rightarrow \mu^+ \mu^-$ decays is employed because its number of events is larger compared to the other possible sample. Comparative testing of this choice found no significant differences from the decays in which the J/ψ candidates stem from B -meson decays. As described above, the calibration samples are obtained with strict selection conditions on the *tag* particles to select the signal decay, while no PID selection criteria are applied to the corresponding *probe* particle. Since PID conditions are correlated to the L0 trigger criteria (for example, hits in the muon stations lead to both L0Muon decisions and isMuon PID decisions), the events of the calibration data are required to be triggered as TIS to avoid a possible selection and thus calibration bias. Except for the electron sample, remaining background is further suppressed with the *sPlot* method [224]. The treatment of the electron calibration samples is described in more detail in Section 7.2.3.

Table 7.4 – PID calibration samples.

Particle	RUN 1	RUN 2
K/π	$D^{*+} \rightarrow D^0(\rightarrow K^- \pi^+) \pi^+$	$D^{*+} \rightarrow D^0(\rightarrow K^- \pi^+) \pi^+$
μ	$B^+ \rightarrow K^+ J/\psi(\rightarrow \mu^+ \mu^-)$	Prompt $J/\psi \rightarrow \mu^+ \mu^-$ $B^+ \rightarrow K^+ J/\psi(\rightarrow \mu^+ \mu^-)$
e	$B^+ \rightarrow K^+ J/\psi(\rightarrow e^+ e^-)$	$B^+ \rightarrow K^+ J/\psi(\rightarrow e^+ e^-)$

7.2.2 PID calibration for hadrons and muons

Because the PID efficiency depends significantly on the kinematic properties of the particles, the choice of an adequate binning scheme that covers efficiency variations depending on these quantities is crucial. For the PID calibration of hadrons and muons,

the individual regions of the calibration maps are divided independently into the three parameterisation dimensions. These dimensions are the particle momentum p , pseudorapidity η , and track multiplicity $n\text{Tracks}$. Three equally populated regions form the $n\text{Tracks}$ binning. Within these $n\text{Tracks}$ regions, the p and η bins are chosen to be sufficiently small so that the assumption that the efficiency within the bins is approximately constant is valid. At the same time, the bins need to be broad enough to contain a sufficient number of events to perform a statistically meaningful efficiency determination and avoid possible fluctuations. For this purpose, an iterative algorithm was developed that optimises the division for each dimension. First, the calibration data sample is divided into iso-populated bins, i.e., containing the same number of candidates. Following that, in an iterative procedure adjacent bins are merged if the difference in their efficiencies is less than five times their statistical uncertainty.

The one-dimensional binnings are then assembled into three-dimensional efficiency maps for each year of data collection and each particle type. As described above, the per-event calibration weight w_{PID} is calculated from the application of the individual efficiency maps to the decay particles. First, the corresponding efficiency maps are selected for the individual tracks depending on the correct identification or mis-identification, determined by the true initial identity in the simulation. Afterwards, a linear interpolation between the p and η bins is performed within the corresponding $n\text{Tracks}$ area where this particle is located, and the resulting PID track efficiency is readout. If individual tracks lie outside the kinematic limits of the efficiency maps, the nearest bins of the maps are read out, and unphysical values, which can arise from effects of the $\mathcal{P}\text{lot}$ method or empty bins, are assigned the closest physical value.

An alternative approach to calculating the binning scheme was developed, using Kernel Density Estimators (KDEs) to parameterise the efficiency maps. The method shows compatible results with the previously described approach.

7.2.3 PID calibration for electrons

Analogous to the PID calibration for hadrons and muons, efficiency maps with kinematic regions of the electron candidates are calculated. In this case, the transverse momentum p_{T} , the pseudorapidity η , and the number of tracks in the event $n\text{Tracks}$ are used as parameterisation variables. The transverse momentum is chosen here because it is easier to generate uniformly distributed kinematic regions with this variable.

Compared to the calibration samples for muons and hadrons, there is a significantly smaller number of calibration events with a much higher background rate for the electron samples. Consequently, the $\mathcal{P}\text{lot}$ method cannot reliably be utilised to compute the efficiencies because negative $\mathcal{P}\text{lot}$ weights can occur in bins with very few entries, leading to unphysical efficiencies. Therefore, the $\mathcal{P}\text{lot}$ approach can only be used for bins with a sufficient number of events. Next to this technical problem, the main reason why this approach cannot be utilised for electrons is that the bremsstrahlung emission induces correlations between the B -meson mass and the electron kinematics and electron PID. And because the B -meson mass is used as the discriminating variable in the $\mathcal{P}\text{lot}$ approach this dependency introduces a bias on the calibration. In practice, what

makes the use of this approach impossible is that the shape of the mass distributions to be modelled depend significantly on the kinematic region and the number of added bremsstrahlung photons. So, the central $sPlot$ fits that are performed non-differentially for the whole calibration sample cannot be used.

For this reason, a new approach to extract the PID efficiencies for electrons was developed within the `PIDCalib` tool. This method is called the *fit-and-count approach* because it fits the PID efficiencies for each kinematic bin individually. For this purpose, the electron calibration samples listed in Table 7.4 are used, to which the fiducial selection described in Section 6.3.1 is applied to align the calibration data with the signal data and to reduce possible background contributions already in a first filtering step. The PID performance of the ECAL, and so the PID performance of the combined PID variables depends on the number of recovered bremsstrahlung photons in the calorimeter in contrast to, for example, pions and kaons, which do not significantly emit bremsstrahlung. Thus, the PID efficiency for the two electron bremsstrahlung categories is very different. Furthermore, the shape of the reconstructed B mass depends on this number of reconstructed photons as well. Therefore, two separate efficiency maps are generated depending on the number of bremsstrahlung photons added to the *probe* electron (0γ or $\geq 1\gamma$). The binning schemes are calculated analogously to the procedure described in Section 7.2.2 but with four regions of `nTracks`.

Fits in the individual bins calculate the efficiencies of the PID selection. For this purpose, a simultaneous fit determines the number of signal candidates that are selected by the PID criteria (*pass*) and those that do not pass (*fail*). To ensure sufficient fit quality, a stringent requirement on the B -meson mass calculated with the J/ψ mass constraint is also required, and the invariant B -meson mass must lie in the range of 5239 to 5319 MeV/c^2 as a fit variable. The shape of the signal is described by a double-sided Crystal Ball (DCB) function [225] and is determined with simulated $B^+ \rightarrow K^+ J/\psi(\rightarrow e^+e^-)$ decays selected identically to the calibration data decays. In the fit to calibration data, this shape is kept fixed, and only the mean and resolution parameters of the DCB function are determined. For what concerns the principal background components, the combinatorial background is modelled with an exponential function. An Argus distribution [226] describes the partially reconstructed background. The invariant mass distribution of the partially reconstructed background is validated using simulated $B^0 \rightarrow K^{*0} J/\psi(\rightarrow e^+e^-)$ decays reconstructed as $B^+ \rightarrow K^+ J/\psi(\rightarrow e^+e^-)$ signal.

Figs. 7.4 and 7.5 show fits to the *pass* and *fail* sub-samples for the two bremsstrahlung categories. The 0γ category fit shows a higher combinatorial background, which is mainly due to mis-identified charged pions. However, this background is significantly reduced with added bremsstrahlung photons, highlighting the need to separate the fits into bremsstrahlung categories.

In the case of the PID efficiencies for hadrons and muons, calibration weights directly encode the efficiencies and thus replace the direct PID selection for each event. This approach is valid as long as the assumption holds that the efficiencies are fully parameterised by the binning variables used and factorise for the single tracks. A study with simulation confirms that the PID efficiencies for hadrons or muons are

7 Calibration of simulation

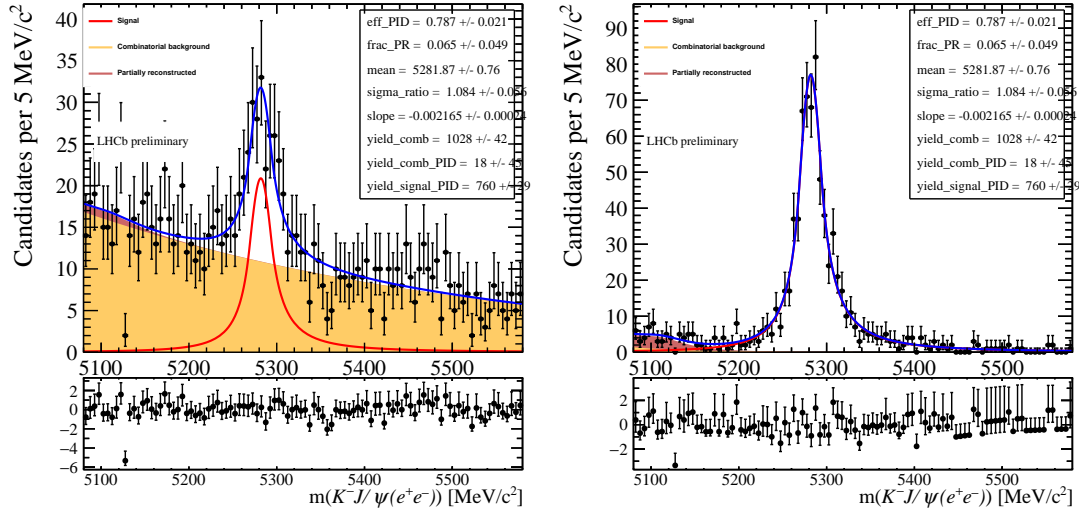


Figure 7.4 – Simultaneous fits on data to extract electron PID efficiencies for the 2018 sample with more than 0 bremsstrahlung photons added. On the left the *failed* and on the right the *passed* category is shown.

independent of the PID selection criteria for other decay particles. Since for electrons, due to the low resolution of the ECAL and other electrons in the event, which are located nearby and may affect the PID of a given electron, the efficiencies for electrons do not factorise completely. The probability of two electrons being measured in the same ECAL cell depends mainly on the geometric aperture angle and momentum of the two particles. Thus, the effect of non-factorisation is thus different in the signal and control regions of the R_K and $R_{K \neq 0}$ measurements (see Section 5.1). As a first mitigation of this effect, events whose electron tracks are separated less than 100 mm from each other in the ECAL are removed. This requirement roughly corresponds to the distance between two calorimeter cells in the inner region of the ECAL and is empirically found to significantly reduce the factorisation bias [227]. But still the calibration data cannot describe the impact of the remaining non-factorisation because the PID efficiency is only determined with the single *probe* particle, and possible correlations of the dielectron system cannot be addressed.

For this reason, the original PID approach is modified for electrons. It computes the PID efficiency from simulation with a *cut-and-count* approach with the same p_T , η , and nTracks binning as in the determination of electron PID efficiencies on data. This method has the advantage that the calculation on simulation already includes secondary correlations between other decay properties. However, since the simulation does not correctly describe the absolute scale of the PID efficiencies, this is corrected by calibration weights, which are determined as ratios of the PID efficiencies calculated on data and simulation.

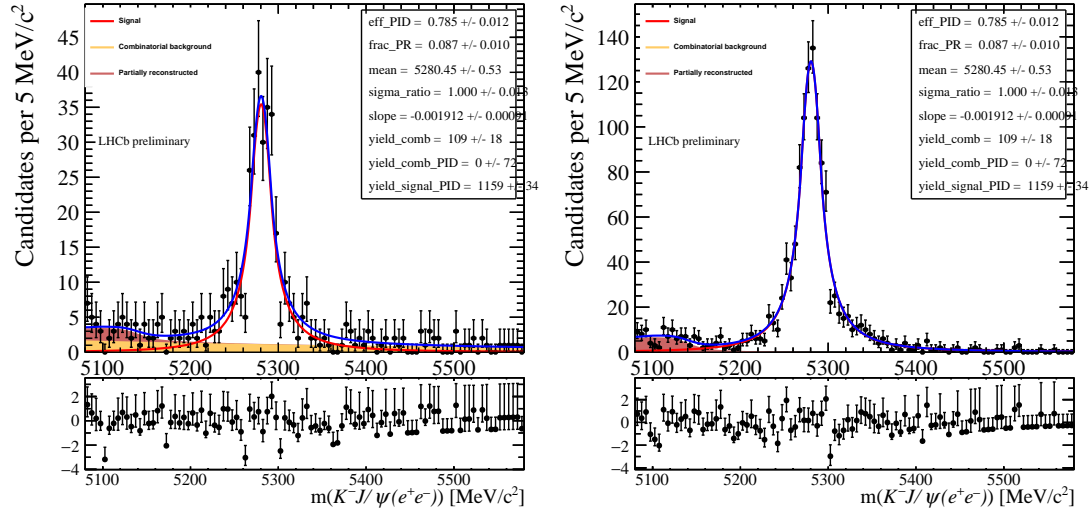


Figure 7.5 – Simultaneous fits on data to extract electron PID efficiencies for the 2018 sample with more than 0 bremsstrahlung photons added. On the left the *failed* and on the right the *passed* category is shown.

7.2.4 Alternative calibration methods

There are currently two alternative approaches to calibrate the PID response [228]. Both of them are determining the probability density functions (PDF) of the PID variables depending on p_T , η , and $nTracks$ in an unbinned approach with Kernel Density Estimators (KDEs).

The first alternative approach is called *PID resampling*. Here, the KDEs are employed to draw random numbers according to the extracted PDFs of the PID variables in the calibration samples. Unfortunately, with this approach only one PID variable can be calibrated simultaneously and it cannot take into account correlations between multiple variables. So for the composite PID selections used in this thesis, this approach can only be used as a cross-check.

The second alternative conducts a transformation of PID variables so that the variable distributions in simulation match the distributions of the calibration data. With this approach, the correlation between different PID variables is conserved. Still, the systematic uncertainty of this approach is more significant as it uses simulation templates to conserve the correlations and the simulation potentially again mismodels or biases the efficiencies. Thus, the second approach is used as a cross-check only as well.

For both alternative approaches the resulting PID efficiencies are in good agreement with the nominal approach described in Sections 7.2.2 and 7.2.3.

7.3 Track reconstruction

In this analysis, the track reconstruction efficiency is determined with simulation. Therefore, it is essential to calibrate possible differences between data and simulation

in this respect. In the case of hadrons, it is assumed that possible efficiency differences between data and simulation cancel out in the double ratio of the measurement of R_K or R_{K^*0} .

Muon modes. To calibrate the efficiencies of the track reconstruction (see Section 3.2.1), the decays with muons and electrons in the final state are investigated separately. For muon tracks, a data-driven method is used to determine the track reconstruction performance [229]. Calibration samples with $J/\psi \rightarrow \mu^+ \mu^-$ decays are employed because they are very similar to the decays used in the final measurement of R_K and R_{K^*0} and are abundant. The purity of the signal is optimised by requiring that the J/ψ candidate decays from a b hadron. The method used employs a *tag-and-probe* approach, where the muon pairs are divided into a *probe* and a *tag* particle. The *tag* particle marks the muon decay and is fully reconstructed and identified as a muon with good quality. The *probe* track is required to be not entirely reconstructed by at least one subdetector of the tracking system. Thus, the *probe* muon, for example, has hits in the muon stations, which can be used to build the *probe* track without specific tracking detectors. Thus, with other fully reconstructed tracks, the reconstruction efficiency of these specific detector components can be determined (cf. [229]).

Because no significant differences between the tracking efficiencies computed with this method and those determined with uncalibrated simulation are observed, no calibration is applied for the muon channel.

Electron modes. A similar *tag-and-probe* approach is used for electrons [230]. However, the overall reconstruction efficiency is lower for electrons than for muons due to bremsstrahlung effects, so simulation does not precisely describe the efficiency. The calibration employed uses a data set of $B^+ \rightarrow K^+ J/\psi (\rightarrow e^+ e^-)$ decays in which, as in the case of the muon calibration, one electron track was completely reconstructed as a long track. In contrast, the second electron was detected only in VELO as a *velo* track. The ratio ϵ with which these *velo* tracks were simultaneously reconstructed as *long* tracks is determined on both data and simulation. This calculation of efficiency is performed differentially in regions of the electron momentum $p_T(e)$, pseudorapidity $\eta(e)$, as well as azimuthal angle $\phi(e)$ of the electron track in the VELO. These variables resemble the kinematic properties of the electrons and the instrumentation of the VELO, both of which influence the magnitude of the radiated bremsstrahlung and thus the reconstruction efficiency. In these regions, the ratio of efficiencies ϵ between data and simulation is calculated as calibration weights w_{TRK} with

$$w_{\text{TRK}} = \frac{\epsilon(\text{long}|\text{velo})^{\text{Data}}}{\epsilon(\text{long}|\text{velo})^{\text{Simulation}}}. \quad (7.3)$$

The calibration is performed for the individual electron tracks and finally calculated for the whole signal candidate as $w_{\text{TRK}} = w_{\text{TRK}}(e_1) \times w_{\text{TRK}}(e_2)$.

Fig. 7.6 presents these ratio maps for the year 2018 of LHCb data taking. Appendix A.2 shows the tracking efficiency maps for all years of the data taking.

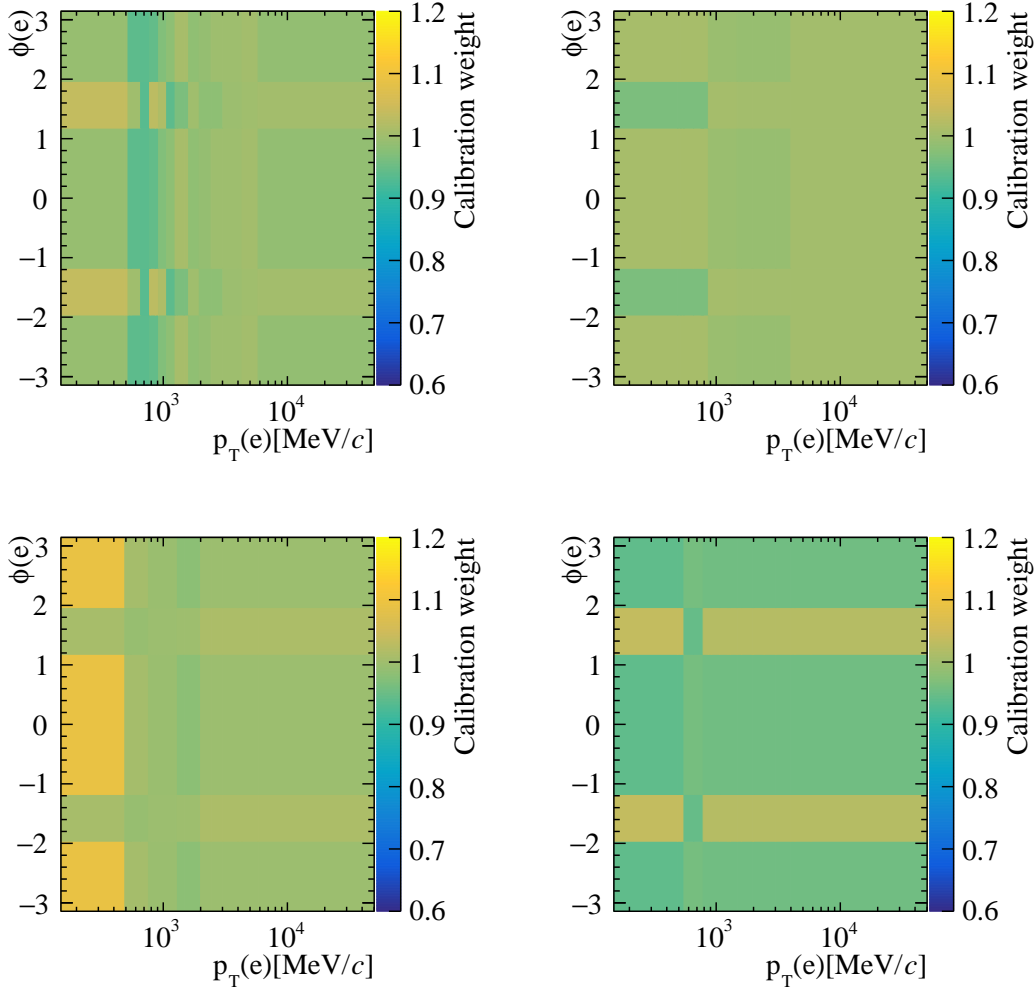


Figure 7.6 – Track reconstruction calibration maps for electrons in regions of $\phi(e)$ and $p_T(e)$ and (from left to right and top to bottom) bins of the electron pseudorapidity with the edges of $\eta = [1.90, 2.90, 3.45, 4.00, 4.50]$. Data and simulation ratios of the track reconstruction efficiency for the year 2018 are shown. The maps for the other years can be found in Appendix A.2.

7.4 Kinematics and event multiplicity

The kinematic properties of the B mesons and the associated event multiplicity are not perfectly simulated. The following reasons can be given for this: first, the simulation of the initial proton-proton collisions of the LHC is limited by the PYTHIA simulation software (see Section 3.2.5). Second, it is impossible to fully describe all properties and detector components changing due to environmental influences and ageing processes in the simulation. Third, the simulation of secondary decays and interactions of the decay products with the detector has imperfections. These include, in particular, the imperfect simulation of decay particles with low momentum, the description of particle showers, and other secondary interactions such as photon conversions. Consequently, differences in the distributions of the simulated samples and the recorded data in both kinematic and event multiplicity variables exist. Since various detector components determine these variables and the output of the detector components are simulated with distinct precision, it is impossible to calibrate the simulation with a single variable. Therefore, a multidimensional calibration procedure is performed. One of the main features of the multidimensional calibration procedure is that correlations between the reweighting of the different observables used as calibration proxies are taken into account.

The calibration of the simulated kinematic properties of the B meson takes place in three dimensions. These are the momentum $p(B)$, the transverse momentum $p_T(B)$, and the pseudorapidity $\eta(B)$.

Event multiplicity calibration. As mentioned before, it is not possible to correct all other variables by calibrating a single variable, which is especially true for the variables representing the track multiplicity of the event. For example, suppose the distribution of the number of hits in the SPD detector `nSPDhits` is corrected. In that case, the agreement between data and simulation for the total number of tracks reconstructed in a collision, for example described by the variable `nTracks`, can be worsened. The imperfect description of the `nSPDhits` variable can mainly be attributed to imperfect budgeting of the material of the first muon chamber M1 and therefore lack of secondary particles produced in M1, which is located directly in front of the SPD detector (see Fig. 3.3). In the multidimensional calibration, the variable `nTracks` is used for the track multiplicity since it parameterises the PID calibration described in Section 7.2. Two different facts account for the remaining differences between data and simulation of the multiplicity variables. First, the distributions between muons and electrons are very similar (see, e.g., Fig. 7.2), so possible simulation inaccuracies resulting from mismodelling largely cancel out in the R_K and R_{K^*0} ratios. The cross-checks described in Chapter 11 confirm this. Second, all residual effects due to differences between data and simulation for the multiplicity variables are considered as a possible source of systematic uncertainty.

Calibration method. The calibration is performed with data samples and simulated samples of the decays $B \rightarrow K^{(*)0} J/\psi (\rightarrow \mu^+ \mu^-)$ in the L0M trigger category. As explained at the beginning of this chapter, calibrations based on this sample are also applicable to electron samples. Thus, it is chosen because of its high signal purity and an abundant number of signal candidates. As described above, the kinematics and event multiplicity calibrations for the electron channel are also carried out with the muon sample. In the prior calibration chain (see Fig. 7.1), possible remaining differences induced by the PID and trigger selection must be compensated.

For the actual calibration, the *GBreweighter* algorithm from the `hep_ml` library [231] is used. The algorithm uses a BDT and systematically varies the weighted distributions of the simulation until the classifier can no longer distinguish the data distributions from simulation to a specified degree. The four proxy variables of the B -meson kinematics and event multiplicity calibration, $p(B)$, $p_T(B)$, $\eta(B)$, and `nTracks`, are used as input to the BDT. The method produces calibration weights $w_{\text{Mult\&Kin}}$ that compensate for the differences between simulation and data by weighting the statistical relevance of each event in the final efficiency calculation (see Chapter 8). The calibration samples are selected with the entire selection except for the MVA selection (see Chapter 6). With fits to the invariant mass of the $m(K\ell\ell)_{J/\psi}$ system, the *sPlot* method [224] suppresses additional background contributions.

As already done for the multivariate classifiers in the selection (see Section 6.5), this calibration step uses the *k-fold* method to train and apply the calibration BDT. Here, the final calibration weights are calculated as the mean of all training folds.

7.5 Trigger

After the simulation has been calibrated for the track reconstruction, PID, the B -meson kinematics, and the event multiplicity, the trigger response in the nominal correction chain is calibrated. The efficiency of the trigger selections (see Section 6.1) is not known a priori and must be determined with simulation. Since the trigger response is not perfectly described in the simulation, correction factors must also be determined in this case. This is done in two steps, first for the efficiency of the L0 trigger selection presented in Section 7.5.1 and second for the efficiency of the HLT selection described in Section 7.5.2. Since the selection criteria for the muon and electron modes is different, this is done separately. The calibration uses efficiency ratios, calculated on data and simulation, as correction factors. For this purpose, the data-based TISTOS method [232] is used with decays of the channels $B^+ \rightarrow K^+ J/\psi (\rightarrow e^+ e^-)$, $B^+ \rightarrow K^+ J/\psi (\rightarrow \mu^+ \mu^-)$, $B^0 \rightarrow K^{*0} J/\psi (\rightarrow e^+ e^-)$, and $B^0 \rightarrow K^{*0} J/\psi (\rightarrow \mu^+ \mu^-)$. This approach ensures that the calibrations based on the B^+ channels are consistent with those based on the B^0 channels. The trigger response calibrations are performed for each year separately because of the changing trigger and data taking conditions.

Calibration method. With the TISTOS method, two sub-samples of each, the simulation and the data samples are used. The first sample requires the events to be

triggered independently of the signal (TIS), and the second sample requires the events to be triggered on signal (TOS). Access to the trigger efficiencies on data is not possible directly because only the already triggered events are saved. The assumption now is that the efficiency $\epsilon_{\text{TOS}} = \frac{N_{\text{TIS\&\&TOS}}}{N_{\text{TIS}}}$ is a good proxy for the trigger TOS efficiency. Here the efficiency ϵ_{TOS} is the ratio of the number of events that have passed both the TIS and TOS requirement ($N_{\text{TIS\&\&TOS}}$) and of the number of events that have the TIS requirement (N_{TIS}). The computation of the calibration factors uses efficiency ratios computed on data (ϵ^{Data}) and on simulation ($\epsilon^{\text{Simulation}}$). There are four elements of the method that vary between the different cases of application used in the framework of this thesis. First, the calibration samples must be selected on which the calibration will be carried out. This selection depends on which calibration step and which trigger category has to be calibrated, and whether the calibration takes place in the prior calibration chain or the nominal calibration chain. Second, the calibration is parameterised in regions of significant variables for the specific trigger selection. Third, the definitions of the TIS and TOS categories depend on the trigger requirement and also, as a fourth point, the final formulas of how to apply the computed calibration weights. The following description addresses these four ingredients.

7.5.1 L0 hardware trigger

For the calibration of the L0 trigger, the calibration samples are pre-selected with all filter criteria as described in Chapter 6 but without the L0 trigger conditions. Further background suppression is achieved by requiring the B^+ (B^0) mass, calculated with the J/ψ -mass constraint (i.e., the mass of the dilepton system fixed to the resonance masses in the reconstruction), to lie in the range of $\pm 45 \text{ MeV}/c^2$ around the nominal B -meson mass. The efficiencies for the inclusive trigger categories L0I and L0L are calculated according to the formulae

$$\epsilon_{\text{L0I}}^{\text{Data/Simulation}} = \left(\frac{N_{\text{TIS\&\&TOS}}}{N_{\text{TOS}}} \right)^{\text{Data/Simulation}}, \quad (7.4)$$

$$\epsilon_{\text{L0L}}^{\text{Data/Simulation}} = \left(\frac{N_{\text{TIS\&\&TOS}}}{N_{\text{TIS}}} \right)^{\text{Data/Simulation}}. \quad (7.5)$$

With these efficiencies $\epsilon_{\text{L0L}, \text{L0I}}^{\text{Data/Simulation}}$ the following calibration weights are calculated

$$w_{\text{L0}}^{\text{L0I}} = \frac{\epsilon_{\text{L0I}}^{\text{Data}}}{\epsilon_{\text{L0I}}^{\text{Simulation}}}, \quad (7.6)$$

$$w_{\text{L0}}^{\text{L0L}} = \frac{\epsilon_{\text{L0L}}^{\text{Data}}}{\epsilon_{\text{L0L}}^{\text{Simulation}}}. \quad (7.7)$$

As can be seen from Eqs. (7.4) and (7.5), the efficiencies for the exclusive L0L! trigger category cannot be computed in such a way. This is not possible because this trig-

ger category only contains TOS events, with which the sample categories cannot be defined. Therefore, the calibration weights for this trigger category are computed as a combination of the inclusive trigger categories. To calculate the calibration weights for the $L\theta L!$ trigger category, Eqs. (7.6) and (7.7) are combined to form

$$w_{L\theta}^{L\theta L!} = w_{L\theta}^{L\theta L} \cdot \frac{1 - \epsilon_{L\theta I}^{\text{Data}}}{1 - \epsilon_{L\theta I}^{\text{Simulation}}} = \frac{\epsilon_{L\theta L}^{\text{Data}}}{\epsilon_{L\theta L}^{\text{Simulation}}} \cdot \frac{1 - \epsilon_{L\theta I}^{\text{Data}}}{1 - \epsilon_{L\theta I}^{\text{Simulation}}}. \quad (7.8)$$

Final weight expressions. The final weight expressions for the $L\theta L$ category are calculated based on the lepton candidates being TOS in the trigger. There the logical OR of the two candidates has to be employed as done in the trigger requirement. With the formula $P(A|B) = P(A) + P(B) - P(A\&B)$ for the probabilities of the classes A and B , which is true if the classes A and B are not mutually exclusive, the efficiency expressions for the $L\theta L$ trigger category for both leptons are

$$\begin{aligned} \epsilon_{L\theta L}^{\text{Data/Simulation}} &= \epsilon_{L\theta L}^{\text{Data/Simulation}}(\ell^+) + \epsilon_{L\theta L}^{\text{Data/Simulation}}(\ell^-) \\ &\quad - \epsilon_{L\theta L}^{\text{Data/Simulation}}(\ell^+) \cdot \epsilon_{L\theta L}^{\text{Data/Simulation}}(\ell^-) \\ &= \left(1 - \left(1 - \epsilon_{L\theta L}^{\text{Data/Simulation}}(\ell^+)\right)\right) \cdot \left(1 - \epsilon_{L\theta L}^{\text{Data/Simulation}}(\ell^-)\right). \end{aligned} \quad (7.9)$$

From this, after Eq. (7.7) the final calibration factor for the $L\theta L$ trigger category follows with

$$w_{L\theta}^{L\theta L} = \frac{\epsilon_{L\theta L}^{\text{Data}}}{\epsilon_{L\theta L}^{\text{Simulation}}} = \frac{\left(1 - \left(1 - \epsilon_{L\theta L}^{\text{Data}}(\ell^+)\right) \cdot \left(1 - \epsilon_{L\theta L}^{\text{Simulation}}(\ell^-)\right)\right)}{\left(1 - \left(1 - \epsilon_{L\theta L}^{\text{Simulation}}(\ell^+)\right) \cdot \left(1 - \epsilon_{L\theta L}^{\text{Simulation}}(\ell^-)\right)\right)}. \quad (7.10)$$

These weights are applied per event and are parameterised according to the kinematics of the events. This parameterisation is described separately for the individual trigger categories below. Through the specific alignment of the $L\theta E$ trigger category, which is described in Section 7.1, the following substitution is additionally carried out, which observes the threshold of the transversal energy of the individual electron candidates with

$$\epsilon_{L\theta E}^{\text{Data/Simulation}}(e^\pm) \rightarrow \epsilon_{L\theta E}^{\text{Data/Simulation}}(e^\pm) \times (E_T^{L0}(e^\pm) > \text{Threshold}), \quad (7.11)$$

with the term $(E_T^{L0}(e^\pm) > \text{Threshold})$ is evaluated as true if the electron transverse energy lies above the defined threshold. The final calibration factors for the inclusive $L\theta I$ trigger category are already given in Eq. (7.6) with $w_{L\theta}^{L\theta I} = \epsilon_{L\theta I}^{\text{Data}} / \epsilon_{L\theta I}^{\text{Simulation}}$. According to Eq. (7.8), this results in the combination with Eq. (7.10) for the final calibration weights for the $L\theta L!$ trigger category with

$$w_{L0}^{L0I} = \frac{(1 - (1 - \epsilon_{L0L}^{\text{Data}}(\ell^+)) \cdot (1 - \epsilon_{L0L}^{\text{Data}}(\ell^-)))}{(1 - (1 - \epsilon_{L0L}^{\text{Simulation}}(\ell^+)) \cdot (1 - \epsilon_{L0L}^{\text{Simulation}}(\ell^-)))} \cdot \frac{1 - \epsilon_{L0I}^{\text{Data}}}{1 - \epsilon_{L0I}^{\text{Simulation}}}. \quad (7.12)$$

As announced above, these calibration weights are computed using the B^+ and B^0 control samples, respectively. It turns out that the calibration weights extracted in this way are consistent between both control channels. Likewise, the L0I calibration weights are compatible between the muon and electron channels, so the weights extracted from the muon channel are consistently applied to the electron signal channel. The calibration based on the muon channel is chosen as the muon samples have a higher number of candidates and thus reduce the uncertainty of the results.

The following describes the parameterisation of the different trigger categories and the choice of the sample definitions to be used within the calibration method. For this purpose, the sample categories TIS (TIS&&TOS) will be referred to as *tag(probe)* in the following for reasons of simplicity. Now, details about the calibration for the trigger categories L0M, L0E, and L0I of the nominal correction chain and the category L0M for the prior correction chain are described.

Nominal chain L0M. In the L0M trigger conditions, the muon candidates must exceed a minimum transverse momentum $p_T(\mu)$ (see Table 3.2) to be triggered. Consequently, the trigger efficiency is calibrated as a function of $p_T(\mu)$ and of three regions of pseudorapidity $\eta(\mu)$. The *tag* category is defined to include TIS events and the *probe* category includes TIS events, which were also triggered as TOS. The *tag* category is composed of events that were triggered as TIS by either the L0Hadron or L0Electron trigger (B_L0Hadron_TIS or B_L0Electron_TIS). This definition was chosen because it has the largest number of candidates. Here, as in all other definitions described below, compatibility with other *tag* definitions has been checked and confirmed.

The kinematic regions in which the efficiencies are evaluated are chosen so that each region contains a sufficient number of events and that the turn-on curve of the efficiency distribution is covered with a fine region granularity. In addition, the efficiency distribution is fitted to mitigate possible resolution effects that may occur due to this binning. Fig. 7.7 shows the corresponding efficiency distributions for data and simulation and the resulting ratio in three regions of the electron pseudorapidity as a function of the electron transverse momentum for the 2018 $B^0 \rightarrow K^{*0} J/\psi(\rightarrow \mu^+ \mu^-)$ sample. The distributions for other years and calibration samples show similar behaviour.

The trigger threshold described above is drawn as a dashed line in these plots. There are still entries to the left of this threshold because of the low ECAL resolution and differences in the E_T thresholds, which occur because the TCKs in the nominal correction chain were not aligned. For higher transverse momenta beyond the threshold, data and simulation agree well, although in the threshold region significant differences can be seen.

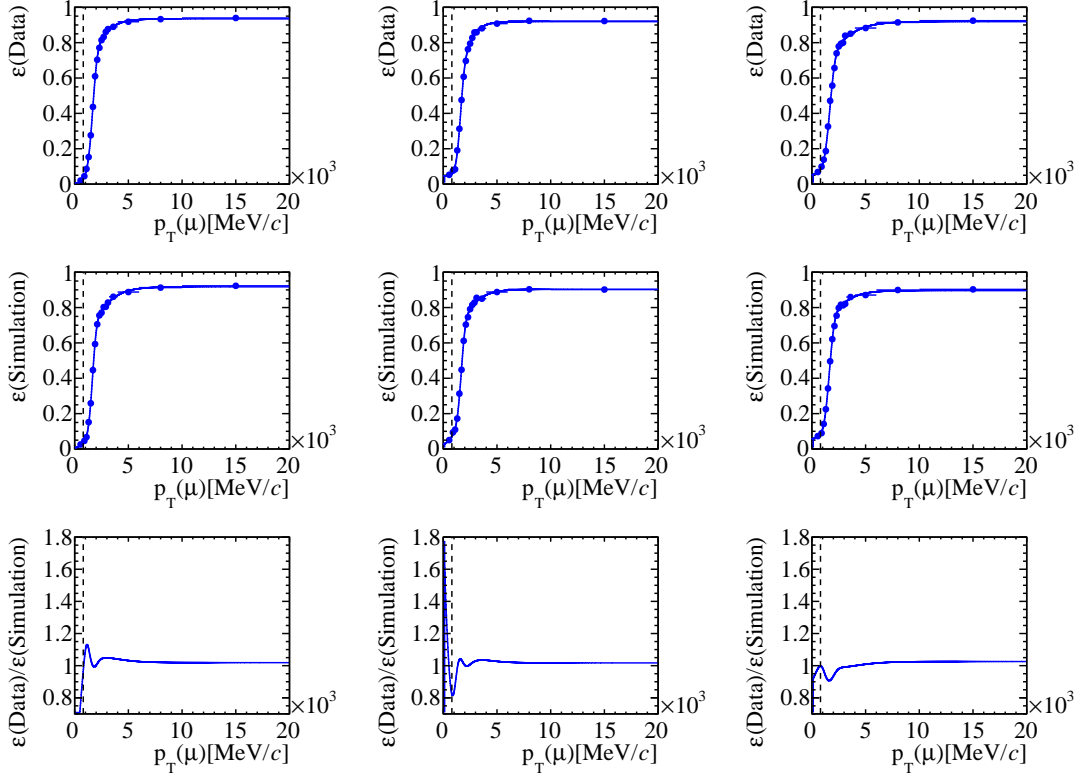


Figure 7.7 – Nominal calibration chain: L0M trigger efficiencies calculated on (top) data and (middle) simulation samples for the 2018 $B^0 \rightarrow K^{*0} J/\psi(\rightarrow \mu^+ \mu^-)$ decays as a function of the transverse muon momentum in three bins of the muon pseudorapidity. The solid blue line indicates the fit function to model the efficiency distribution. The bottom row shows the ratios of the data and simulation efficiencies. The black dashed line indicates the trigger threshold. The large deviations in the region of the threshold line are explained in the text.

Nominal calibration chain L0E. The efficiency calibration for the L0E trigger category is similar to the L0M category described before. Similarly, the *probe* and *tag* samples are selected. However, the *tag* sample is composed of hadron or muon TIS events. To be triggered in the L0E electron trigger, the electrons must deposit a minimum transverse energy E_T in the ECAL (see Table 3.2). Since the accuracy of the measurement of this energy in the ECAL depends on the granularity of its calorimeter zones (see Fig. 3.8), the L0 efficiency is determined in regions of the transverse energy of the electrons as well as in the three detector regions of the ECAL. The efficiency distributions are also fitted before the efficiency ratios determine the calibration weights. Fig. 7.8 shows the data and simulation efficiencies and their ratios for the representative 2018 $B^0 \rightarrow K^{*0} J/\psi(\rightarrow e^+ e^-)$ sample.

Nominal calibration chain L0I. The L0I trigger category consists mainly of events triggered on the B hadron, which hadronised from the \bar{b} (b) quark opposing the b (\bar{b}) quark forming the B -meson signal. It is assumed that the kinematics of the two b

7 Calibration of simulation

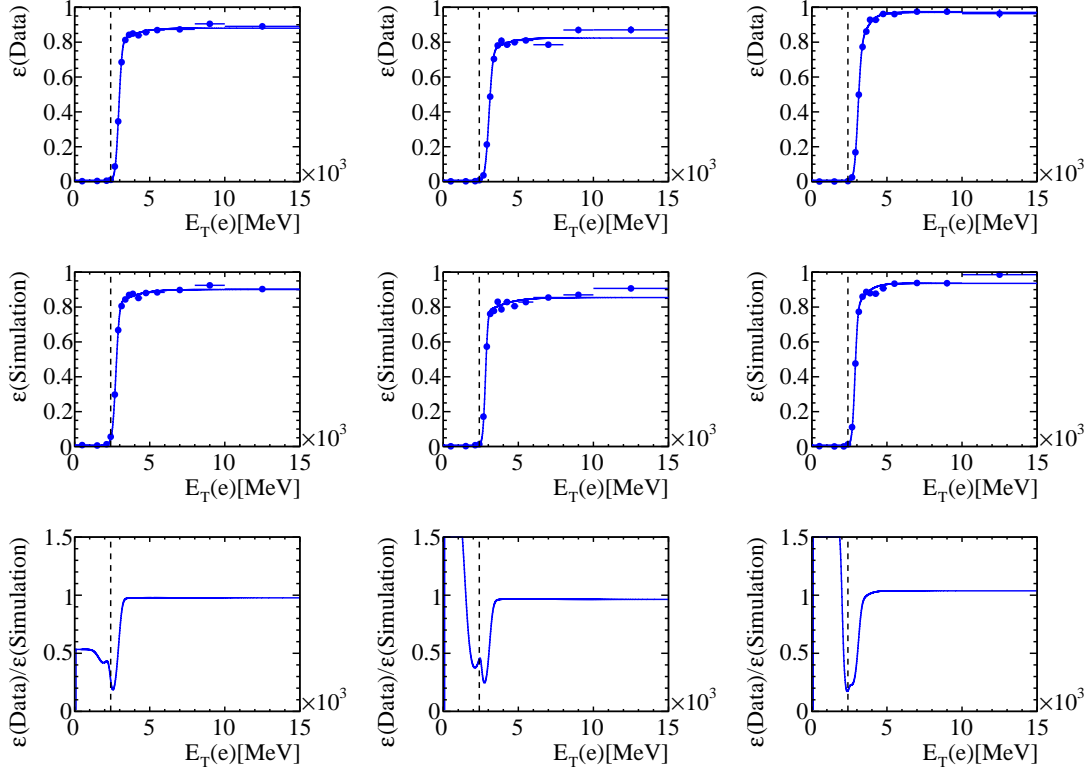


Figure 7.8 – Nominal calibration chain: L0E trigger efficiencies calculated on (top) data and (middle) simulation samples for the 2018 $B^0 \rightarrow K^{*0} J/\psi(\rightarrow e^+e^-)$ samples as a function of the transverse electron energy in the three ECAL regions, the solid blue line indicates the fit function to model the efficiency distribution. The bottom row shows the ratios of the data and simulation efficiencies. The black dashed line indicates the trigger threshold.

quarks are correlated. For this reason, the efficiency calculation for this category is parameterised by the transverse momentum of the signal B meson $p_T(B)$. Since the TIS category is more likely to be triggered at larger track multiplicities, the efficiencies are also parameterised in six regions of track multiplicity $nTracks$. Events in which the L0 triggered leptons or hadrons of the signal part as TOS are selected as *tag* samples since this category contains the largest number of events. Other possible definitions of the *tag* category have been evaluated and provide compatible results. Since the L0I trigger category is shared between the muon and electron modes, the efficiencies and calibration weights for both the muon and electron control channels are calculated in a preliminary study. However, as described earlier, the resulting results are expected to be independent, which is confirmed by the direct comparison of the calibration weights. Since the muon control sample contains a much higher purity and a more significant number of events, the L0I calibration weights from the muon channel calibration are also applied to the electron channels in the following. Fig. 7.9 shows the calibration weights as a function of the transverse momentum of the B meson in six regions of track multiplicity $nTracks$ for the 2018 $B^0 \rightarrow K^{*0} J/\psi(\rightarrow e^+e^-)$

sample. The distributions for other years of data taking and the control channel $B^+ \rightarrow K^+ J/\psi(\rightarrow \mu^+ \mu^-)$ show comparable results.

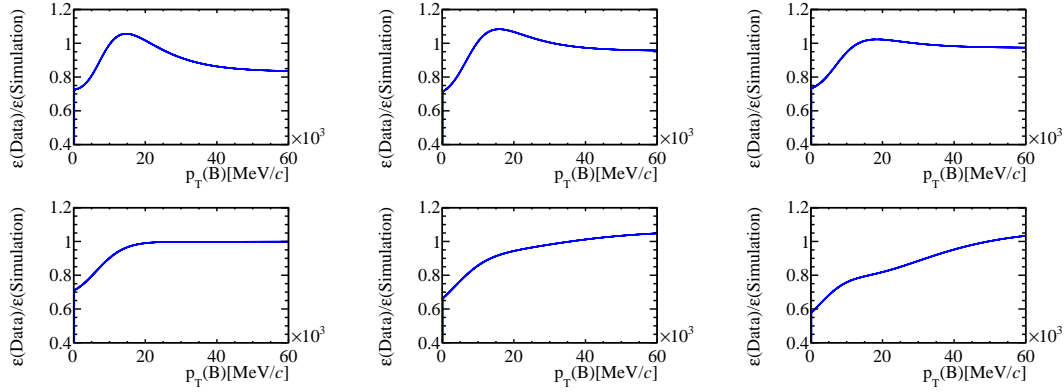


Figure 7.9 – Nominal calibration chain: L0I trigger efficiency weights for the 2018 $B^0 \rightarrow K^{*0} J/\psi(\rightarrow \mu^+ \mu^-)$ sample as a function of the B -meson transverse momentum in six nTracks regions.

Prior calibration chain L0M. As shown in Fig. 7.1, the samples for the $w_{\text{Mult\&Kin}}$ computation are previously calibrated for the L0 trigger response in the prior calibration chain. The TCK configuration between data and simulation is aligned as described in Section 7.1 using the inclusive L0M trigger category. For this purpose, the same procedure as used for the L0 calibration in the main calibration chain is performed for the L0M trigger category with identical parameterisation but exploiting the TCK alignment. Fig. 7.10 shows the corresponding calibration results for the 2018 $B^0 \rightarrow K^{*0} J/\psi(\rightarrow \mu^+ \mu^-)$ sample. Calibrations for other years and the $B^+ \rightarrow K^+ \mu^+ \mu^-$ samples show similar behaviour. However, it is noticeable that for the RUN 1 samples, the distributions are flatter in comparison to the main calibration chain. For this sample, a large part of the trigger differences between data and simulation are already compensated because of the strict TCK alignment.

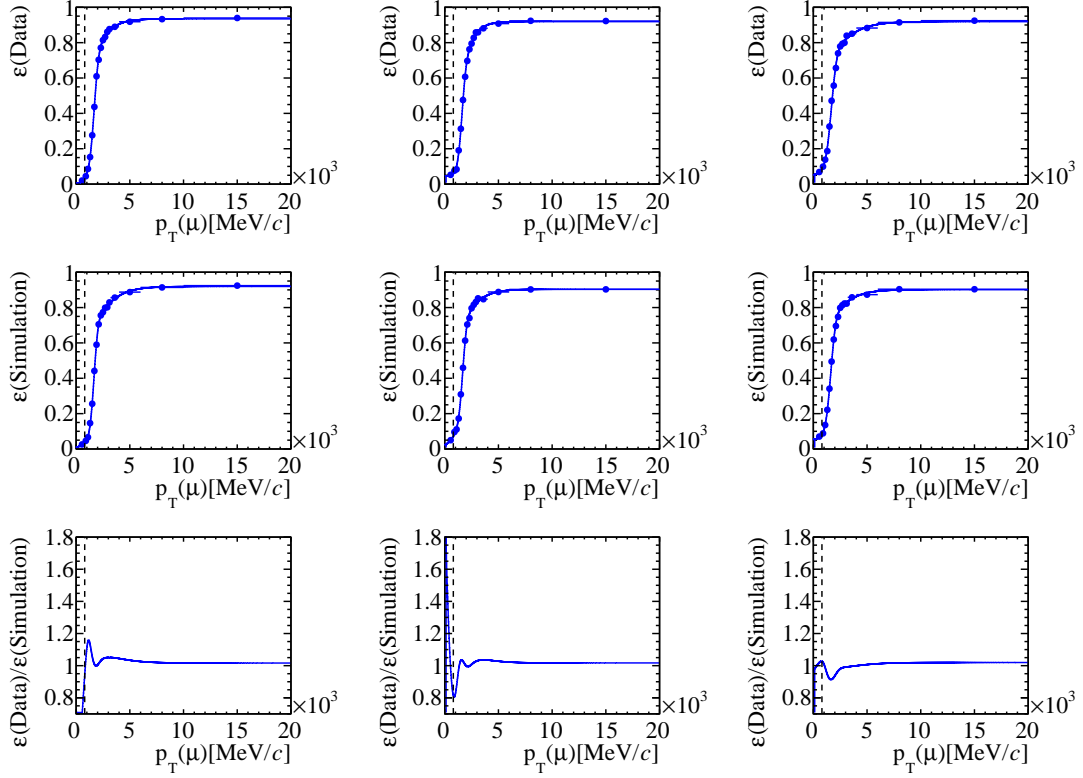


Figure 7.10 – Prior calibration chain: L0M trigger efficiencies calculated on (top) data and (middle) simulation samples for the 2018 $B^0 \rightarrow K^{*0} J/\psi (\rightarrow \mu^+ \mu^-)$ samples as a function of the transverse muon momentum in three bins of the muon pseudorapidity, the solid blue line indicates the fit function to model the efficiency distribution. The bottom row shows the ratios of the data and simulation efficiencies. The black dashed line indicates the trigger threshold.

7.5.2 HLT software trigger

The selection of data and simulation uses the trigger conditions listed in Table 6.1 for the HLT2 and HLT2 trigger. Similarly to the L0 trigger, the efficiencies (see Chapter 8) are calibrated with weights. However, in contrast to the hardware trigger, the calibration of the response for the software HLT is more complex. This higher complexity is firstly because reconstruction efficiencies of the final states are included with HLT1 and HLT2 for two different trigger levels. Second, the efficiencies are influenced by the various selection criteria of the different HLT trigger conditions, and thirdly, there are correlations between the two trigger stages that need to be taken into account.

Besides differences in the generation of the physical quantities of the simulation, two further aspects cause differences in the trigger response between data and simulation: Firstly, there are so-called “prescale factors” which limit the trigger input rates. These prescale factors differ for the trigger lines selected in this thesis. On the other hand, misalignment is caused by different TCK settings, which cannot be compensated entirely by the trigger configuration alignment (see Section 7.1).

Strategy As in the case of the calibration of the L0 trigger response (see Section 7.5.1), the *TISTOS* method is used for calibration. The two sample categories TIS&TOS and TIS are similarly employed. The TOS sample is defined as the combination of the individual HLT conditions and the TIS sample as a combination of different trigger conditions that are triggered independently of the signal. Accordingly, the calibration weights are calculated with

$$w_{\text{HLT}} = \frac{\epsilon^{\text{Data}} = \left(\frac{N_{\text{TIS\&TOS}}}{N_{\text{TIS}}} \right)^{\text{Data}}}{\epsilon^{\text{Simulation}} = \left(\frac{N_{\text{TIS\&TOS}}}{N_{\text{TIS}}} \right)^{\text{Simulation}}}. \quad (7.13)$$

The HLT efficiencies $\epsilon^{\text{Data/Simulation}}$ are thereby calculated as ratios of the signal candidates N in the corresponding categories. The extraction of the weights is performed on data and simulation of the decays $B^0 \rightarrow K^{*0} J/\psi (\rightarrow \ell^+ \ell^-)$ and $B^+ \rightarrow K^+ J/\psi (\rightarrow \ell^+ \ell^-)$ separately for the two L0 categories of this thesis. The ratio of the two efficiencies ϵ^{Data} and $\epsilon^{\text{Simulation}}$ is finally applied to the simulation as a calibration weight w_{HLT} . A simultaneous fit on the TIS&TOS and TIS data sub-samples extracts ϵ^{Data} . Possible background pollution in these samples is previously suppressed by the full analysis selection described in Chapter 6 except for the MVA condition and the HLT requirements. The efficiency $\epsilon^{\text{Simulation}}$ is computed identically to the selected simulation on which the PID, kinematics, multiplicity, and L0 calibrations are already applied.

The calibration of the HLT efficiencies is performed as a function of different proxy variables. The variables $n\text{Tracks}$, $p_{\text{T}}(B)$ and $\eta(B)$ were tested. The division into regions is made in such a way that all regions contain approximately the same number of candidates for the TIS&TOS subsample. This region definition guarantees good stability of the fits described above, given the few signal candidates within this category. Because the calibration for the electron and muon decay channels, as well as the trigger categories, is done individually, this also applies to this optimisation.

Although the measured efficiencies for the proxy variable $p_{\text{T}}(B)$ show a trend in the data sample, the simulation can describe this effect well. However, it finds a trend for the number of tracks in the event $n\text{Tracks}$ that is not mapped, which is why it is selected for the final calibration. Since the same trend can be reproduced in a cross-check with the alternative multiplicity variable $n\text{SPDHits}$, a dependence of the trigger efficiency on the event multiplicity can be assumed. Fig. 7.11 shows exemplary HLT efficiencies calculated with $B^0 \rightarrow K^{*0} J/\psi (\rightarrow \ell^+ \ell^-)$ decays from 2018 for the primary L0I trigger category.

Prior calibration chain. Just like for the L0 trigger response, the HLT efficiencies are calibrated in the prior calibration chain to prepare the L0Muon sample for the correction of the B -meson kinematics and event multiplicity. As can be seen in Fig. 7.1, the PID and the L0 mismodelling are calibrated beforehand. Since the muon samples have very high purity and a high number of signal candidates, it is possible to parameterise the

7 Calibration of simulation

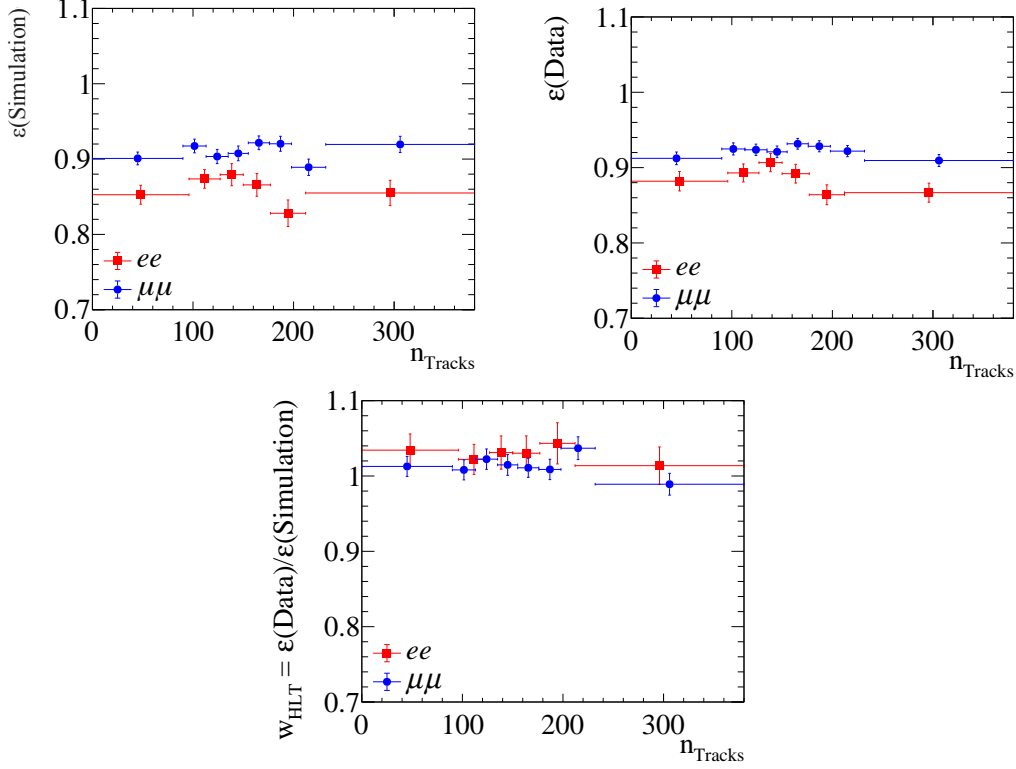


Figure 7.11 – HLT efficiencies measured with the TISTOS method on (top left) simulation and (top right) data on 2018 $B^0 \rightarrow K^{*0} J/\psi(\rightarrow \ell^+ \ell^-)$ decays in the L0I trigger category. Also shown (bottom) is their ratio for the computation of the calibrations weights w_{HLT} .

calibration in two dimensions. For this purpose, a kinematic proxy of the B meson $p_{\text{T}}(B)$, as well as the n_{Tracks} variable, are used.

Nominal calibration chain. The nominal correction chain is performed for the decay channels with electrons and muons and for the trigger categories as mentioned above. When calculating the calibration weights, it is found that the efficiencies of the inclusive and exclusive L0E and L0M trigger categories show good agreement. For this reason, the calibration weights for the exclusive L0E and L0M trigger categories are calculated from samples of the inclusive trigger categories since they contain a larger number of signal candidates. Figs. 7.12 and 7.13 shows the calibration weights for all years of the LHCb data taking from 2011-2018 extracted with $B^0 \rightarrow K^{*0} J/\psi(\rightarrow \ell^+ \ell^-)$ and $B^+ \rightarrow K^+ J/\psi(\rightarrow \ell^+ \ell^-)$ decays for the L0I trigger category. The calibration weights for the L0L trigger category can be found in Appendix A.4 showing similar behaviour in all trigger categories and years.

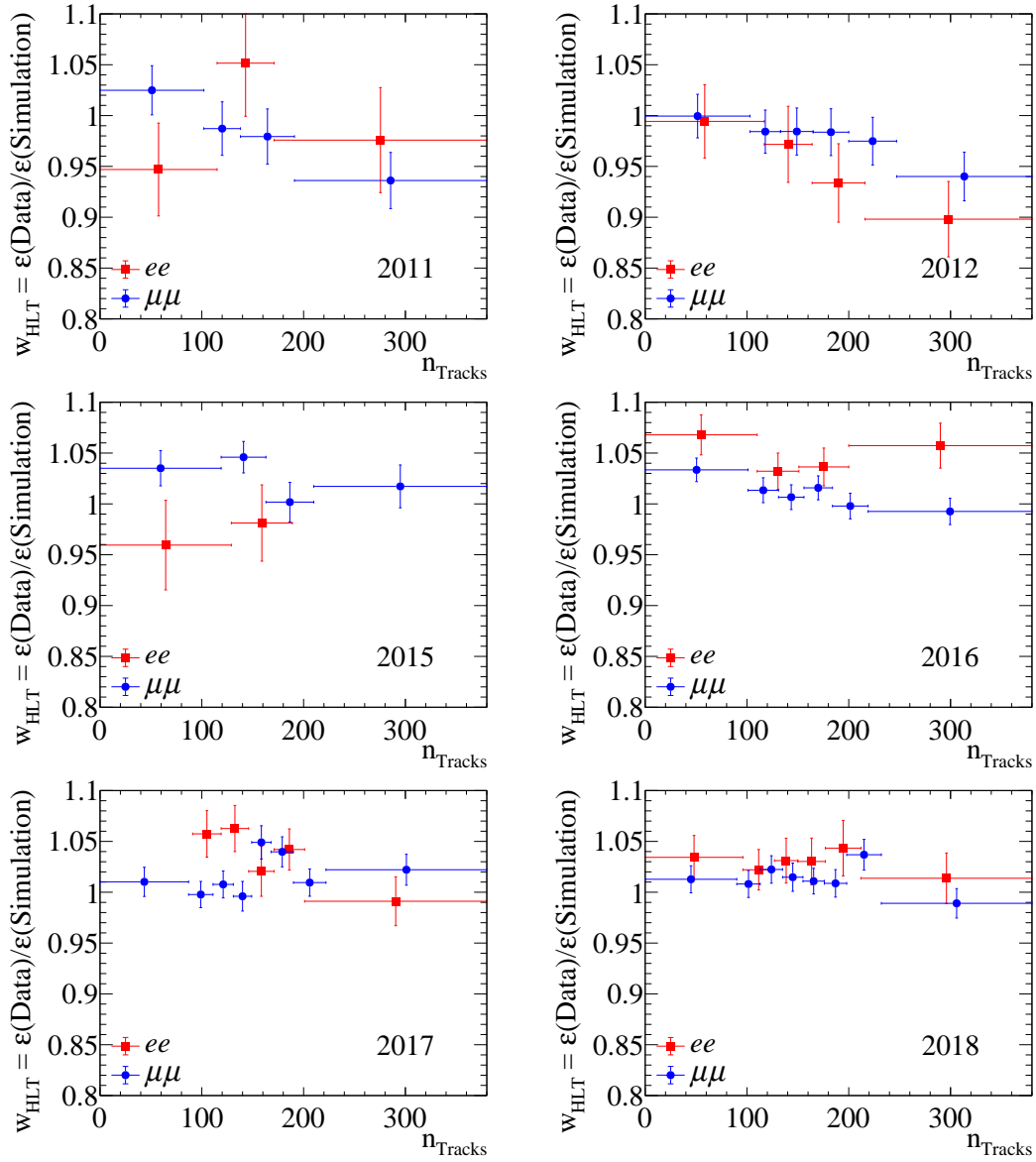


Figure 7.12 – HLT1 and HLT2 trigger calibration weights w_{HLT} of the nominal correction chain computed as the ratio of the trigger efficiency in data and simulation in regions of n_{Tracks} . Shown are weights computed with the $B^0 \rightarrow K^{*0} J/\psi (\rightarrow e^+ e^-)$ and $B^0 \rightarrow K^{*0} J/\psi (\rightarrow \mu^+ \mu^-)$ decay channels for the L0I trigger category in the years 2011-2018.

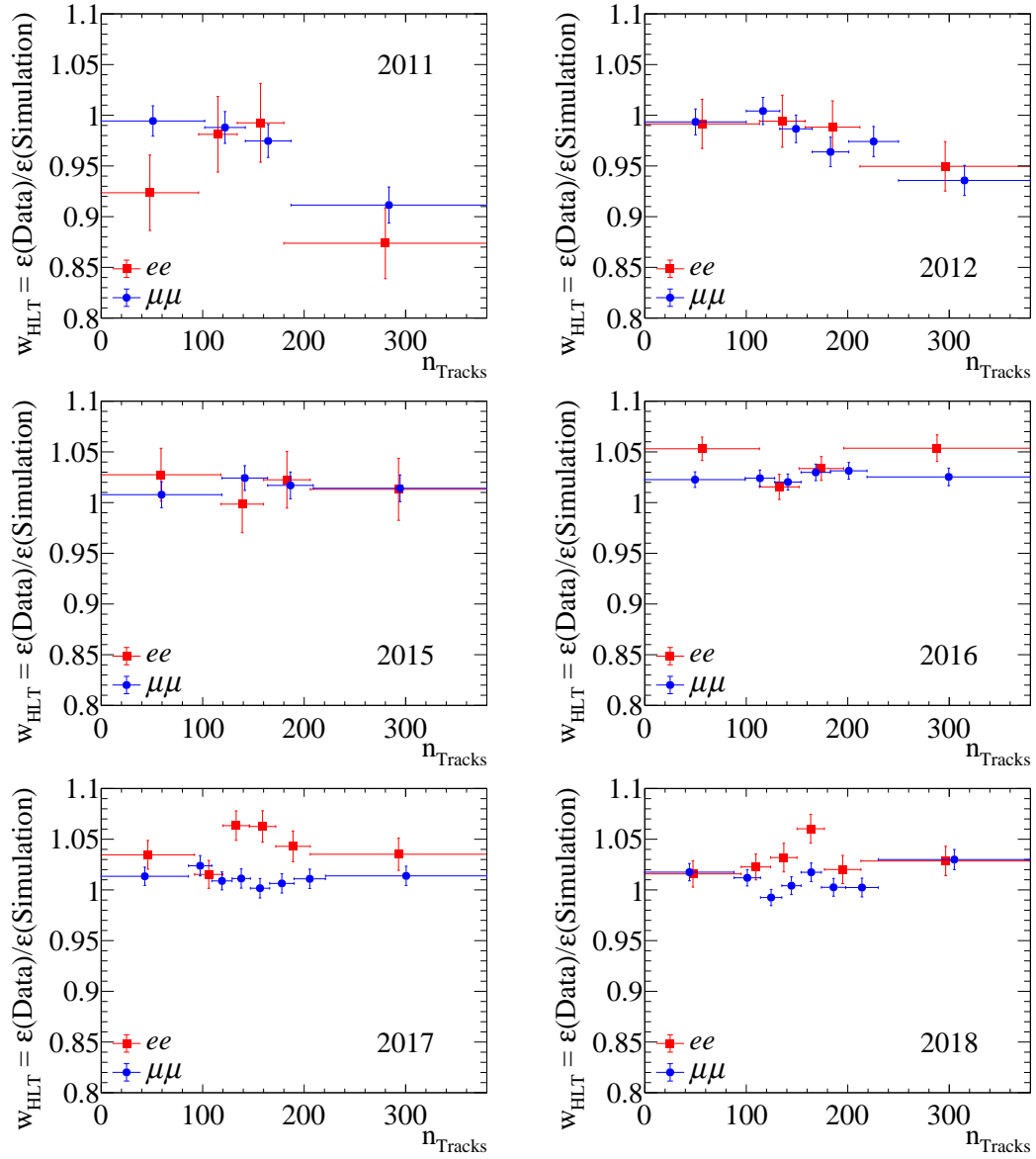


Figure 7.13 – Software trigger calibration weights w_{HLT} of the nominal correction chain computed as the ratio of the trigger efficiency in data and simulation in regions of n_{Tracks} . Shown are weights computed with the $B^+ \rightarrow K^+ J/\psi(\rightarrow e^+e^-)$ and $B^+ \rightarrow K^+ J/\psi(\rightarrow \mu^+\mu^-)$ decay channels for the L0I trigger category in the years 2011-2018.

7.6 Candidate reconstruction

Similar to the kinematic and multiplicity calibration presented in Section 7.4, differences between the distributions of data and simulation for candidate reconstruction variables need to be compensated. As a proxy variable for the candidate reconstruction, the χ_{IP}^2 of the B meson and the χ_{IP}^2 of the J/ψ meson are chosen because they are used in the training of the MVA classifiers against combinatorial and partially reconstructed background (see Section 6.5). Furthermore, as the vertex-fit qualities are particularly affected by the track reconstruction's uncertainty, they constitute a suitable proxy for the calibration.

Since the calibration of these variables depends on the lepton type in the final state of the respective signal decays, it cannot be transferred from calibration with muons to the electron channels as in the case of the weights $w_{\text{Mult\&Kin}}$. Consequently, a separate calibration for the muon and electron channels is performed in this step.

The weights $w_{\text{Mult\&Kin}}$ are also applied when training this step. This strategy is similar to calibrating the kinematic and multiplicity variables in the second BDT. The resonant J/ψ decay channel of the respective trigger category is used as a calibration sample. The full analysis selection, including the MVA requirements, is applied to obtain a pure calibration sample. To further suppress background, the B -meson mass computed with the J/ψ -mass constraint is required to lie in a mass window of $60 \text{ MeV}/c^2$ around the known B mass. Also, the k -fold method is used in training and applying the calibration outputs.

Validation of calibration. The Kolmogorov-Smirnov test [233] is used to quantify the differences between the distributions of the data and simulation and thus to validate the method. The comparison plots show the distributions in data as well as uncalibrated and finally calibrated simulation. Figs. 7.14 and 7.15 show the good agreement after the full calibration chain presented in Fig. 7.1 for the measurement of R_{K^*0} in the LOI trigger category and the data collection year 2018. Appendix A.3 shows more example plots of this kind.

7 Calibration of simulation

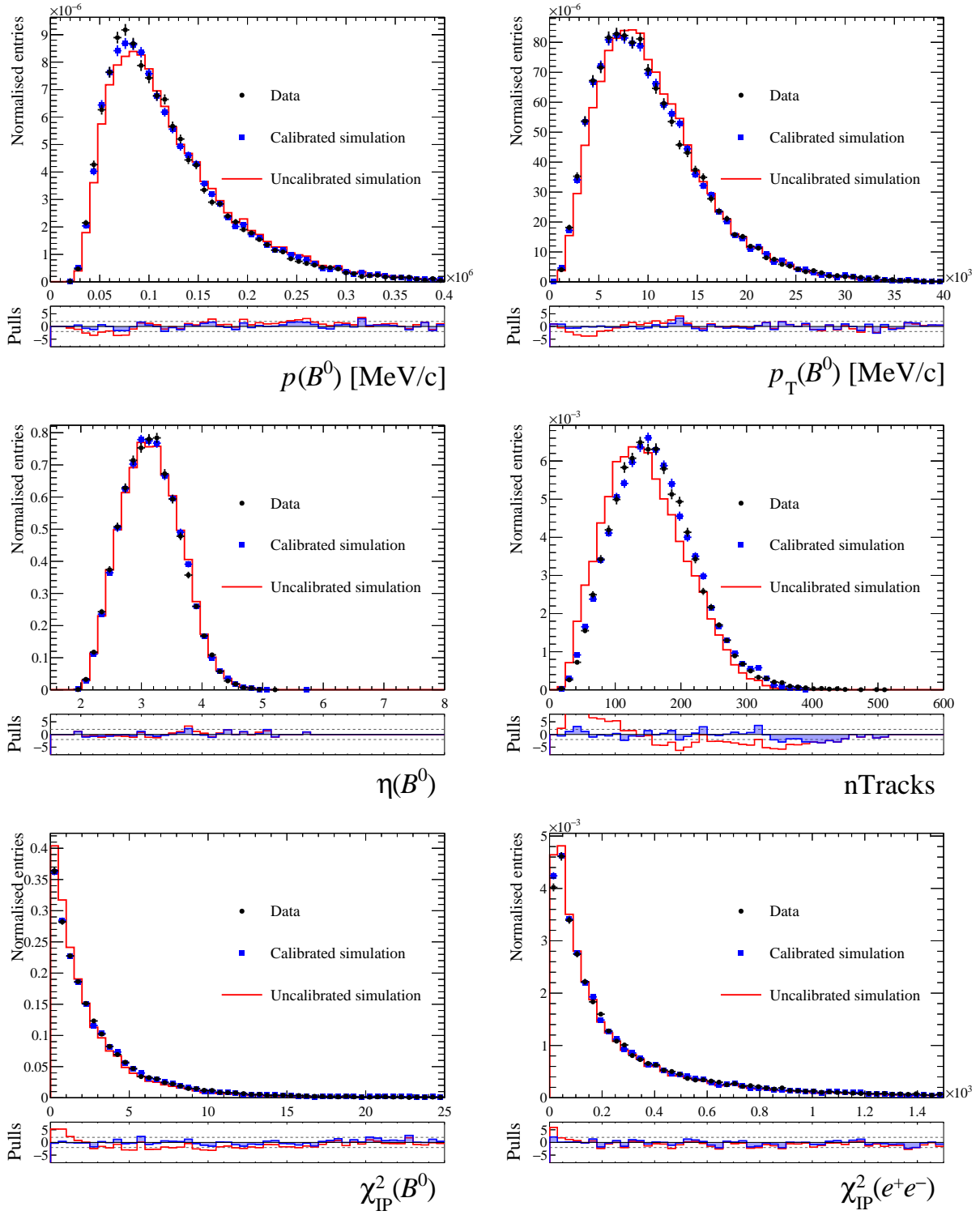


Figure 7.14 – $w_{\text{Mult\&Kin}}$ and w_{Reco} calibration: Comparisons of selected (black) data with (red) uncalibrated and (blue) calibrated simulation for the 2018 L0I $B^0 \rightarrow K^{*0} J/\psi (\rightarrow e^+e^-)$ sample with the full calibration chain applied except the q^2 bin migration. Shown are the distributions for momentum $p(B^0)$, transverse momentum $p_T(B^0)$, pseudorapidity $\eta(B^0)$ of the B^0 meson, the multiplicity proxy $nTracks$, and the candidate reconstruction variables χ_{IP}^2 of the B^0 meson and the dielectron system. The bottom part of each plot shows the residuals normalised with the data uncertainties.

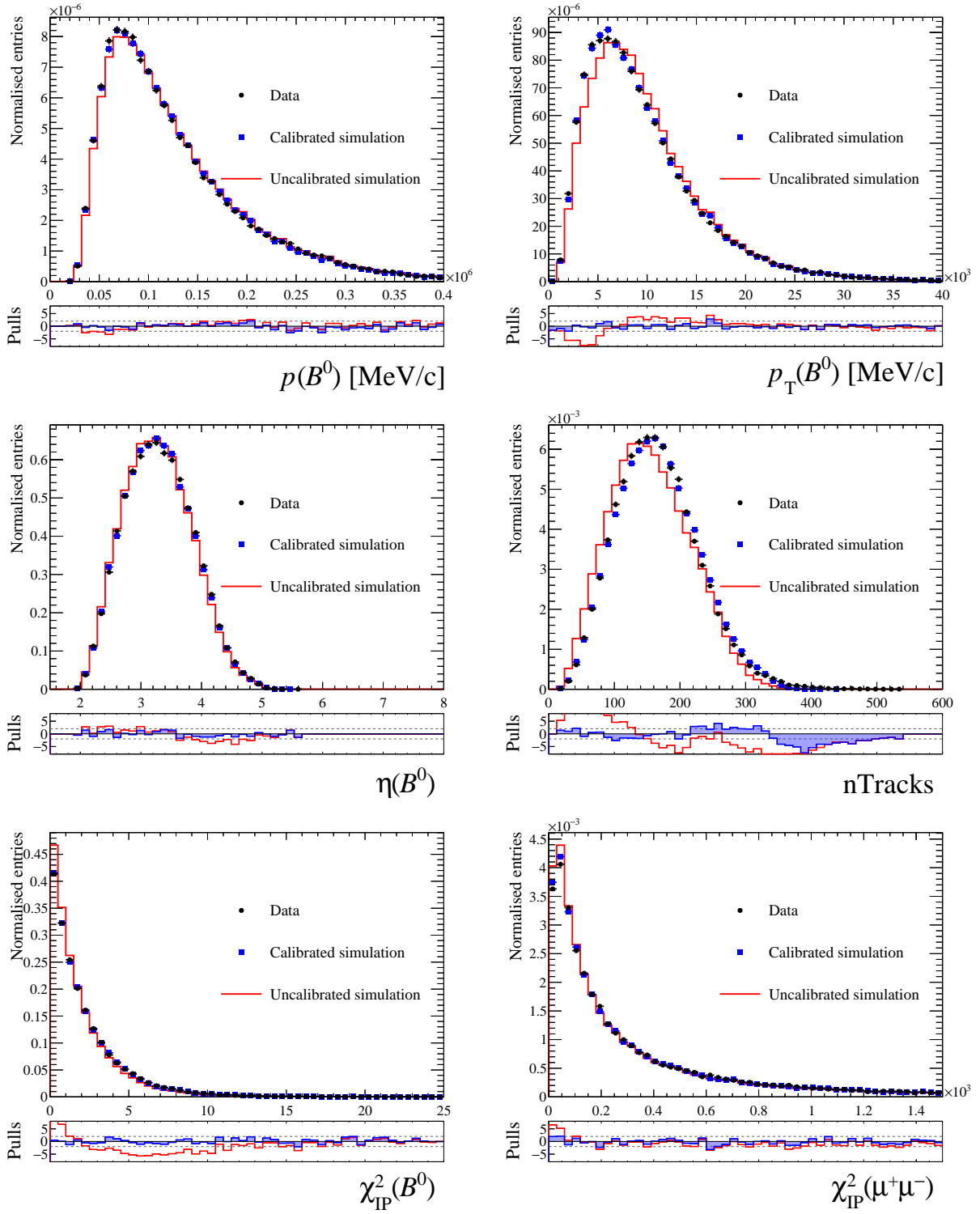


Figure 7.15 – $w_{\text{Mult\&Kin}}$ and w_{Reco} calibration: Comparisons of selected (black) data with (red) uncalibrated and (blue) calibrated simulation for the 2018 L0I $B^0 \rightarrow K^{*0} J/\psi (\rightarrow \mu^+ \mu^-)$ sample with the full calibration chain applied except the q^2 bin migration. Shown are the distributions for momentum $p(B^0)$, transverse momentum $p_T(B^0)$, pseudorapidity $\eta(B^0)$ of the B^0 meson, the multiplicity proxy nTracks, and the candidate reconstruction variables χ_{IP}^2 of the B^0 meson and the dielectron system. The plots below the comparison distributions show the residuals normalised with the data uncertainties.

7.7 Bin migration

In addition to the previous calibration of the simulation, migration of events of electron channels between q^2 regions must be considered, are which caused by bremsstrahlung effects and correspond to a effect of roughly 10 %. These events are located in the tails of the q^2 distributions. After the previous calibration step, the remaining differences between data and simulation are present here.

Differences between the resolution of the q^2 spectrum originate mainly from two reasons. One is the imperfect simulation of material budget in the detector. As a consequence, bremsstrahlung effects are different, which biases the momentum resolution of the electron measurement. On the other hand, both occupancy and calorimeter outputs are only simulated with limited precision and thus reduce the accuracy of the bremsstrahlung recovery procedure (see Section 3.2.4) and hence also the resulting q^2 spectrum. The occupancy of the calorimeter is biased in simulation because the number of secondary particles produced in material interactions is biased if the material budget before the calorimeter is not perfectly simulated. The approach used here allows to calibrate the q^2 spectrum on simulation for these resulting discrepancies. In the following, the application of this calibration step is given as w_{q^2} , although it is not a weight that is applied but a recalculation of the q^2 spectrum. For the final efficiency calculation, this corrected q^2 spectrum is used to evaluate the efficiencies of the q^2 selection.

Calibration strategy. Since the simulation is used to determine the migration efficiencies, the differences of the q^2 spectra must be calibrated accordingly for the simulation. For this purpose, an empirical calibration function is defined, applied to the simulated q^2 spectrum. The parameters of the “smearing function” are determined with fits to the invariant q^2 spectrum with

$$m^{\text{Smeared}} = m^{\text{True}} + s_{\sigma} \cdot (m^{\text{Reco.}} - m^{\text{True}}) + \Delta\mu + (1 - s_{\sigma}) \cdot (\mu^{\text{Simulation}} - m(J/\psi)_{\text{PDG}}). \quad (7.14)$$

The calibration function thus calculates an adjusted dilepton mass m^{Smeared} , which is used in further analysis to determine the efficiencies.

In this formula, m^{True} is the true dilepton mass generated in the simulation. This mass is calculated from the four-momenta of the B meson and the hadronic system of the decays. $m^{\text{Reco.}}$, on the other hand, is the simulated reconstructed dilepton mass. s_{σ} is the mass-distribution width ratio σ in simulation and data calculated as $\frac{\sigma_{\text{Data}}}{\sigma_{\text{Simulation}}}$, and $\Delta\mu$ is the difference of the means μ of their mass distributions with $\Delta\mu = \mu_{\text{Data}} - \mu_{\text{Simulation}}$ determined with fits to data and simulation. $m(J/\psi)_{\text{PDG}}$ is the known value for the mass of the J/ψ meson.

Parameter extraction with maximum-likelihood fits. To extract the parameters occurring in Eq. (7.14), unbinned maximum-likelihood fits to the dielectron spectrum

$m(e^+e^-)$ are performed. The fits extract the parameters separately for the B^+ and B^0 decay channels, for the three bremsstrahlung categories, for the individual years of the LHCb data collection, for the trigger categories of the measurement of R_K and R_{K^*0} , and for three bremsstrahlung categories. The bremsstrahlung categories are defined as zero, or one or more bremsstrahlung photons reconstructed. By applying the preselection of the measurement presented here and an additional condition of $5.20 \text{ GeV}/c^2 < m(B)_{\text{DTF}} < 5.68 \text{ GeV}/c^2$ for the B meson, excellent signal purity is achieved. With this condition, both partially reconstructed backgrounds and leakage contributions from $B \rightarrow K\psi(2S)(\rightarrow \ell^+\ell^-)$ decays are suppressed. Thus, the only background component expected in data is combinatorial background. The entire calibration procedure is applied to the simulation. An additional study shows that the previous calibration chain can already compensate for about 10 % of the observed differences between data and simulation.

The signal component of the $m(\ell^+\ell^-)$ mass spectrum in both data and simulation is described with a double-sided Crystal Ball function [225]. An exponential function describes the combinatorial background. Fig. 7.16 shows these fits for the decay channels $B^+ \rightarrow K^+ J/\psi(\rightarrow e^+e^-)$ and $B^0 \rightarrow K^{*0} J/\psi(\rightarrow e^+e^-)$ reconstructed for 2018 in the L0I trigger category with no bremsstrahlung photon. Other years and trigger categories show similar behaviour.

The calibration is validated by applying the fits a second time to the now calibrated dielectron mass. A value compatible with unity is expected for s_σ and a value compatible with zero for $\Delta\mu$. This check shows good agreement.

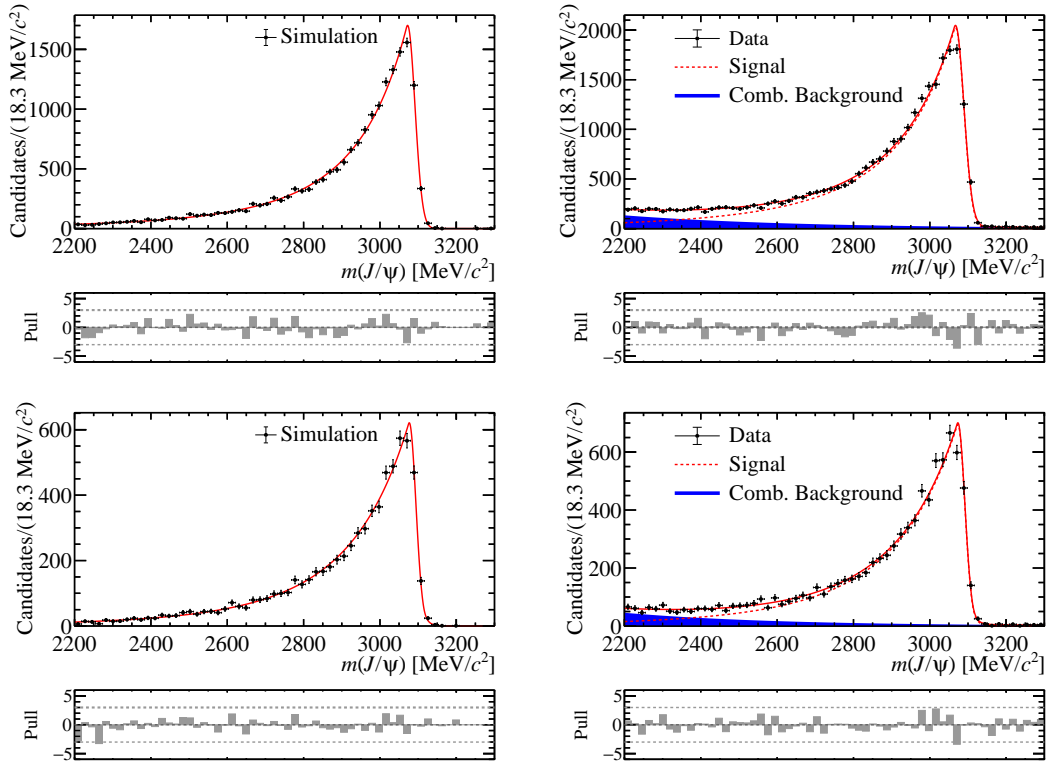


Figure 7.16 – Results of the maximum-likelihood fits to extract the q^2 -migration parameters described in Eq. (7.14) to the dielectron spectrum for (left) calibrated simulation and (right) data. The total fit components are shown in a solid red line, the signal component for the fit to data in a dashed red line and the combinatorial background as a blue area. Shown are the fits performed with the L0I trigger category with 0 reconstructed bremsstrahlung photons for the (top) $B^+ \rightarrow K^+ J/\psi (\rightarrow e^+ e^-)$ and (bottom) $B^0 \rightarrow K^{*0} J/\psi$ decay for the year 2018.

8 Efficiencies

After applying the entire previously described calibration chain to the simulation, the efficiencies for all signal decay modes are computed. These are the rare and resonant decay modes for each year of data taking and each trigger category, respectively. The total efficiency $\varepsilon_{\text{Total}}$ consists of different factors given by

$$\varepsilon_{\text{Total}} = \varepsilon_{\text{Geo}} \cdot \left(\varepsilon_{\text{Stripping}} \cdot \varepsilon_{\text{MVA}} \cdot \varepsilon_{\text{Preselection}} \cdot \varepsilon_{\text{Trigger}} \cdot \varepsilon_{\text{PID}} \right) \Big|_{\text{Geo}} . \quad (8.1)$$

In this formula, ε_{Geo} is the efficiency of the geometric detector acceptance. Due to limited storage capacities, only simulated events with all decay products inside the LHCb acceptance are saved to storage. The geometric efficiency is determined using dedicated simulation samples covering the whole solid angle region with details given in Section 8.1. The second term in the formula corresponds to the efficiencies of the full calibrated selection given the geometric acceptance. These include the centralised preselection (stripping), MVA selection, offline preselection, trigger selection, and PID selection as described in Chapter 6.

One of the primary approaches of this thesis is to base the calibration of the R_K and R_{K^*0} measurement on the calibration of B^0 and B^+ calibration samples, respectively. This means crossing the calibration samples by calibrating the R_K efficiencies with the B^0 calibration sample and the R_{K^*0} efficiencies with a B^+ calibration sample. In that way, correlations between the calibration procedure and the efficiency calculation on the actual signal samples are reduced, where the resonant B^+ (B^0) are used as normalisation modes. Section 8.2 presents the determination of the efficiency correlations and the handling of their residual effects. Finally, Section 8.3 describes the measurement of the final efficiencies and reports their results for the resonant normalisation modes. Efficiencies used to model background components in the fits to the invariant mass of the B meson are determined following the same approach.

Because the final results of R_K and R_{K^*0} are not published at the time of the submission of this thesis, no efficiencies for the rare signal modes except geometrical and filtering efficiencies are reported. The other efficiencies are not calculated because of the blinding strategy of the analysis. This strategy is introduced to avoid possible experimenter bias.

8.1 Geometric efficiency

The simulation used in this analysis only includes events where all daughter particles of the decays have been detected within the geometrical LHCb detector acceptance, which corresponds to the condition of a VELO polar angle ϕ (see Fig. 3.6) between 100

and 400 mrad. The fractions of tracks lying in this acceptance are calculated centrally in the simulation production. Their individual values are reported for the years of data taking and the two magnetic polarities, respectively. The corresponding efficiencies are listed in Table A.4, where the luminosity-weighted mean between the respective magnetic polarities is used for the calculation of the total efficiencies $\varepsilon_{\text{Total}}$. Since the centrally provided list of geometric efficiencies includes only one common value for the efficiencies of the low- q^2 and central- q^2 region of the signal sample, an additional simulation sample was generated with which these differences between the efficiencies can be determined. Table A.5 presents the resulting efficiencies, which have a maximum deviation of about 2 % from the aforementioned averaged values.

8.2 Efficiency correlations

As mentioned above, the measurement strategy of crossing the calibration chains based on B^0 and B^+ decay modes to measure R_K and R_{K^*0} , respectively, is minimising efficiency correlations already. But there are remaining factors of correlations that need to be taken into account.

- Calibration factors are ported from the muon mode computed on the L0I trigger category to the electron mode for the w_{L0} trigger weights. Also, the kinematic and multiplicity calibration for the electron modes is performed with the L0M calibration sample.
- There is an inherent overlap of the trigger categories of this measurement because the inclusive L0L trigger category shares events with the L0I trigger category (see Fig. 5.4). This overlap leads to statistical correlations of the calibration weights computed in these two categories.
- Trigger efficiency calibrations as well as kinematics and track multiplicity calibrations are based on the non-crossed L0M resonant signal samples. In this case, the crossing of the B^+ and B^0 calibration chains is not applied.

The remaining correlations between the efficiencies of different decay channels, trigger categories, and run periods are covered with the computation of covariance matrices, using a *resampling* approach, which will be explained in the following. In the final result extraction, these covariance matrices are employed when all subsamples are simultaneously combined to measure R_K and R_{K^*0} for all trigger categories and years at once.

Resampling approach. With the *resampling* approach, each reconstructed candidate is assigned 100 different Poisson-distributed weights around the mean of 1. These weights are randomised with a starting value based on the unique combination of RunNumber and EventNumber of the candidates. In addition, 100 different variations of each of the calibration maps of the particular calibration steps are generated in a

computationally intensive procedure. Each map is assigned to one of these 100 weights of the signal candidates. With this assignment, the correlation of the calibration samples with the signal candidates can be determined in the final extraction of the results, in which the i^{th} efficiency is compared with the i^{th} signal candidate. The distributions of the individual efficiencies after the *resampling* procedure show a behaviour according to the Gaussian distribution and thus a stable behaviour.

8.3 Measurement of the total calibrated efficiencies

The total efficiencies are computed in the same way as the efficiency of the overall selection, but using the different calibration factors as described in Chapter 7. Therefore, the whole selection is employed except for those PID requirements absorbed in the PID calibration weights. The tracking and trigger weights are applied to the corresponding subsamples as per-event weights. Because the $w_{\text{Mult\&Kin}}$ and w_{Reco} weights were extracted using the L0M triggered resonant calibration sample, these need additional normalisation, which is additionally included.

As a first step the total efficiencies are calculated for each year and each magnet polarity, respectively. The combination of the efficiencies is evaluated as a luminosity weighted sum with

$$\varepsilon_{\text{Total}} = \frac{\sum_{i=\text{Year}, j=\text{Polarity}} \mathcal{L}_j^i \times \varepsilon_{\text{Total}}^{i,j}}{\sum_{i=\text{Year}, j=\text{Polarity}} \mathcal{L}_j^i} \quad (8.2)$$

with the integrated luminosities \mathcal{L}_j^i and the single efficiencies $\varepsilon_{\text{Total}}^{i,j}$ per year i and magnet polarity j . Table 8.1 shows a summary of the total efficiencies for the $B \rightarrow K^{(*0)} J/\psi (\rightarrow \ell^+ \ell^-)$ normalisation channels in two trigger categories. Table 8.2 and Tables A.6 and A.7 show the efficiencies of the steps of the selection procedure and the uncalibrated resulting total efficiency $\varepsilon_{\text{Total}}$. Additionally, the total efficiencies are presented after the different calibration weights are activated step by step. The last two columns of these efficiency overview tables show the total efficiencies based on the B^0 or B^+ resonant samples, including the q^2 -migration correction as the last calibration step. It shows that the final efficiencies are compatible between the two calibration chains, which validates the interchangeability. One of the goals of this measurement is to generate two independent but compatible calibration chains. A further, very stringent validation of the efficiency calibration procedure is presented with the measurements of the ratios $r_{J/\psi}$ and $R_{\psi(2S)}$ (see Eqs. (5.5) to (5.8)) in Chapter 11.

Table 8.1 – Total efficiencies $\varepsilon_{\text{Total}}$ measured in the resonant normalisation modes with the $B^+ \rightarrow K^+ J/\psi(\rightarrow \ell^+ \ell^-)$ and $B^0 \rightarrow K^{*0} J/\psi(\rightarrow \ell^+ \ell^-)$ decays in years of data taking.

Sample	Year	$\varepsilon_{\text{Total}}[10^{-3}]$	
		L0I	L0L!
$B^+ \rightarrow K^+ J/\psi(\rightarrow \mu^+ \mu^-)$	2011	4.77 ± 0.10	13.91 ± 0.21
	2012	4.58 ± 0.06	12.27 ± 0.13
	2015	5.50 ± 0.14	11.83 ± 0.28
	2016	6.24 ± 0.07	15.26 ± 0.16
	2017	6.49 ± 0.08	16.38 ± 0.16
	2018	5.85 ± 0.06	16.44 ± 0.13
$B^+ \rightarrow K^+ J/\psi(\rightarrow e^+ e^-)$	2011	1.81 ± 0.09	2.34 ± 0.09
	2012	1.65 ± 0.05	1.61 ± 0.05
	2015	2.15 ± 0.11	2.42 ± 0.10
	2016	2.84 ± 0.06	3.31 ± 0.06
	2017	2.95 ± 0.05	3.18 ± 0.05
	2018	2.58 ± 0.04	3.07 ± 0.04
$B^0 \rightarrow K^{*0} J/\psi(\rightarrow \mu^+ \mu^-)$	2011	1.74 ± 0.02	4.67 ± 0.04
	2012	1.67 ± 0.02	4.26 ± 0.03
	2015	2.08 ± 0.03	4.25 ± 0.06
	2016	2.41 ± 0.02	5.48 ± 0.04
	2017	2.51 ± 0.02	5.87 ± 0.04
	2018	2.20 ± 0.02	5.79 ± 0.03
$B^0 \rightarrow K^{*0} J/\psi(\rightarrow e^+ e^-)$	2011	0.67 ± 0.02	0.85 ± 0.02
	2012	0.65 ± 0.01	0.645 ± 0.01
	2015	0.86 ± 0.03	0.98 ± 0.03
	2016	1.08 ± 0.01	1.23 ± 0.02
	2017	1.11 ± 0.02	1.22 ± 0.02
	2018	0.98 ± 0.01	1.15 ± 0.01

Table 8.2 – Uncalibrated efficiencies of selection steps with total uncalibrated efficiency ϵ_{Total} for the $B^+ \rightarrow K^+ J/\psi (\rightarrow \ell^+ \ell^-)$ normalisation mode in RUN 2P2. Below the total uncalibrated efficiencies, the effects of sequentially turning on the calibrations are shown in terms of stepwise calibrated total efficiencies. For the selection steps the geometrical acceptance (see Section 8.1), the stripping selection (see Section 6.2), the ECAL distance requirement (see Section 7.2), the offline preselection including the PID selection (see Section 6.3), the $L0$ and HLT requirements (see Section 6.1), the selection criteria to suppress exclusive background (see Section 6.4), and the fit range requirements of the invariant mass fits (see Chapter 9) are included.

Selection step	$L0I e^+e^-$	$L0I \mu^+\mu^-$	$L0L! e^+e^-$	$L0L! \mu^+\mu^-$
ϵ_{Geo}	17.21 %	17.32 %	17.21 %	17.32 %
$\epsilon_{\text{Stripping}}$	16.02 %	33.15 %	16.02 %	33.15 %
$\epsilon_{\text{ECAL distance}}$	99.73 %	100.00 %	99.73 %	100.00 %
$\epsilon_{\text{Preselection}}$	73.60 %	69.03 %	73.60 %	69.03 %
ϵ_{L0}	24.75 %	27.14 %	27.29 %	58.15 %
$\epsilon_{L0 \text{ alignment}}$	100.00 %	87.88 %	95.03 %	87.52 %
ϵ_{HLT1}	90.15 %	95.08 %	95.91 %	94.98 %
ϵ_{HLT2}	94.03 %	93.33 %	98.28 %	93.34 %
$\epsilon_{\text{Excl. backgrounds vetoes}}$	88.13 %	91.08 %	88.76 %	91.21 %
ϵ_{MVA}	99.32 %	99.34 %	99.27 %	99.37 %
$\epsilon_{\text{Fit range}}$	98.95 %	99.43 %	99.20 %	99.48 %
ϵ_{Total}	0.37 %	0.75 %	0.43 %	1.61 %
+ w_{PID}	0.34 %	0.74 %	0.40 %	1.59 %
+ w_{TRK}	0.34 %	0.74 %	0.39 %	1.59 %
+ $w_{\text{Mult\&Kin}}$	0.33 %	0.76 %	0.33 %	1.48 %
+ w_{L0}	0.27 %	0.61 %	0.32 %	1.60 %
+ w_{HLT}	0.28 %	0.62 %	0.31 %	1.65 %
+ w_{Reco}	0.28 %	0.61 %	0.31 %	1.64 %
+ w_{q^2} (total B^0 chain)	0.27 %	0.61 %	0.31 %	1.64 %
+ w_{q^2} (total B^+ chain)	0.27 %	0.61 %	0.32 %	1.64 %

9 Modelling of the invariant mass distributions

In order to evaluate the ratios R_K and R_{K^*0} , maximum likelihood fits on the reconstructed masses of the B^0 and B^+ candidates with the RooFIT package [234] to extract the number of $K^+\ell^+\ell^-$ ($K^+\pi^-\ell^+\ell^-$) signal candidates in data are performed. The fits are binned for the resonant modes to allow a time-efficient computation and unbinned for the rare modes. The resolution on the invariant masses is improved using the DecayTreeFitter (DTF) [210]. One requirement applied with this tool is that the final state particles must originate from the same primary vertex (PV) as indicated by the $m(K^+\ell^+\ell^-)$ ($m(K^+\pi^-\ell^+\ell^-)$) track combination. As a general approach, the DTF tunes the momenta of the child particles to satisfy a given condition, e.g., all tracks originating from the same vertex or a track combination having a given invariant mass. More complex properties such as the invariant B -meson mass are calculated with these tuned track momenta. In addition to the PV condition, the mass of the dilepton system decaying through the J/ψ or $\psi(2S)$ resonances can be constrained to the known masses of the J/ψ or $\psi(2S)$ resonances. This additional constraint improves the resolution of the invariant mass of the B -meson candidates in the electron modes by mitigating momentum and energy losses due to bremsstrahlung. This additional condition is indicated with the notation $m_{\text{DTF}}^{J/\psi}$ or $m_{\text{DTF}}^{\psi(2S)}$ in the following. This constraint is applied when computing cross-checks and certain systematic uncertainties, but is not used when preparing the final results extraction to match the rare decays signal modelling. The small amount of radiated bremsstrahlung makes this feature unnecessary for the muon modes because of the higher resolution of the mass spectrum.

Large numbers of pseudo experiments, e.g., with modifications in the model of the background composition or the number of candidates for particular components, are conducted to evaluate the stability of the alternative fit configurations and the modelling of the data distributions. The same procedure enables to determine possible fit biases and determine uncertainties of the fits.

This chapter presents an overview of the fit strategy and the results of the rare and resonant fits. For a more detailed description, see Ref.[208]. Section 9.1 describes the setup of the fit framework and the fit ranges used for the different data samples. Section 9.2 gives an overview of how the signal decays are modelled in the fit and Section 9.3 lists the considered background components. Section 9.4 presents the final fits to the collision data, listing the resulting fit yields and sensitivities in Section 9.4.1.

9.1 Fit ranges and fit setups

The fitting framework can be configured to run simultaneously or individually for single trigger categories, data-taking periods, and particular decay modes. A simultaneous fit to all categories in $R_{K^{*0}}$ and R_K is performed for the final measurement. Both, the single ratios $r_{J/\psi}^{K^{*0}}$, $r_{J/\psi}^K$, and double ratios $R_{K^{*0}}$, R_K , $R_{\psi(2S)}^{K^{*0}}$, $R_{\psi(2S)}^K$ are computed by the direct insertion of the calibrated efficiencies and efficiency correlations from the *resampling* approach (see Chapters 7 and 8) in the fit.

In the following, the fit ranges of the invariant B -meson mass are described, where for the B^+ and B^0 modes, the same mass windows are employed. If not stated differently, the lower edges of the ranges are chosen so that the partially reconstructed and *leakage* background components can be well modelled. The upper limit is determined such that the combinatorial background can be appropriately described.

- Muon J/ψ mode: For all fits to the resonant J/ψ muon modes of the $m(K\pi\mu\mu)$, $m(K\mu\mu)$, $m(K\pi\mu\mu)_{\text{DTF}}^{J/\psi}$, and $m(K\mu\mu)_{\text{DTF}}^{J/\psi}$ masses, the fit range is from 5100 MeV/ c^2 to 6100 MeV/ c^2 . Because of negligible bremsstrahlung losses, the mass resolution of the muon mode does not require further corrections via constraints.
- Muon $\psi(2S)$ mode: For the fits to the resonant $\psi(2S)$ muon modes of the $m(K\pi\mu\mu)_{\text{DTF}}^{\psi(2S)}$ and $m(K\mu\mu)_{\text{DTF}}^{\psi(2S)}$ masses, a fit range from 5100 MeV/ c^2 to 5750 MeV/ c^2 is chosen. This choice can be justified with the same arguments as for the for the muon J/ψ mode.
- Rare muon mode: For the rare muon decays in the central- q^2 and low- q^2 regions, the fits are performed with the $m(K\pi\mu\mu)$ and $m(K\mu\mu)$ masses in a mass window of 5150 MeV/ c^2 to 5850 MeV/ c^2 .
- Electron J/ψ mode: For the electron J/ψ modes fits, two different setups are considered in this measurement. For fits to the $m(K\pi ee)$ or $m(Kee)$ masses, the same range as for the electron low- q^2 and central- q^2 regions of 4600 MeV/ c^2 to 6200 MeV/ c^2 is used. When fitting to the J/ψ -constrained mass $m(K\pi ee)_{\text{DTF}}^{J/\psi}$ or $m(Kee)_{\text{DTF}}^{J/\psi}$ the window can be reduced to 4900 MeV/ c^2 – 6200 MeV/ c^2 because of the improved resolution.
- Electron $\psi(2S)$ mode: The fit range for the resonant $\psi(2S)$ electron mode fits of the $m(K\pi ee)_{\text{DTF}}^{\psi(2S)}$ and $m(Kee)_{\text{DTF}}^{\psi(2S)}$ masses is 5100 MeV/ c^2 to 5750 MeV/ c^2 . Using this lower limit enables for exact modelling of the partially reconstructed background, while the higher limit prevents combinatorial background and $B^0 \rightarrow K^{*0} J/\psi (\rightarrow e^+ e^-)$ and $B^+ \rightarrow K^+ J/\psi (\rightarrow e^+ e^-)$ decays from entering into the central- q^2 region.
- Rare electron mode: For the rare electron mode fits with the $m(K\pi ee)$ and $m(Kee)$ masses, the fit region of 4600 MeV/ c^2 to 6200 MeV/ c^2 is selected.

9.2 Signal descriptions in the rare and resonant modes

To model the different signal contributions for the rare and resonant modes, probability density functions (PDFs) are used. Fits of analytical functions on signal simulation determine their parameters. The extracted function parameters are then fixed in the fits to collision data to extract the final fit results. This is motivated by the fact that for an adequate description of the data, the detector resolution has to be modelled. A single Gauss function cannot describe this resolution due to various factors, for example, energy losses in the detector or multiple scattering. Furthermore, the selection requirements affect the resolution model with for example the choice of the mass windows or constraints on the invariant mass, bremsstrahlung emission, and bremsstrahlung recovery. As a consequence, a dedicated resolution model is needed for each data set, i.e., muon and electron modes in the rare or resonant q^2 regions, which is based on studies of the signal simulation.

In this thesis, the signal shapes of the rare and J/ψ channels without the DTF mass constraints of the muon modes are modelled with a sum of a double-sided Crystal Ball (DSCB) function [225] and two Gauss functions. The DTF-mass-constrained J/ψ and $\psi(2S)$ signal modes are described by the sum of a double-sided Hypatia function (DSH) [235] and two Gauss functions.

The signal PDFs for electron modes are computed based on the quantity of bremsstrahlung photons added to the final state dielectrons since the reconstructed invariant mass distribution is highly dependent on it. Afterwards, their extracted shapes are combined according to the proportions of their categories. The categories are defined as 0γ for events with no photons recovered, 1γ for events with one photon recovered for the electron pair, and 2γ for events with two or more photons recovered. For the rare electron signal modes, all three categories are modelled with a DSCB. The unconstrained J/ψ electron mode is described by a DSCB function with a Gauss function on the left-hand side of the core distribution for 0γ and 1γ . For the 2γ category, a DSCB function with a Gauss function on the left side of its distribution and a Gauss function on the right side of the DSCB distribution is employed.

9.3 Background descriptions

Background contributions that are not filtered out by the offline preselection (see Section 6.3) or the dedicated exclusive background requirements (see Section 6.4) need to be modelled in the invariant-mass fits. In the following, a description of the handling of combinatorial and *leakage* background is given, followed by an overview of the specific decays, which form the residual background components described in the fits. All background components are modelled with analytical functions or kernel density estimators (KDEs), both determining their shapes from simulation. As implementation for the KDEs, the `RooKeysPdf` class of the `ROOT` package [234] is employed to determine the PDFs.

Tables 9.1 to 9.3 describe the specific background components used for the B^+ mode fits and Tables 9.4 to 9.6 for the fits of the B^0 mode. The abbreviation ‘‘p.r.’’ indicates partially reconstructed decays, where inclusive simulation samples are used, e.g., $B \rightarrow XJ/\psi(\rightarrow ee)$ decays. These samples consist of a mixture of B^0, B^+, B_s^0 decays, with X indicating all allowed hadrons. Their content is combined, corresponding to the known branching fractions of the decays.

In the fits to the rare muon modes, only the combinatorial background has to be modelled. There are no significant other background components due to the purity of the muon reconstruction.

J/ψ candidate migration into rare- q^2 regions. For the electron modes, due to bremsstrahlung energy losses, candidates of a different q^2 region can ‘leak’ into another q^2 region. Due to energy losses, J/ψ mesons decaying to two electrons may significantly reduce the reconstructed dielectron mass. Due to the resulting dilution in their reconstructed invariant mass distributions, J/ψ decays can have a dielectron mass in the central- q^2 region. There is no leakage background for the muon decays because of their negligible amount of radiated bremsstrahlung.

Combinatorial background. The combinatorial background, i.e., background reconstructed from random tracks, is modelled with a single exponential function. Its shape is determined with same-sign data, e.g., for B^+ -meson decays with the reconstructed data set of $B^+ \rightarrow K^+\ell^+\ell^+$ and $B^+ \rightarrow K^-\ell^-\ell^-$ events. These decays are not allowed due to charge conservation, thus they are reconstructed with specific trigger requirements.

Table 9.1 – Specific background components for the fits to the resonant $B^+ \rightarrow K^+ J/\psi(\rightarrow \mu^+ \mu^-)$ and $B^+ \rightarrow K^+ \psi(2S)(\rightarrow \mu^+ \mu^-)$ decays.

Contribution	Description
J/ψ mode	
$B^+ \rightarrow \pi^+ J/\psi(\rightarrow \mu^+ \mu^-)$	Modelled with a DSCB with parameters determined from simulation.
P.r. $B \rightarrow XJ/\psi(\rightarrow \mu\mu)$	Modelled with a RooKeysPdf using inclusive simulation samples of $B^0, B^+,$ and B_s^0 decays.
$\psi(2S)$ mode	
P.r. $B \rightarrow X\psi(2S)(\rightarrow \mu\mu)$	Same as for p.r. $B \rightarrow XJ/\psi(\rightarrow \mu\mu)$.

Table 9.2 – Specific background components for the fits to the resonant $B^+ \rightarrow K^+ J/\psi(\rightarrow e^+e^-)$ and $B^+ \rightarrow K^+ \psi(2S)(\rightarrow e^+e^-)$ decays.

Contribution	Description
J/ψ mode	
$B^+ \rightarrow \pi^+ J/\psi(\rightarrow e^+e^-)$	Modelled with a DSCB with parameters from simulation of the decay.
P.r. $B \rightarrow X J/\psi(\rightarrow ee)$	Modelled with a RooKeysPdf using inclusive simulation samples of B^0 , B^+ , and B_s^0 decays.
$\psi(2S)$ mode	
P.r. $B \rightarrow X \psi(2S)(\rightarrow ee)$	Same as for p.r. $B \rightarrow X J/\psi(\rightarrow ee)$.
$B^+ \rightarrow K^+ J/\psi(\rightarrow e^+e^-)$ leakage	Modelled with a RooKeysPdf using simulation which passes the $\psi(2S)$ q^2 selection.
P.r. $B^+ \rightarrow K \psi(2S)(\rightarrow \pi^+ \pi^- J/\psi(\rightarrow e^+e^-))$	Modelled with a RooKeysPdf using simulation of the decay.

Table 9.3 – Specific background components for the fits to the rare $B^+ \rightarrow K^+ e^+ e^-$ decays.

Contribution	Description
P.r. $B^0 \rightarrow K^{*0} e^+ e^-$	Modelled with a RooKeysPdf using $B^0 \rightarrow K^{*0} e^+ e^-$ simulation.
P.r. $B^+ \rightarrow K^{*+} e^+ e^-$	Modelled with a RooKeysPdf using $B^+ \rightarrow K^{*+} e^+ e^-$ simulation.
P.r. $B^0 \rightarrow K^+ \pi^- e^+ e^-$	Modelled with a RooKeysPdf using $B^0 \rightarrow K^+ \pi^- e^+ e^-$ simulation.
P.r. $B^+ \rightarrow K^+ \pi^0 e^+ e^-$	Modelled with a RooKeysPdf using $B^+ \rightarrow K^+ \pi^0 e^+ e^-$ simulation..
central- q^2 region only	
$B^+ \rightarrow K^+ J/\psi(\rightarrow e^+e^-)$ leakage	Modelled using a RooKeysPdf using $B^+ \rightarrow K^+ J/\psi(\rightarrow e^+e^-)$ simulation passing the central- q^2 selection.
low- q^2 region only	
P.r. $B^+ \rightarrow K^+ \eta'(\rightarrow e e \gamma)$	Modelled using a RooKeysPdf using $B^+ \rightarrow K^+ \eta'(\rightarrow e e \gamma)$ simulation passing the low- q^2 selection.

Table 9.4 – Specific background components for the fits to the resonant $B^0 \rightarrow K^{*0} J/\psi(\rightarrow \mu^+ \mu^-)$ and $B^0 \rightarrow K^{*0} \psi(2S)(\rightarrow \mu^+ \mu^-)$ decays.

Contribution	Description
J/ψ mode	
$\Lambda_b^0 \rightarrow pKJ/\psi(\rightarrow \mu^+ \mu^-)$	Modelled with a RooKeysPdf using simulation of the decay.
$B_s^0 \rightarrow \phi(1020)J/\psi(\rightarrow \mu\mu)$	Modelled with a RooKeysPdf using simulation of the decay.
$K \leftrightarrow \pi$ swaps	Swaps in signal decays. Modelled with a RooKeysPdf based on the resonant mode simulation with truth-matched $K \leftrightarrow \pi$ events.
P.r. $B \rightarrow XJ/\psi(\rightarrow \mu\mu)$	Modelled with a RooKeysPdf using inclusive simulation samples of B^0 , B^+ , and B_s^0 decays.
$\psi(2S)$ mode	
$\Lambda_b^0 \rightarrow pK\psi(2S)(\rightarrow \mu^+ \mu^-)$	Modelled with a RooKeysPdf using simulation of the decay.
P.r. $B \rightarrow X\psi(2S)(\rightarrow \mu\mu)$	Same as for p.r. $B \rightarrow XJ/\psi(\rightarrow \mu\mu)$.

Table 9.5 – Specific background components for the fits to the resonant $B^0 \rightarrow K^{*0} J/\psi(\rightarrow e^+e^-)$ and $B^0 \rightarrow K^{*0} \psi(2S)(\rightarrow e^+e^-)$ decays.

Contribution	Description
J/ψ mode	
$\Lambda_b^0 \rightarrow pKJ/\psi(\rightarrow e^+e^-)$	Modelled with a RooKeysPdf using simulation.
$B_s^0 \rightarrow \phi(1020)J/\psi(\rightarrow ee)$	Modelled with a RooKeysPdf using simulation.
$K \leftrightarrow \pi$ swaps	Modelled with a RooKeysPdf.
P.r. $B \rightarrow XJ/\psi(\rightarrow ee)$	Modelled with a RooKeysPdf using inclusive simulation samples of B^0 , B^+ , and B_s^0 decays.
$\psi(2S)$ mode	
$\Lambda_b^0 \rightarrow pK\psi(2S)(\rightarrow e^+e^-)$	Same as for $\Lambda_b^0 \rightarrow pKJ/\psi(\rightarrow e^+e^-)$.
$K \leftrightarrow \pi$ swaps	Same as above for the J/ψ mode.
P.r. $B \rightarrow X\psi(2S)(\rightarrow ee)$	Modelled with $B^+ \rightarrow K\pi\pi(\psi(2S) \rightarrow ee)$ simulation.
$B^0 \rightarrow K^{*0} J/\psi(\rightarrow e^+e^-)$ leakage	Modelled with a RooKeysPdf using simulation passing the $\psi(2S)q^2$ selection.
P.r. $B^0 \rightarrow K^{*0} \psi(2S)(\rightarrow \pi^+\pi^- J/\psi(\rightarrow e^+e^-))$	Modelled with a RooKeysPdf using simulation.

Table 9.6 – Specific background components for the fits to the rare $B^0 \rightarrow K^{*0} e^+e^-$ decays.

Contribution	Description
P.r. $B^+ \rightarrow K\pi^+\pi^-e^+e^-$	Modelled with a RooKeysPdf using simulation containing decays of higher K^{*0} resonances.
central- q^2 region only	
$B^0 \rightarrow K^{*0} J/\psi(\rightarrow e^+e^-)$ leakage	Modelled with a RooKeysPdf using simulation passing the central- q^2 selection.

9.4 Extended maximum likelihood fits to LHCb collision data

Together with the modelling of the previously described background components, the fits to the collision data of the LHCb experiment are performed. For the final extraction of the results for R_K and R_{K^*0} , the decays through the J/ψ resonance as well as the rare decays in the low- and central- q^2 regions are simultaneously fitted in all trigger categories and years of data taking combined. Cross-checks to validate the compatibility of the results obtained in each of these categories are performed with separate fits. For example, the fits for the cross-check ratios $r_{J/\psi}$ and $R_{\psi(2S)}$ are conducted using the J/ψ ($\psi(2S)$)-mass constraints without simultaneously fitting the rare mode samples. Fig. 9.1 shows the simultaneous *nominal* fits for the entire 2011 - 2018 LHCb data set for the muon decay channels and Fig. 9.2 depicts them for the electron decay channels.

In addition to the *nominal* procedure, fits to the resonant J/ψ and $\psi(2S)$ modes are conducted using the $m(B)_{\text{DTF}}^{J/\psi, \psi(2S)}$ mass, for the cross-checks described in Chapter 11. These fits are performed simultaneously for both resonant q^2 regions, the electron and muon channels, and the B^0 and B^+ modes. Figs. A.17 and A.18 in the appendix show the results of the fits. The obtained numbers of signal candidates, called “fit yields”, are presented in Tables 9.7 and 9.8.

Table 9.7 – Fit yields for $B^+ \rightarrow K^+ J/\psi(\rightarrow \ell^+ \ell^-)$ and $B^+ \rightarrow K^+ \psi(2S)(\rightarrow \ell^+ \ell^-)$ decays using the $m(B)_{\text{DTF}}^{J/\psi, \psi(2S)}$ mass.

Sample	RUN 1	RUN 2P1	RUN 2P2
L0I trigger category			
$\mathcal{N}(B^+ \rightarrow K^+ J/\psi(\rightarrow e^+ e^-))$	68718 ± 287	90405 ± 326	174290 ± 457
$\mathcal{N}(B^+ \rightarrow K^+ J/\psi(\rightarrow \mu^+ \mu^-))$	198420 ± 451	20846 ± 463	396570 ± 638
$\mathcal{N}(B^+ \rightarrow K^+ \psi(2S)(\rightarrow e^+ e^-))$	4558 ± 87	6405 ± 96	11773 ± 135
$\mathcal{N}(B^+ \rightarrow K^+ \psi(2S)(\rightarrow \mu^+ \mu^-))$	15996 ± 128	16714 ± 131	31833 ± 181
L0L! trigger category			
$\mathcal{N}(B^+ \rightarrow K^+ J/\psi(\rightarrow e^+ e^-))$	74922 ± 301	107042 ± 362	205130 ± 504
$\mathcal{N}(B^+ \rightarrow K^+ J/\psi(\rightarrow \mu^+ \mu^-))$	556610 ± 755	521840 ± 732	1074800 ± 1050
$\mathcal{N}(B^+ \rightarrow K^+ \psi(2S)(\rightarrow e^+ e^-))$	6140 ± 96	8629 ± 111	16195 ± 150
$\mathcal{N}(B^+ \rightarrow K^+ \psi(2S)(\rightarrow \mu^+ \mu^-))$	47185 ± 220	44249 ± 213	90511 ± 305

Table 9.8 – Fit yields for the $B^0 \rightarrow K^{*0} J/\psi(\rightarrow \ell^+ \ell^-)$ and $B^0 \rightarrow K^{*0} \psi(2S)(\rightarrow \ell^+ \ell^-)$ decays using the $m(B)_{\text{DTF}}^{J/\psi, \psi(2S)}$ mass.

Sample	RUN 1	RUN 2P1	RUN 2P2
L0I trigger category			
$\mathcal{N}(B^0 \rightarrow K^{*0} J/\psi(\rightarrow e^+ e^-))$	24301 ± 207	31810 ± 229	60803 ± 319
$\mathcal{N}(B^0 \rightarrow K^{*0} J/\psi(\rightarrow \mu^+ \mu^-))$	65946 ± 261	72463 ± 273	138640 ± 378
$\mathcal{N}(B^0 \rightarrow K^{*0} \psi(2S)(\rightarrow e^+ e^-))$	1238 ± 48	1623 ± 55	3217 ± 75
$\mathcal{N}(B^0 \rightarrow K^{*0} \psi(2S)(\rightarrow \mu^+ \mu^-))$	4018 ± 64	4338 ± 67	8007 ± 91
L0L! trigger category			
$\mathcal{N}(B^0 \rightarrow K^{*0} J/\psi(\rightarrow e^+ e^-))$	26792 ± 201	37226 ± 239	70305 ± 328
$\mathcal{N}(B^0 \rightarrow K^{*0} J/\psi(\rightarrow \mu^+ \mu^-))$	172640 ± 425	169040 ± 417	349510 ± 601
$\mathcal{N}(B^0 \rightarrow K^{*0} \psi(2S)(\rightarrow e^+ e^-))$	1712 ± 54	2235 ± 63	4081 ± 81
$\mathcal{N}(B^0 \rightarrow K^{*0} \psi(2S)(\rightarrow \mu^+ \mu^-))$	10532 ± 104	10319 ± 103	21209 ± 148

9 Modelling of the invariant mass distributions

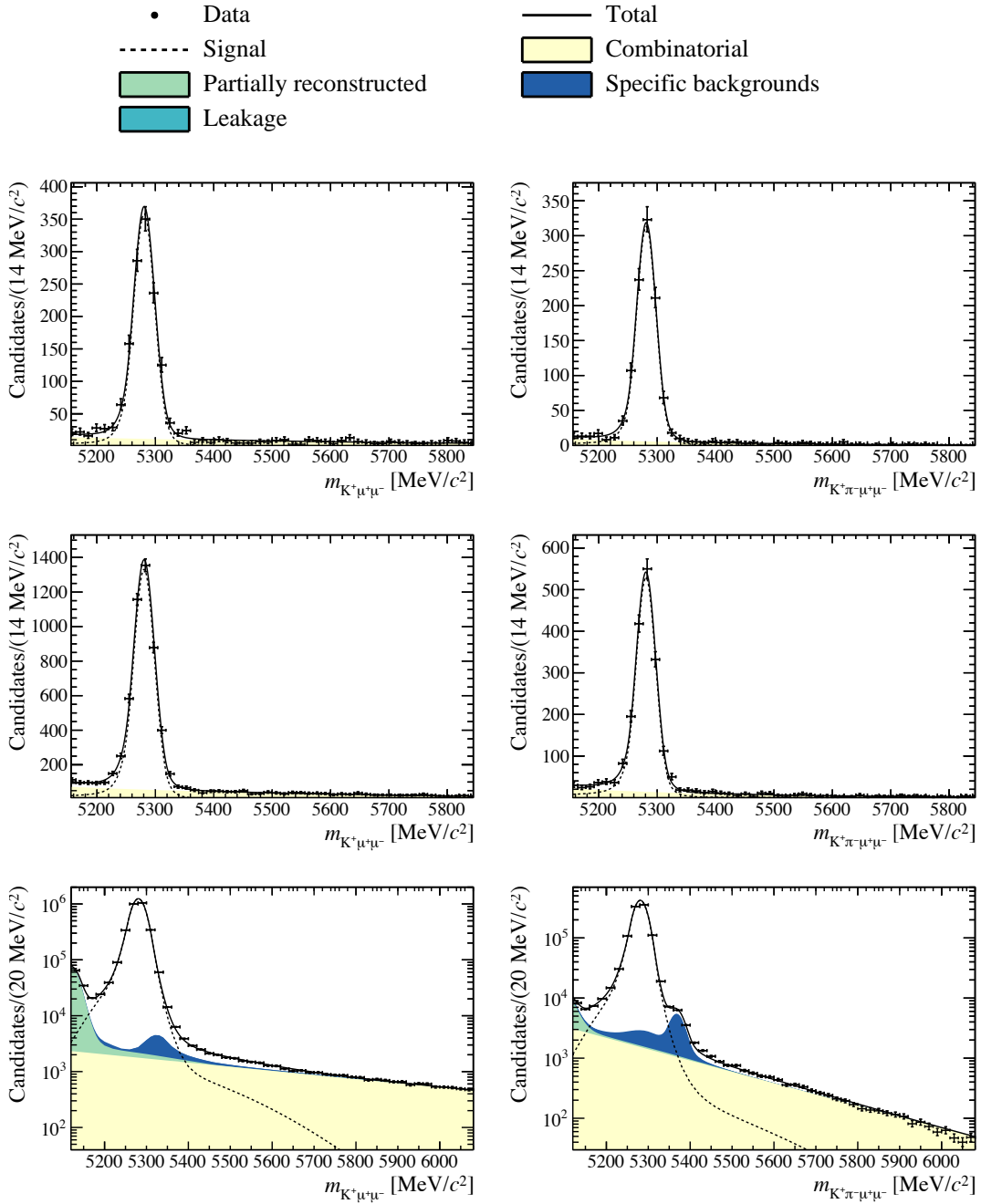


Figure 9.1 – Nominal fit to the signal and resonant J/ψ modes for the muon final states for all years of data taking. Shown are the (left) $B^+ \rightarrow K^+ \mu^+ \mu^-$ and (right) $B^0 \rightarrow K^{*0} \mu^+ \mu^-$ decays in the (from top to bottom) low-, central-, and J/ψ - q^2 regions. Fits reproduced from Ref.[209]

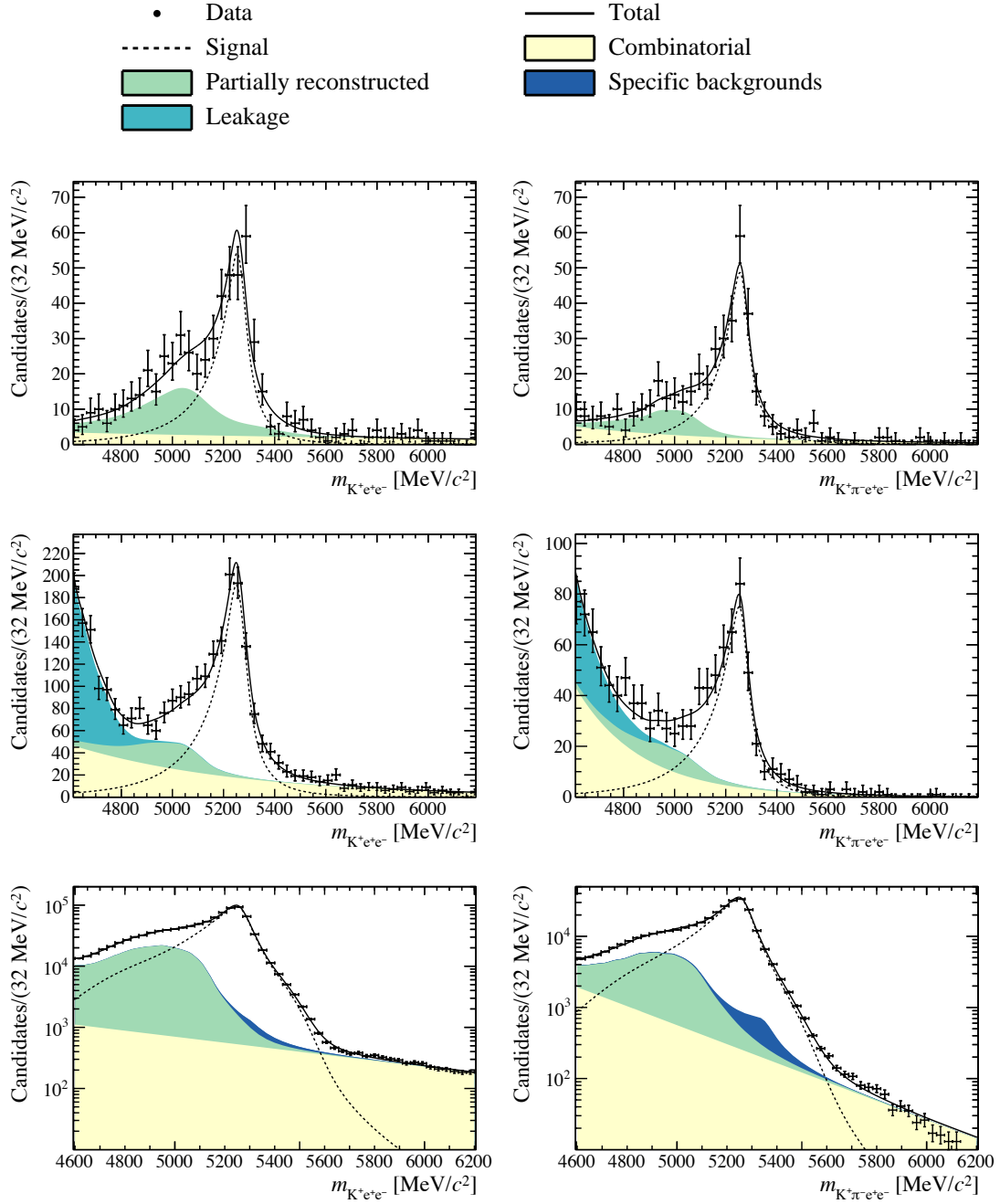


Figure 9.2 – Nominal fit to the signal and resonant J/ψ modes for the electron final states for all years of data taking. Shown are the (left) $B^+ \rightarrow K^+ e^+ e^-$ and (right) $B^0 \rightarrow K^{*0} e^+ e^-$ decays in the (from top to bottom) low-, central-, and J/ψ - q^2 regions. Fits reproduced from Ref.[209]

9.4.1 Fit sensitivities

As mentioned above, the fit to data can be run in two different modes, either extracting yields from the fits, or the ratios R_K and $R_{K^{*0}}$ are extracted directly by taking into account the efficiencies and correlations, indicated in the following by “ R_X fit”, which is the full simultaneous fit to both decay modes. To perform the R_X fit in a blind way and at the same time measure the expected sensitivities, independent randomised scale factors are applied to the efficiencies and correlations to keep them blind. Only for the partially reconstructed background $B^0 \rightarrow K^{*0} e^+ e^-$ for the measurement of R_K and the signal $B^0 \rightarrow K^{*0} e^+ e^-$ decay for the B^0 mode in the central- q^2 region, the efficiency scale factors are shared to allow for a consistent determination of the fit results. The sensitivity on R_K and $R_{K^{*0}}$ is defined as their uncertainty divided by their value. Table 9.9 shows a comparison of the sensitivities for the measurement of R_K and $R_{K^{*0}}$ with the extracted raw numbers of signal candidates in each analysis category. The uncertainties used stem from the uncertainties returned from the fit only, where the last column shows the expected sensitivity, including the efficiency uncertainties and correlations and the statistical error of the data sets used. The main limiting factor of the precision of the measurement of R_K and $R_{K^{*0}}$ is the number of electron candidates, as can be seen in the number of yields with their corresponding uncertainties. Chapter 12 provides a detailed interpretation and comparison of the sensitivities, including the results of the previously published measurements.

Table 9.9 – Results of simultaneous blind data fits to extract R_X . Shown are the rare decay mode yields $\mathcal{N}(\mu)$ and $\mathcal{N}(e)$ with corresponding sensitivities for R_K and R_{K^*0} split by trigger categories and run periods computed with raw yield numbers (simultaneous fit result). Also shown are the sensitivities (from left to right) merged by trigger categories or run periods. The last column shows the expected sensitivity for an overall simultaneous fit of all run periods and trigger categories.

Mode	q^2	Run period	L0	$\mathcal{N}(\mu)$	$\mathcal{N}(e)$	σ_{R_X}/R_X	σ_{R_X}/R_X	$\sigma_{R_X^{L0I}}/R_X^{L0I}$	$\sigma_{R_X^{L0L!}}/R_X^{L0L!}$	σ_{R_X}/R_X			
$B^+ \rightarrow K^+ \ell^+ \ell^-$	low	RUN 1	L0I	85 ± 11	34 ± 8	25.9(26.0)%	16.0%	12.2%	10.6%	8.0%			
			L0L!	238 ± 17	45 ± 8	19.4(19.6)%							
		RUN 2P1	L0I	88 ± 10	46 ± 9	23.5(23.6)%	15.9%						
			L0L!	230 ± 17	41 ± 8	21.4(21.6)%							
		RUN 2P2	L0I	169 ± 14	94 ± 14	17.0(17.0)%	11.3%						
			L0L	440 ± 23	85 ± 12	15.0(15.0)%							
	central	RUN 1	L0I	307 ± 20	155 ± 18	13.3(13.3)%	8.5%						
			L0L!	899 ± 33	151 ± 16	11.0(11.1)%							
		RUN 2P1	L0I	340 ± 21	163 ± 18	12.9(12.9)%	8.2%	6.8%	5.5%	4.3%			
			L0L!	831 ± 32	176 ± 17	10.5(10.6)%							
		RUN 2P2	L0I	681 ± 30	284 ± 26	10.0(10.0)%	6.2%						
			L0L!	1630 ± 45	319 ± 23	7.9(7.9)%							
$B^0 \rightarrow K^{*0} \ell^+ \ell^-$	low	RUN 1	L0I	84 ± 10	26 ± 7	28.6(28.7)%	18.3%				13.5%	11.3%	8.8%
			L0L!	171 ± 14	32 ± 7	22.9(23.1)%							
		RUN 2P1	L0I	100 ± 10	29 ± 8	30.4(30.5)%	19.1%						
			L0L!	152 ± 13	34 ± 8	23.9(24.1)%							
		RUN 2P2	L0I	154 ± 13	72 ± 11	17.7(17.8)%	11.7%						
			L0L!	340 ± 19	75 ± 11	15.3(15.4)%							
	central	RUN 1	L0I	114 ± 12	52 ± 10	22.3(22.4)%	14.9%						
			L0L!	266 ± 18	43 ± 8	19.8(19.9)%							
		RUN 2P1	L0I	155 ± 14	56 ± 11	20.7(20.8)%	13.5%	9.7%	8.8%	6.5%			
			L0L!	294 ± 19	62 ± 10	17.3(17.4)%							
		RUN 2P2	L0I	297 ± 19	139 ± 15	12.4(12.5)%	8.63%						
			L0L!	617 ± 27	127 ± 14	11.8(11.9)%							

10 Evaluation of systematic uncertainties

For the specific analysis approach presented in this thesis, systematic uncertainties arise due to either imperfections in the experimental methods to determine the signal efficiencies using calibrated simulation or the measurement of signal yields with invariant mass fits. Therefore, this thesis makes a distinction between three relevant classes of systematic uncertainties.

The first kind are uncertainties that affect the efficiency calculation, which is caused by the limited size of the calibration samples. To determine the resulting systematic uncertainties, the *resampling* procedure described in Section 8.2 is exploited. Although it is a *statistical* uncertainty of the calibration samples it systematically limits the precision of the calibration methods and thus represents a systematic uncertainty of the analysis.

The specific choice and configuration of the calibration procedures applied to the simulated samples is the origin of the second class of systematic uncertainties as explained in Section 10.1.

Third, the assumptions on the models used in the mass fits may also affect the final result. Here, the determination of the associated systematic uncertainties is described in Section 10.2, where pseudo experiments with varying fit setups are carried out and determine alternative values of R_K or R_{K^*0} .

The uncertainties regarding the last two sources are evaluated by using the method of the root of the variance from the nominal values R_{Nom} of R_K or R_{K^*0} . With that approach, alternative methods of with n different variations result in n alternative values R_i . The systematic uncertainty σ_R on the nominal result R_{Nom} , i.e., R_K or R_{K^*0} , is thus calculated as the root of the variance of these values with

$$\sigma_R = \sqrt{\frac{1}{n} \sum_{i=1}^n (R_i - R_{\text{Nom}})^2}. \quad (10.1)$$

Section 10.3 presents a summary of the systematic uncertainties described.

10.1 Uncertainties of the efficiencies

The systematic uncertainties corresponding to the efficiency computation can be divided into the statistical part relating to the finite size of the calibration samples and the methodological part corresponding to the choices of methods used in each calibration

step. In the following, only non-negligible sources of systematic uncertainties are listed, although many more studies were carried out.

Uncertainties due to limited calibrations samples. The uncertainties corresponding to the limited size of the resonant J/ψ calibration samples (see Section 5.3) are computed with the *resampling* approach. This method additionally allows for determining the correlations of these samples, which are used as normalisation channels and to extract the fit results. Here, 100 different resampled versions of each calibration map are created with random sets of Poisson weights with the mean value of one. These 100 different calibration maps per calibration step are then applied to the simulation samples. The uncertainties and correlations are evaluated from these weights in the final efficiency calculation and the final fits. The following list describes more details on this approach.

- For the B -meson kinematics, event multiplicity ($w_{\text{Mult\&Kin}}$) and reconstruction quality (w_{Reco}) calibrations (see Sections 7.4 and 7.6) are recalculated in 100 different variations. For this, each multivariate classifier used to reweight the variable distributions is trained with 100 different Poisson weights applied to the input samples. The computation includes the *resampling* weights of the previous calibration steps.
- For the $L0$ efficiency calibration (see Section 7.5.1), data and simulated samples are fitted for each assigned Poisson weight, resulting in a corresponding weight map.
- In the case of the HLT efficiency calibration (see Section 7.5.2) the same strategy as for the $L0$ calibration optimised for the HLT is used.
- For the PID calibration (see Section 7.2), the approach is not applicable because the calibration samples are separate from the measurement control mode samples. In this case, all PID weight maps are recomputed 100 times with Gaussian weights assigned to each bin in the calibration weight maps. The mean value of this Gauss function is set to the central value of the efficiency in each bin of the weight maps, and the width is defined as the statistical uncertainty of the efficiencies in each bin. Finally, the resulting 100 weight maps are propagated to the calibration chain, and the final computation of the systematic uncertainty is as explained for the other calibration steps.

Form factors in simulation. The signal simulation for the measurement of R_K and R_{K^*0} was generated using the hadronic form factor described in Ref.[236]. This form factor significantly influences the simulated q^2 spectrum and thus the efficiencies of the q^2 selection. To determine any associated systematic uncertainty, the effect of alternative form-factor models [237, 238] on the final results of this measurement is evaluated. Here, the systematic uncertainty $\sigma_{\text{Form factor}}$ is computed as

$$\sigma_{\text{Form factor}} = \frac{\frac{\epsilon_e^f}{\epsilon_\mu^f} - \frac{\epsilon_e^{\text{Nom}}}{\epsilon_\mu^{\text{Nom}}}}{\frac{\epsilon_e^{\text{Nom}}}{\epsilon_\mu^{\text{Nom}}}} \quad (10.2)$$

with ϵ_ℓ^f as the efficiency reweighted with the alternative form-factor model and $\epsilon_\ell^{\text{Nom}}$ as the nominal efficiency.

Bin migration calibration. To compute a systematic uncertainty for the approach to calibrate the q^2 spectrum (see Section 7.7), the mass model used to extract the calibration parameters is systematically varied. In addition, the calibration is applied separately for the trigger categories, and the calibration parameters are extracted as a function of the transverse momentum of the B meson $p_T(B)$ and the number of hits in the SPD detector `nSPDHits`.

PID efficiency calibration. For the PID efficiencies of electrons (see Section 7.2.3), systematic uncertainties concerning the choice of the binning schemes and residual effects of non-factorisation of the electrons are computed. The effect of alternative binning schemes together with the *fit-and-count* approach is evaluated by a systematic variation of the boundaries of the binning schemes in the transverse momentum and pseudorapidity dimensions. Additionally, the number of `nTracks` regions is alternated. Moreover, the difference between an interpolation and non-interpolation approach to assigning the PID weights is considered. Here, one approach is to interpolate the weights within the weight map. In contrast, the non-interpolation approach is only reading out single weight-map bins corresponding to the parametrisation given by the electron to calibrate.

Due to the more extensive size of the muon and hadron PID calibration samples and the fact that no *fit-and-count* approach has to be employed, it is possible to model such PID efficiencies with unbinned KDEs. Therefore, this KDE parametrisation is used as an alternative binning approach. The number of `nTracks` regions is systematically alternated with a similar to the electron PID calibration.

Kinematics and multiplicity calibration. For the calibration of the B kinematics and event multiplicity, in contrast to the nominal setup, `L0Muon TIS` samples are employed to extract the calibration weights. Additionally, a different multiplicity proxy is used. Compared to the overall number of tracks in the event `nTracks`, the number of tracks in the VELO `nVeloTracks` is employed.

Trigger efficiency calibration. For the calibration of the `L0` efficiencies, the dependency of the final result of the choice of the binning scheme used in the calibration is determined by using interpolated maps versus weight maps in bins. As a second source of systematic uncertainty, the claim that the `TIS` efficiencies computed with the muon calibration sample are applicable for the electron mode calibration is tested. For that reason, the `TIS` efficiencies are calculated based on an electron calibration sample

and are compared to the nominal results. As a third factor of systematic uncertainty, the effect of the factorisation of L0 trigger efficiencies is determined. Here, a direct computation of the dielectron efficiencies is compared with a separate calculation per track employed in the nominal calibration chain. The systematic uncertainties corresponding to these methodological changes are measured as the discrepancies of the resulting double ratios R_K and R_{K^*0} .

For the calibration of the HLT efficiencies, the parametrising variable of the transverse momentum of the B meson with an altered binning scheme is used to determine the systematic uncertainty corresponding to the original choice of the nTracks variable and the original binning scheme.

Differential $r_{J/\psi}$. As one of the main cross-checks of the measurement of R_K and R_{K^*0} , the single ratios $r_{J/\psi}^K$ and $r_{J/\psi}^{K^*0}$ (see Eqs. (5.5) and (5.6)) are computed. Their compatibility with unity indicates a proper calibration of the simulation. In addition to the integrated ratios, these cross-checks are evaluated differentially in regions of the main analysis observables. Chapter 11 presents the cross-checks in more detail. The parameter d_f is a metric of any residual deficiencies of the calibration procedure and is defined in Eq. (11.1).

It turns out that the parameter d_f points to deviations in two variable distributions: the dilepton opening angle θ_ℓ and the dilepton impact parameter. Because the value of d_f for the dilepton opening angle is always greater than the value for the impact parameter, it is used as a systematic uncertainty as described in Section 10.1.

HOP mass calibration. In the nominal measurement approach, the selection requirement on the $m(K^{(*)}\ell\ell)_{\text{HOP}}$ mass (see Section 6.5.2) is applied on the rare signal modes for electron decays only. To compute a corresponding systematic uncertainty, this selection criterion is calculated on the resonant normalisation channels. The difference of the resulting double ratios R_K and R_{K^*0} compared to the nominal results is used as a systematic uncertainty.

10.2 Uncertainties of the mass fits

The following section gives a short overview of the systematic uncertainties related to the mass fits. Large numbers of pseudo experiments are performed with variations on the fit setup. For that, a pseudo-experiment generator was developed, which uses the converged *nominal* data fit models as a generator seed. The generator produces individual signal and background components and stores them to nTuples. With this approach, peculiar combinations of the components can be chosen for each systematic uncertainty study. On these generator “truth” datasets, two fits are performed. They use first the nominal fit model and second an alternative fit model. These two fits result in two sets of fit parameters. Where not stated differently, these fits are performed 1000 times with the respective alternative parameters of the alternative model varied within a given range, for example, the uncertainty of the parameter value from the

nominal fit. For each iteration of the pseudo experiments, the nominal fit result is compared with the fit result of the variations tested. The distribution of the differences in the resulting parameters is modelled with a Gauss function. The squared sum of this function's mean value and width is taken as the corresponding systematic uncertainty of the respective variation. Relevant studies of systematic uncertainties due to the fit procedure are described in the following.

Resonant fit model and partially reconstructed background. The fit modelling of the resonant J/ψ decay channels depends significantly on the description of the partially reconstructed backgrounds (see Section 9.3). This is particularly important because modelling the rare signal decays in the simultaneous fit is directly correlated with that of the resonant decays. The systematic uncertainty associated with the modelling of the J/ψ fit is evaluated by four description variations. First, the J/ψ fits for the measurement of R_K and R_{K^*0} are performed without the DTF constraints on the invariant dilepton mass; second, in addition to this change, contributions from the partially reconstructed background are minimised by setting an additional constraint on the invariant mass of the B mesons of $m_B > 5200 \text{ MeV}/c^2$. Third, independent fits to the resonant decays, with the J/ψ DTF mass constraint as described in Chapter 9, are performed and fourth, for these fits, the lower limit of the electron channel fit range is extended to $4650 \text{ MeV}/c^2$ to investigate the effects of the partially reconstructed background.

Fit parameters. To study the impact of fit parameters, fixed parameters in the nominal fit are varied within their uncertainties in pseudo experiments. Additionally, the fraction of signal candidates per bremsstrahlung category is systematically varied within their uncertainties for the rare and resonant modes separately. Consequently, a systematic uncertainty is computed from the differences in the resulting values for R_K and R_{K^*0} compared to the nominal results. Of the two studies with the rare and resonant channel, the larger difference is used as the systematic uncertainty in each case.

Combinatorial background. The combinatorial background is modelled as an exponential function with its parameters determined with same-sign data as described in Section 9.3. To compute a corresponding systematic uncertainty, these parameters are varied within their uncertainties in pseudo experiments.

Description of specific backgrounds. The relative fractions of the $B \rightarrow K\pi\ell^+\ell^-$ decays (see Section 9.3) of the $B^+ \rightarrow K^+e^+e^-$ signal are varied within their uncertainties in pseudo experiments. The resulting differences in the extracted values for R_K and R_{K^*0} are assigned as a systematic uncertainty.

For the double mis-identified background components $B^+ \rightarrow K^+\pi^+\pi^-$ and $B^0 \rightarrow K^{*0}\pi^+\pi^-$ the mis-identification rates are determined with fits to a control dataset where the pion mass hypothesis is assigned to the leptons. For the muon channels, this background contribution is found to be negligible. In contrast, a systematic uncertainty

is set as the ratio of the expected background yields and the measured signal yield on the electron channels.

10.3 Overall systematic uncertainties

Table 10.1 lists all corresponding systematic uncertainties for the measurements of R_K and R_{K^*0} in the low- and central- q^2 regions.

Table 10.1 – Systematic uncertainties for the measurements of R_K and R_{K^*0} in the low- and central- q^2 regions with values in percent relative to the central values of the measurements.

Source	low q^2 R_K	central q^2 R_K	low q^2 R_{K^*0}	central q^2 R_{K^*0}
Simulation form factors	0.09	0.08	0.83	0.76
Bin migration calibration	0.30	0.19	0.28	0.31
PID efficiency calibration	0.17	0.22	0.10	0.12
Kinematics and multiplicity calibration	0.35	0.26	0.57	0.52
Trigger efficiency calibration	0.27	0.16	0.26	0.13
Differential $r_{J/\psi}$	0.78	0.38	1.79	0.47
HOP mass calibration	0.25	0.24	0.33	0.33
Resonant fit model	0.35	0.35	0.40	0.40
Fit parameters	0.14	0.07	0.25	0.16
Combinatorial background	1.86	0.23	1.86	0.58
Part. reco. background for rare mode fits	0.24	0.20	1.24	0.51
Double mis-identified background	1.50	0.30	0.80	0.40
Total	2.63	0.83	3.22	1.57

11 Cross-checks

As explained in Section 5.1, the measurement of R_K and R_{K^*0} is performed as a double ratio of the rare and resonant J/ψ decay modes. As a stringent cross-check to test the measurement strategy with the efficiency calibration and the fit procedure, the single ratios $r_{J/\psi}^K$ and $r_{J/\psi}^{K^*0}$ as defined in Eqs. (5.5) and (5.6) are evaluated. For these single ratios, the expected value is unity in the SM and is experimentally validated as reported in Eq. (2.5). The single-ratio computation is sensitive to residual imperfections of either the efficiency calibration or the mass fits because in comparison to the double ratios systematic uncertainties do not largely cancel out. Section 11.1 shows the results of this cross-check.

As a second cross-check, the double ratios $R_{\psi(2S)}^K$ and $R_{\psi(2S)}^{K^*0}$ as described in Eqs. (5.7) and (5.8) as a double ratio of the resonant J/ψ and $\psi(2S)$ modes are evaluated. This test validates that residual inaccuracies of the measurement procedure indeed cancel out in the double ratios. In addition, it represents a closure test of the portability of the calibration weights to different q^2 regions because the J/ψ mode based calibration is applied on the $\psi(2S)$ modes and therefore a different q^2 region. Section 11.2 presents the results of this double-ratio cross-check.

The third cross-check is similar to the measurement of $r_{J/\psi}$, but is performed differentially as a function of the most relevant kinematic and topological observables, track reconstruction qualities, and event multiplicity proxies. Compared to the integrated measurement of $r_{J/\psi}$, this additional test is more stringent because possible discrepancies from unity that would be diluted in the integrated value can become visible. Section 11.3 shows the corresponding results, which are partially used in the determination of the systematic uncertainties related to residual imperfections of the analysis procedure described in Chapter 10.

The last cross-check presented in this chapter is a study of the dependency of the final efficiency ratios of the calibration steps. Section 11.4 presents the final efficiency ratios as inputs to the measurement of R_K and R_{K^*0} in the low- and central- q^2 regions as a function of the calibration steps. To keep the measurement blind, only the relative deviations in comparison to the efficiency double ratio computed without efficiency calibration applied are shown.

Additionally, the compatibility of the efficiency calibrations based on either B^+ or B^0 calibration samples is evaluated for all cross-checks.

The uncertainties of the cross-check results arise from the statistical uncertainties of the mass fits extracted as explained in Section 9.4 and the systematic uncertainties evaluated with the *resampling* approach for the efficiencies as described in Section 10.1.

11.1 Integrated single ratio $r_{J/\psi}$

For the measurement of the integrated single ratio $r_{J/\psi}$, the J/ψ -decay mass fits in the B^+ and B^0 modes as described in Chapter 9 are performed independently for the different modes, years, and trigger categories. This approach makes it possible to be sensitive to potential issues within single years or measurement categories. Fully corrected simulation samples (see Chapter 7) are used to extract the resonant mode efficiencies as described in Chapter 8. For this extraction, the corrections based on both the B^+ and B^0 calibration samples are compared for each value of $r_{J/\psi}^K$ and $r_{J/\psi}^{K^*0}$. However, the calibrations are only used in the swapped combination of the final measurement. So with this further test, the portability of the calibrations is evaluated. Following the strategy of this analysis (see Chapter 5) the ratios $r_{J/\psi}$ are computed as ratios of the muon and electron modes with the L0I muon and L0I electron samples for the L0I trigger category and the exclusive L0M! and L0E! samples for the L0L! trigger category, respectively. As inputs the corresponding resonant fit yields can be seen in Tables 9.7 and 9.8 and the resonant efficiencies in Section 8.3. Tables 11.1 and 11.2 show the resulting values for $r_{J/\psi}$ in the two trigger categories of the measurement for the three run periods. Additionally, the tables include a comparison between the results extracted without applying any calibration and with the full calibration procedure applied. These two cases are indicated by $w_{\text{No calibration}}$ and w_{Full} . The three uncertainties listed are the statistical uncertainty from the mass fits on data, the statistical uncertainty of the efficiencies based on the size of the calibration samples, and the systematic uncertainty of the simulation corrections based on the *resampling* approach, which is only available for w_{Full} . It shows that the $r_{J/\psi}$ results are compatible with unity and within the trigger categories and data-taking periods when including the calibration. Also, the values computed based on the B^+ or B^0 calibration chain prove compatible, showing the portability of the calibration weights.

Furthermore, Figs. 11.1 and 11.2 present the ratios as function of the different intermediate calibration steps, starting with no calibrations applied. The uncertainties given are the squared sum of the three uncertainties shown in Tables 11.1 and 11.2. When no efficiency calibration is applied, the values for $r_{J/\psi}$ are not compatible with unity. But the sequential addition of calibration steps decreases the deviation.

11.2 Integrated double ratio $R_{\psi(2S)}$

In contrast to the stepwise check for the $r_{J/\psi}$ single ratio Figs. 11.3 and 11.4 show that the result for $R_{\psi(2S)}$ is consistent with unity even without efficiency calibration. The sequential application of the calibration steps leaves this fact untouched. Thus, the claim that imperfections of the efficiency calibration procedure of the measurement cancel out well in the double ratios is validated.

Table 11.1 – Integrated single ratios $r_{J\psi}^K$ for different data-taking periods and trigger categories. The results are computed with no calibration applied or the full calibration procedure applied on simulation. The weights based on the B^+ or B^0 calibration samples are compared for the calibration. The three uncertainties listed are the statistical uncertainty from the mass fits on data, the statistical uncertainty of the efficiencies based on the size of the calibration samples, and the systematic uncertainty of the simulation corrections based on the *resampling* approach.

Type	$w_{\text{No calibration}}$	w_{Full}
RUN 1 L0I $w(B^+)$	$1.146 \pm 0.005 \pm 0.003$	$1.063 \pm 0.005 \pm 0.003 \pm 0.015$
RUN 1 L0I $w(B^0)$	$1.146 \pm 0.005 \pm 0.003$	$1.054 \pm 0.005 \pm 0.003 \pm 0.028$
RUN 1 L0L! $w(B^+)$	$1.299 \pm 0.005 \pm 0.003$	$1.020 \pm 0.004 \pm 0.003 \pm 0.017$
RUN 1 L0L! $w(B^0)$	$1.299 \pm 0.005 \pm 0.003$	$1.053 \pm 0.004 \pm 0.003 \pm 0.025$
RUN 2P1 L0I $w(B^+)$	$1.131 \pm 0.005 \pm 0.003$	$1.010 \pm 0.004 \pm 0.003 \pm 0.009$
RUN 2P1 L0I $w(B^0)$	$1.131 \pm 0.005 \pm 0.003$	$1.033 \pm 0.004 \pm 0.003 \pm 0.019$
RUN 2P1 L0L! $w(B^+)$	$1.392 \pm 0.005 \pm 0.003$	$1.035 \pm 0.004 \pm 0.003 \pm 0.010$
RUN 2P1 L0L! $w(B^0)$	$1.392 \pm 0.005 \pm 0.003$	$1.046 \pm 0.004 \pm 0.003 \pm 0.012$
RUN 2P2 L0I $w(B^+)$	$1.117 \pm 0.003 \pm 0.003$	$1.012 \pm 0.003 \pm 0.003 \pm 0.007$
RUN 2P2 L0I $w(B^0)$	$1.117 \pm 0.003 \pm 0.003$	$1.016 \pm 0.003 \pm 0.003 \pm 0.012$
RUN 2P2 L0L! $w(B^+)$	$1.412 \pm 0.004 \pm 0.003$	$1.014 \pm 0.003 \pm 0.003 \pm 0.006$
RUN 2P2 L0L! $w(B^0)$	$1.412 \pm 0.004 \pm 0.003$	$0.993 \pm 0.003 \pm 0.003 \pm 0.007$

11.3 Differential single ratio $r_{J\psi}$

As a third main cross-check of the measurement, the ratios $r_{J\psi}$ are computed differentially as functions of a set of main variables used in the data analysis. This check is sensitive to possible residual imperfections of the efficiency calibration and mass fit procedure. These imperfections could be diluted in the integrated measurement of $r_{J\psi}$.

For the differential measurement, a binning scheme is determined so that each of the bins roughly contains a similar number of candidates. Because the number of candidates of the electron modes is generally lower than in the muon modes, a statistical weight is assigned to the electron mode bins. This statistical weight mitigates the differences induced by the particular datasets.

Table 11.2 – Integrated single ratios $r_{J/\psi}^{K^*0}$ for different data-taking periods and trigger categories. The results are computed with no calibration applied or with the full calibration procedure applied on simulation. The weights based on the B^+ or B^0 calibration samples are compared for the calibration. The three uncertainties listed are the statistical uncertainty from the mass fits on data, the statistical uncertainty of the efficiencies based on the size of the calibration samples, and the systematic uncertainty of the simulation corrections based on the *resampling* approach.

Type	$w_{\text{No calibration}}$	w_{Full}
RUN 1 L0I $w(B^+)$	$1.116 \pm 0.010 \pm 0.004$	$1.046 \pm 0.010 \pm 0.004 \pm 0.016$
RUN 1 L0I $w(B^0)$	$1.116 \pm 0.010 \pm 0.004$	$1.038 \pm 0.010 \pm 0.004 \pm 0.027$
RUN 1 L0L! $w(B^+)$	$1.280 \pm 0.010 \pm 0.004$	$1.033 \pm 0.008 \pm 0.004 \pm 0.018$
RUN 1 L0L! $w(B^0)$	$1.280 \pm 0.010 \pm 0.004$	$1.065 \pm 0.008 \pm 0.004 \pm 0.025$
RUN 2P1 L0I $w(B^+)$	$1.120 \pm 0.009 \pm 0.004$	$1.003 \pm 0.008 \pm 0.004 \pm 0.010$
RUN 2P1 L0I $w(B^0)$	$1.120 \pm 0.009 \pm 0.004$	$1.028 \pm 0.008 \pm 0.004 \pm 0.018$
RUN 2P1 L0L! $w(B^+)$	$1.352 \pm 0.009 \pm 0.005$	$1.022 \pm 0.007 \pm 0.005 \pm 0.010$
RUN 2P1 L0L! $w(B^0)$	$1.352 \pm 0.009 \pm 0.005$	$1.033 \pm 0.007 \pm 0.005 \pm 0.012$
RUN 2P2 L0I $w(B^+)$	$1.115 \pm 0.007 \pm 0.005$	$1.011 \pm 0.006 \pm 0.005 \pm 0.007$
RUN 2P2 L0I $w(B^0)$	$1.115 \pm 0.007 \pm 0.005$	$1.016 \pm 0.006 \pm 0.005 \pm 0.011$
RUN 2P2 L0L! $w(B^+)$	$1.382 \pm 0.007 \pm 0.006$	$1.009 \pm 0.005 \pm 0.006 \pm 0.004$
RUN 2P2 L0L! $w(B^0)$	$1.382 \pm 0.007 \pm 0.006$	$0.990 \pm 0.005 \pm 0.006 \pm 0.006$

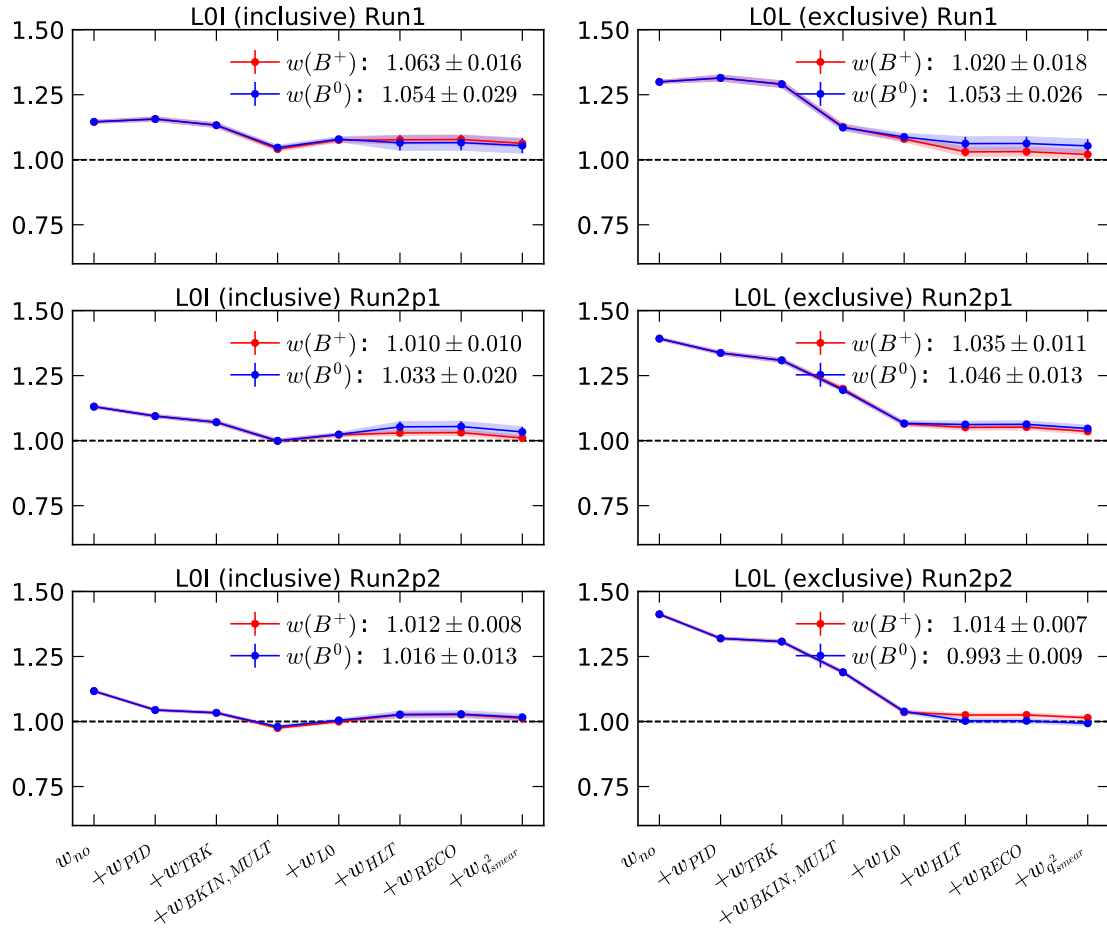


Figure 11.1 – Integrated single ratio $r_{J/\psi}^K$ for different data-taking periods and trigger categories as a function of the calibration steps (see Chapter 7). Shown are the results computed based on the (red) B^+ or (blue) B^0 calibrations. The uncertainty given is the squared sum of the three uncertainties reported in Table 11.1.

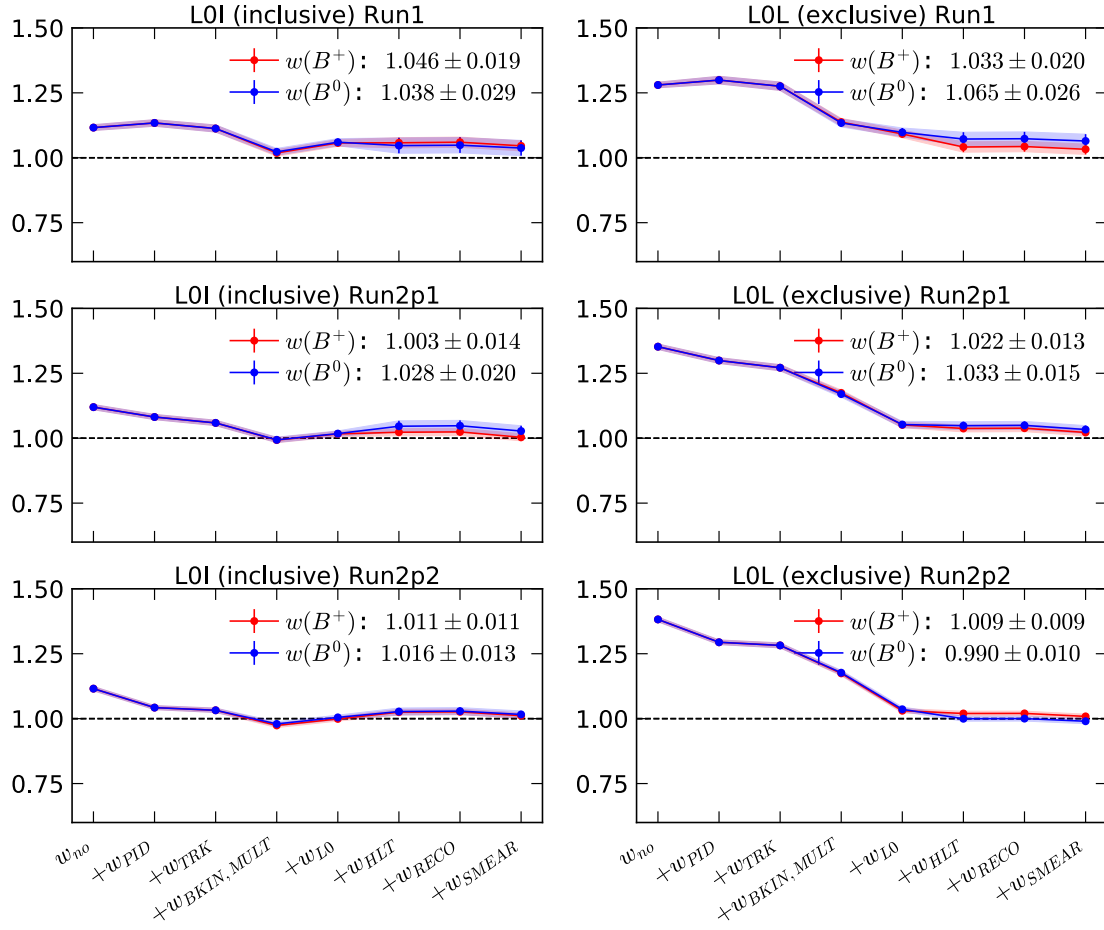


Figure 11.2 – Integrated single ratio $r_{J/\psi}^{K^*0}$ for different data-taking periods and trigger categories as a function of the calibration steps (see Chapter 7). Shown are the results computed based on the (red) B^+ or (blue) B^0 calibrations. The uncertainty given is the squared sum of the three uncertainties reported in Table 11.2.

Table 11.3 – Integrated double ratios $R_{\psi(2S)}^K$ for different data-taking periods and trigger categories. The results are computed with no calibration applied or the full calibration procedure applied on simulation. The weights based on the B^+ or B^0 calibration samples are compared for the calibration. The three uncertainties listed are the statistical uncertainty on the fitted signal yields in data, the statistical uncertainty of the efficiencies based on the size of the signal simulation samples, and the systematic uncertainty of the simulation calibration based on the *resampling* approach.

Type	$w_{\text{No calibration}}$	w_{Full}
RUN 1 L0I $w(B^+)$	$1.010 \pm 0.021 \pm 0.005$	$0.993 \pm 0.021 \pm 0.005 \pm 0.001$
RUN 1 L0I $w(B^0)$	$1.010 \pm 0.021 \pm 0.005$	$0.996 \pm 0.021 \pm 0.005 \pm 0.001$
RUN 1 L0L! $w(B^+)$	$0.993 \pm 0.017 \pm 0.004$	$0.979 \pm 0.016 \pm 0.004 \pm 0.002$
RUN 1 L0L! $w(B^0)$	$0.993 \pm 0.017 \pm 0.004$	$0.982 \pm 0.016 \pm 0.004 \pm 0.003$
RUN 2P1 L0I $w(B^+)$	$0.976 \pm 0.017 \pm 0.004$	$0.945 \pm 0.017 \pm 0.004 \pm 0.001$
RUN 2P1 L0I $w(B^0)$	$0.976 \pm 0.017 \pm 0.004$	$0.947 \pm 0.017 \pm 0.004 \pm 0.001$
RUN 2P1 L0L! $w(B^+)$	$0.985 \pm 0.014 \pm 0.003$	$0.986 \pm 0.014 \pm 0.003 \pm 0.003$
RUN 2P1 L0L! $w(B^0)$	$0.985 \pm 0.014 \pm 0.003$	$0.987 \pm 0.014 \pm 0.003 \pm 0.003$
RUN 2P2 L0I $w(B^+)$	$1.015 \pm 0.013 \pm 0.004$	$0.992 \pm 0.013 \pm 0.004 \pm 0.001$
RUN 2P2 L0I $w(B^0)$	$1.015 \pm 0.013 \pm 0.004$	$0.994 \pm 0.013 \pm 0.004 \pm 0.001$
RUN 2P2 L0L! $w(B^+)$	$1.005 \pm 0.010 \pm 0.003$	$0.999 \pm 0.010 \pm 0.003 \pm 0.002$
RUN 2P2 L0L! $w(B^0)$	$1.005 \pm 0.010 \pm 0.003$	$1.000 \pm 0.010 \pm 0.003 \pm 0.002$

Table 11.4 – Integrated double ratios $R_{\psi(2S)}^{K^*0}$ for different data-taking periods and trigger categories. The results are computed with no calibration applied or the full calibration procedure applied on simulation. The weights based on the B^+ or B^0 calibration samples are compared for the calibration. The three uncertainties listed are the statistical uncertainty from the mass fits on data, the statistical uncertainty of the efficiencies based on the size of the calibration samples, and the systematic uncertainty of the simulation corrections based on the *resampling* approach.

Sample	$w_{\text{No calibration}}$	w_{Full}
RUN 1 L0I $w(B^+)$	$1.065 \pm 0.045 \pm 0.009$	$1.051 \pm 0.044 \pm 0.009 \pm 0.002$
RUN 1 L0I $w(B^0)$	$1.065 \pm 0.045 \pm 0.009$	$1.053 \pm 0.044 \pm 0.009 \pm 0.002$
RUN 1 L0L! $w(B^+)$	$1.005 \pm 0.034 \pm 0.007$	$0.988 \pm 0.033 \pm 0.007 \pm 0.002$
RUN 1 L0L! $w(B^0)$	$1.005 \pm 0.034 \pm 0.007$	$0.990 \pm 0.033 \pm 0.007 \pm 0.004$
RUN 2P1 L0I $w(B^+)$	$1.057 \pm 0.040 \pm 0.008$	$1.030 \pm 0.039 \pm 0.008 \pm 0.002$
RUN 2P1 L0I $w(B^0)$	$1.057 \pm 0.040 \pm 0.008$	$1.032 \pm 0.039 \pm 0.008 \pm 0.002$
RUN 2P1 L0L! $w(B^+)$	$0.987 \pm 0.029 \pm 0.006$	$0.991 \pm 0.029 \pm 0.006 \pm 0.004$
RUN 2P1 L0L! $w(B^0)$	$0.987 \pm 0.029 \pm 0.006$	$0.993 \pm 0.029 \pm 0.006 \pm 0.005$
RUN 2P2 L0I $w(B^+)$	$0.967 \pm 0.026 \pm 0.006$	$0.954 \pm 0.025 \pm 0.006 \pm 0.001$
RUN 2P2 L0I $w(B^0)$	$0.967 \pm 0.026 \pm 0.006$	$0.956 \pm 0.025 \pm 0.006 \pm 0.001$
RUN 2P2 L0L! $w(B^+)$	$1.057 \pm 0.023 \pm 0.006$	$1.059 \pm 0.023 \pm 0.006 \pm 0.002$
RUN 2P2 L0L! $w(B^0)$	$1.057 \pm 0.023 \pm 0.006$	$1.060 \pm 0.023 \pm 0.006 \pm 0.002$

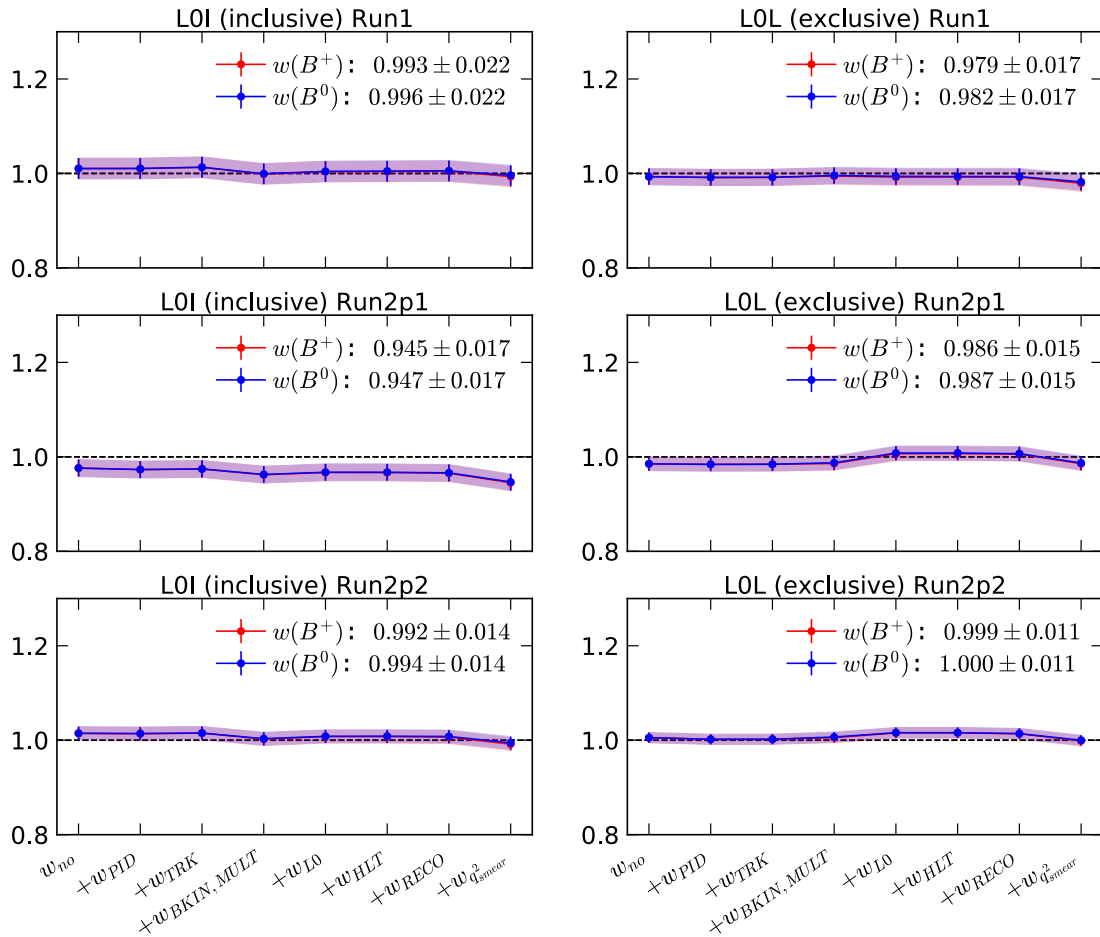


Figure 11.3 – Integrated double ratio $R_{\psi(2S)}^K$ for different data-taking periods and trigger categories as a function of the calibration steps (see Chapter 7). Shown are the results computed based on the (red) B^+ or (blue) B^0 calibrations. The uncertainty given is the squared sum of the three uncertainties reported in Table 11.3

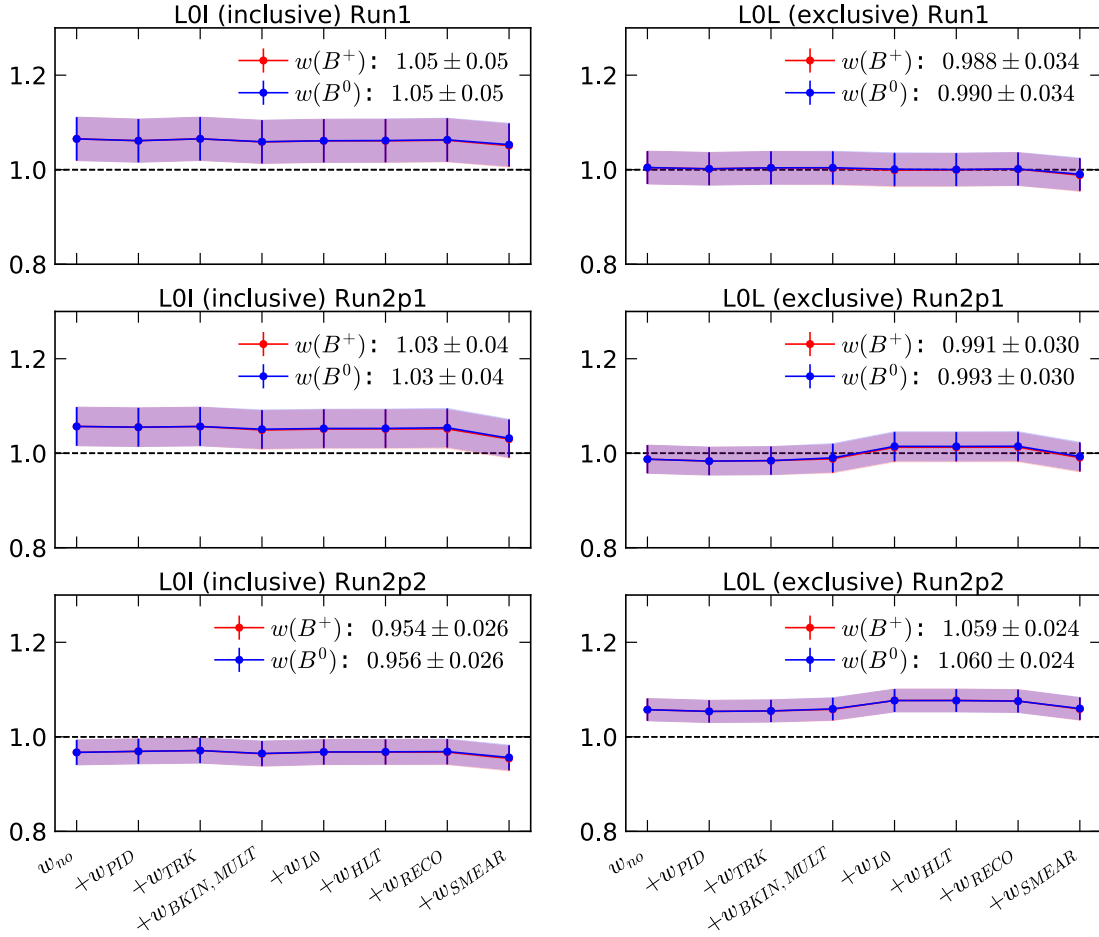


Figure 11.4 – Integrated double ratio $R_{\psi(2S)}^{K^*0}$ for different data-taking periods and trigger categories as a function of the calibration steps (see Chapter 7). Shown are the results computed based on the (red) B^+ or (blue) B^0 calibrations. The uncertainty given is the squared sum of the three uncertainties reported in Table 11.4

The variables used in the differential measurements are kinematic properties of the decay particles and event multiplicity proxies as well as fit quality variables. Under the assumption of a perfect calibration and modelling of the invariant mass distributions of the signal decays, the resulting $r_{J/\psi}$ distributions are expected to only vary around unity within their statistical uncertainty. Possible discrepancies can be quantified by the parameter d_f which accounts for deviations from unity over the full spectrum of the differential measurement with

$$d_f = \frac{\sum_i^8 \epsilon_{\text{rare},\mu}^i \cdot \mathcal{Y}_\mu^i}{\sum_i^8 \epsilon_{\text{rare},\mu}^i} \cdot \frac{\sum_i^8 \epsilon_{J/\psi,\mu}^i}{\sum_i^8 N_\mu^i} \bigg/ \frac{\sum_i^8 \epsilon_{\text{rare},e}^i \cdot \mathcal{Y}_e^i}{\sum_i^8 \epsilon_{\text{rare},e}^i} \cdot \frac{\sum_i^8 \epsilon_{J/\psi,e}^i}{\sum_i^8 N_e^i} - 1, \quad (11.1)$$

with $\epsilon_{J/\psi,\ell}^i$ as the control mode efficiency in the i_{th} bin and N_ℓ^i as the corresponding yield. \mathcal{Y}_ℓ^i indicates the efficiency corrected yields of the control channel and is defined as

$$\mathcal{Y}_\ell^i = \frac{N_\ell^i}{\epsilon_{J/\psi,\ell}^i}. \quad (11.2)$$

The rare mode yields are substituted with the product of the rare efficiency in bin i and the efficiency corrected control mode yields as $\epsilon_{\text{rare},\ell}^i \cdot \mathcal{Y}_\ell^i$. With this definition, the parameter d_f is expected to be zero.

The cross-check shows that d_f for all variables, except the dilepton opening angle of the electrons and the impact parameter, are compatible with zero. For the residual discrepancies in these two variables, a systematic uncertainty is assigned as described in Section 10.1.

11.4 Calibration dependency of the efficiency ratios

For this check the efficiency double ratios which are input to the R_K and $R_{K^{*0}}$ measurement are computed as

$$\frac{\epsilon_{B \rightarrow K^{(*)} e^+ e^-} \cdot \epsilon_{B \rightarrow K^{(*)} J/\psi (\rightarrow \mu^+ \mu^-)}}{\epsilon_{B \rightarrow K^{(*)} \mu^+ \mu^-} \cdot \epsilon_{B \rightarrow K^{(*)} J/\psi (\rightarrow e^+ e^-)}}.$$

The 100 versions of the *resampled* efficiencies are taken into account and as the resulting values the mean and uncertainties are extracted. The uncertainties computed account for the statistic uncertainties of the simulation samples and the *resampling* uncertainties originating from the calibration procedure. Fig. 11.5 and Figs. A.19 to A.21 present the corresponding stepwise evolution of the efficiency variations for all run periods and trigger categories. It is found that the variations are well compatible between the B^+ and B^0 calibration chains. This behaviour shows that possible systematic uncertainties related to the calibration chain approach largely cancel out in the double-ratio approach. In addition, it can be seen that for the double-ratios the effect of the calibration procedure is much less dramatic compared to the single ratios as presented in Section 11.1.

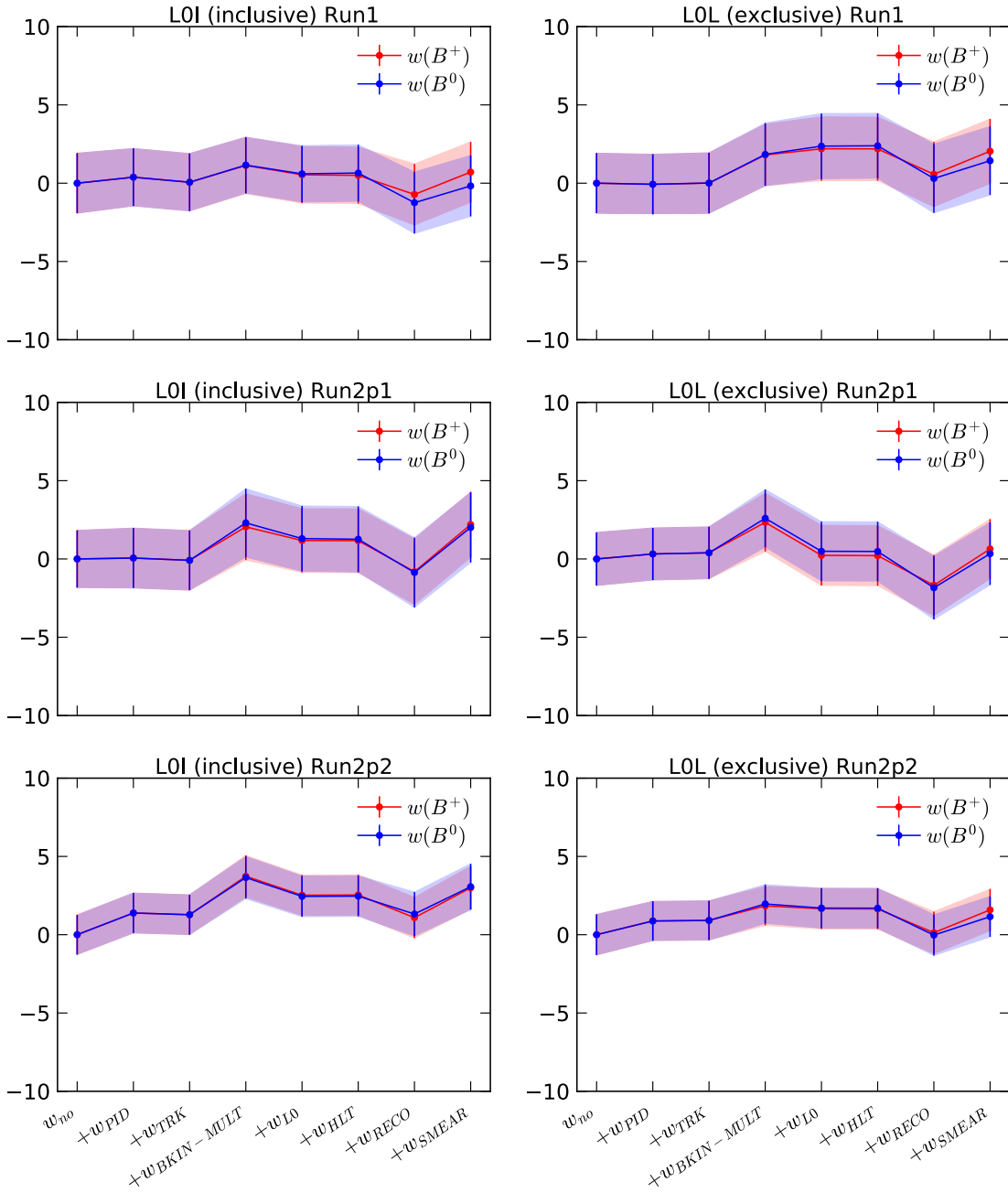


Figure 11.5 – Stepwise variation of the efficiency double ratio $\frac{\epsilon_{B^0 \rightarrow K^*0} \epsilon_{e^+ e^-} \epsilon_{B^0 \rightarrow K^*0} \int \psi(\rightarrow \mu^+ \mu^-)}{\epsilon_{B^0 \rightarrow K^*0} \mu^+ \mu^- \epsilon_{B^0 \rightarrow K^*0} \int \psi(\rightarrow e^+ e^-)}$ as a function of the calibration steps in the central- q^2 region. The values shown are the relative differences in percent of the double ratios to the double ratio with no calibration applied. The efficiency calibrations are either computed with the procedure based on the (red) B^+ or the (blue) B^0 calibration samples. The uncertainty bands include the statistical uncertainty based on the limited size of the simulation samples and the *resampling* uncertainties of the calibration chain and their correlations.

12 Conclusion and outlook

The Standard Model of particle physics is the most precise theory of the fundamental particles and their interactions. One of its most essential properties is the principle of lepton flavour universality. It states that the coupling of the electroweak bosons is the same for all leptons except for kinematic effects due to the lepton masses. Lepton flavour universality can be tested by experimentally measuring the ratios of the branching fractions of similar decays, which differ by the lepton type in their final states. Observables that are especially clean of theoretical and experimental uncertainties and thus very sensitive to possible new physics effects are the ratios $R_{K^{*0}}$ and R_K . They are defined as the ratios of the branching fractions of the decays $B^0 \rightarrow K^{*0} \mu^+ \mu^-$ and $B^0 \rightarrow K^{*0} e^+ e^-$, or $B^+ \rightarrow K^+ \mu^+ \mu^-$ and $B^+ \rightarrow K^+ e^+ e^-$, respectively.

Recent measurements by the LHCb collaboration of R_K [23] and $R_{K^{*0}}$ [22] show tensions with the SM in the range of 2.1 to 3.1 standard deviations. These results establish evidence for the violation of lepton flavour universality. They are consistent with a range of other experimental results with $b \rightarrow s \ell^+ \ell^-$ transitions as described in Chapter 2. Any further experimental investigation is thus extremely relevant to either falsify or strengthen these anomalies.

This thesis presents the experimental procedure of the first simultaneous measurement of the LFU ratios R_K and $R_{K^{*0}}$ with the full LHCb data set recorded in the years 2011 to 2018. This data set corresponds to an integrated luminosity of 9.0 fb^{-1} with the collision energies of 7 TeV for 2011, 8 TeV for 2012, and 13 TeV for 2015-2018.

The analysis is performed in two regions of the invariant mass of the dilepton system q^2 , which are defined as the low- q^2 region with $0.1 < q^2 < 1.1 \text{ GeV}^2/c^4$ and the central- q^2 region with $1.1 < q^2 < 6.0 \text{ GeV}^2/c^4$. The approach of determining R_K and $R_{K^{*0}}$ simultaneously allows for the first time to include correlations of the statistical and systematic uncertainties between the two observables. In addition, the simultaneous fits to all decay modes, trigger categories, and years of data taking allow for an accurate description of background components shared between the different years and trigger categories. With that, also the cross-feed background between the decay mode can be constrained.

The updated methodology significantly improves the precision of the previously published measurements. In addition, it will for the first time measure R_K in the low- q^2 region and, for the first time will determine $R_{K^{*0}}$ with the complete LHCb data set including 2015-2018 data. Although the central values of the measurement are kept blind, the evaluation of the sensitivities shows that the analysis of R_K and $R_{K^{*0}}$ described in this thesis will be the most precise today.

Sensitivities of the measurements. The sensitivities are a benchmark of the precision of the measurements of R_K and R_{K^*0} . They are defined as σ_R/R with σ_R as the total uncertainty of the ratio R . Table 12.1 shows a comparison of the sensitivities of the previously published LHCb measurements of R_K and R_{K^*0} and this thesis. These numbers for the already published measurements are computed with the sum in quadrature of the statistical and systematic uncertainties with the larger values of the asymmetric uncertainties chosen. Compared to the previous measurements, an optimised choice of trigger categories is employed, leading to smaller systematic uncertainties by aligning the treatment of the electron and muon decay channels as much as possible. The procedure is further optimised with an improved signal selection strategy, which allows for a clean extraction of the signal candidates while suppressing the background decay modes.

Table 12.1 – Sensitivities σ_R/R with σ_R as the total uncertainties of the ratios R of the previous measurements of R_K and R_{K^*0} [22, 23] and this thesis.

Measurement	Refs.[22, 23]	This thesis
R_{K^*0} low- q^2	16 %	8.8 %
R_{K^*0} central- q^2	17 %	6.5 %
R_K low- q^2	-	8.0 %
R_K central- q^2	5.2 %	4.3 %

The first LFU measurement of the ratio R_K by the LHCb collaboration in 2014 [24] relied upon the assumption that possible effects due to simulation imperfections would cancel in the ratio. However, in the light of the raised evidence of a breaking of the SM, a more rigorous calibration of the efficiencies is needed to validate this assumption. Therefore, this thesis presents a highly complex and sophisticated multi-step calibration chain, which is thoroughly validated and will be summarised in the following.

Efficiency calibration. Chapter 7 presents the sequential efficiency calibration procedure, which includes the calibration of PID, track reconstruction, trigger, and q^2 -bin migration efficiencies, as well as a reweighting of distributions of the decay kinematics, event multiplicity proxies, and candidate reconstruction qualities. When calibrating the B^+ (B^0) signal mode efficiencies with calibration samples of the same B^+ (B^0) mode, this can lead to unwanted correlations. Thus, within the simultaneous approach of this analysis, two separate calibration chains based on either the B^+ or B^0 decay modes are developed and cross-applied in the R_{K^*0} or R_K measurement, respectively.

One of the most challenging aspects of the measurement of R_K and R_{K^*0} is determining accurate electron detection efficiencies, which are especially difficult to measure due to the high amount of bremsstrahlung radiation emitted by the electrons. As a consequence, for the computation of PID efficiencies, new methods are developed to guarantee a precise extraction of the electron PID efficiencies and to reduce effects of

non-factorisation of the efficiencies of the two final state electrons. For the calibration of the kinematics and event multiplicity distributions, a clean and unbiased calibration sample is generated with a separate *prior calibration chain* using a separate tight data-simulation alignment. These developments of the efficiency calibration procedure are validated with several cross-checks.

Cross-checks. Chapter 11 describes three main cross-checks to validate the effects of the efficiency calibration. All cross-checks presented include a portability validation of the B^+ and B^0 mode based calibrations.

The first cross-check of measuring the LFU ratios of only the *resonant* $B \rightarrow K^{(*)0} J/\psi(\rightarrow \ell^+ \ell^-)$ decays, which are employed as normalisation modes, shows good compatibility with unity. For these ratios systematic uncertainties do not cancel out as in the ratios R_K and $R_{K^{*0}}$. Thus, the cross-check represents a rigorous test of the stability and integrity of the experimental setup.

A *stepwise* evaluation of these ratios of the resonant decay modes, i.e., sequentially switching on the efficiency calibration, shows the significant effect of the calibration in the order of 20 to 40 % when comparing the results for uncalibrated simulation to the application of the entire calibration procedure.

An even more sensitive cross-check to residual imperfections of the efficiency determination is a *differential evaluation* of the aforementioned LFU ratios of the resonant decay modes. It is computed differentially for all main observables of the analysis. These include, among others, the observables that are used in the extraction of the calibration weights and thus are further validating this procedure. It shows that the resulting distributions only deviate in the sub-percent level from unity except for the two observables where a dedicated systematic uncertainty is assigned.

Although the efficiency calibration significantly affects the single ratios, evaluating the *double ratios* of the branching fractions of the resonant $B \rightarrow K^{(*)0} J/\psi(\rightarrow \ell^+ \ell^-)$ and $B \rightarrow K^{(*)0} \psi(2S)(\rightarrow \ell^+ \ell^-)$ decays shows that possible imperfections of the efficiency determination cancel out to a large extent.

The evaluation of the *blinded variations* of R_K and $R_{K^{*0}}$ in steps of the calibration procedure shows that the effect of applying the calibration weights lies in the order of $\mathcal{O}(1 - 5\%)$ for the final measurement, which proves the excellent robustness of the double ratio approach. Furthermore, the corresponding residual imperfections are shown to be resolved with the presented calibration procedure.

Outlook. In the future, for the LHCb experiment, a measurement of R_K and $R_{K^{*0}}$ in the high- q^2 region with $q^2 > m^2(\psi(2S))$ could shed additional light on the flavour anomalies. This q^2 region contains different background contributions compared to the already studied regions, thus providing complementary insights. Also, LFU measurements with $b \rightarrow s \tau^+ \tau^-$ decays would offer an additional window. However, their measurement is challenging in the LHCb experiment because the tau particles always decay to final states including at least one neutrino, which is not directly detectable with the LHCb detector.

In addition, the upgrades of the LHCb detector [239, 240] are expected to provide a significantly higher amount of data corresponding to an estimated total integrated luminosity of 23 fb^{-1} in RUN 3 and 50 fb^{-1} in RUN 4. After RUN 4 an integrated luminosity of 300 fb^{-1} is expected in RUN 5 [58]. A main improvement in the detector upgrades will be the different trigger strategy. Systematic uncertainties that arised from the separate handling of the electrons and muons in the L0 trigger will vanish because the new trigger system processes them with an identical approach. Because the precision of the current LFU measurements with the LHCb experiment is mainly driven by the statistical uncertainties of the electron modes, the precision will significantly improve with larger data sets [58].

Although this larger LHCb data set would suffice to confirm a possible effect of new physics, if it persists similarly to what was already measured in the published analyses, other experiments will verify the presented tests of LFU in the future. This will be a critical cross-check for the LHCb measurement with orthogonal experimental setups. Here, the Belle II experiment [160], which has already started taking data in 2018, will provide independent results in a continuation of the LFU measurements of the Belle experiment. In addition, the CMS collaboration has stored data containing b -meson decays within their *data-parking* strategy [241], which also allows for measuring LFU ratios. The Belle II experiment will collect a data set corresponding to an integrated luminosity of 50 ab^{-1} until 2027, which will allow for measurements of R_K and R_{K^*0} in the central- q^2 region with precisions comparable to the LHCb results [242]. Studies with a sub-data set could be published even earlier, but also, the CMS experiment will need a couple of years to reach the LHCb precision for these observables.

In the light of these considerations the analysis presented in this thesis will provide new insights concerning the flavour anomalies. It represents a legacy analysis of the R_K and R_{K^*0} observables before the promising start of RUN 3 of the LHCb experiment.

A Appendix

A.1 Selection requirements

Table A.1 – Stripping selection requirements of the stripping lines Bu2LLKmmLine and Bu2LLKeelLine2.

Particle candidate	Selection requirement
μ	isMuon (only data), hasMuon $p_T > 300 \text{ MeV}/c$ $\chi_{\text{IP}}^2 > 9$
e	PIDe > 0 (only data) $p_T > 300 \text{ MeV}/c$ $\chi_{\text{IP}}^2 > 9$
$\ell^+\ell^-$	$m < 5500 \text{ MeV}/c^2$ $\chi^2/\text{ndf} < 9$ $\chi_{\text{FD}}^2 > 16$
K^+	PIDK > -5 (only data) $\chi_{\text{IP}}^2 > 9$ $p_T > 400 \text{ MeV}/c$ (only for R_K)
$\pi^- (R_{K^{*0}})$	$\chi_{\text{IP}}^2 > 9$
$K^{*0} (R_{K^{*0}})$	$ m - m(K^{*0})_{\text{PDG}} < 300 \text{ MeV}/c^2$ $p_T > 500 \text{ MeV}/c$ $\chi_{\text{vtx}}^2/\text{ndf} < 25$
B	$ m - m(B)_{\text{PDG}} < 1500 \text{ MeV}/c^2$ $\cos(\text{DIRA}) > 0.9995$ $\chi_{\text{IP}}^2 < 25$ $\chi_{\text{vtx}}^2/\text{ndf} < 9$ $\chi_{\text{FD}}^2 > 100$
Global event cut	nSPDHits < 600

Type		Requirement
Acceptance	e	$!(x_{\text{ECAL}} < 363.6 \text{ mm} \ \&\& \ y_{\text{ECAL}} < 282.6 \text{ mm})$
		$\text{region}_{\text{ECAL}} \geq 0$ $(e^+e^-) - \text{Distance}_{\text{ECAL}} > 100 \text{ mm}$
K^{*0}	K^{*0}	$ m(K\pi) - m_{K^{*0}}^{\text{PDG}} < 100 \text{ MeV}/c^2$ $p_{\text{T}} > 500 \text{ MeV}/c$
	$K(B^+ \text{ modes only})$	$p_{\text{T}} > 400 \text{ MeV}/c$
PID	K	$\text{PIDK} > 0$ $\text{ProbNNk} \cdot (1 - \text{ProbNNp}) > 0.05$
	π	$\text{ProbNNpi} \cdot (1 - \text{ProbNNk}) \cdot (1 - \text{ProbNNp}) > 0.1$
	μ	$\text{IsMuon}==1$ $\text{ProbNNmu} > 0.2$
	e	$\text{PIDe} > 2$ $\text{ProbNNe} > 0.2$
	Multiplicity	$n\text{SPDHits} < 600(450) \text{ RUN 1 (RUN 2)}$
Quality, Acceptance, Calibration	all tracks	$\chi_{\text{track/ndf}}^2 < 3$ $\chi_{\text{IP}}^2 > 9$ $\text{hasRICH}==1$ $\text{GhostProb} < 0.4$
	K, π	$p_{\text{T}} > 250 \text{ MeV}/c$ $p > 2 \text{ GeV}/c \ \& \ p < 200 \text{ GeV}/c$ $\text{InAccMuon}==1$
	e	$p_{\text{T}} > 500 \text{ MeV}/c$ $p > 3 \text{ GeV}/c \ \& \ p < 200 \text{ GeV}/c$ $\text{hasCalo}==1$
	μ	$p_{\text{T}} > 800 \text{ MeV}/c$ $p > 3 \text{ GeV}/c \ \& \ p < 200 \text{ GeV}/c$ $\text{InAccMuon}==1$
	Clones	$\theta(\ell_{1,2}, h) > 0.5 \text{ mrad}$ $\theta(\ell_1, \ell_2) > 0.5 \text{ mrad}$

Table A.2 – Summary of the offline selection requirements.

Table A.3 – MVA input variables used in the classification against combinatorial background. A definition of the variables can be found in Table 3.3.

Particle	Input variables
B^0 decay modes	
B^0	$p_T, \chi_{IP}^2, \chi_{FD}^2, \chi_{\text{vtx}}^2/\text{ndf}, \chi_{\text{DTF}}^2/\text{ndf}, \text{DIRA}$
K^{*0}	$p_T, \chi_{IP}^2, \chi_{FD}^2, \chi_{\text{vtx}}^2/\text{ndf}, \text{DIRA}$
$\ell^+\ell^-$	$p_T, \chi_{IP}^2, \chi_{FD}^2, \chi_{\text{vtx}}^2/\text{ndf}, \text{DIRA}$
h	$\min, \max(p_{T,K}, p_{T,\pi}), \min, \max(\chi_{IP,K}^2, \chi_{IP,\pi}^2)$
ℓ	$\min, \max(p_{T,\ell^+}, p_{T,\ell^-}), \min(\chi_{IP,\ell^+}^2, \chi_{IP,\ell^-}^2)$
B^+ decay modes	
B^+	$p_T, \chi_{IP}^2, \chi_{FD}^2, \chi_{\text{vtx}}^2/\text{ndf}, \chi_{\text{DTF}}^2/\text{ndf}, \text{DIRA}$
K	p_T, χ_{IP}^2
$\ell^+\ell^-$	$p_T, \chi_{IP}^2, \chi_{FD}^2, \chi_{\text{vtx}}^2/\text{ndf}, \text{DIRA}$
ℓ	$\min(p_{T,\ell^+}, p_{T,\ell^-}), \min, \max(\chi_{IP,\ell^+}^2, \chi_{IP,\ell^-}^2)$

A.2 Track reconstruction calibration

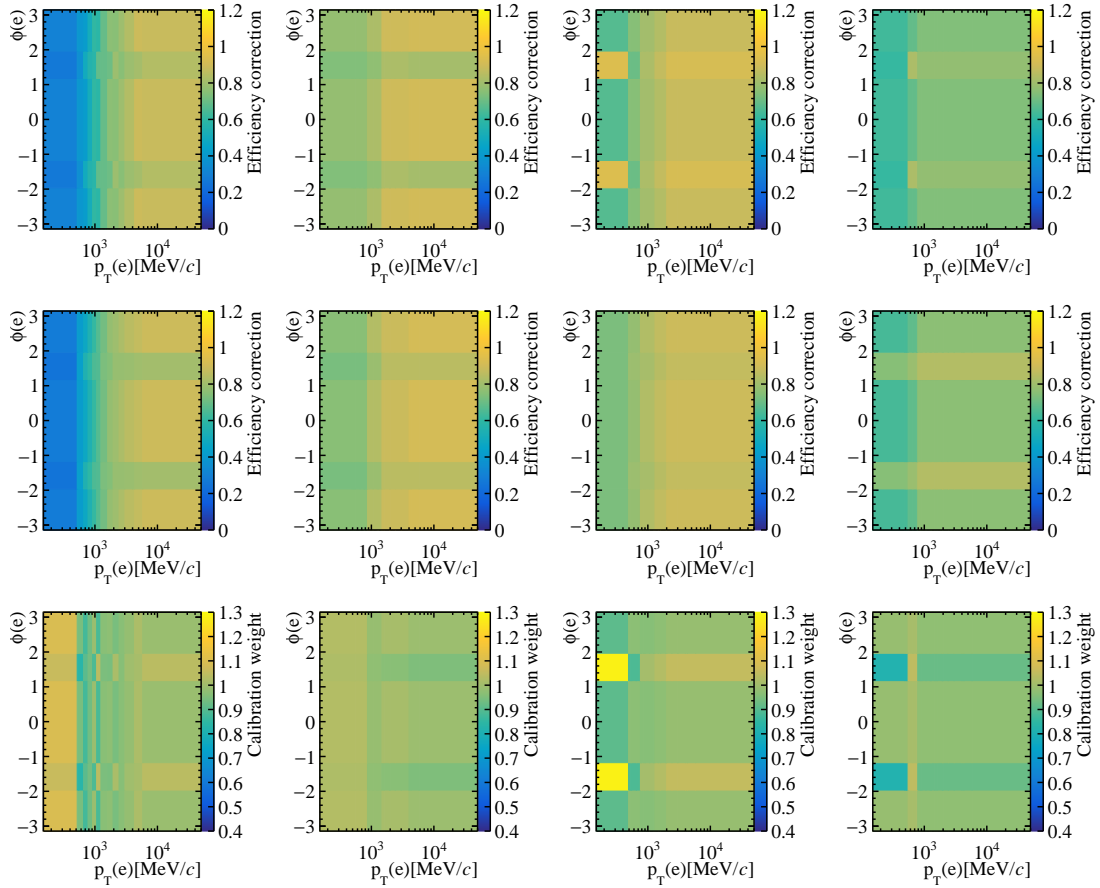


Figure A.1 – Track reconstruction calibration maps for electrons in regions of $\phi(e)$ and $p_T(e)$ and (from left to right and top to bottom) bins of the electron pseudorapidity with the edges of $\eta = [1.90, 2.90, 3.45, 4.00, 4.50]$. Data and simulation ratios of the track reconstruction efficiency for the year 2011 are shown.

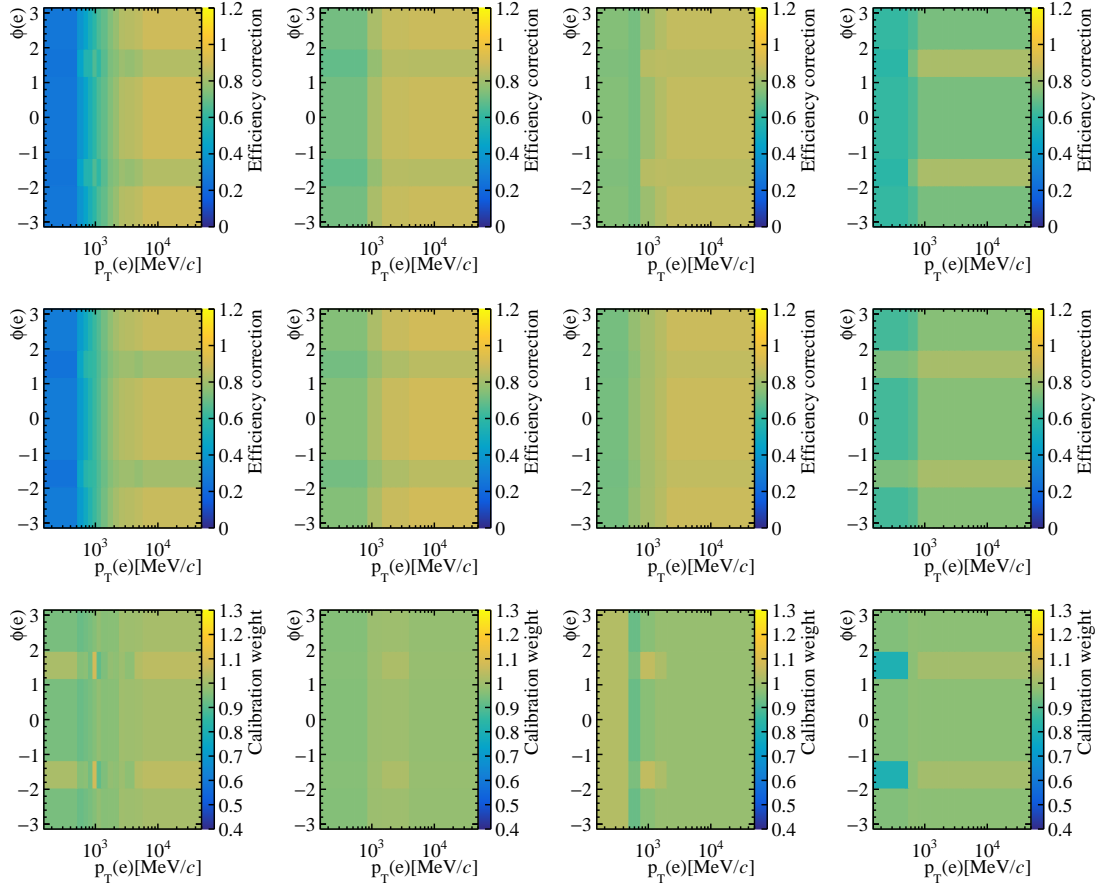


Figure A.2 – Track reconstruction calibration maps for electrons in regions of $\phi(e)$ and $p_T(e)$ and (from left to right and top to bottom) bins of the electron pseudorapidity with the edges of $\eta = [1.90, 2.90, 3.45, 4.00, 4.50]$. Data and simulation ratios of the track reconstruction efficiency for the year 2012 are shown.

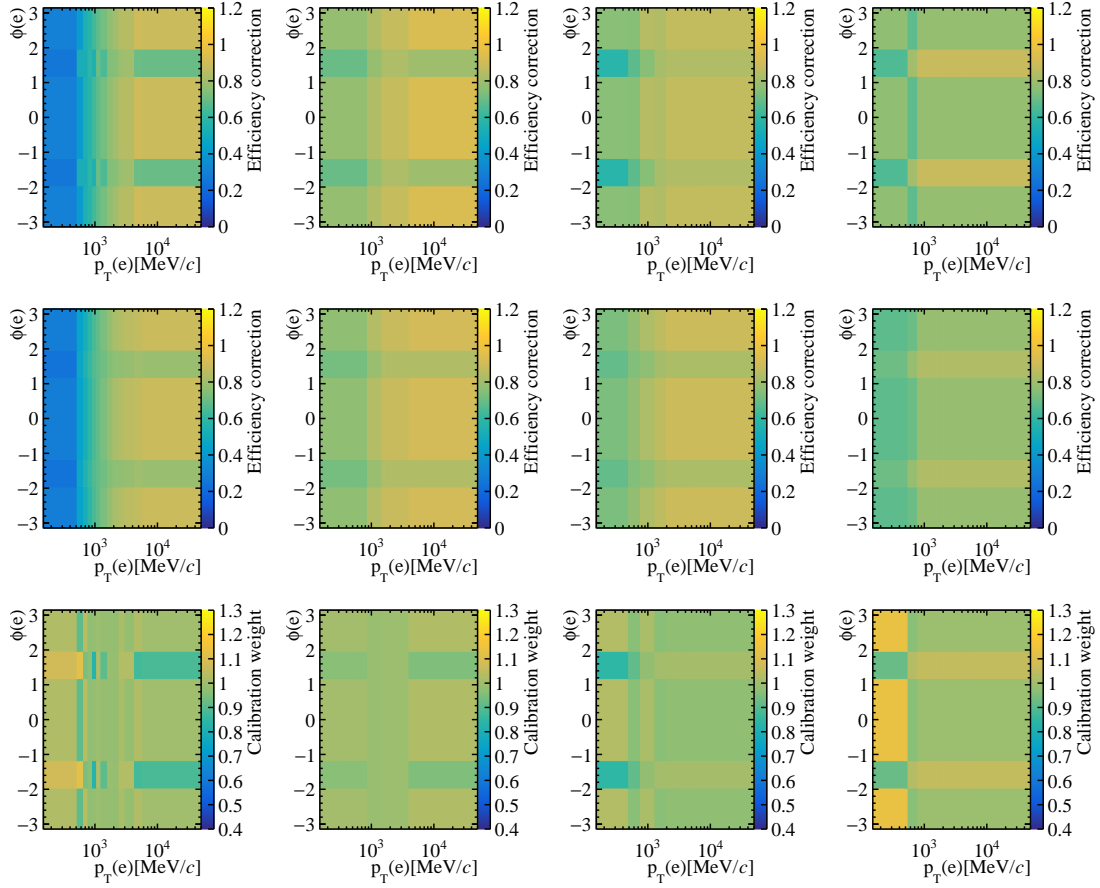


Figure A.3 – Track reconstruction calibration maps for electrons in regions of $\phi(e)$ and $p_T(e)$ and (from left to right and top to bottom) bins of the electron pseudorapidity with the edges of $\eta = [1.90, 2.90, 3.45, 4.00, 4.50]$. Data and simulation ratios of the track reconstruction efficiency for the year 2015 are shown.

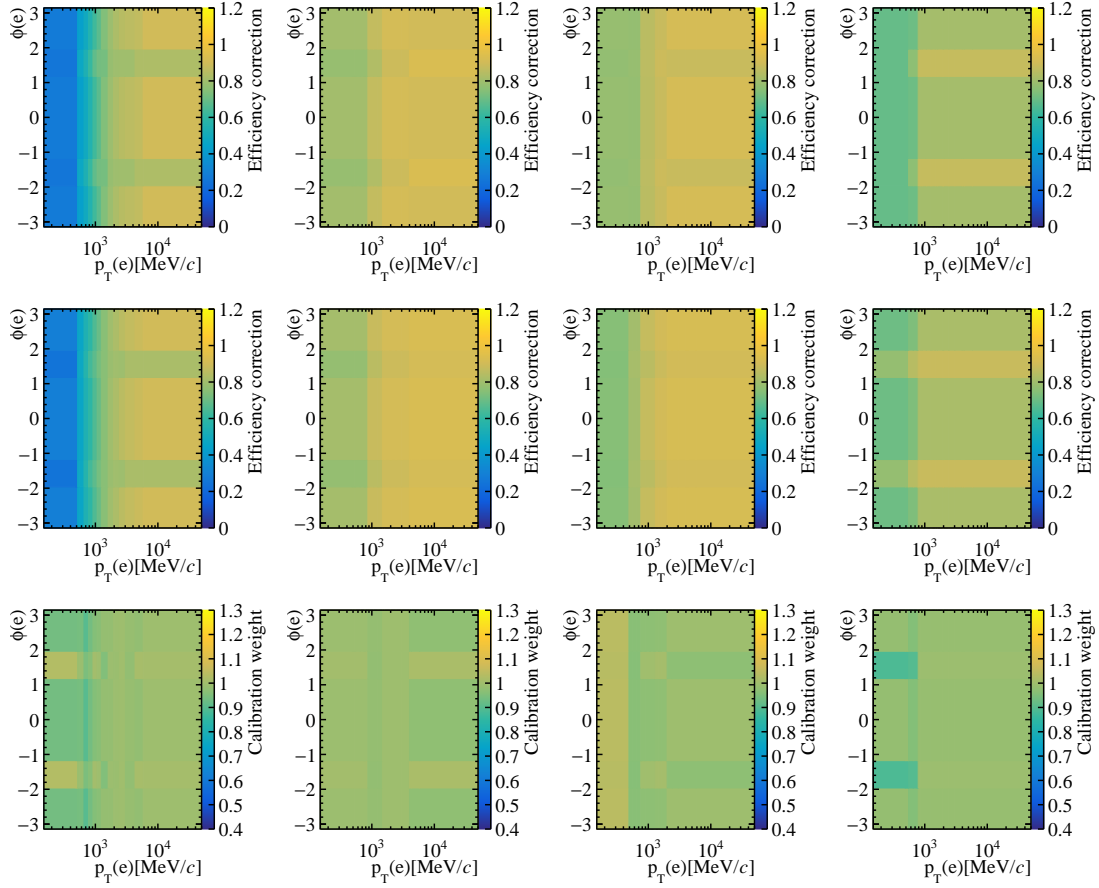


Figure A.4 – Track reconstruction calibration maps for electrons in regions of $\phi(e)$ and $p_T(e)$ and (from left to right and top to bottom) bins of the electron pseudorapidity with the edges of $\eta = [1.90, 2.90, 3.45, 4.00, 4.50]$. Data and simulation ratios of the track reconstruction efficiency for the year 2016 are shown.

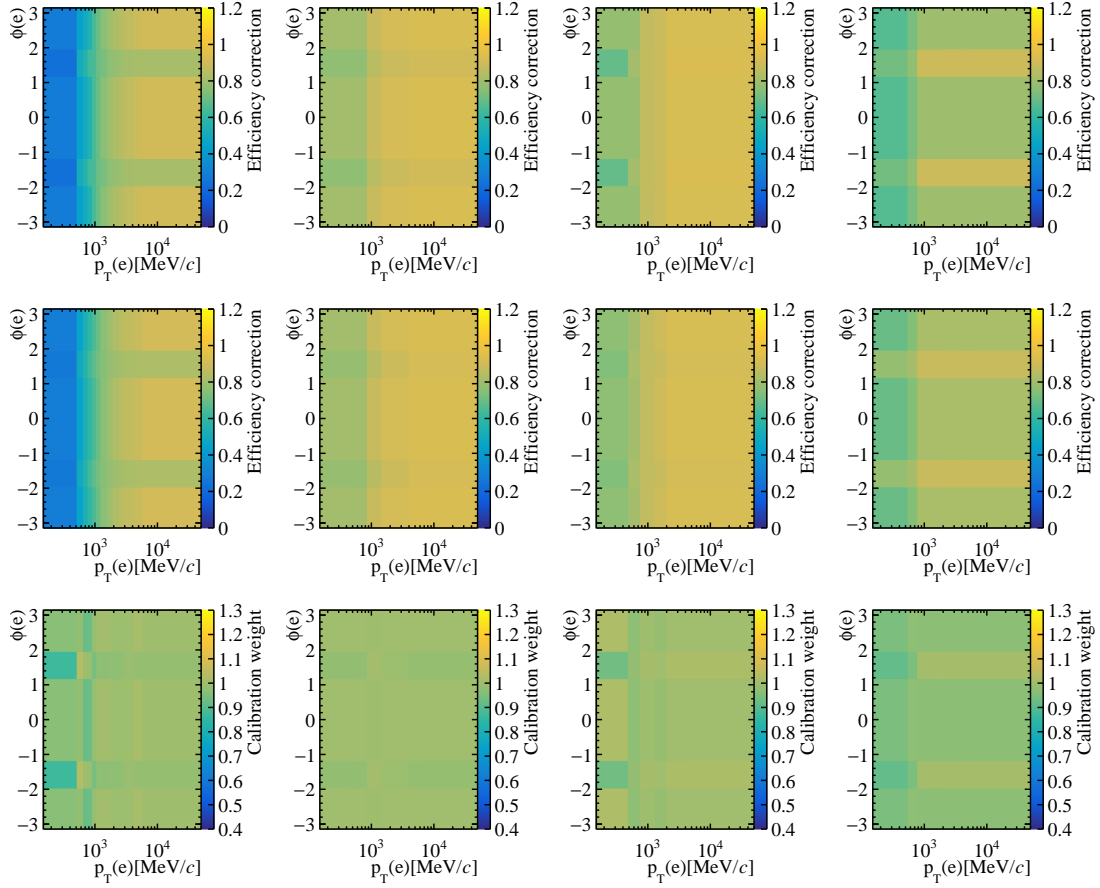


Figure A.5 – Track reconstruction calibration maps for electrons in regions of $\phi(e)$ and $p_T(e)$ and (from left to right and top to bottom) bins of the electron pseudorapidity with the edges of $\eta = [1.90, 2.90, 3.45, 4.00, 4.50]$. Data and simulation ratios of the track reconstruction efficiency for the year 2017 are shown.

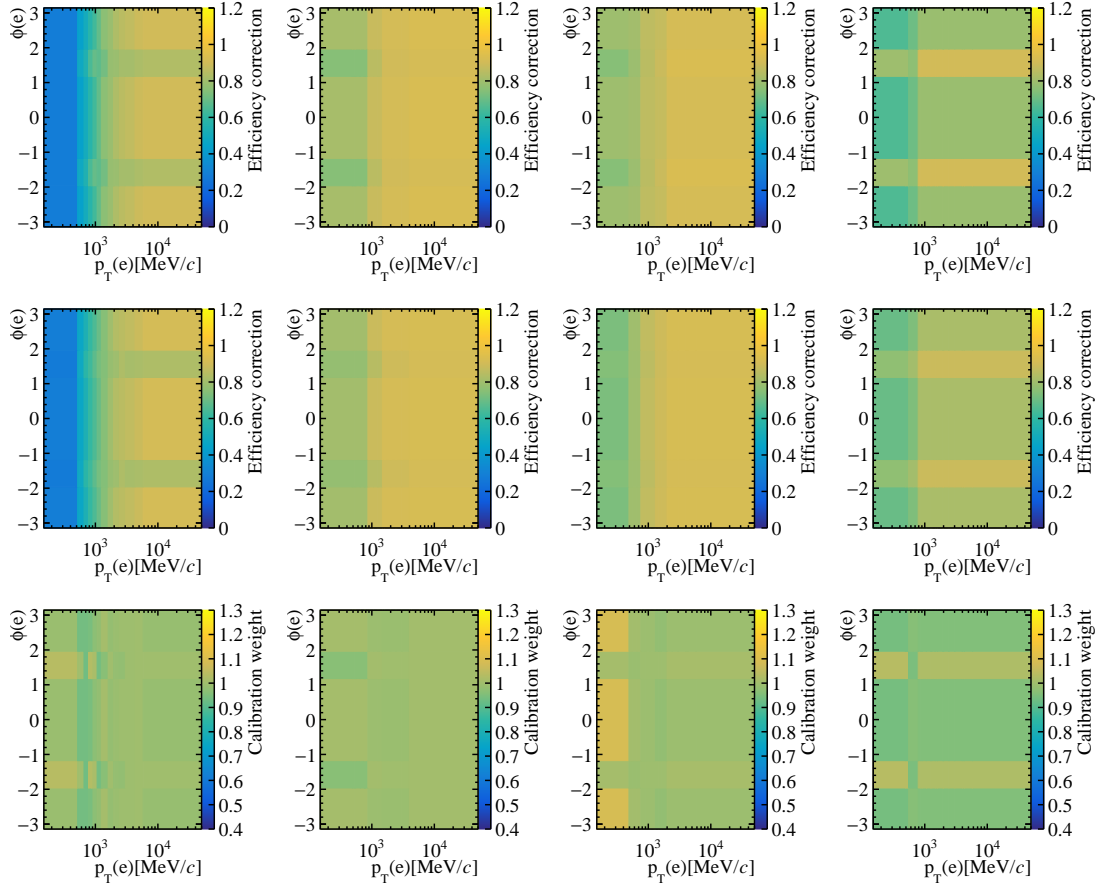


Figure A.6 – Track reconstruction calibration maps for electrons in regions of $\phi(e)$ and $p_T(e)$ and (from left to right and top to bottom) bins of the electron pseudorapidity with the edges of $\eta = [1.90, 2.90, 3.45, 4.00, 4.50]$. Data and simulation ratios of the track reconstruction efficiency for the year 2018 are shown.

A.3 Kinematic, multiplicity, and reconstruction calibration

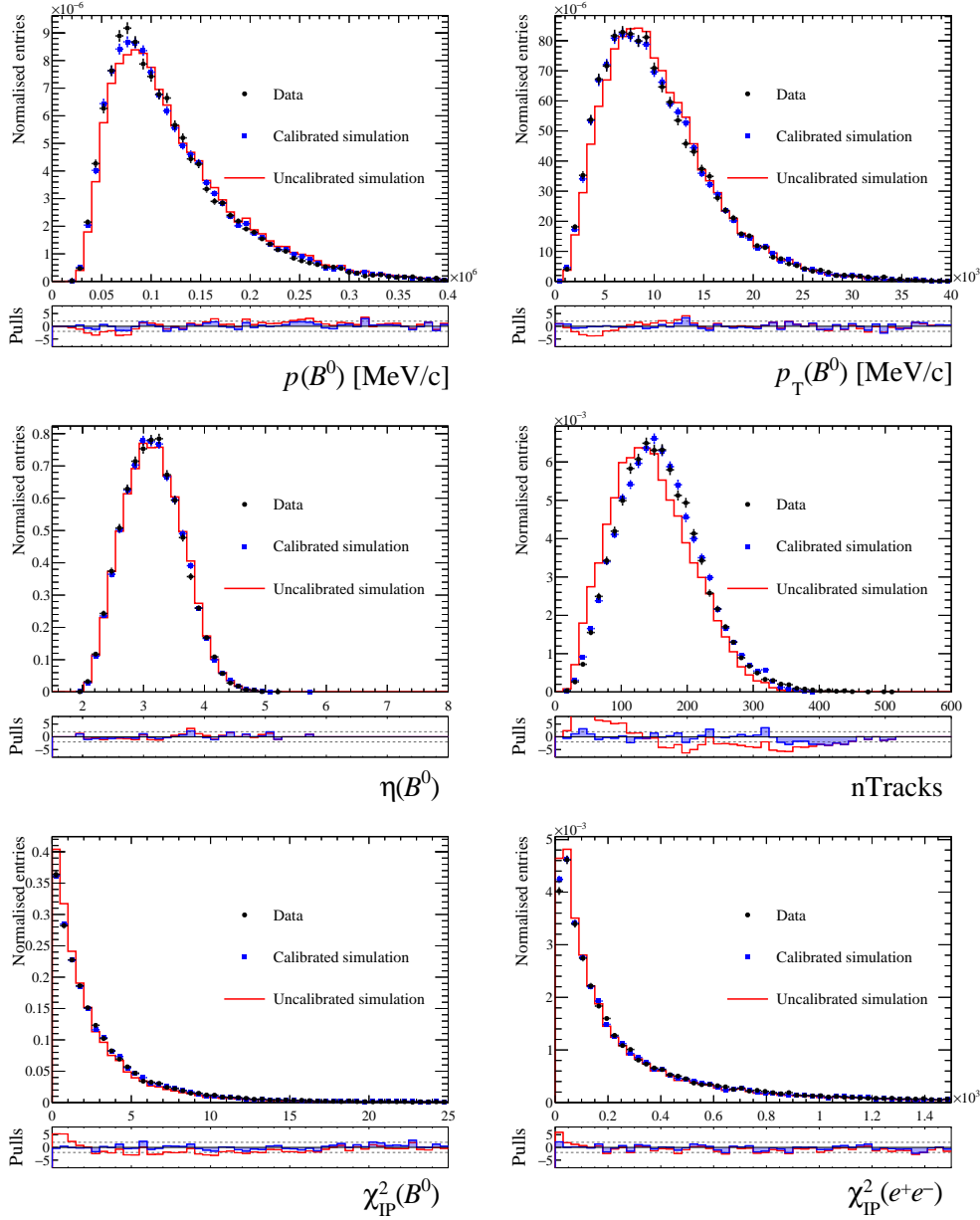


Figure A.7 – Comparisons of selected (black) detector data with (red) uncalibrated and (blue) simulation for 2018 L0I $B^0 \rightarrow K^{*0} J/\psi(\rightarrow e^+e^-)$ simulation. Shown are the distributions for momentum $p(B^0)$, transverse momentum $p_T(B^0)$, pseudorapidity $\eta(B^0)$ of the B^0 meson, the multiplicity proxy nTracks, and the candidate reconstruction variables χ_{IP}^2 of the B^0 meson and the dilepton system. The plots below the comparison distributions show the residuals normalised with the data uncertainties.

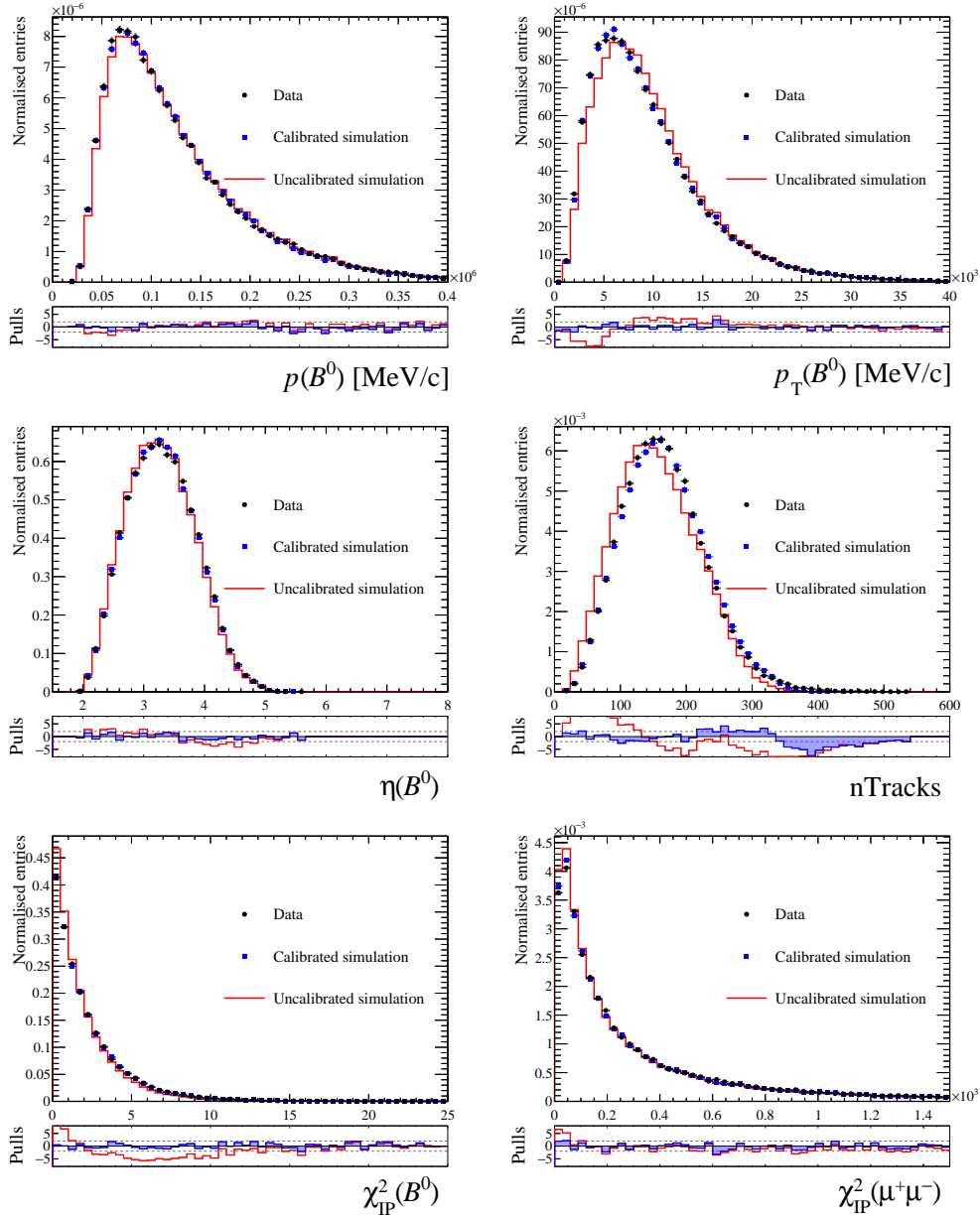


Figure A.8 – Comparisons of selected (black) detector data with (red) uncalibrated and (blue) simulation for 2018 L0I $B^0 \rightarrow K^{*0} J/\psi (\rightarrow \mu^+ \mu^-)$ simulation. Shown are the distributions for momentum $p(B^0)$, transverse momentum $p_T(B^0)$, pseudorapidity $\eta(B^0)$ of the B^0 meson, the multiplicity proxy nTracks, and the candidate reconstruction variables χ^2_{IP} of the B^0 meson and the dilepton system. The plots below the comparison distributions show the residuals normalised with the data uncertainties.

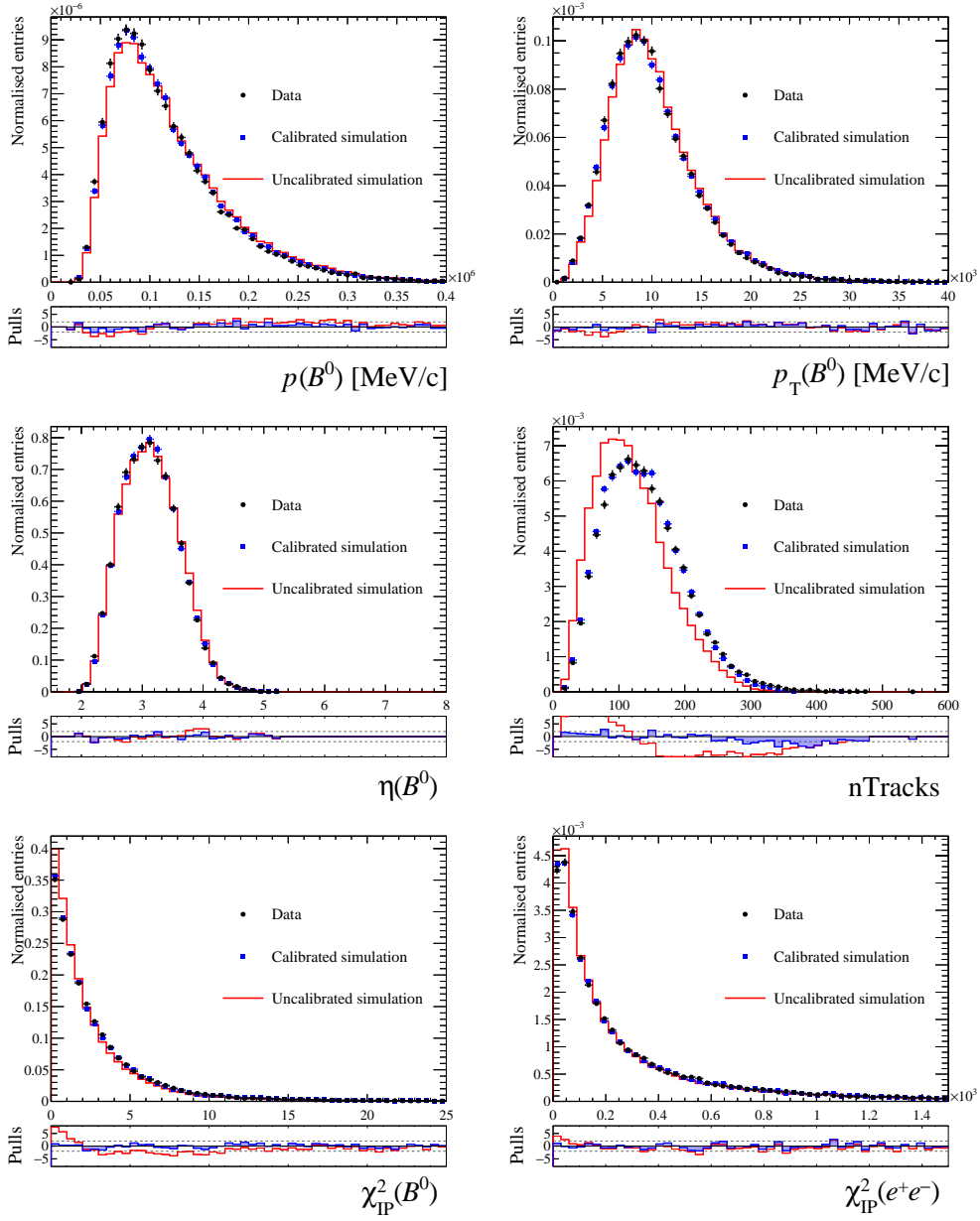


Figure A.9 – Comparisons of selected (black) detector data with (red) uncalibrated and (blue) simulation for 2018 L0E! $B^0 \rightarrow K^{*0} J/\psi(\rightarrow e^+e^-)$ simulation. Shown are the distributions for momentum $p(B^0)$, transverse momentum $p_T(B^0)$, pseudorapidity $\eta(B^0)$ of the B^0 meson, the multiplicity proxy nTracks, and the candidate reconstruction variables χ_{IP}^2 of the B^0 meson and the dilepton system. The plots below the comparison distributions show the residuals normalised with the data uncertainties.

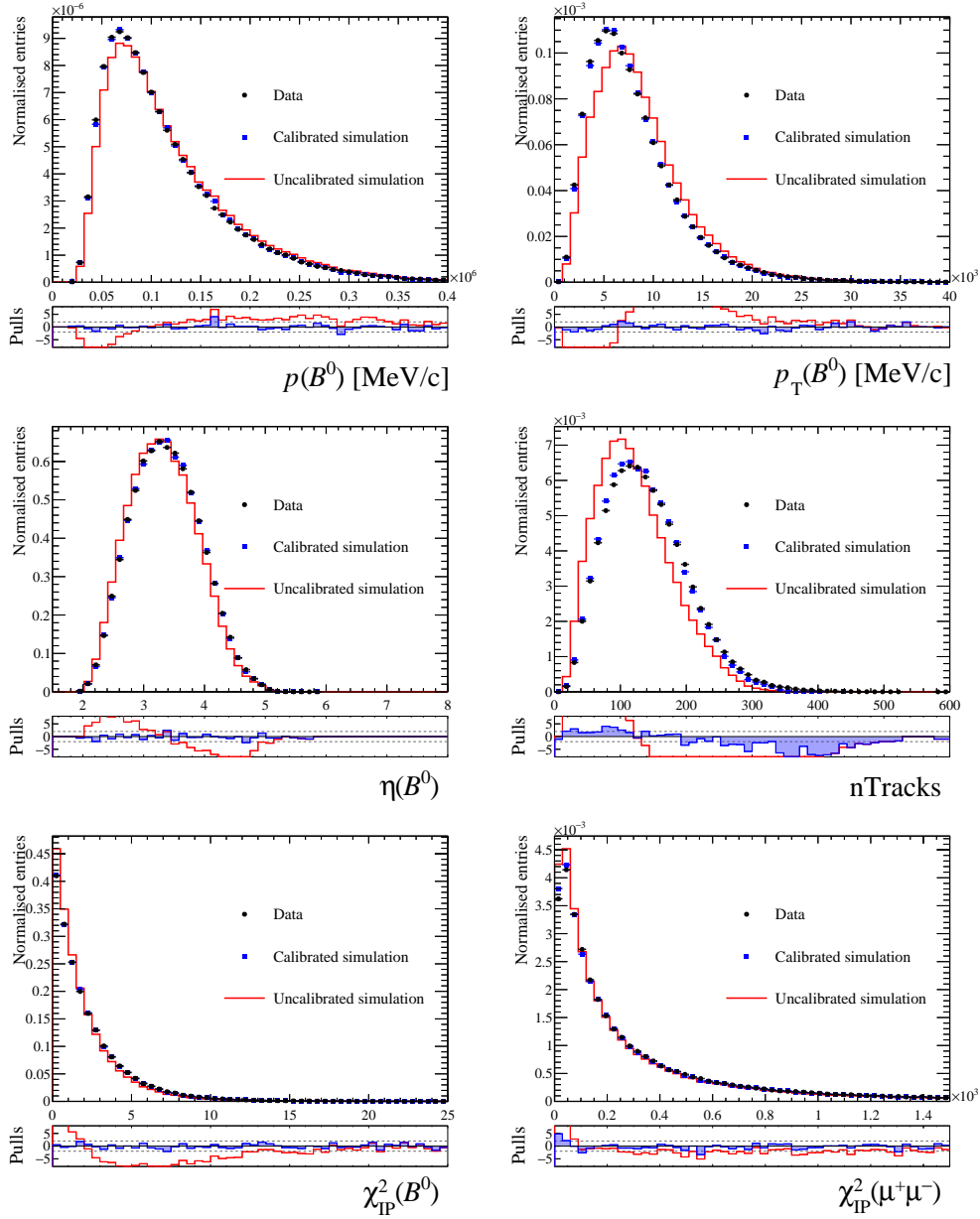


Figure A.10 – Comparisons of selected (black) detector data with (red) uncalibrated and (blue) simulation for 2018 L0M1 $B^0 \rightarrow K^{*0} J/\psi (\rightarrow \mu^+ \mu^-)$ simulation. Shown are the distributions for momentum $p(B^0)$, transverse momentum $p_T(B^0)$, pseudorapidity $\eta(B^0)$ of the B^0 meson, the multiplicity proxy nTracks, and the candidate reconstruction variables χ^2_{IP} of the B^0 meson and the dilepton system. The plots below the comparison distributions show the residuals normalised with the data uncertainties.

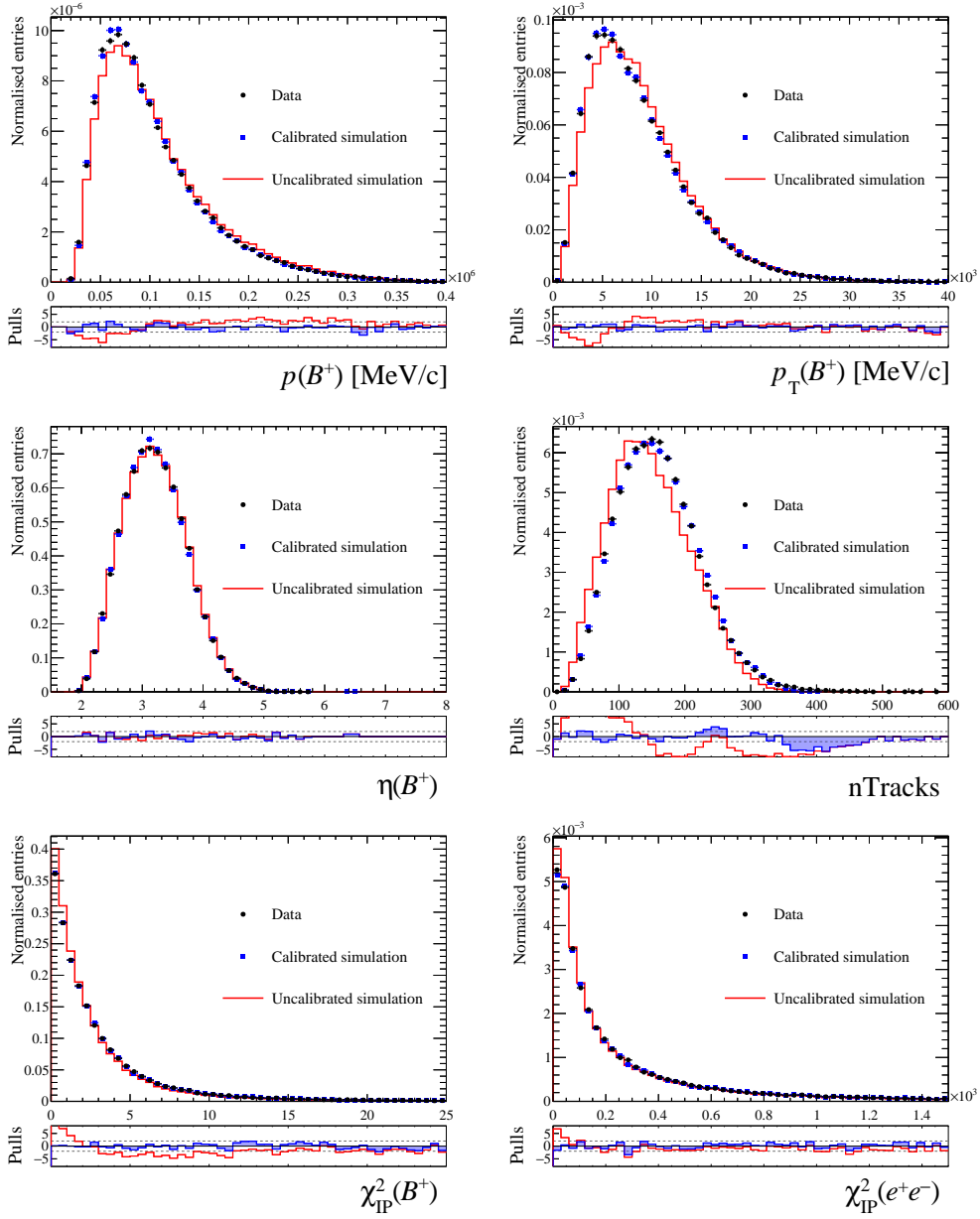


Figure A.11 – Comparisons of selected (black) detector data with (red) uncalibrated and (blue) simulation for 2018 L0I $B^+ \rightarrow K^+ J/\psi(\rightarrow e^+e^-)$ simulation. Shown are the distributions for momentum $p(B^+)$, transverse momentum $p_T(B^+)$, pseudorapidity $\eta(B^+)$ of the B^+ meson, the multiplicity proxy nTracks, and the candidate reconstruction variables χ_{IP}^2 of the B^+ meson and the dilepton system. The plots below the comparison distributions show the residuals normalised with the data uncertainties.

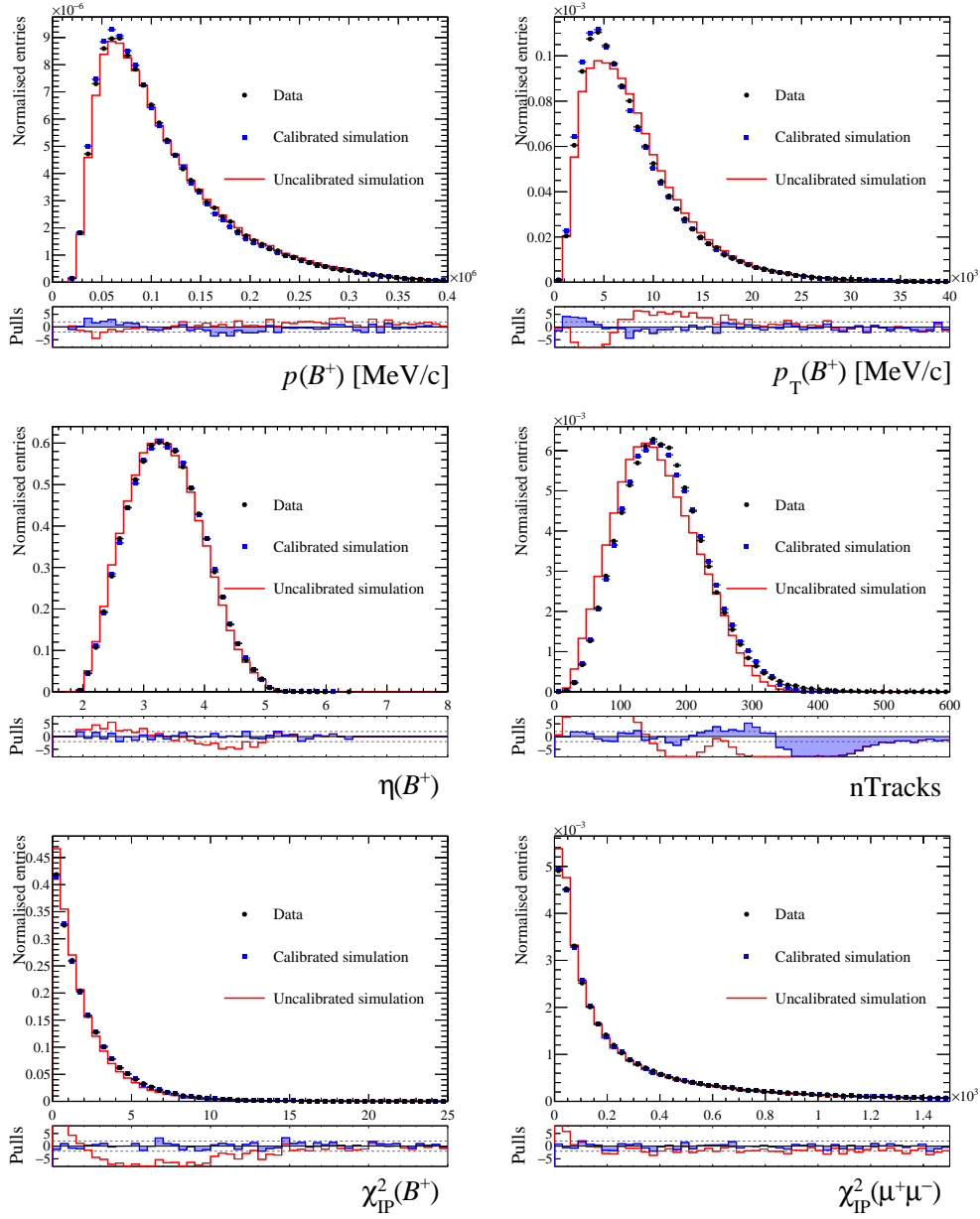


Figure A.12 – Comparisons of selected (black) detector data with (red) uncalibrated and (blue) simulation for 2018 L0I $B^+ \rightarrow K^+ J/\psi (\rightarrow \mu^+ \mu^-)$ simulation. Shown are the distributions for momentum $p(B^+)$, transverse momentum $p_T(B^+)$, pseudorapidity $\eta(B^+)$ of the B^+ meson, the multiplicity proxy nTracks, and the candidate reconstruction variables χ_{IP}^2 of the B^+ meson and the dilepton system. The plots below the comparison distributions show the residuals normalised with the data uncertainties.

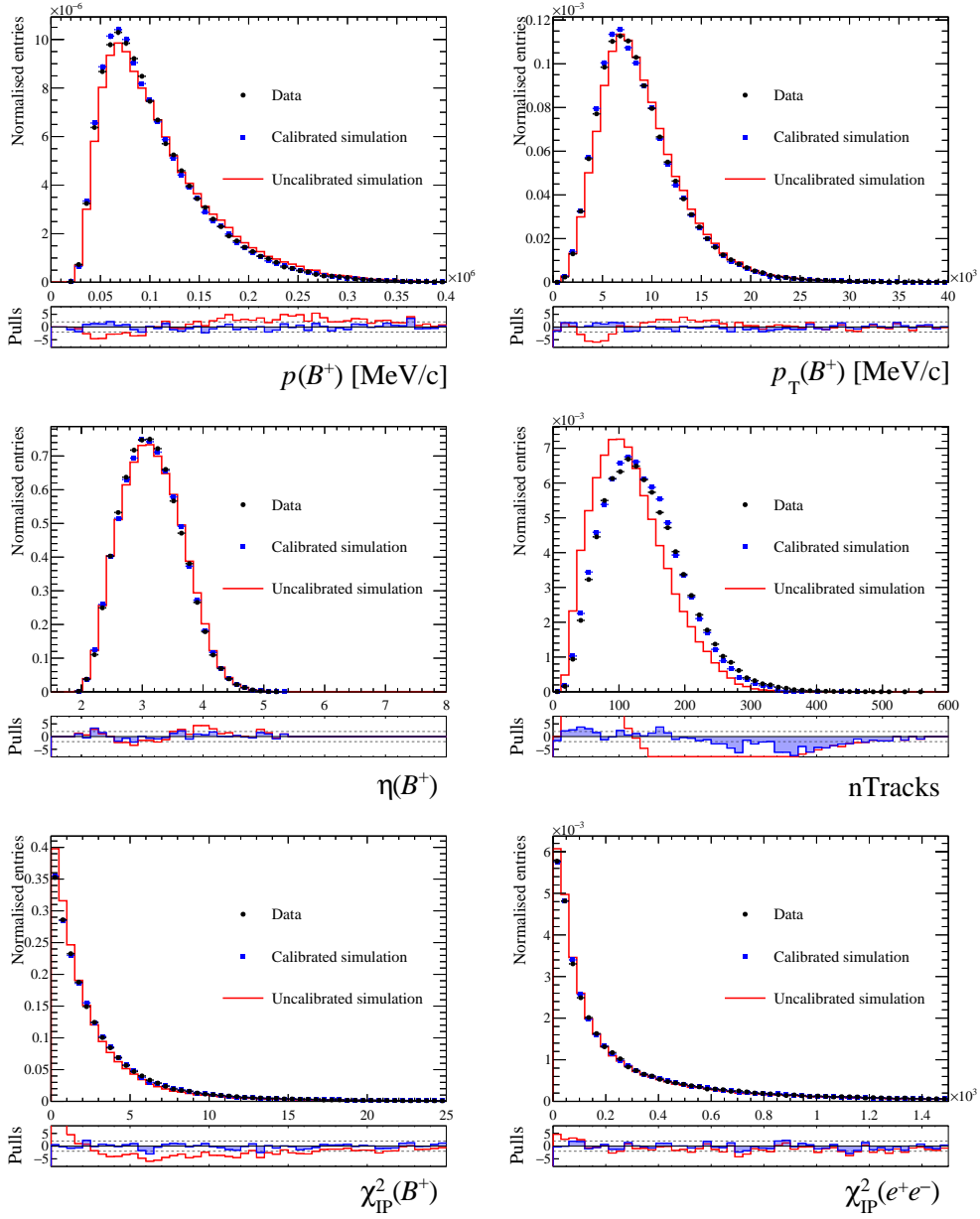


Figure A.13 – Comparisons of selected (black) detector data with (red) uncalibrated and (blue) simulation for 2018 L0E! $B^+ \rightarrow K^+ J/\psi (\rightarrow e^+ e^-)$ simulation. Shown are the distributions for momentum $p(B^+)$, transverse momentum $p_T(B^+)$, pseudorapidity $\eta(B^+)$ of the B^+ meson, the multiplicity proxy nTracks, and the candidate reconstruction variables χ_{IP}^2 of the B^+ meson and the dilepton system. The plots below the comparison distributions show the residuals normalised with the data uncertainties.

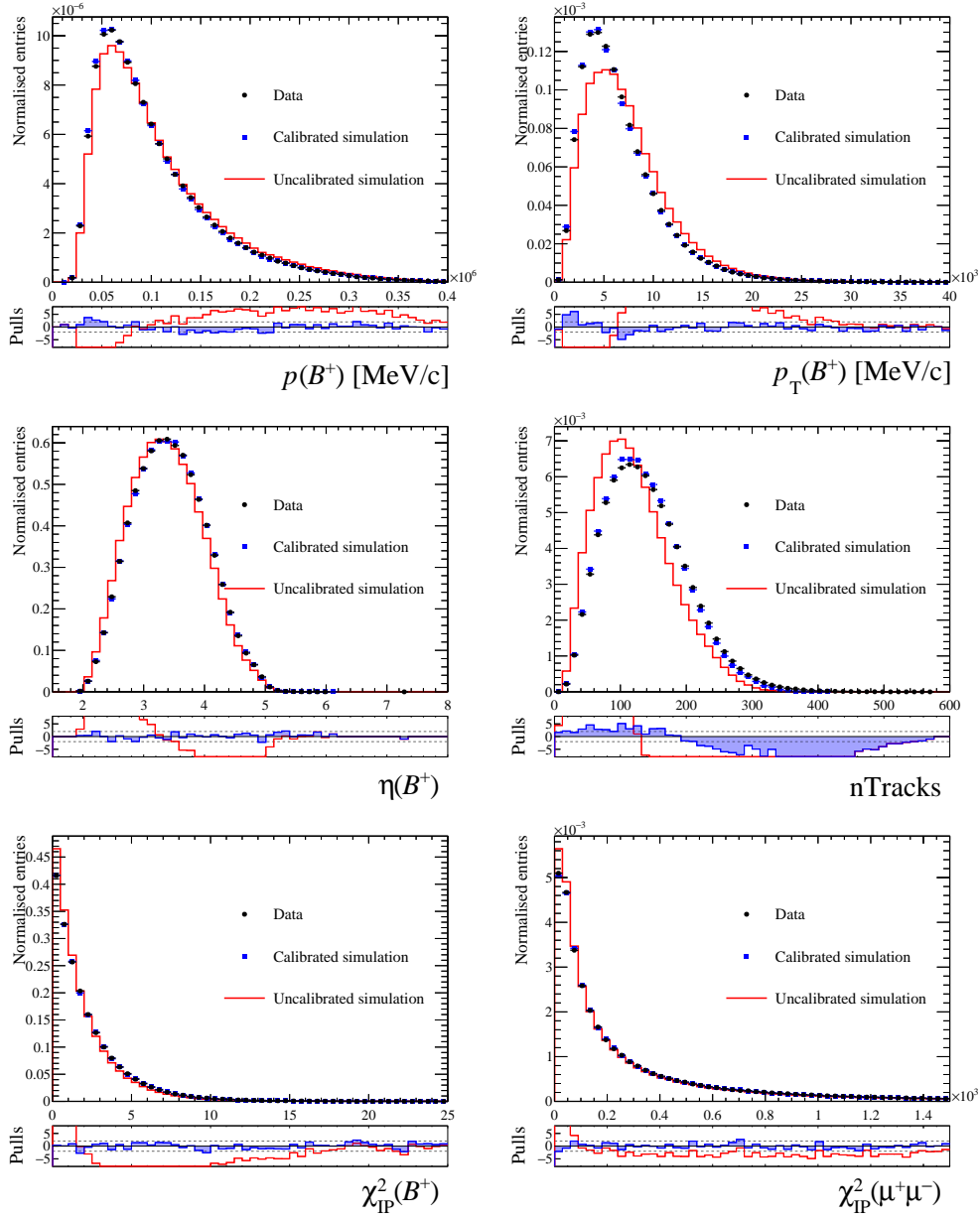


Figure A.14 – Comparisons of selected (black) detector data with (red) uncalibrated and (blue) simulation for 2018 L0M! $B^+ \rightarrow K^+ J/\psi (\rightarrow \mu^+ \mu^-)$ simulation. Shown are the distributions for momentum $p(B^+)$, transverse momentum $p_T(B^+)$, pseudorapidity $\eta(B^+)$ of the B^+ meson, the multiplicity proxy nTracks, and the candidate reconstruction variables χ_{IP}^2 of the B^+ meson and the dilepton system. The plots below the comparison distributions show the residuals normalised with the data uncertainties.

A.4 HLT calibration weights

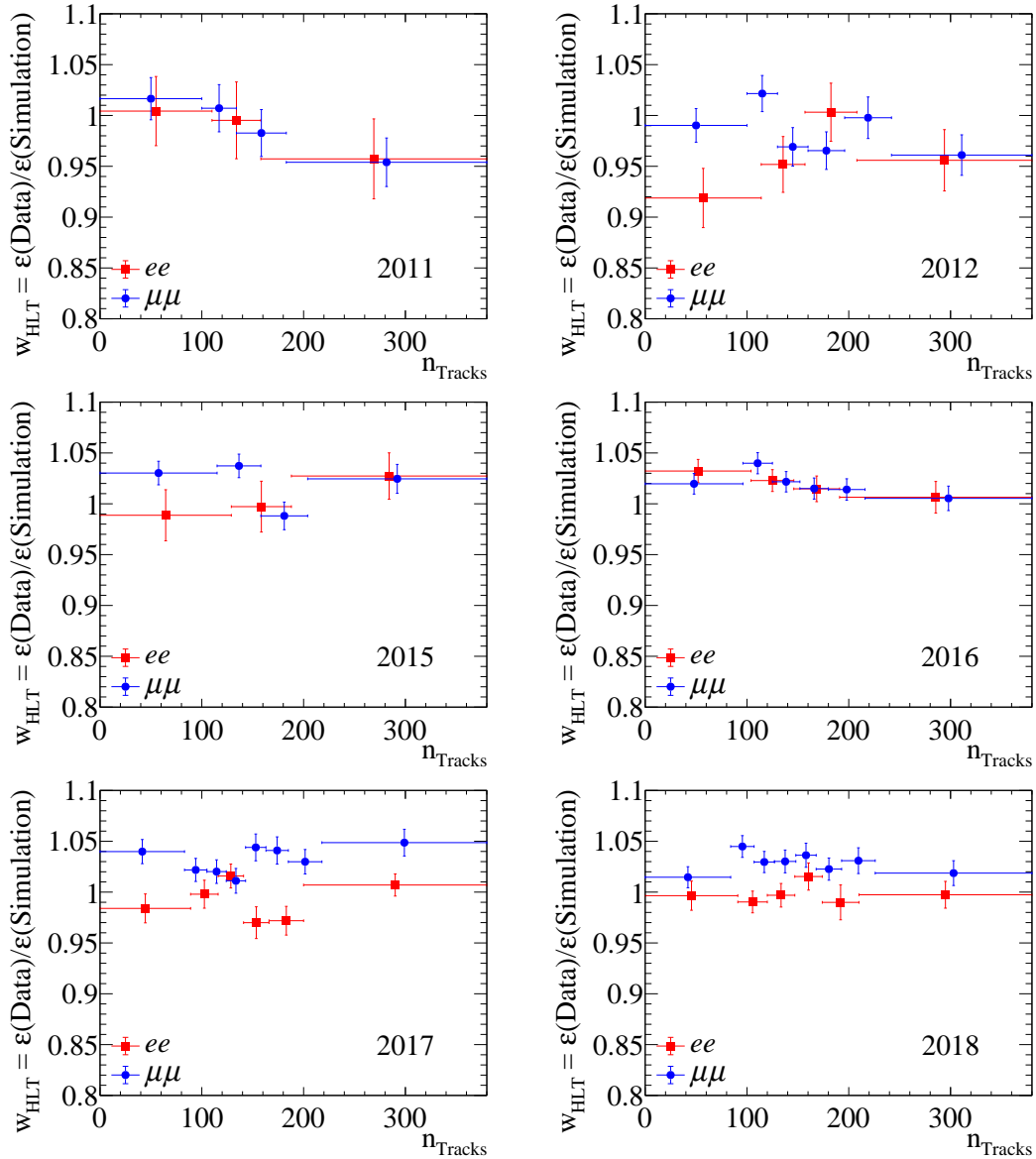


Figure A.15 – HLT calibration weights w_{HLT} of the nominal correction chain computed as the ratio of the trigger efficiency in data and simulation in regions of the n_{Tracks} proxy variable. Shown are weights computed with the $B^0 \rightarrow K^{*0} J/\psi(\rightarrow e^+e^-)$ and $B^0 \rightarrow K^{*0} J/\psi(\rightarrow \mu^+\mu^-)$ decay channels for the L0L trigger category in years (from left to right and top to bottom) 2011-2018.

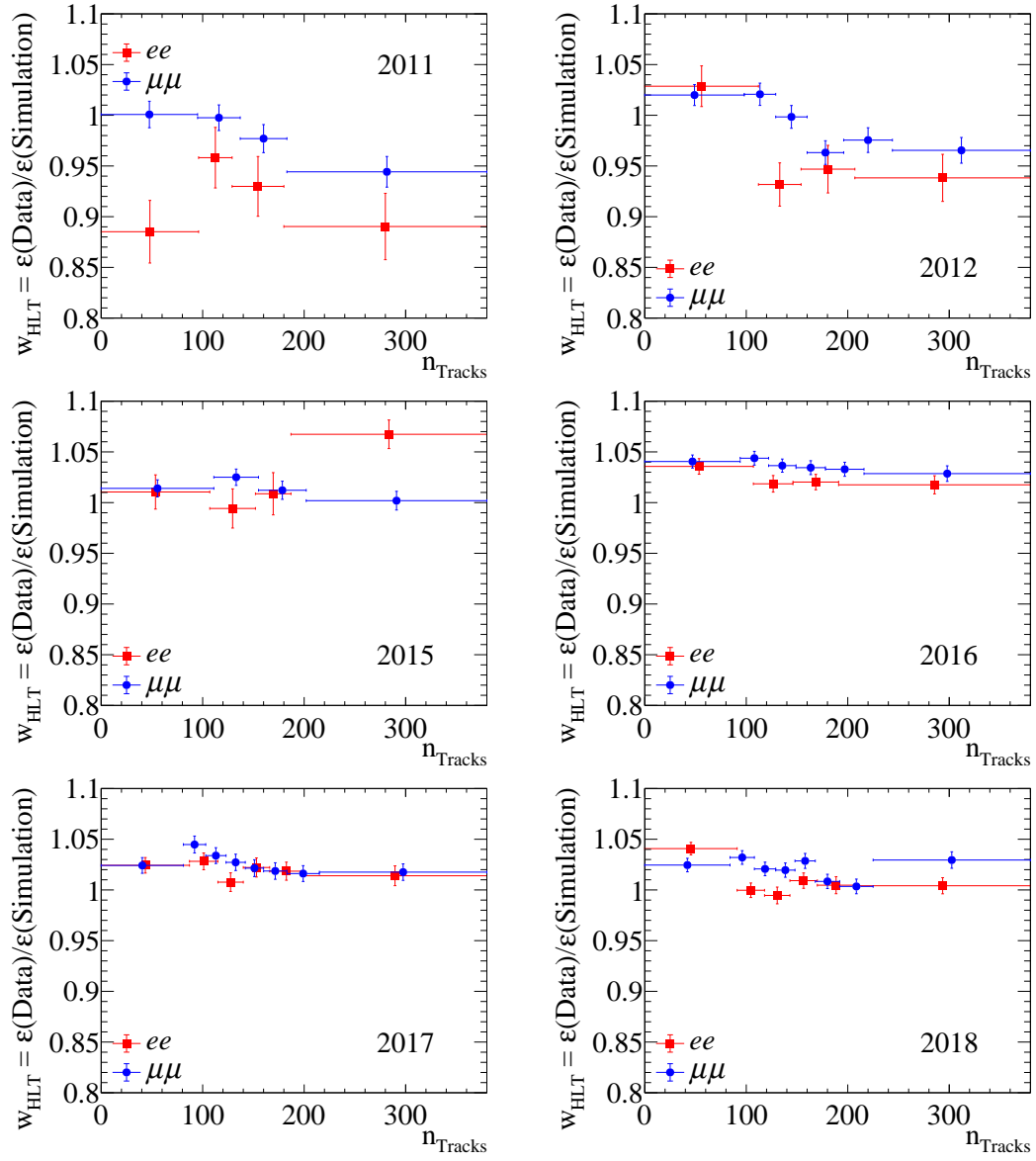


Figure A.16 – HLT calibration weights w_{HLT} of the nominal correction chain computed as the ratio of the trigger efficiency in data and simulation in regions of the n_{Tracks} proxy variable. Shown are weights computed with the $B^+ \rightarrow K^+ J/\psi(\rightarrow e^+e^-)$ and $B^+ \rightarrow K^+ J/\psi(\rightarrow \mu^+\mu^-)$ decay channels for the L0L trigger category in years (from left to right and top to bottom) 2011-2018.

A.5 Geometric efficiencies

Table A.4 – Geometric efficiency ϵ_{Geo} for the rare and resonant decay modes.

Sample	$B^0 \rightarrow K^{*0} J/\psi(\rightarrow \mu^+ \mu^-)$	$B^0 \rightarrow K^{*0} J/\psi(\rightarrow e^+ e^-)$	$B^+ \rightarrow K^+ J/\psi(\rightarrow \mu^+ \mu^-)$	$B^+ \rightarrow K^+ J/\psi(\rightarrow e^+ e^-)$
2011 MD	(15.39 ± 0.04)%	(15.30 ± 0.04)%	(15.96 ± 0.04)%	(15.88 ± 0.04)%
2011 MU	(15.43 ± 0.04)%	(15.28 ± 0.04)%	(15.96 ± 0.04)%	(15.82 ± 0.04)%
2012 MD	(15.75 ± 0.03)%	(15.66 ± 0.03)%	(16.30 ± 0.04)%	(16.23 ± 0.03)%
2012 MU	(15.70 ± 0.04)%	(15.64 ± 0.03)%	(16.29 ± 0.04)%	(16.23 ± 0.04)%
2015 MD	(16.78 ± 0.06)%	(16.72 ± 0.06)%	(17.45 ± 0.06)%	(17.12 ± 0.06)%
2015 MU	(16.72 ± 0.06)%	(16.61 ± 0.06)%	(17.36 ± 0.06)%	(17.28 ± 0.06)%
2016 MD	(16.77 ± 0.07)%	(16.67 ± 0.06)%	(17.47 ± 0.06)%	(17.30 ± 0.06)%
2016 MU	(16.71 ± 0.06)%	(16.64 ± 0.06)%	(17.37 ± 0.06)%	(17.27 ± 0.06)%
2017 MD	(16.73 ± 0.06)%	(16.64 ± 0.06)%	(17.32 ± 0.06)%	(17.17 ± 0.06)%
2017 MD	(16.69 ± 0.06)%	(16.62 ± 0.06)%	(17.34 ± 0.06)%	(17.19 ± 0.06)%
2018 MU	(16.68 ± 0.06)%	(16.58 ± 0.06)%	(17.35 ± 0.06)%	(17.30 ± 0.06)%
Sample	$B^0 \rightarrow K^{*0} \psi(2S)(\rightarrow \mu^+ \mu^-)$	$B^0 \rightarrow K^{*0} \psi(2S)(\rightarrow e^+ e^-)$	$B^+ \rightarrow K^+ \psi(2S)(\rightarrow \mu^+ \mu^-)$	$B^+ \rightarrow K^+ \psi(2S)(\rightarrow \mu^+ \mu^-)$
2011 MD	(15.68 ± 0.03)%	(15.61 ± 0.03)%	(16.24 ± 0.03)%	(16.16 ± 0.03)%
2011 MU	(15.66 ± 0.03)%	(15.57 ± 0.03)%	(16.20 ± 0.04)%	(16.13 ± 0.03)%
2012 MD	(15.93 ± 0.04)%	(15.88 ± 0.04)%	(16.63 ± 0.04)%	(16.58 ± 0.04)%
2015 MD	(16.98 ± 0.06)%	(16.91 ± 0.06)%	(17.62 ± 0.06)%	(17.46 ± 0.06)%
2015 MU	(16.86 ± 0.06)%	(16.98 ± 0.05)%	(17.66 ± 0.06)%	(17.54 ± 0.06)%
2016 MD	(17.02 ± 0.06)%	(16.92 ± 0.06)%	(17.67 ± 0.06)%	(17.65 ± 0.06)%
2016 MU	(17.00 ± 0.06)%	(16.97 ± 0.06)%	(17.64 ± 0.06)%	(17.54 ± 0.06)%
2017 MD	(16.88 ± 0.06)%	(16.98 ± 0.06)%	(17.64 ± 0.06)%	(17.60 ± 0.06)%
2017 MU	(16.99 ± 0.06)%	(16.81 ± 0.06)%	(17.65 ± 0.06)%	(17.59 ± 0.06)%
2018 MD	(16.91 ± 0.06)%	(16.82 ± 0.06)%	(17.69 ± 0.06)%	(17.52 ± 0.06)%
2018 MU	(16.98 ± 0.06)%	(16.95 ± 0.06)%	(17.56 ± 0.06)%	(17.60 ± 0.06)%
Sample	$B^0 \rightarrow K^{*0} \mu^+ \mu^-$	$B^0 \rightarrow K^{*0} e^+ e^-$	$B^+ \rightarrow K^+ \mu^+ \mu^-$	$B^+ \rightarrow K^+ e^+ e^-$
2011 MD	(15.64 ± 0.03)%	(16.01 ± 0.03)%	(16.28 ± 0.03)%	(16.11 ± 0.03)%
2011 MU	(15.66 ± 0.03)%	(16.02 ± 0.03)%	(16.21 ± 0.03)%	(16.10 ± 0.03)%
2012 MD	(16.06 ± 0.04)%	(16.33 ± 0.04)%	(16.63 ± 0.04)%	(16.51 ± 0.04)%
2012 MU	(16.07 ± 0.03)%	(16.32 ± 0.04)%	(16.63 ± 0.04)%	(16.49 ± 0.04)%
2015 MD	(17.02 ± 0.05)%	(17.32 ± 0.06)%	(17.67 ± 0.06)%	(17.58 ± 0.06)%
2015 MU	(16.89 ± 0.05)%	(17.31 ± 0.06)%	(17.58 ± 0.06)%	(17.55 ± 0.06)%
2016 MD	(17.07 ± 0.06)%	(17.35 ± 0.06)%	(17.70 ± 0.06)%	(17.62 ± 0.06)%
2016 MU	(16.95 ± 0.06)%	(17.43 ± 0.06)%	(17.68 ± 0.06)%	(17.55 ± 0.06)%
2017 MD	(17.12 ± 0.06)%	(17.38 ± 0.06)%	(17.62 ± 0.06)%	(17.53 ± 0.06)%
2017 MU	(17.00 ± 0.06)%	(17.36 ± 0.06)%	(17.73 ± 0.06)%	(17.58 ± 0.06)%
2018 MD	(16.99 ± 0.06)%	(17.34 ± 0.06)%	(17.69 ± 0.06)%	(17.49 ± 0.06)%
2018 MU	(16.99 ± 0.06)%	(17.36 ± 0.06)%	(17.66 ± 0.06)%	(17.58 ± 0.06)%

Table A.5 – Geometric efficiency for the rare modes as a function of q^2 and data-taking period.

Sample	$B^0 \rightarrow K^{*0} \mu^+ \mu^-$	$B^0 \rightarrow K^{*0} e^+ e^-$	$B^+ \rightarrow K^+ \mu^+ \mu^-$	$B^+ \rightarrow K^+ e^+ e^-$
2011 low q^2	$(16.45 \pm 0.03)\%$	$(16.02 \pm 0.05)\%$	$(17.06 \pm 0.05)\%$	$(16.79 \pm 0.05)\%$
2011 central q^2	$(15.43 \pm 0.02)\%$	$(15.24 \pm 0.04)\%$	$(16.01 \pm 0.02)\%$	$(15.86 \pm 0.02)\%$
2012 low q^2	$(16.76 \pm 0.02)\%$	$(16.36 \pm 0.03)\%$	$(17.38 \pm 0.03)\%$	$(17.03 \pm 0.04)\%$
2012 central q^2	$(15.74 \pm 0.02)\%$	$(15.57 \pm 0.02)\%$	$(16.36 \pm 0.02)\%$	$(16.20 \pm 0.02)\%$
RUN 2 low q^2	$(17.81 \pm 0.03)\%$	$(17.29 \pm 0.04)\%$	$(18.38 \pm 0.04)\%$	$(18.09 \pm 0.04)\%$
RUN 2 central q^2	$(16.73 \pm 0.02)\%$	$(16.60 \pm 0.03)\%$	$(17.42 \pm 0.02)\%$	$(17.25 \pm 0.02)\%$

A.6 Total efficiencies by calibration step

Table A.6 – Uncalibrated efficiencies of selection steps with total uncalibrated efficiency $\varepsilon_{\text{Total}}$ for the $B^+ \rightarrow K^+ J/\psi(\rightarrow \ell^+ \ell^-)$ normalisation mode in RUN 1. Below the total uncalibrated efficiencies the effects of sequentially turning on the calibrations are shown in terms of stepwise calibrated total efficiencies.

Step	L0I e^+e^-	L0I $\mu^+\mu^-$	L0L! e^+e^-	L0L! $\mu^+\mu^-$
ε_{Geo}	16.12%	16.20%	16.12%	16.20%
$\varepsilon_{\text{Stripping}}$	15.06%	32.82%	15.06%	32.82%
$\varepsilon_{\text{ECAL distance}}$	99.78%	100.00%	99.78%	100.00%
$\varepsilon_{\text{Preselection}}$	74.19%	69.59%	74.19%	69.59%
ε_{L0}	24.40%	24.97%	20.42%	60.19%
$\varepsilon_{\text{L0 alignment}}$	100.00%	87.94%	99.21%	87.47%
$\varepsilon_{\text{HLT1}}$	74.25%	81.89%	82.07%	82.14%
$\varepsilon_{\text{HLT2}}$	79.87%	93.22%	92.54%	93.41%
$\varepsilon_{\text{Excl. backgrounds vetoes}}$	85.78%	90.74%	86.32%	90.93%
ε_{MVA}	99.29%	99.39%	99.22%	99.38%
$\varepsilon_{\text{Fit range}}$	99.10%	99.53%	99.27%	99.57%
$\varepsilon_{\text{Total}}$	0.22%	0.56%	0.24%	1.34%
+w _{PID}	0.22%	0.55%	0.23%	1.32%
+w _{TRK}	0.21%	0.55%	0.23%	1.32%
+w _{Mult&Kin}	0.21%	0.57%	0.18%	1.21%
+w _{L0}	0.18%	0.48%	0.19%	1.29%
+w _{HLT}	0.17%	0.47%	0.18%	1.28%
+w _{Reco}	0.17%	0.46%	0.18%	1.28%
+w _{q²} (all B^0 chain)	0.17%	0.46%	0.18%	1.28%
+w _{q²} (all B^+ chain)	0.17%	0.46%	0.17%	1.27%

Table A.7 – Uncalibrated efficiencies of selection steps with total uncalibrated efficiency $\varepsilon_{\text{Total}}$ for the $B^+ \rightarrow K^+ J/\psi(\rightarrow \ell^+ \ell^-)$ normalisation mode in RUN 2P1. Below the total uncalibrated efficiencies the effects of sequentially turning on the calibrations are shown in terms of stepwise calibrated total efficiencies.

Step	L0I e^+e^-	L0I $\mu^+\mu^-$	L0L! e^+e^-	L0L! $\mu^+\mu^-$
ε_{Geo}	17.27%	17.42%	17.27%	17.42%
$\varepsilon_{\text{Stripping}}$	16.08%	33.30%	16.08%	33.30%
$\varepsilon_{\text{ECAL distance}}$	99.72%	100.00%	99.72%	100.00%
$\varepsilon_{\text{Preselection}}$	73.17%	68.55%	73.17%	68.55%
ε_{L0}	24.94%	27.01%	29.17%	53.86%
$\varepsilon_{\text{L0 alignment}}$	100.00%	87.87%	88.73%	86.92%
$\varepsilon_{\text{HLT1}}$	87.19%	92.53%	93.51%	92.68%
$\varepsilon_{\text{HLT2}}$	93.00%	92.87%	97.54%	94.01%
$\varepsilon_{\text{Excl. backgrounds vetoes}}$	88.17%	91.02%	88.82%	91.23%
ε_{MVA}	99.24%	99.40%	99.23%	99.46%
$\varepsilon_{\text{Fit range}}$	99.01%	99.43%	99.23%	99.47%
$\varepsilon_{\text{Total}}$	0.36%	0.73%	0.42%	1.46%
+w _{PID}	0.34%	0.72%	0.39%	1.44%
+w _{TRK}	0.33%	0.72%	0.38%	1.44%
+w _{Mult&Kin}	0.33%	0.76%	0.31%	1.28%
+w _{L0}	0.27%	0.61%	0.32%	1.45%
+w _{HLT}	0.28%	0.62%	0.32%	1.48%
+w _{Reco}	0.28%	0.62%	0.32%	1.48%
+w _{q²} (all B^0 chain)	0.27%	0.62%	0.32%	1.48%
+w _{q²} (all B^+ chain)	0.27%	0.63%	0.32%	1.50%

A.7 Resonant mass fits

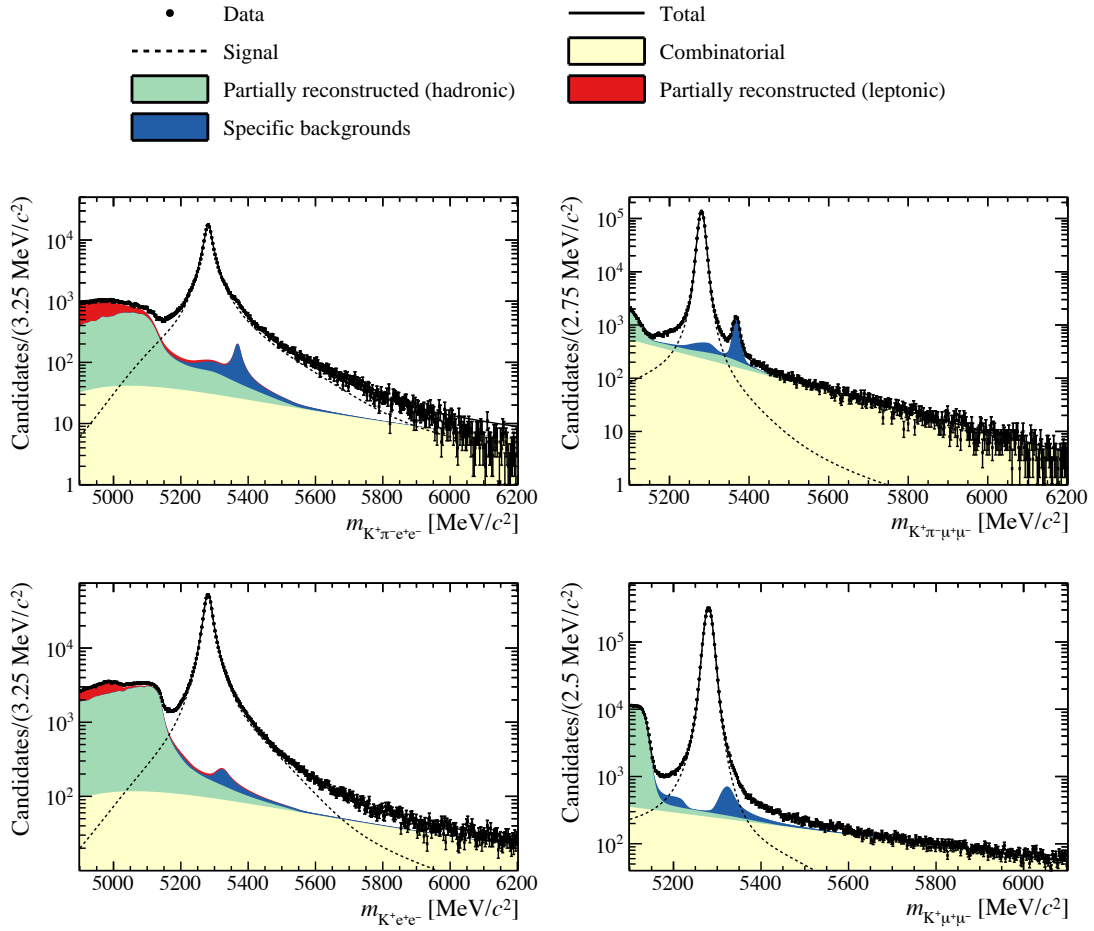


Figure A.17 – Nominal fit to resonant J/ψ modes with DTF J/ψ -mass constraint for the (left) electron and (right) muon final states for all years of data taking. Shown are the (top) B^0 and (bottom) B^+ decay modes. Figures reproduced from Ref.[209]

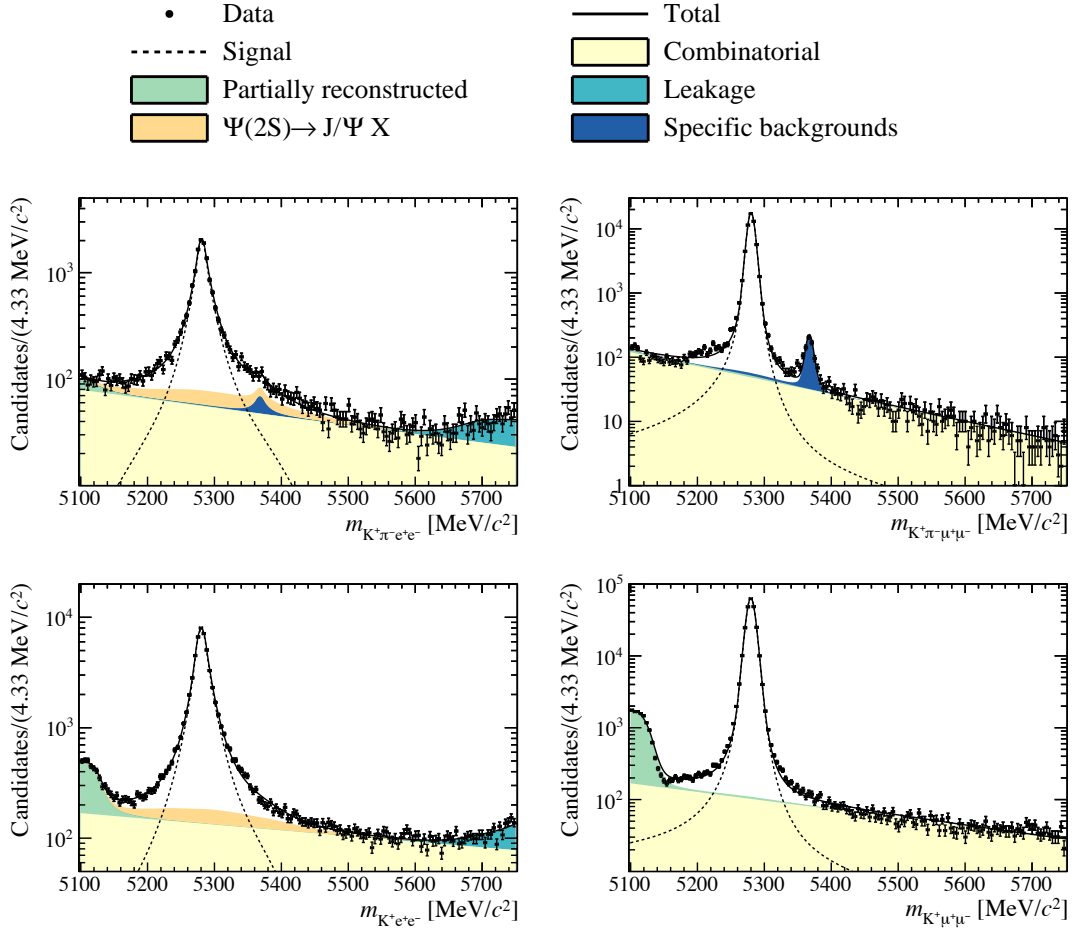


Figure A.18 – Nominal fit to resonant $\psi(2S)$ modes with DTF $\psi(2S)$ -mass constraint for the (left) electron and (right) muon final states for all years of data taking. Shown are the (top) B^0 and (bottom) B^+ decay modes. Figures reproduced from Ref.[209]

A.8 Cross-checks

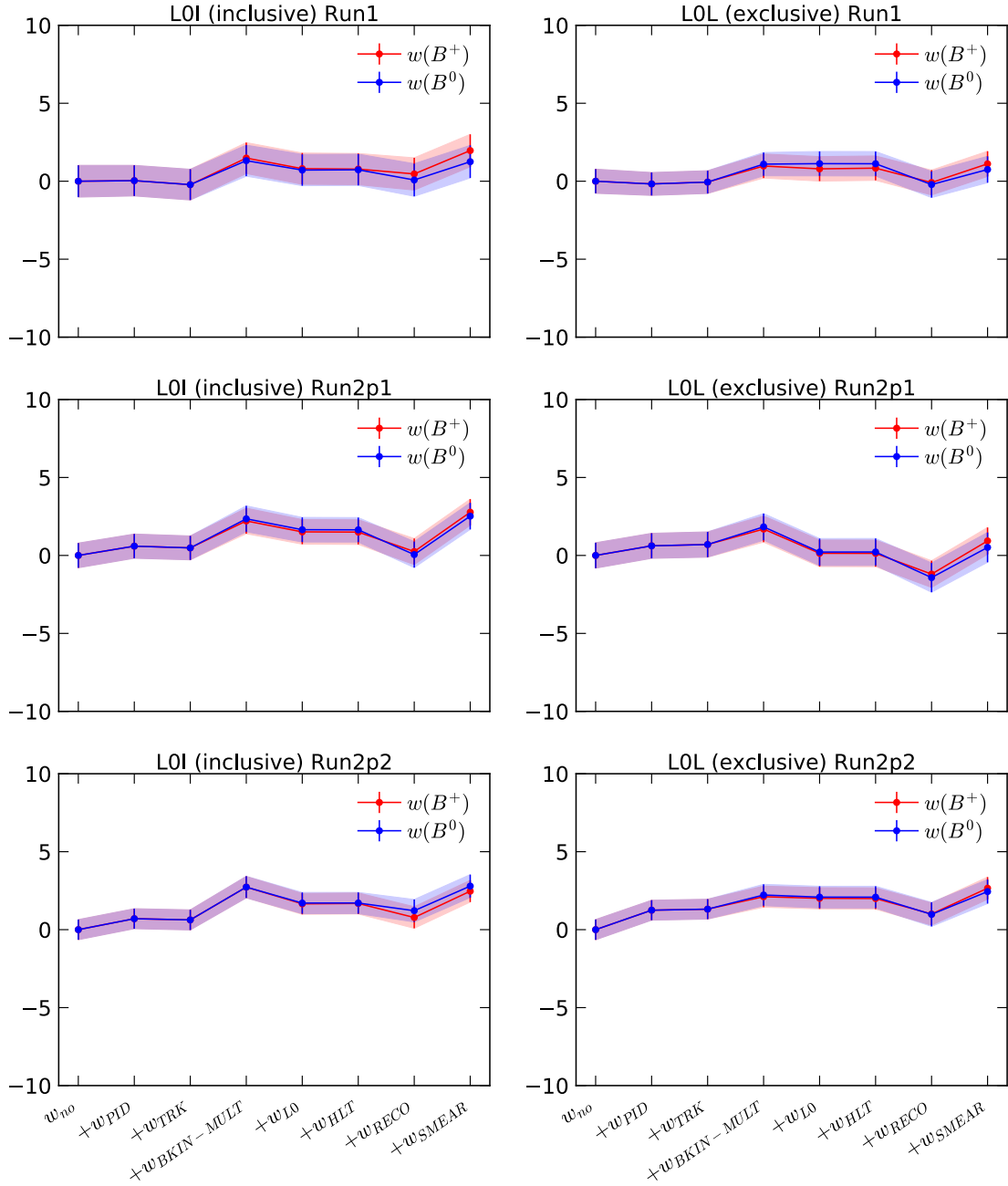


Figure A.19 – Stepwise variation of the efficiency double ratio $\frac{\epsilon_{B^+ \rightarrow K^+ e^+ e^-} \epsilon_{B^+ \rightarrow K^+ \mu^+ \mu^-}}{\epsilon_{B^+ \rightarrow K^+ \psi(\rightarrow \mu^+ \mu^-)} \epsilon_{B^+ \rightarrow K^+ \psi(\rightarrow e^+ e^-)}}$ as a function of the calibration steps in the central- q^2 region. The values shown are the relative differences in % of the double ratios to the double ratio with no calibration applied. The efficiency calibrations are either computed with the procedure based on the (red) B^+ or the (blue) B^0 calibration samples. The uncertainty bands include the statistical uncertainty based on the limited size of the simulation samples and the *resampling* uncertainties of the calibration chain and their correlations.

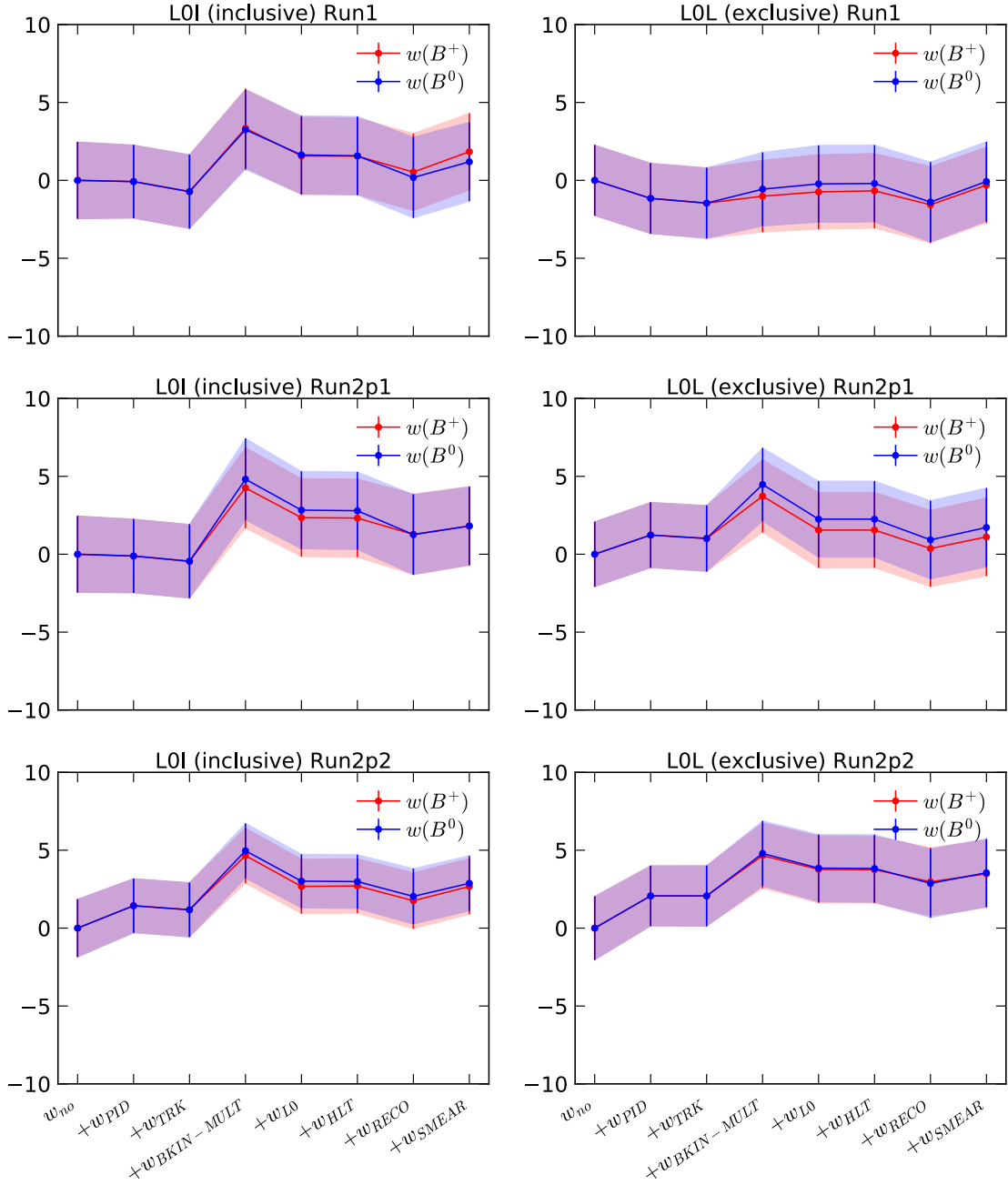


Figure A.20 – Stepwise variation of the efficiency double ratio $\frac{\epsilon_{B^0 \rightarrow K^*0} \epsilon_{e^+ e^-} \epsilon_{B^0 \rightarrow K^*0} J/\psi(\rightarrow \mu^+ \mu^-)}{\epsilon_{B^0 \rightarrow K^*0} \mu^+ \mu^- \epsilon_{B^0 \rightarrow K^*0} J/\psi(\rightarrow e^+ e^-)}$ as a function of the calibration steps in the low- q^2 region. The values shown are the relative differences in % of the double ratios to the double ratio with no calibration applied. The efficiency calibrations are either computed with the procedure based on the (red) B^+ or the (blue) B^0 calibration samples. The uncertainty bands include the statistical uncertainty based on the limited size of the simulation samples and the *resampling* uncertainties of the calibration chain and their correlations.

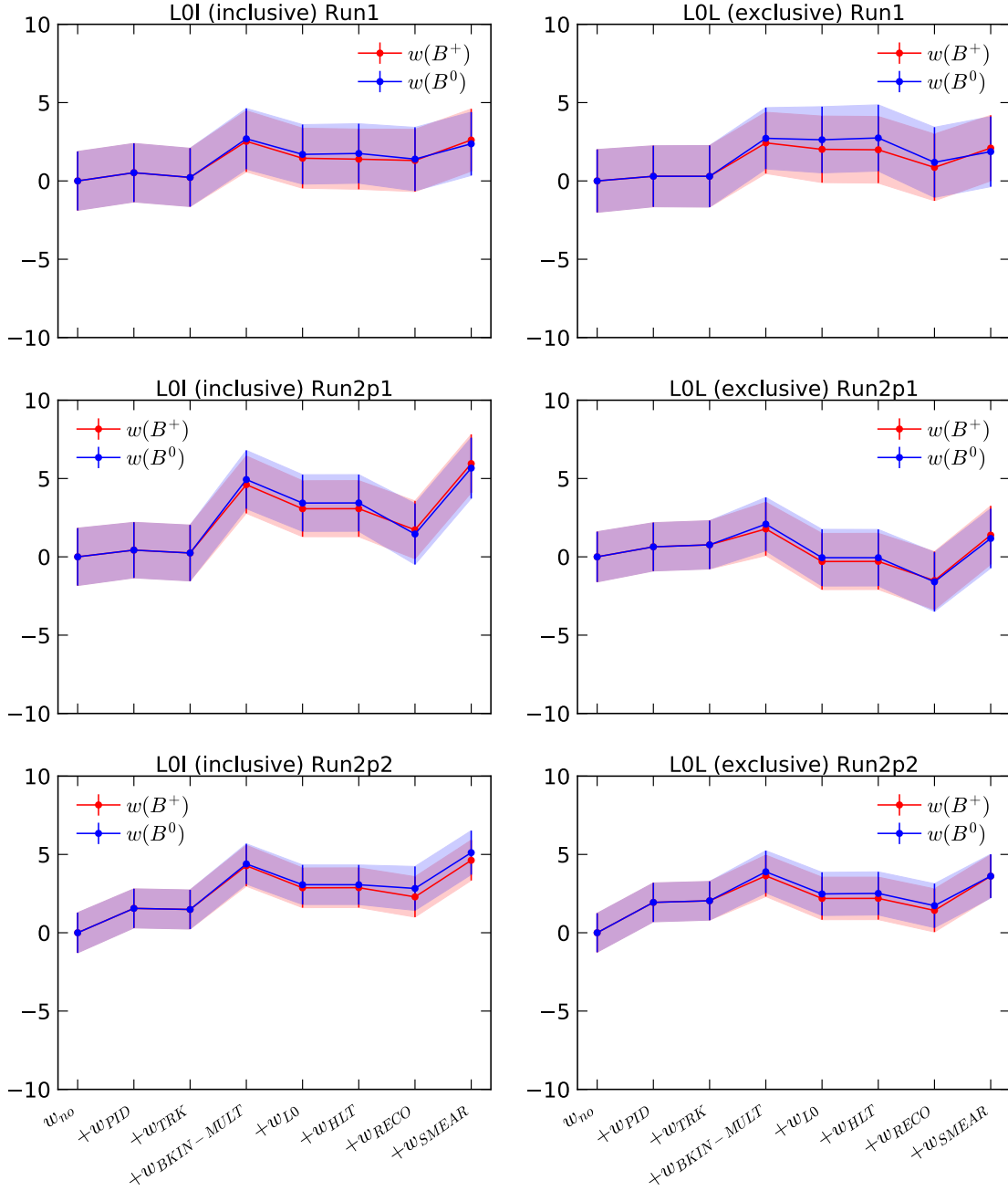


Figure A.21 – Stepwise variation of the efficiency double ratio $\frac{\epsilon_{B^+ \rightarrow K^+ e^+ e^-} \cdot \epsilon_{B^+ \rightarrow K^+ \mu^+ \mu^-}}{\epsilon_{B^+ \rightarrow K^+ J/\psi(\rightarrow \mu^+ \mu^-)} \cdot \epsilon_{B^+ \rightarrow K^+ J/\psi(\rightarrow e^+ e^-)}}$ as a function of the calibration steps in the low- q^2 region. The values shown are the relative differences in % of the double ratios to the double ratio with no calibration applied. The efficiency calibrations are either computed with the procedure based on the (red) B^+ or the (blue) B^0 calibration samples. The uncertainty bands include the statistical uncertainty based on the limited size of the simulation samples and the *resampling* uncertainties of the calibration chain and their correlations.

Bibliography

- [1] A. Einstein, *Näherungsweise Integration der Feldgleichungen der Gravitation*, Sitzungsberichte der Preußischen Akademie der Wissenschaften 1914–1932 (1916) 99–108 (cited on page 1).
- [2] B. P. Abbott *et al.*, LIGO scientific collaboration and Virgo collaboration, *Observation of gravitational waves from a binary black hole merger*, Phys. Rev. Lett. **116.6** (2016) 061102, DOI: 10.1103/PhysRevLett.116.061102 (cited on page 1).
- [3] S. L. Glashow, *Partial-symmetries of weak interactions*, Nucl. Phys. **22.4** (1961) 579–588, DOI: 10.1016/0029-5582(61)90469-2 (cited on pages 1, 5).
- [4] A. Salam and J. C. Ward, *Electromagnetic and weak interactions*, Phys. Lett. **13.2** (1964) 168–171, DOI: 10.1016/0031-9163(64)90711-5 (cited on pages 1, 5).
- [5] S. Weinberg, *A model of leptons*, Phys. Rev. Lett. **19.21** (1967) 1264–1266, DOI: 10.1103/PhysRevLett.19.1264 (cited on pages 1, 5).
- [6] M. Gell-Mann and Y. Ne’eman, *The eightfold way*, W.A. Benjamin, 1964 (cited on pages 1, 5, 6).
- [7] F. Englert and R. Brout, *Broken symmetry and the mass of gauge vector mesons*, Phys. Rev. Lett. **13.9** (1964) 321–323, DOI: 10.1103/PhysRevLett.13.321 (cited on pages 1, 7).
- [8] P. W. Higgs, *Broken symmetries, massless particles and gauge fields*, Phys. Lett. **12.2** (1964) 132–133, DOI: 10.1016/0031-9163(64)91136-9 (cited on pages 1, 7).
- [9] P. W. Higgs, *Broken symmetries and the masses of gauge bosons*, Phys. Rev. Lett. **13.16** (1964) 508–509, DOI: 10.1103/PhysRevLett.13.508 (cited on pages 1, 7).
- [10] G. Aad *et al.*, ATLAS collaboration, *Observation of a new particle in the search for the Standard Model Higgs boson with the ATLAS detector at the LHC*, Phys. Lett. B **716.1** (2012) 1–29, DOI: 10.1016/j.physletb.2012.08.020 (cited on pages 1, 8, 27).
- [11] S. Chatrchyan *et al.*, CMS collaboration, *Observation of a new boson at a mass of 125 GeV with the CMS experiment at the LHC*, Phys. Lett. B **716.1** (2012) 30–61, DOI: 10.1016/j.physletb.2012.08.021 (cited on pages 1, 8, 27).
- [12] V. Trimble, *Existence and nature of dark matter in the universe*, Ann. Rev. Astron. Astrophys. **25.1** (1987) 425–472, DOI: 10.1146/annurev.aa.25.090187.002233 (cited on pages 1, 8).

- [13] S. Turner and D. Huterer, *Cosmic acceleration, dark energy, and fundamental physics*, J. Phys. Soc. Jap. **76**.11 (2007) 111015, DOI: 10.1143/JPSJ.76.111015 (cited on pages 1, 8).
- [14] N. Aghanim *et al.*, Planck collaboration, *Planck 2018 results - VI. Cosmological parameters*, A&A **641**.A6 (2020) 67, DOI: 10.1051/0004-6361/201833910 (cited on pages 1, 8).
- [15] Y. Fukuda *et al.*, Super-Kamiokande collaboration, *Evidence for oscillation of atmospheric neutrinos*, Phys. Rev. Lett. **81**.8 (1998) 1562–1567, DOI: 10.1103/PhysRevLett.81.1562 (cited on pages 1, 8, 9).
- [16] Q. R. Ahmad *et al.*, SNO collaboration, *Measurement of the rate of $\nu_e + d \rightarrow p + p + e^-$ interactions produced by ^8B solar neutrinos at the Sudbury Neutrino Observatory*, Phys. Rev. Lett. **87**.7 (2001) 071301, DOI: 10.1103/PhysRevLett.87.071301 (cited on pages 1, 8).
- [17] Q. R. Ahmad *et al.*, SNO collaboration, *Direct evidence for neutrino flavor transformation from neutral current interactions in the Sudbury Neutrino Observatory*, Phys. Rev. Lett. **89**.1 (2002) 11301, DOI: 10.1103/PhysRevLett.89.011301 (cited on pages 1, 8, 9).
- [18] L. Canetti, M. Drewes and M. Shaposhnikov, *Matter and antimatter in the universe*, New J. Phys. **14**.9 (2012) 095012, DOI: 10.1088/1367-2630/14/9/095012 (cited on pages 1, 8).
- [19] S. Dimopoulos and L. Susskind, *Baryon asymmetry in the very early universe*, Phys. Lett. B **81**.3-4 (1979) 416–418, DOI: 10.1016/0370-2693(79)90366-6 (cited on pages 1, 8).
- [20] A. J. Buras, *Flavour expedition to the zeptouniverse*, PoS FWNP (2015) 3, DOI: 10.22323/1.220.0003 (cited on page 2).
- [21] A. J. Buras and J. Girrbach, *Towards the identification of new physics through quark flavour violating processes*, Rep. Prog. Phys. **77**.8 (2014) 086201, DOI: 10.1088/0034-4885/77/8/086201 (cited on page 2).
- [22] R. Aaij *et al.*, LHCb collaboration, *Test of lepton universality with $B^0 \rightarrow K^{*0} \ell^+ \ell^-$ decays*, J. High Energ. Phys. **08** (2017) 055, DOI: 10.1007/JHEP08(2017)055 (cited on pages 2, 20, 21, 49, 53, 59, 143, 144).
- [23] R. Aaij *et al.*, LHCb collaboration, *Test of lepton universality in beauty-quark decays*, Nature Phys. **18**.3 (2022) 277–282, DOI: 10.1038/s41567-021-01478-8 (cited on pages 2, 20, 21, 49, 143, 144).
- [24] R. Aaij *et al.*, LHCb collaboration, *Test of lepton universality using $B^+ \rightarrow K^+ \ell^+ \ell^-$ decays*, Phys. Rev. Lett. **113**.15 (2014) 151601, DOI: 10.1103/PhysRevLett.113.151601 (cited on pages 3, 20, 144).
- [25] D. Griffiths, *Introduction to elementary particles*, John Wiley & Sons, 2020 (cited on pages 5, 9).

- [26] F. Halzen and A. D. Martin, *Quark & leptons: an introductory course in modern particle physics*, John Wiley & Sons, 1984 (cited on page 5).
- [27] P. A. Zyla *et al.*, Particle Data Group, *Review of particle physics and 2021 update*, PTEP **2020.8** (2020), DOI: 10.1093/ptep/ptaa104 (cited on pages 6, 7, 9, 18, 44).
- [28] S.-K. Choi *et al.*, *Observation of a narrow charmoniumlike state in exclusive $B^\pm \rightarrow K^\pm \pi^+ \pi^- J/\psi$ decays*, Phys. Rev. Lett. **91.26** (2003) 262001, DOI: 10.1103/PhysRevLett.91.262001 (cited on page 6).
- [29] R. Aaij *et al.*, LHCb collaboration, *Observation of $J/\psi\phi$ structures consistent with exotic states from amplitude analysis of $B^+ \rightarrow J/\psi\phi K^+$ decays*, Phys. Rev. Lett. **118.2** (2017) 022003, DOI: 10.1103/PhysRevLett.118.022003 (cited on page 6).
- [30] R. Aaij *et al.*, LHCb collaboration, *Observation of $J/\psi p$ resonances consistent with pentaquark states in $\Lambda_b^0 \rightarrow J/\psi p K^-$ decays*, Phys. Rev. Lett. **115.7** (2015) 072001, DOI: 10.1103/PhysRevLett.115.072001 (cited on page 6).
- [31] R. Aaij *et al.*, LHCb collaboration, *Observation of a narrow pentaquark state, $P_c(4312)^+$, and of the two-peak structure of the $P_c(4450)^+$* , Phys. Rev. Lett. **122.22** (2019) 22001, DOI: 10.1103/physrevlett.122.222001 (cited on page 6).
- [32] LHCb collaboration, *List of hadrons observed at the LHC*, LHCb-FIGURE-2021-001 (2021), <https://cds.cern.ch/record/2749030> (cited on page 6).
- [33] P. Koppenburg, *New particles discovered at the LHC*, 2022, <https://www.nikhef.nl/~pkoppenb/particles.html> (visited on 25/03/2022) (cited on page 6).
- [34] M. Aker *et al.*, KATRIN collaboration, *Direct neutrino-mass measurement with sub-electronvolt sensitivity*, Nature Phys. **18.2** (2022) 160–166, DOI: 10.1038/s41567-021-01463-1 (cited on page 7).
- [35] Y. Ne’eman, *Derivation of strong interactions from a gauge invariance*, Nucl. Phys. **26.2** (1961) 222–229, DOI: 10.1016/0029-5582(61)90134-1 (cited on page 6).
- [36] D. J. Gross and F. Wilczek, *Ultraviolet behavior of nonabelian gauge theories*, Phys. Rev. Lett. **30.26** (1973) 1343–1346, DOI: 10.1103/PhysRevLett.30.1343 (cited on page 7).
- [37] H. D. Politzer, *Reliable perturbative results for strong interactions?*, Phys. Rev. Lett. **30.26** (1973) 1346–1349, DOI: 10.1103/PhysRevLett.30.1346 (cited on page 7).
- [38] K. Nishijima, *Charge independence theory of V particles*, Prog. Theor. Phys. **13.3** (1955) 285–304, DOI: 10.1143/PTP.13.285 (cited on page 7).
- [39] M. Gell-Mann, *The interpretation of the new particles as displaced charge multiplets*, Nuovo Cim. **4.S2** (1956) 848–866, DOI: 10.1007/BF02748000 (cited on page 7).

- [40] N. Cabibbo, *Unitary symmetry and leptonic decays*, Phys. Rev. Lett. **10**.12 (1963) 531–533, DOI: 10.1103/PhysRevLett.10.531 (cited on page 9).
- [41] M. Kobayashi and T. Maskawa, *CP-violation in the renormalizable theory of weak interaction*, Progr. Theor. Exp. Phys. **49**.2 (1973) 652, DOI: 10.1143/PTP.49.652 (cited on page 9).
- [42] K. Eguchi *et al.*, KamLAND collaboration, *First results from KamLAND: evidence for reactor antineutrino disappearance*, Phys. Rev. Lett. **90**.2 (2003) 021802, DOI: 10.1103/PhysRevLett.90.021802 (cited on page 9).
- [43] B. Pontecorvo, *Inverse beta processes and nonconservation of lepton charge*, Zhur. Eksptl'. i Teoret. Fiz. **34** (1958), <https://www.osti.gov/biblio/4349231> (cited on page 9).
- [44] B. Pontecorvo, *Mesonium and antimesonium*, Zhur. Eksptl'. i Teoret. Fiz. **33** (1957), <https://www.osti.gov/biblio/4343073> (cited on page 9).
- [45] Z. Maki, M. Nakagawa and S. Sakata, *Remarks on the unified model of elementary particles*, Prog. Theor. Phys. **28**.5 (1962) 870–880, DOI: 10.1143/PTP.28.870 (cited on page 9).
- [46] A. Tumasyan *et al.*, CMS collaboration, *Search for new particles in events with energetic jets and large missing transverse momentum in proton-proton collisions at $\sqrt{s} = 13$ TeV*, J. High Energ. Phys. **11** (2021) 153, DOI: 10.1007/JHEP11(2021)153 (cited on page 9).
- [47] G. Aad *et al.*, ATLAS collaboration, *Search for new phenomena in pp collisions in final states with tau leptons, b-jets, and missing transverse momentum with the ATLAS detector*, Phys. Rev. D **104**.11 (2021) 112005, DOI: 10.1103/PhysRevD.104.112005 (cited on page 9).
- [48] J. H. Christenson *et al.*, *Evidence for the 2π decay of the K_2^0 meson*, Phys. Rev. Lett. **13**.4 (1964) 138–140, DOI: 10.1103/PhysRevLett.13.138 (cited on page 9).
- [49] S. W. Herb, D. C. Hom, L. M. Lederman *et al.*, *Observation of a dimuon resonance at 9.5 GeV in 400-GeV proton-nucleus collisions*, Phys. Rev. Lett. **39**.5 (1977) 252–255, DOI: 10.1103/PhysRevLett.39.252 (cited on page 9).
- [50] H. Albrecht *et al.*, ARGUS collaboration, *Observation of $B^0 - \bar{B}^0$ mixing*, Phys. Lett. B **192**.1-2 (1987) 245–252, DOI: 10.1016/0370-2693(87)91177-4 (cited on page 9).
- [51] F. Abe *et al.*, CDF collaboration, *Observation of top quark production in $\bar{p}p$ collisions with the Collider Detector at Fermilab*, Phys. Rev. Lett. **74**.14 (1995) 2626–2631, DOI: 10.1103/physrevlett.74.2626 (cited on page 9).
- [52] S. Abachi *et al.*, D0 collaboration, *Search for high mass top quark production in $p\bar{p}$ collisions at $\sqrt{s} = 1.8$ TeV*, Phys. Rev. Lett. **74**.13 (1995) 2422–2426, DOI: 10.1103/physrevlett.74.2422 (cited on page 9).

- [53] S. L. Glashow, J. Iliopoulos and L. Maiani, *Weak interactions with lepton-hadron symmetry*, Phys. Rev. D **2.7** (1970) 1285–1292, DOI: 10.1103/PhysRevD.2.1285 (cited on page 10).
- [54] A. J. Buras *et al.*, *Can we reach the zeptouniverse with rare K and $B_{s,d}$ decays?*, J. High Energ. Phys. **11** (2014) 121, DOI: 10.1007/jhep11(2014)121 (cited on page 10).
- [55] A. Bharucha *et al.*, *Implications of LHCb measurements and future prospects*, Eur. Phys. J. **73.4** (2013) 2373, DOI: 10.1140/epjc/s10052-013-2373-2 (cited on page 10).
- [56] G. Isidori, Y. Nir and G. Perez, *Flavor physics constraints for physics beyond the standard model*, Ann. Rev. Nucl. Part. Sci. **60.1** (2010) 355–380, DOI: 10.1146/annurev.nucl.012809.104534 (cited on page 10).
- [57] T. Blake, T. Gershon and G. Hiller, *Rare b hadron decays at the LHC*, Ann. Rev. Nucl. Part. Sci. **65.1** (2015) 113–143, DOI: 10.1146/annurev-nucl-102014-022231 (cited on page 10).
- [58] R. Aaij *et al.*, LHCb collaboration, *Physics case for an LHCb upgrade II - opportunities in flavour physics, and beyond, in the HL-LHC era*, CERN-LHCC-2018-027 (2018), arXiv:1808.08865 [hep-ex] (cited on pages 10, 146).
- [59] Y. Wang and D. Atwood, *Rate difference between $\vec{b} s \mu^+ \mu^-$ and $\vec{b} s e^+ e^-$ in supersymmetry with large $\tan \beta$* , Phys. Rev. D **68.9** (2003) 094016, DOI: 10.1103/PhysRevD.68.094016 (cited on page 11).
- [60] G. Hiller and F. Kruger, *More model-independent analysis of $b \rightarrow s$ processes*, Phys. Rev. D **69.7** (2004) 074020, DOI: 10.1103/PhysRevD.69.074020 (cited on pages 11, 19).
- [61] S. Bifani *et al.*, *Review of lepton universality tests in B decays*, J. Phys. G: Nucl. Part. Phys. **46.2** (2019) 023001, DOI: 10.1088/1361-6471/aaf5de (cited on pages 12, 15, 51).
- [62] R. Aaij *et al.*, LHCb collaboration, *Differential branching fractions and isospin asymmetries of $\rightarrow K^{(*)} \mu^+ \mu^-$ decays*, J. High Energ. Phys. **06** (2014) 133, DOI: 10.1007/JHEP06(2014)133 (cited on pages 13, 15, 16).
- [63] K. Abe *et al.*, Belle collaboration, *Observation of the decay $B \rightarrow K \ell^+ \ell^-$* , Phys. Rev. Lett. **88.2** (2001) 021801, DOI: 10.1103/physrevlett.88.021801 (cited on page 14).
- [64] A. Ishikawa *et al.*, Belle collaboration, *Observation of $B \rightarrow K^* \ell^+ \ell^-$* , Phys. Rev. Lett. **91.26** (2003) 261601, DOI: 10.1103/PhysRevLett.91.261601 (cited on page 14).
- [65] D. London and J. Matias, *B Flavour Anomalies: 2021 Theoretical Status Report* (2021), arXiv:2110.13270v2 [hep-ph] (cited on pages 15, 24).

- [66] J. Albrecht, D. van Dyk and C. Langenbruch, *Flavour anomalies in heavy quark decays*, Prog. Part. and Nucl. Phys. **120** (2021) 103885, DOI: 10.1016/j.pnnp.2021.103885 (cited on pages 15, 16, 24).
- [67] R. Aaij *et al.*, LHCb collaboration, *Measurements of the S-wave fraction in $B^0 \rightarrow K^+ \pi^- \mu^+ \mu^-$ decays and the $B^0 \rightarrow K^*(892)^0 \mu^+ \mu^-$ differential branching fraction*, J. High Energy Phys. **11** (2016) 047, DOI: 10.1007/JHEP11(2016)047, [Erratum: J. High Energy Phys. 04 (2017) 142] (cited on pages 15, 16).
- [68] R. Aaij *et al.*, LHCb collaboration, *Angular analysis and differential branching fraction of the decay $B_s^0 \rightarrow \phi \mu^+ \mu^-$* , J. High Energy Phys. **09** (2015) 179, DOI: 10.1007/JHEP09(2015)179 (cited on pages 15, 16, 17).
- [69] R. Aaij *et al.*, LHCb collaboration, *Branching fraction measurements of the rare $B_s^0 \rightarrow \phi \mu^+ \mu^-$ and $B_s^0 \rightarrow f_2'(1525) \mu^+ \mu^-$ decays*, Phys. Rev. Lett. **127.15** (2021) 151801, DOI: 10.1103/PhysRevLett.127.151801 (cited on pages 15, 16).
- [70] R. Aaij *et al.*, LHCb collaboration, *Differential branching fraction and angular analysis of $\Lambda_b^0 \rightarrow \Lambda \mu^+ \mu^-$ decays*, J. High Energy Phys. **06** (2015) 115, DOI: 10.1007/JHEP06(2015)115, [Erratum: J. High. Energy Phys. 09, 145 (2018)] (cited on pages 15, 16).
- [71] V. Khachatryan *et al.*, CMS collaboration, *Angular analysis of the decay $B^0 \rightarrow K^{*0} \mu^+ \mu^-$ from pp collisions at $\sqrt{s}=8$ TeV*, Phys. Lett. B **753** (2016) 424–448, DOI: 10.1016/j.physletb.2015.12.020 (cited on pages 15, 16, 17).
- [72] J.-T. Wei *et al.*, Belle collaboration, *Measurement of the differential branching fraction and forward-backward asymmetry for $B \rightarrow K^{(*)} l^+ l^-$* , Phys. Rev. Lett. **103.17** (2009) 171801, DOI: 10.1103/PhysRevLett.103.171801 (cited on pages 15, 16, 17, 20).
- [73] J. P. Lees *et al.*, BaBar collaboration, *Measurement of branching fractions and rate asymmetries in the rare decays $B \rightarrow K^{(*)} \ell^+ \ell^-$* , Phys. Rev. D **86.3** (2012) 032012, DOI: 10.1103/physrevd.86.032012 (cited on pages 15, 16, 20, 21).
- [74] T. Aaltonen *et al.*, CDF collaboration, *Observation of the baryonic flavor-changing neutral current decay $\Lambda_b^0 \rightarrow \Lambda \mu^+ \mu^-$* , Phys. Rev. Lett. **107.20** (2011) 201802, DOI: 10.1103/physrevlett.107.201802 (cited on pages 15, 16).
- [75] A. Bharucha, D. M. Straub and R. Zwicky, *$B \rightarrow V \ell^+ \ell^-$ in the standard model from light-cone sum rules*, J. High Energy Phys. **08** (2016) 98, DOI: 10.1007/jhep08(2016)098 (cited on pages 15, 16, 17, 19).
- [76] R. R. Horgan *et al.*, *Rare B decays using lattice QCD form factors*, PoS LATTICE2014 (2015) 372, DOI: 10.22323/1.214.0372 (cited on pages 15, 16, 17).
- [77] R. R. Horgan *et al.*, *Lattice QCD calculation of form factors describing the rare decays $B \rightarrow K^* \ell^+ \ell^-$ and $B_s^0 \rightarrow \phi \ell^+ \ell^-$* , Phys. Rev. D **89.9** (2014) 094501, DOI: 10.1103/physrevd.89.094501 (cited on pages 15, 16, 17).

- [78] S. Descotes-Genon *et al.*, *Optimizing the basis of $B \rightarrow K^* \ell \ell$ observables in the full kinematic range*, J. High Energ. Phys. **5** (2013) 137, DOI: 10.1007/jhep05(2013)137 (cited on pages 17, 21).
- [79] A. M. Sirunyan *et al.*, CMS collaboration, *Measurement of angular parameters from the decay $B^0 \rightarrow K^{*0} \mu^+ \mu^-$ in proton–proton collisions at $\sqrt{s} = 8$ TeV*, Phys. Lett. B **781** (2018) 517–541, DOI: 10.1016/j.physletb.2018.04.030 (cited on page 17).
- [80] A. M. Sirunyan *et al.*, CMS collaboration, *Angular analysis of the decay $B^+ \rightarrow K^*(892) \mu^+ \mu^-$ in proton–proton collisions at $\sqrt{s} = 8$ TeV*, J. High Energ. Phys. **2021** (2021) 124, DOI: 10.1007/jhep04(2021)124 (cited on page 17).
- [81] T. Aaltonen *et al.*, CDF collaboration, *Measurements of the angular distributions in the decays $B \rightarrow K^{(*)} \mu^+ \mu^-$ at CDF*, Phys. Rev. Lett. **108.8** (2012) 081807, DOI: 10.1103/physrevlett.108.081807 (cited on page 17).
- [82] M. Aaboud *et al.*, ATLAS collaboration, *Angular analysis of $B_d^0 \rightarrow K^{*0} \mu^+ \mu^-$ decays in pp collisions at $\sqrt{s} = 8$ TeV with the ATLAS detector*, J. High Energ. Phys. **10** (2018) 047, DOI: 10.1007/JHEP10(2018)047 (cited on page 17).
- [83] B. Aubert *et al.*, BaBar collaboration, *Measurements of branching fractions, rate asymmetries, and angular distributions in the rare decays $B \rightarrow K \ell^+ \ell^-$ and $B \rightarrow K^* \ell^+ \ell^-$* , Phys. Rev. D **73.9** (2006), DOI: 10.1103/physrevd.73.092001 (cited on page 17).
- [84] J. P. Lees *et al.*, BaBar collaboration, *Measurement of angular asymmetries in the decays $B \rightarrow K^* \ell^+ \ell^-$* , Phys. Rev. D **93.5** (2016) 052015, DOI: 10.1103/physrevd.93.052015 (cited on page 17).
- [85] R. Aaij *et al.*, LHCb collaboration, *Measurement of form-factor-independent observables in the decay $B^0 \rightarrow K^{*0} \mu^+ \mu^-$* , Phys. Rev. Lett. **111.19** (2013) 191801, DOI: 10.1103/PhysRevLett.111.191801 (cited on page 17).
- [86] R. Aaij *et al.*, LHCb collaboration, *Angular analysis of the $B^0 \rightarrow K^{*0} \mu^+ \mu^-$ decay using 3 fb^{-1} of integrated luminosity*, J. High Energ. Phys. **02** (2016) 104, DOI: 10.1007/JHEP02(2016)104 (cited on page 17).
- [87] R. Aaij *et al.*, LHCb collaboration, *Measurement of CP-averaged observables in the $B^0 \rightarrow K^{*0} \mu^+ \mu^-$ decay*, Phys. Rev. Lett. **125.1** (2020) 011802, DOI: 10.1103/PhysRevLett.125.011802 (cited on page 17).
- [88] R. Aaij *et al.*, LHCb collaboration, *Angular analysis of the $B^+ \rightarrow K^{*+} \mu^+ \mu^-$ decay*, Phys. Rev. Lett. **126.16** (2021) 161802, DOI: 10.1103/PhysRevLett.126.161802, eprint: 2012.13241 (cited on page 17).
- [89] S. Wehle *et al.*, Belle collaboration, *Lepton-flavor-dependent angular analysis of $B \rightarrow K^* \ell^+ \ell^-$* , Phys. Rev. Lett. **118.11** (2017) 111801, DOI: 10.1103/PhysRevLett.118.111801 (cited on pages 17, 21).

- [90] R. Aaij *et al.*, LHCb collaboration, *Angular analysis of the rare decay $B_s^0 \rightarrow \phi \mu^+ \mu^-$* , J. High Energ. Phys. **11** (2021) 043, DOI: 10.1007/JHEP11(2021)043 (cited on page 17).
- [91] M. Ablikim *et al.*, BESIII collaboration, *Precision measurements of $B[\psi(3686) \rightarrow \pi^+ \pi^- J/\psi]$ and $B[J/\psi \rightarrow l^+ l^-]$* , Phys. Rev. D **88.3** (2013) 032007, DOI: 10.1103/PhysRevD.88.032007 (cited on page 18).
- [92] C. Lazzeroni *et al.*, NA62 collaboration, *Precision measurement of the ratio of the charged kaon leptonic decay rates*, Phys. Lett. B **719.4-5** (2013) 326–336, DOI: 10.1016/j.physletb.2013.01.037 (cited on page 18).
- [93] A. Aguilar-Arevalo *et al.*, PIENU collaboration, *Improved measurement of the $\pi \rightarrow e \nu$ branching ratio*, Phys. Rev. Lett. **115.7** (2015) 071801, DOI: 10.1103/PhysRevLett.115.071801 (cited on page 18).
- [94] A. Pich, *Precision tau physics*, Prog. Part. Nucl. Phys. **75** (2014) 41–85, DOI: 10.1016/j.pnpnp.2013.11.002 (cited on page 18).
- [95] C. Albajar *et al.*, UA1 collaboration, *Studies of intermediate vector boson production and decay in UA1 at the CERN Proton-Antiproton Collider*, Z. Phys. C **44** (1989) 15–61, DOI: 10.1007/BF01548582 (cited on page 18).
- [96] F. Abe *et al.*, CDF collaboration, *Measurement of the ratio $(W \rightarrow \tau \nu)/(W \rightarrow e \nu)$, in $p\bar{p}$ collisions at $\sqrt{s} = 1.8$ TeV*, Phys. Rev. Lett. **68.23** (1992) 3398–3402, DOI: 10.1103/PhysRevLett.68.3398 (cited on page 18).
- [97] J. Alitti *et al.*, UA2 collaboration, *A Search for charged Higgs from top quark decay at the CERN $p\bar{p}$ collider*, Phys. Lett. B **280.1-2** (1992) 137–145, DOI: 10.1016/0370-2693(92)90787-5 (cited on page 18).
- [98] F. Abe *et al.*, CDF collaboration, *A Measurement of the production and muonic decay rate of W and Z bosons in $p\bar{p}$ collisions at $\sqrt{s} = 1.8$ TeV*, Phys. Rev. Lett. **69.1** (1992) 28–32, DOI: 10.1103/PhysRevLett.69.28 (cited on page 18).
- [99] S. Abachi *et al.*, D0 collaboration, *W and Z boson production in $p\bar{p}$ collisions at $\sqrt{s} = 1.8$ TeV*, Phys. Rev. Lett. **75.8** (1995) 1456–1461, DOI: 10.1103/PhysRevLett.75.1456 (cited on page 18).
- [100] B. Abbott *et al.*, D0 collaboration, *A measurement of the $W \rightarrow \tau \nu$ production cross-section in $p\bar{p}$ collisions at $\sqrt{s} = 1.8$ TeV*, Phys. Rev. Lett. **84.25** (2000) 5710–5715, DOI: 10.1103/PhysRevLett.84.5710 (cited on page 18).
- [101] S. Schael *et al.*, ALEPH, DELPHI, L3, OPAL, SLD, LEP Electroweak Working Group, SLD Electroweak Group, SLD Heavy Flavour Group, *Precision electroweak measurements on the Z resonance*, Phys. Rept. **427.1-2** (2006) 257–454, DOI: 10.1016/j.physrep.2005.12.006 (cited on page 18).
- [102] S. Schael *et al.*, ALEPH, DELPHI, L3, OPAL, LEP Electroweak, *Electroweak measurements in electron-positron collisions at W -boson-pair energies at LEP*, Phys. Rept. **532.4** (2013) 119–244, DOI: 10.1016/j.physrep.2013.07.004 (cited on page 18).

- [103] M. Aaboud *et al.*, ATLAS collaboration, *Precision measurement and interpretation of inclusive W^+ , W^- and Z/γ^* production cross sections with the ATLAS detector*, Eur. Phys. J. C **77.6** (2017) 367, DOI: 10.1140/epjc/s10052-017-4911-9 (cited on page 18).
- [104] R. Aaij *et al.*, LHCb collaboration, *Measurement of forward $W \rightarrow ev$ production in pp collisions at $\sqrt{s} = 8$ TeV*, J. High Energ. Phys. **10** (2016) 030, DOI: 10.1007/JHEP10(2016)030 (cited on page 18).
- [105] R. Aaij *et al.*, LHCb collaboration, *Measurement of $Z \rightarrow \tau^+ \tau^-$ production in proton-proton collisions at $\sqrt{s} = 8$ TeV*, J. High Energ. Phys. **09** (2018) 159, DOI: 10.1007/JHEP09(2018)159 (cited on page 18).
- [106] CMS collaboration, *A precision measurement of the W boson decay branching fractions in pp collisions at $\sqrt{s} = 13$ TeV*, CMS-PAS-SMP-18-011 (2021), <https://cds.cern.ch/record/2758905> (cited on page 18).
- [107] G. Aad *et al.*, ATLAS collaboration, *Test of the universality of τ and μ lepton couplings in W -boson decays with the ATLAS detector*, Nature Phys. **17** (2021) 813–818, DOI: 10.1038/s41567-021-01236-w (cited on page 18).
- [108] J. L. Hewett, *τ polarization asymmetry in $B \rightarrow X_s \tau^+ \tau^-$* , Phys. Rev. D **53.9** (1996) 4964–4969, DOI: 10.1103/PhysRevD.53.4964 (cited on page 19).
- [109] D. Guetta and E. Nardi, *Searching for new physics in rare $\vec{B}\tau$ decays*, Phys. Rev. D **58.1** (1998) 012001, DOI: 10.1103/PhysRevD.58.012001 (cited on page 19).
- [110] C. Bobeth and U. Haisch, *New Physics in $\Gamma_{12}^S: (\bar{s}b)(\bar{\tau}\tau)$ Operators*, Acta Phys. Polon. B **44.2** (2013) 127–176, DOI: 10.5506/APhysPolB.44.127 (cited on page 19).
- [111] B. Capdevila *et al.*, *Searching for New Physics with $b \rightarrow s \tau^+ \tau^-$ processes*, Phys. Rev. Lett. **120.18** (2018) 181802, DOI: 10.1103/PhysRevLett.120.181802 (cited on page 19).
- [112] J. F. Kamenik *et al.*, *Lepton polarization asymmetries in rare semi-tauonic $b \rightarrow s$ exclusive decays at FCC-ee*, Eur. Phys. J. C **77.10** (2017) 701, DOI: 10.1140/epjc/s10052-017-5272-0 (cited on page 19).
- [113] B. Capdevila *et al.*, *Hadronic uncertainties in $B \rightarrow K^* \mu^+ \mu^-$: a state-of-the-art analysis*, J. High Energ. Phys. **04** (2017) 016, DOI: 10.1007/jhep04(2017)016 (cited on page 19).
- [114] S. Descotes-Genon *et al.*, *On the impact of power corrections in the prediction of $B \rightarrow K^* \mu^+ \mu^-$ observables*, J. High Energ. Phys. **12** (2014) 125, DOI: 10.1007/jhep12(2014)125 (cited on page 19).
- [115] C. Bobeth *et al.*, *Long-distance effects in $B \rightarrow K^* \ell \ell$ from analyticity*, Eur. Phys. J. C **73.6** (2018) 451, DOI: 10.1140/epjc/s10052-018-5918-6 (cited on page 19).
- [116] M. Bordone, G. Isidori and P. A. Pattori, *On the standard model predictions for R_K and R_{K^*}* , Eur. Phys. J. C **76.8** (2016) 440, DOI: 10.1140/epjc/s10052-016-4274-7 (cited on pages 19, 49).

- [117] W. Altmannshofer, P. Stangl and D. M. Straub, *Interpreting hints for lepton flavor universality violation*, Phys. Rev. D **96.5** (2017) 055008, DOI: 10.1103/PhysRevD.96.055008 (cited on page 19).
- [118] S. Descotes-Genon *et al.*, *Global analysis of $b \rightarrow s\ell\ell$ anomalies*, J. High Energ. Phys. **06** (2016) 92, DOI: 10.1007/jhep06(2016)092 (cited on page 19).
- [119] B. Capdevila, *Assessing lepton-flavour non-universality from $B \rightarrow K^*\ell\ell$ angular analyses*, J. Phys.: Conf. Ser. **873** (2016) 012039, DOI: 10.1088/1742-6596/873/1/012039 (cited on pages 19, 21).
- [120] N. Serra, R. S. Coutinho and D. van Dyk, *Measuring the breaking of lepton flavor universality in $B \rightarrow K^*\ell^+\ell^-$* , Phys. Rev. D **95.3** (2017) 35029, DOI: 10.1103/physrevd.95.035029 (cited on page 19).
- [121] D. van Dyk *et al.*, *EOS ("delta456" release)*, 2016, DOI: 10.5281/zenodo.159680, <https://doi.org/10.5281/zenodo.159680> (cited on page 19).
- [122] W. Altmannshofer *et al.*, *Status of the $B \rightarrow K^*\mu^+\mu^-$ anomaly after Moriond 2017*, Eur. Phys. J. C **77.6** (2017) 377, DOI: 10.1140/epjc/s10052-017-4952-0 (cited on page 19).
- [123] D. M. Straub *et al.*, *flav-io/flavio*, version v2.3.1, 2021, DOI: 10.5281/zenodo.5543714 (cited on page 19).
- [124] S. Jäger *et al.*, *Reassessing the discovery potential of the $B \rightarrow K^*\ell^+\ell^-$ decays in the large-recoil region: SM challenges and BSM opportunities*, Phys. Rev. D **93.1** (2016) 14028, DOI: 10.1103/physrevd.93.014028 (cited on page 19).
- [125] R. Aaij *et al.*, LHCb collaboration, *Search for lepton-universality violation in $B^+ \rightarrow K^+\ell^+\ell^-$ decays*, Phys. Rev. Lett. **122.19** (2019) 191801, DOI: 10.1103/PhysRevLett.122.191801 (cited on page 20).
- [126] S. Choudhury *et al.*, Belle collaboration, *Test of lepton flavor universality and search for lepton flavor violation in $B \rightarrow K\ell\ell$ decays*, J. High Energ. Phys. **3** (2021) 105, DOI: 10.1007/jhep03(2021)105 (cited on pages 20, 21, 22).
- [127] S. Wehle *et al.*, Belle collaboration, *Test of lepton-flavor universality in $B \rightarrow K^*\ell^+\ell^-$ decays at Belle*, Phys. Rev. Lett. **126.16** (2021) 161801, DOI: 10.1103/physrevlett.126.161801 (cited on pages 21, 22).
- [128] R. Aaij *et al.*, LHCb collaboration, *Test of lepton universality using $\Lambda_b^0 \rightarrow pK^-\ell^+\ell^-$ decays*, J. High Energ. Phys. **05** (2020) 040, DOI: 10.1007/JHEP05(2020)040 (cited on page 20).
- [129] R. Aaij *et al.*, LHCb collaboration, *Tests of lepton universality using $B^0 \rightarrow K_S^0\ell^+\ell^-$ and $B^+ \rightarrow K^{*+}\ell^+\ell^-$ decays* (2021), arXiv:2110.09501 (cited on pages 21, 22).
- [130] J. Matias *et al.*, *Complete anatomy of $\bar{B}_d \rightarrow \bar{K}^{*0} (\rightarrow K\pi)\ell^+\ell^-$ and its angular distribution*, J. High Energ. Phys. **2012.4** (2012) 104, DOI: 10.1007/jhep04(2012)104 (cited on page 21).

- [131] S. Descotes-Genon *et al.*, *Implications from clean observables for the binned analysis of $B \rightarrow K^* \mu^+ \mu^-$ at large recoil*, J. High Energ. Phys. **01** (2013) 048, DOI: 10.1007/jhep01(2013)048 (cited on page 21).
- [132] J. Aebischer *et al.*, *B-decay discrepancies after Moriond 2019*, Eur. Phys. J. C **80.3** (2020) 252, DOI: 10.1140/epjc/s10052-020-7817-x (cited on page 22).
- [133] M. Algueró *et al.*, *Emerging patterns of new physics with and without lepton flavour universal contributions*, Eur. Phys. J. C **79.8** (2019) 714, DOI: 10.1140/epjc/s10052-019-7216-3, [Addendum: Eur. Phys. J. C **80**, 511 (2020)] (cited on pages 22, 23).
- [134] A. Arbey *et al.*, *Update on the $b \rightarrow s$ anomalies*, Phys. Rev. D **100** (2019) 015045, DOI: 10.1103/physrevd.100.015045 (cited on page 22).
- [135] M. Ciuchini *et al.*, *New Physics in $b \rightarrow s \ell^+ \ell^-$ confronts new data on lepton universality*, Eur. Phys. J. C **79.8** (2019) 719, DOI: 10.1140/epjc/s10052-019-7210-9 (cited on page 22).
- [136] A. K. Alok *et al.*, *Continuing search for new physics in $b \rightarrow s \mu^+ \mu^-$ decays: two operators at a time*, J. High Energ. Phys. **6** (2019) 089, DOI: 10.1007/jhep06(2019)089 (cited on page 22).
- [137] A. Arbey *et al.*, *Update on the $b \rightarrow s$ anomalies*, Phys. Rev. D **100.1** (2019) 015045, DOI: 10.1103/PhysRevD.100.015045 (cited on page 22).
- [138] T. Hurth, F. Mahmoudi and S. Neshatpour, *Implications of the new LHCb angular analysis of $B \rightarrow K^* \mu^+ \mu^-$: Hadronic effects or new physics?*, Phys. Rev. D **102.5** (2020) 055001, DOI: 10.1103/PhysRevD.102.055001 (cited on page 22).
- [139] G. Isidori *et al.*, *On the significance of new physics in $b \rightarrow s \ell^+ \ell^-$* , Phys. Lett. B **822** (2021) 136644, DOI: 10.1016/j.physletb.2021.136644 (cited on page 22).
- [140] W. Altmannshofer and P. Stangl, *New physics in rare B decays after Moriond 2021*, Eur. Phys. J. C **81.10** (2021) 952, DOI: 10.1140/epjc/s10052-021-09725-1 (cited on page 23).
- [141] B. Gripaio, M. Nardecchia and S. A. Renner, *Composite leptoquarks and anomalies in B-meson decays*, J. High Energ. Phys. **2015** (2015) 6, DOI: 10.1007/JHEP05(2015)006 (cited on page 22).
- [142] G. Hiller and M. Schmaltz, *R_K and future $b \rightarrow s \ell \ell$ physics beyond the standard model opportunities*, Phys. Rev. D **90.5** (2014) 54014, DOI: 10.1103/physrevd.90.054014 (cited on page 22).
- [143] S. Sahoo and R. Mohanta, *Scalar leptoquarks and the rare B meson decays*, Phys. Rev. D **91.9** (2015) 094019, DOI: 10.1103/physrevd.91.094019 (cited on page 22).
- [144] M. Bauer *et al.*, *Minimal leptoquark explanation for the $R_{D^{(*)}}$, R_K , and $(g - 2)_g$ anomalies*, Phys. Rev. Lett. **116.14** (2016) 141802, DOI: 10.1103/PhysRevLett.116.141802 (cited on page 22).

- [145] W. Altmannshofer *et al.*, *Quark flavor transitions in $L_\mu - L_\tau$ models*, Phys. Rev. D **89**.9 (2014) 095033, DOI: 10.1103/PhysRevD.89.095033 (cited on page 22).
- [146] A. J. Buras, F. De Fazio and J. Girrbach, *331 models facing new $b \rightarrow s\mu^+\mu^-$ data*, J. High Energ. Phys. **2** (2014) 112, DOI: 10.1007/jhep02(2014)112 (cited on page 22).
- [147] T. Blake, G. Lanfranchi and D. M. Straub, *Rare B decays as tests of the Standard Model*, Prog. Part. Nucl. Phys. **92** (2017) 50, DOI: <https://doi.org/10.1016/j.ppnp.2016.10.001> (cited on page 22).
- [148] J. P. Lees *et al.*, BaBar-Kollaboration, *Evidence for an excess of $\bar{B} \rightarrow D^{(*)}\tau^-\bar{\nu}_\tau$ decays*, Phys. Rev. Lett. **109**.10 (2012) 101802, DOI: 10.1103/physrevlett.109.101802 (cited on page 23).
- [149] R. Aaij *et al.*, LHCb collaboration, *Measurement of the ratio of branching fractions $\mathcal{B}(\bar{B}^0 \rightarrow D^{*+}\tau^-\bar{\nu}_\tau)/\mathcal{B}(\bar{B}^0 \rightarrow D^{*+}\mu^-\bar{\nu}_\mu)$* , Phys. Rev. Lett. **115**.11 (2015) 111803, DOI: 10.1103/PhysRevLett.115.111803, [Erratum: Phys. Rev. Lett. 115 (2015) 159901] (cited on page 23).
- [150] R. Aaij *et al.*, LHCb collaboration, *Test of lepton flavor universality by the measurement of the $B^0 \rightarrow D^{*-}\tau^+\nu_\tau$ branching fraction using three-prong τ decays*, Phys. Rev. D **97**.7 (2018) 072013, DOI: 10.1103/PhysRevD.97.072013 (cited on page 23).
- [151] M. Huschle *et al.*, Belle collaboration, *Measurement of the branching ratio of $\bar{B} \rightarrow D^{(*)}\tau^-\bar{\nu}_\tau$ relative to $\bar{B} \rightarrow D^{(*)}\ell^-\bar{\nu}_\ell$ decays with hadronic tagging at Belle*, Phys. Rev. D **92**.7 (2015) 72014 (cited on page 23).
- [152] S. Hirose *et al.*, Belle collaboration, *Measurement of the τ lepton polarization and $R(D^*)$ in the decay $\bar{B} \rightarrow D^*\tau^-\bar{\nu}_\tau$* , Phys. Rev. Lett. **118**.21 (2017) 211801 (cited on page 23).
- [153] Y. Amhis *et al.*, HFLAV, *Averages of b -hadron, c -hadron, and τ -lepton properties as of summer 2016*, Update on <http://www.slac.stanford.edu/xorg/hfag/semi/fpcp17/RDRDs.html>, 2016, arXiv:1612.07233 [hep-ex] (cited on page 23).
- [154] F. Kurylo, *Ferdinand Braun: Leben und Wirken des Erfinders der Braunschen Röhre, Nobelpreisträger 1909*, Heinz Moos Verlag, 1965 (cited on page 25).
- [155] E. O. Lawrence and M. S. Livingston, *The Production of high speed light ions without the use of high voltages*, Phys. Rev. **40**.1 (1932) 19–35, DOI: 10.1103/PhysRev.40.19 (cited on page 25).
- [156] E. M. McMillan, *The Synchrotron—A proposed high energy particle accelerator*, Phys. Rev. **68**.5–6 (1945) 143–144, DOI: 10.1103/PhysRev.68.143 (cited on page 25).
- [157] J.-P. Burnet *et al.*, *Fifty years of the CERN Proton Synchrotron: volume 1*, CERN Yellow Reports: Monographs, 2011, DOI: 10.5170/CERN-2011-004 (cited on page 25).

- [158] B. Aubert *et al.*, BaBar collaboration, *The BaBar detector*, Nucl. Instrum. Meth. A **479.1** (2002) 1–116, DOI: 10.1016/S0168-9002(01)02012-5 (cited on page 25).
- [159] A. Abashian *et al.*, Belle collaboration, *The Belle detector*, Nucl. Instrum. Meth. A **479.1** (2002) 117–232, DOI: 10.1016/S0168-9002(01)02013-7 (cited on page 26).
- [160] T. Abe *et al.*, Belle II collaboration, *Belle II technical design report*, 2010, arXiv: 1011.0352 [physics.ins-det] (cited on pages 26, 146).
- [161] L. Evans and P. Bryant, *LHC Machine*, J. Instrum. **3** (2008) 08001, DOI: 10.1088/1748-0221/3/08/S08001 (cited on page 26).
- [162] O. S. Brüning *et al.*, *LHC design report*, CERN Yellow Reports: Monographs, 2004, DOI: 10.5170/CERN-2004-003-V-1 (cited on page 26).
- [163] G. Rumolo *et al.*, *LHC experience with different bunch spacings in 2011 (25, 50, 75 ns)*, Chamonix 2012 Workshop on LHC Performance (2012), DOI: 10.5170/CERN-2012-006.89 (cited on page 27).
- [164] A. A. Alves *et al.*, LHCb collaboration, *The LHCb Detector at the LHC*, J. Instrum. **3** (2008) S08005, DOI: 10.1088/1748-0221/3/08/S08005 (cited on pages 27, 29, 30, 33, 36).
- [165] S. Chatrchyan *et al.*, CMS collaboration, *The CMS experiment at the CERN LHC*, J. Instrum. **3** (2008) S08004, DOI: 10.1088/1748-0221/3/08/S08004 (cited on page 27).
- [166] G. Aad *et al.*, ATLAS collaboration, *The ATLAS Experiment at the CERN Large Hadron Collider*, J. Instrum. **3** (2008) S08003, DOI: 10.1088/1748-0221/3/08/S08003 (cited on page 27).
- [167] K. Aamodt *et al.*, ALICE collaboration, *The ALICE experiment at the CERN LHC*, J. Instrum. **3** (2008) S08002, DOI: 10.1088/1748-0221/3/08/S08002 (cited on page 27).
- [168] E. Mobs, *The CERN accelerator complex - August 2018. Complexe des accélérateurs du CERN - Août 2018* (2018), <https://cds.cern.ch/record/2636343> (cited on page 27).
- [169] R. Aaij *et al.*, LHCb collaboration, *Measurement of the b -quark production cross-section in 7 and 13 TeV pp collisions*, Phys. Rev. Lett. **118.5** (2017) 052002, DOI: 10.1103/PhysRevLett.118.052002, [Erratum: Phys. Rev. Lett. 119, 169901 (2017)] (cited on page 28).
- [170] R. Aaij *et al.*, LHCb collaboration, *Measurement of the inelastic pp cross-section at a centre-of-mass energy of $\sqrt{s} = 7$ TeV*, J. High Energ. Phys. **02** (2015) 029, DOI: 10.1007/J.HighEnergy.Phys.02(2015)129 (cited on page 28).
- [171] R. Aaij *et al.*, LHCb collaboration, *Measurement of the inelastic pp cross-section at a centre-of-mass energy of $\sqrt{s} = 13$ TeV*, J. High Energ. Phys. **06** (2018) 100, DOI: 10.1007/JHEP06(2018)100 (cited on page 28).

- [172] C. Elsässer, LHCb collaboration, $\bar{b}b$ production angle plots, https://lhcb.web.cern.ch/lhcb/speakersbureau/html/bb_ProductionAngles.html (cited on page 29).
- [173] LHCb collaboration, *LHCb Operations Plots*, <https://lbggroups.cern.ch/online/OperationsPlots/index.htm> (cited on page 31).
- [174] P. R. Barbosa-Marinho *et al.*, LHCb collaboration, *LHCb VELO (Vertex Locator): technical design report*, CERN, 2001, <https://cds.cern.ch/record/504321> (cited on page 32).
- [175] R. Aaij *et al.*, LHCb VELO group, *Performance of the LHCb Vertex Locator*, J. Instrum. **9** (2014) P09007, DOI: 10.1088/1748-0221/9/09/p09007 (cited on page 32).
- [176] P. R. Barbosa-Marinho *et al.*, LHCb collaboration, *LHCb inner tracker: technical design report*, 2002, <https://cds.cern.ch/record/582793> (cited on page 34).
- [177] P. R. Barbosa-Marinho *et al.*, LHCb Collaboration, *LHCb outer tracker: technical design report*, 2001, <https://cds.cern.ch/record/519146> (cited on page 34).
- [178] R. Arink *et al.*, LHCb Outer Tracker group, *Performance of the LHCb outer tracker*, J. Instrum. **9** (2014) P01002, DOI: 10.1088/1748-0221/9/01/p01002 (cited on page 34).
- [179] M. Adinolfi *et al.*, LHCb RICH collaboration, *Performance of the LHCb RICH detector at the LHC*, Eur. Phys. J. C **73** (2013) 2431, DOI: 10.1140/epjc/s10052-013-2431-9 (cited on pages 34, 36).
- [180] S. Amato *et al.*, LHCb collaboration, *LHCb RICH: technical design report*, 2000, <https://cds.cern.ch/record/494263> (cited on pages 34, 35).
- [181] A. Papanestis and C. D'Ambrosio, LHCb RICH Collaboration, *Performance of the LHCb RICH detectors during the LHC Run II*, Nucl. Instrum. Meth. A **876**.CERN-LHCb-PUB-2017-012 (2017) 221–224, DOI: 10.1016/j.nima.2017.03.009 (cited on page 34).
- [182] D. Derkach *et al.*, LHCb collaboration, *Machine-Learning-based global particle-identification algorithms at the LHCb experiment*, J. Phys.: Conf. Ser. **1085**.4 (2018) 042038, DOI: 10.1088/1742-6596/1085/4/042038 (cited on page 35).
- [183] C. Abellán Beteta *et al.*, LHCb calorimeter group, *Calibration and performance of the LHCb calorimeters in Run 1 and 2 at the LHC*, CERN-LHCb-DP-2020-001 (2020), arXiv:2008.11556 [physics.ins-det] (cited on page 37).
- [184] A. A. Alves *et al.*, *Performance of the LHCb muon system*, J. Instrum. **8** (2013) P02022, DOI: 10.1088/1748-0221/8/02/p02022 (cited on pages 36, 38).
- [185] P. R. Barbosa-Marinho *et al.*, LHCb collaboration, *LHCb muon system: technical design report*, CERN-LHCC-2001-010 (2001), <https://cds.cern.ch/record/504326> (cited on page 36).

- [186] Dordei, F., *LHCb detector and trigger performance in Run II*, EPJ Web Conf. **164** (2017) 01016, DOI: 10.1051/epjconf/201716401016 (cited on page 37).
- [187] F. Alessio *et al.*, *The LHCb data acquisition during LHC Run 1*, J. Phys.: Conf. Ser. **513.1** (2014) 012033, DOI: 10.1088/1742-6596/513/1/012033 (cited on page 37).
- [188] R. Aaij *et al.*, *A comprehensive real-time analysis model at the LHCb experiment*, J. Instrum. **14.4** (2019) P04006, DOI: 10.1088/1748-0221/14/04/P04006 (cited on page 37).
- [189] J. Albrecht *et al.*, *Performance of the LHCb High Level Trigger in 2012*, J. Phys.: Conf. Ser. **513.1** (2014) 012001, DOI: 10.1088/1742-6596/513/1/012001 (cited on pages 37, 39).
- [190] R. Aaij *et al.*, *The LHCb trigger and its performance in 2011*, J. Instrum. **8** (2013) P04022, DOI: 10.1088/1748-0221/8/04/p04022 (cited on pages 37, 39).
- [191] R. Aaij *et al.*, LHCb collaboration, *Design and performance of the LHCb trigger and full real-time reconstruction in Run 2 of the LHC*, J. Instrum. **14** (2019) P04013, DOI: 10.1088/1748-0221/14/04/p04013 (cited on pages 38, 39, 59).
- [192] V. V. Gligorov, C. Thomas and M. Williams, LHCb collaboration, *The HLT inclusive B triggers*, CERN-LHCb-PUB-2011-016 (2011), <https://cds.cern.ch/record/1384380> (cited on page 39).
- [193] R. Aaij *et al.*, *Tesla: an application for real-time data analysis in high energy physics*, Comput. Phys. Commun. **208** (2016) 35–42, DOI: 10.1016/j.cpc.2016.07.022 (cited on page 39).
- [194] G. Barrand *et al.*, *GAUDI — A software architecture and framework for building HEP data processing applications*, Comput. Phys. Commun. **140.1–2** (2001) 45, DOI: 10.1016/S0010-4655(01)00254-5 (cited on page 41).
- [195] *The GAUSS project*, 2021, <https://lhcbdoc.web.cern.ch/lhcbdoc/gauss/> (cited on page 41).
- [196] T. Sjöstrand *et al.*, *PYTHIA 6.4 physics and manual*, J. High Energ. Phys. **05** (2006) 26, DOI: 10.1088/1126-6708/2006/05/026 (cited on page 41).
- [197] I. Belyaev *et al.*, *Handling of the generation of primary events in Gauss, the LHCb simulation framework*, J. Phys.: Conf. Ser. **331** (2011) 032047, DOI: 10.1088/1742-6596/331/3/032047 (cited on page 41).
- [198] D. J. Lange, *The EvtGen particle decay simulation package*, Nucl. Instrum. Meth. A **462.1–2** (2001) 152, DOI: 10.1016/S0168-9002(01)00089-4 (cited on page 41).
- [199] P. Golonka and Z. Was, *PHOTOS Monte Carlo: a precision tool for QED corrections in Z and W decays*, Eur. Phys. J. C **45** (2006) 97–107, DOI: 10.1140/epjc/s2005-02396-4 (cited on page 41).
- [200] S. Agostinelli *et al.*, *GEANT4 — a simulation toolkit*, Nucl. Instrum. Methods. Phys. Res. A **506.3** (2003) 250–303, DOI: 10.1016/S0168-9002(03)01368-8 (cited on page 41).

- [201] *The BOOLE project*, 2021, <https://lhcbdoc.web.cern.ch/lhcbdoc/boole/> (cited on page 41).
- [202] *The MOORE project*, 2021, <https://lhcbdoc.web.cern.ch/lhcbdoc/moore/> (cited on page 42).
- [203] *The BRUNEL project*, 2021, <https://lhcbdoc.web.cern.ch/lhcbdoc/brunel/> (cited on page 42).
- [204] *The DAVINCI project*, 2021, <https://lhcbdoc.web.cern.ch/lhcbdoc/davinci/> (cited on page 42).
- [205] R. Brun and F. Rademakers, *ROOT: An object oriented data analysis framework*, Nucl. Instrum. Meth. A **389**.1–2 (1997) 81–86, DOI: 10.1016/S0168-9002(97)00048-X (cited on page 42).
- [206] F. Desse, *Angular analysis of $B^0 \rightarrow K^{*0} e^+ e^-$ decays with the LHCb detector and upgrade of the electronics of the calorimeters*, Doctoral thesis, 2020, <https://cds.cern.ch/record/2730230> (cited on page 45).
- [207] R. B. Calladine, *Determination of the $r_{J/\psi}^K$ and $r_{J/\psi}^{K^*}$ ratios for lepton flavour universality measurements at LHCb*, Doctoral thesis, 2020, <https://etheses.bham.ac.uk/id/eprint/11577> (cited on page 45).
- [208] D. Y. Tou, *Test of lepton flavour universality in $b \rightarrow s \ell^+ \ell^-$ decays*, Doctoral thesis, Sorbonne University, 2020, <http://www.theses.fr/2020SORUS409> (cited on pages 45, 111).
- [209] R. Aaij *et al.*, LHCb collaboration, *Test of lepton universality in $b \rightarrow s \ell^+ \ell^-$ decays* (2022), in preparation with preliminary title (cited on pages 45, 49, 120, 121, 173, 174).
- [210] W. D. Hulsbergen, *The global covariance matrix of tracks fitted with a Kalman filter and an application in detector alignment*, Nucl. Instrum. Methods Phys. Res. A **600**.2 (2009) 471–477, DOI: 10.1016/j.nima.2008.11.094 (cited on pages 60, 111).
- [211] V. V. Gligorov, LHCb collaboration, *Reconstruction of the channel $B_d^0 \rightarrow D^+ \pi^-$ and background classification at LHCb (revised)*, CERN-LHCb-2007-044 (2007), <https://cds.cern.ch/record/1035682> (cited on page 60).
- [212] A. Perieanu, LHCb collaboration, *A fast algorithm to identify and remove clone tracks*, CERN-LHCb-2008-020 (2008), <https://cds.cern.ch/record/1102942> (cited on page 63).
- [213] M. Needham, LHCb collaboration, *Clone track identification using the Kullback-Liebler distance*, CERN-LHCb-2008-002 (2008), <http://cds.cern.ch/record/1082460> (cited on page 63).
- [214] L. Breiman *et al.*, *Classification and regression trees*, Routledge, 1984, DOI: 10.1201/9781315139470 (cited on page 67).

- [215] J. H. Friedman, *Greedy function approximation: a gradient boosting machine*, *Ann. Stat.* **29.5** (2001) 1189–1232, DOI: 10.1214/aos/1013203451 (cited on page 67).
- [216] L. Prokhorenkova *et al.*, *CatBoost: unbiased boosting with categorical features*, 2019, arXiv:1706.09516 [cs.LG] (cited on page 67).
- [217] T. Likhomanenko *et al.*, *Reproducible Experiment Platform*, *J. Phys.: Conf. Ser.* **664.5** (2015) 052022, DOI: 10.1088/1742-6596/664/5/052022 (cited on page 67).
- [218] A. Blum, A. Kalai and J. Langford, *Beating the hold-out: bounds for k -Fold and progressive cross-validation*, *Proceedings of the twelfth annual conference on computational learning theory COLT '99* (1999) 203–208, DOI: 10.1145/307400.307439 (cited on page 68).
- [219] M.-H. Schune, F. Polci and M. Borsato, LHCb collaboration, *HOP an additional tool for decays involving electrons*, CERN-LHCb-INT-2015-037 (2015), <https://cds.cern.ch/record/2102345> (cited on page 69).
- [220] L. Anderlini *et al.*, LHCb collaboration, *The PIDCalib package*, CERN-LHCb-PUB-2016-021 (2016), <https://cds.cern.ch/record/2202412> (cited on page 78).
- [221] L. Anderlini *et al.*, LHCb collaboration, *Calibration samples for particle identification at LHCb in Run 2*, CERN-LHCb-PUB-2016-005 (2016), <https://cds.cern.ch/record/2134057> (cited on page 79).
- [222] R. Aaij *et al.*, *Selection and processing of calibration samples to measure the particle identification performance of the LHCb experiment in Run 2*, *EPJ Tech. Instrum.* **6.1** (2019) 1, DOI: 10.1140/epjti/s40485-019-0050-z (cited on page 79).
- [223] L. Anderlini *et al.*, LHCb collaboration, *Computing strategy for PID calibration samples for LHCb Run 2*, CERN-LHCb-PUB-2016-020 (2016), <https://cds.cern.ch/record/2199780> (cited on page 79).
- [224] M. Pivk and F. R. Le Diberder, *s Plot: A statistical tool to unfold data distributions*, *Nucl. Instrum. Meth. A* **555.1–2** (2005) 356–369, DOI: 10.1016/j.nima.2005.08.106 (cited on pages 79, 87).
- [225] T. Skwarnicki, *A study of the radiative cascade transitions between the Upsilon-prime and Upsilon resonances*, *Doctoral thesis, Institute of Nuclear Physics, Krakow, 1986*, <http://inspirehep.net/record/230779/%7D%7BDESY-F31-86-02%7D%7D> (cited on pages 81, 103, 113).
- [226] H. Albrecht *et al.*, ARGUS collaboration, *Measurement of the polarization in the decay $B \rightarrow J/\psi K^*$* , *Phys. Lett. B* **340.3** (1994) 217–220, DOI: 10.1016/0370-2693(94)01302-0 (cited on page 81).

- [227] E. A. Smith, S. Schmitt and C. M. Langenbruch, LHCb collaboration, *On the PID-response dependency for dielectron pairs*, CERN-LHCb-INT-2021-008 (2021), <https://cds.cern.ch/record/2772374> (cited on page 82).
- [228] A. Poluektov, LHCb collaboration, *Correction of simulated particle identification response in LHCb using kernel density estimation*. CERN-LHCb-INT-2017-007 (2017), <https://cds.cern.ch/record/2260281> (cited on page 83).
- [229] R. Aaij *et al.*, LHCb collaboration, *Measurement of the track reconstruction efficiency at LHCb*, J. Instrum. **10** (2015) P02007, DOI: 10.1088/1748-0221/10/02/P02007 (cited on page 84).
- [230] R. Aaij *et al.*, LHCb collaboration, *Measurement of the electron reconstruction efficiency at LHCb*, J. Instrum. **14** (2019) P11023, DOI: 10.1088/1748-0221/14/11/P11023 (cited on page 84).
- [231] A. Rogozhnikov, *Reweighting with Boosted Decision Trees*, J. Phys. Conf. Ser. **762**.1 (2016) 012036, DOI: 10.1088/1742-6596/762/1/012036 (cited on page 87).
- [232] S. Tolk *et al.*, LHCb collaboration, *Data driven trigger efficiency determination at LHCb*, CERN-LHCb-PUB-2014-039 (2014), <https://cds.cern.ch/record/1701134> (cited on page 87).
- [233] A. Kolmogorov, *Sulla determinazione empirica di una legge di distribuzione*, Inst. Ital. Attuari, Giorn. **4** (1933) 83–91 (cited on page 99).
- [234] W. Verkerke *et al.*, *The RooFIT toolkit for data modeling*, 2021, <http://roofit.sourceforge.net> (cited on pages 111, 113).
- [235] D. Martínez Santos and F. Dupertuis, *Mass distributions marginalized over per-event errors*, Nucl. Instrum. Meth. A **764** (2014) 150–155, DOI: 10.1016/j.nima.2014.06.081 (cited on page 113).
- [236] P. Ball and R. Zwicky, *$B_{d,s} \rightarrow \rho, \omega, K^*, \phi$ decay form-factors from light-cone sum rules revisited*, Phys. Rev. D **71**.1 (2005) 014029, DOI: 10.1103/PhysRevD.71.014029 (cited on page 126).
- [237] A. Bharucha, D. M. Straub and R. Zwicky, *$B \rightarrow V\ell^+\ell^-$ in the Standard Model from light-cone sum rules*, J. High Energy Phys. **08** (2016) 098, DOI: 10.1007/JHEP08(2016)098 (cited on page 126).
- [238] N. Gubernari, A. Kokulu and D. van Dyk, *$B \rightarrow P$ and $B \rightarrow V$ form factors from B -meson light-cone sum rules beyond leading twist*, J. High Energy Phys. **01** (2019) 150, DOI: 10.1007/JHEP01(2019)150 (cited on page 126).
- [239] I. Bediaga *et al.*, LHCb collaboration, *Framework TDR for the LHCb upgrade: technical design report*, CERN-LHCC-2012-007 (2012), <https://cds.cern.ch/record/1443882> (cited on page 146).
- [240] R. Aaij *et al.*, LHCb collaboration, *Framework TDR for the LHCb upgrade II - opportunities in flavour physics, and beyond, in the HL-LHC era*, CERN-LHCC-2021-012 (2021), <https://cds.cern.ch/record/2776420> (cited on page 146).

- [241] S. Mukherjee, CMS collaboration, *Data scouting and data parking with the CMS high level trigger*, PoS **EPS-HEP2019** (2020) 139, DOI: 10.22323/1.364.0139 (cited on page 146).
- [242] W. Altmannshofer *et al.*, Belle II collaboration, *The Belle II physics book*, PTEP **2019.12** (2019) 123C01, DOI: 10.1093/ptep/ptz106, [Erratum: PTEP 2020, 029201 (2020)] (cited on page 146).

Acknowledgement

I have written this doctoral thesis in dark times. Many pages were written in Covid19 isolation, in the quarantine room, with television images of the war flaring up in Ukraine. It was written when the news of the unexpected death of our esteemed Professor Bernhard Spaan reached us and when the sudden death of our much valued reviewer, Professor Sheldon Stone, became known.

During the work on this project, it was not possible to meet the international colleagues who worked with me on the measurement. Personal contact was not possible for several years due to the rapid pandemic events.

Especially after returning from isolation to semi-normal office life, it became apparent that personal contact and exchange characterise science at its core. It is the encounters, the discussions, and the solidarity that have been missing for so long. I want to thank Professor Spaan who was a first inspiration for me to start with studying physics and who made many things possible for me. This is also why I want to dedicate this thesis to him. His loss is clearly felt.

When I start with the acknowledgements, these will include people who have significantly accompanied the long and rocky path of this work and helped me make it possible in the first place.

First of all, I want to thank my doctoral supervisor Johannes. He suddenly became the sole head of the working group after the death of Bernhard Spaan and he has mastered it insanely well. But he also has accompanied me since my first particle physics lectures. As a curious freshman, I still remember my question to him about what precisely these virtual particles were. Probably he also still remembers this strange email from me? He has always generously supported me in my various scholarships, research stays, and further education. He has always given me the greatest possible freedom in my scientific development. When I needed support, his door was always open. I hope that I can give some of that back with my work.

I would also like to thank my second examiner, Professor Kevin Kröniger, who is not only currently serving our faculty as dean, but was also standing at the front of the blackboard with Johannes in the same first particle physics lecture I attended. So I want to thank him very much for reviewing my thesis.

In the last few weeks of writing, one person, in particular, was admirably there for me. Although his family in Kharkiv in Ukraine was and still is in the most severe danger, he regularly urged me to send him new chapters for correction. He told me that no one would benefit if Ukrainians did not do physics now, which taught me that it is a great privilege to be able to work like we do. Thank you very much, Vitalii, for your support. I hope that over time I have been able to give a small part of it back or that I will be able to do so in the future.

I would also like to thank my colleagues in the “Schaltzentrale” of our working group Maik and Julian, for their support and the enjoyable atmosphere in our office. Your engagement is inspiring and your encouragement helped me a lot Maik. And your dry humour and jokes, Julian, often cheered me up. I still remember the time when I supervised your Master’s thesis. Today we are working together as colleagues and most often I am the person now asking for advice.

I would like to thank all my other colleagues who helped me with comments during the correction of my text: Dirk, Dominik, Elena, Fabio, Jan, Janina, Lukas, Maik, Miroslav, and Sophie.

And I would like to thank the whole Dortmund working group for sticking it out during the pandemic and for what has become such a friendly working atmosphere.

I would like to thank my colleagues in the R_X measurement team. It was nice spending weekends and nights with you dedicated to our common goal. I especially want to thank Simone and Renato for introducing me to the measurement. I want to especially thank Renato for always being so dedicated and kind even in the most stressful times. I want to thank Vava for welcoming me at the Sorbonne in Paris in the old days, and all the team members: Christoph, Da Yu, Eluned, Fabrice, Marie-Helene, Nigel, Sebastian, Stephan, and Vitalii. Many thanks are also going out to Vava, who helped us immensely organise and coordinate the project in the past two years. He selflessly pushed us over many limits and made us work as a team.

I would like to thank all the members of the LHCb collaboration who have made working in the past years an enjoyable and productive endeavour and form an exceptional collaboration.

I would also like to thank the German National Academic Foundation (Studienstiftung des deutschen Volkes) for their support throughout my studies. Furthermore, I would like to thank the Foundation for the prestigious doctoral studies scholarship I was granted, especially Dr Antes, Dr Mayer, and Dr Scheider, for their support and advice. In this context, I would also like to thank my long-time mentor Professor Barbara Welzel, who has accompanied me since I started studying in 2012.

I would like to thank professor, emeritus Dietrich Wegener for the discussion about the thesis.

Then I especially thank all my friends for the many conversations, the support, and the often necessary distraction.

“The good life is a process, not a state of being. It is a direction not a destination.”
(Carl Rogers)

